JOHANNES GUTENBERG UNIVERSITÄT MAINZ

JG|U

Spectral and Chiral Properties of Hot QCD Matter around the Crossover and the Photon Emissivity of the Quark-Gluon Plasma from Lattice QCD

Dissertation
zur Erlangung des Grades
„Doktor der Naturwissenschaften"

am Fachbereich Physik, Mathematik und Informatik
der Johannes Gutenberg-Universität
in Mainz

Ardit Krasniqi
geboren in Prizren

Mainz, 2025

Ardit Krasniqi: *Spectral and Chiral Properties of Hot QCD Matter around the Crossover and the Photon Emissivity of the Quark-Gluon Plasma from Lattice QCD*
Berichterstatter: Prof. Dr. Xxxxxx X. Xxxxx, Prof. Dr. Xxxxx Xxxxxxxxx
Datum der Promotionsprüfung: 25.03.2026

Abstract

In this work, we explore thermal strongly interacting matter across the chiral crossover using the lattice regularization of Quantum Chromodynamics (QCD). While finite temperature is naturally implemented in lattice QCD, the extraction of real-time observables from Monte Carlo data remains a significant challenge.

In the first part, we investigate the properties of the pion quasiparticle along a coarse temperature scan around the finite temperature crossover. Using simulations with $\mathcal{O}(a)$-improved Wilson quarks and physical up, down and strange quark masses, we study the properties of thermal QCD matter at the temperatures $T = \{128, 154, 192\}$ MeV with a fixed lattice spacing $a = 0.064\,\text{fm}$ and volume $V = (6.1\,\text{fm})^3$. At low momenta, the dispersion relation of the pion quasiparticle is governed by a renormalization-group-invariant (RGI) parameter $u(T)$, which is directly accessible on the lattice from screening quantities. This temperature-dependent parameter plays a dual role: it predicts the modified dispersion relation and relates the (*static*) screening mass to the (*dynamic*) pole mass. We find that the pion quasiparticle—defined via the low-energy pole of the axial charge two-point function—becomes lighter with increasing temperature. We argue, based on hydrodynamic considerations, that this pole becomes purely diffusive above the chiral crossover. We further analyze the thermal modifications of the isovector vector and axial-vector spectral functions using the Backus-Gilbert method. The vector channel shows enhancement at low energies and depletion around 1 GeV, while the axial-vector channel exhibits a larger enhancement below 1 GeV. These findings are consistent with spectral sum rules. Additionally, we study several chiral symmetry restoration order parameters, with particular focus on the vector–axial-vector correlator difference, which is phenomenologically relevant and found to be suppressed by over an order of magnitude at the crossover.

The second part of this thesis addresses the photon emissivity of the quark-gluon plasma (QGP). Estimating the full energy-differential photon emissivity from lattice QCD requires solving a numerically ill-posed inverse problem. However, energy-integrated quantities—such as energy moments—can be accessed without this inversion by evaluating spatially transverse Euclidean correlators $H_E(\omega_n)$ at imaginary spatial momenta. We compute the first energy moment $H_E(\omega_1)$ of the thermal electromagnetic spectral function $\sigma_{\text{em}}(\omega)$ across the same three $N_\text{f} = 2 + 1$ ensembles used in the pion study. Our results indicate that $H_E(\omega_1)$ already reaches values typical of the high-temperature phase near the chiral crossover, suggesting substantial photon emission in the late stages of heavy-ion collisions (HICs). Apart from this, we examine the first two energy-moments, this time at a fixed temperature in the chirally restored phase using three $N_\text{f} = 2$ ensembles with lattice spacings in the range of $0.033 - 0.049\,\text{fm}$. Utilizing stochastic momentum wall sources, we improve statistical precision on the relevant correlators by a factor of up to ≈ 40 compared to our previous analysis using point sources. This allows for a controlled continuum extrapolation of the first two energy moments and a detailed assessment of systematic uncertainties related to large source-sink separations. Our result for the difference of these two moments—sensitive to photon energies $\omega \gtrsim \pi T$—is below, but compatible with, the value obtained from integrating the leading-order weak-coupling photon spectrum. These findings contribute to the ongoing effort to resolve the *direct photon puzzle* in HIC phenomenology, where current models struggle to simultaneously account for both photon yield and azimuthal anisotropy.

Finally, we take a first look at the challenging third Matsubara sector and provide a conservative upper bound on the third energy-moment.

Keywords: chiral symmetry restoration, heavy-ion collisions, electromagnetic probes

Zusammenfassung

In dieser Arbeit untersuchen wir thermische, stark wechselwirkende Materie im Bereich des chiralen Crossovers mithilfe der Gitterregularisierung der Quantenchromodynamik (QCD). Obwohl endliche Temperaturen in der Gitter-QCD auf natürliche Weise implementiert sind, stellt die Bestimmung von „real-time“ Observablen aus Monte-Carlo-Daten weiterhin eine erhebliche Herausforderung dar.

Im ersten Teil der Arbeit analysieren wir die Eigenschaften des Pion-Quasiteilchens entlang eines groben Temperaturscans um den chiralen Crossover. Anhand von Simulationen mit $\mathcal{O}(a)$-verbesserten Wilson-Quarks und physikalischen Up-, Down- und Strange-Quarkmassen untersuchen wir Eigenschaften thermischer QCD-Materie für Temperaturen $T = \{128, 154, 192\}$ MeV bei festem Gitterabstand $a = 0{,}064\,\mathrm{fm}$ und einem Volumen von $V = (6{,}1\,\mathrm{fm})^3$. Bei niedrigen Impulsen wird die Dispersionsrelation des Pion-Quasiteilchens durch einen renormierungsgruppeninvarianten Parameter $u(T)$ bestimmt, der direkt über „Screening-Größen“ auf dem Gitter zugänglich ist. Dieser temperaturabhängige Parameter erfüllt eine duale Rolle: Er beschreibt die modifizierte Dispersionsrelation und verknüpft zugleich die (*statische*) „Screening-Masse“ mit der (*dynamischen*) Polmasse. Wir stellen fest, dass das Pion-Quasiteilchen—definiert über den Niederenergie-Pol der Zwei-Punkt-Funktion der axialen Ladung—mit steigender Temperatur leichter wird. Basierend auf hydrodynamischen Überlegungen folgern wir, dass dieser Pol oberhalb des chiralen Crossovers rein diffusiver Natur ist. Darüber hinaus analysieren wir die thermischen Modifikationen der isovektoriellen Vektor- und Axialvektor-Spektralfunktionen unter Anwendung der Backus-Gilbert-Methode. Der Vektorkanal zeigt eine Verstärkung bei niedrigen Energien und eine Abschwächung um 1 GeV, während der Axialvektorkanal eine stärkere Verstärkung unterhalb von 1 GeV aufweist. Diese Beobachtungen sind im Einklang mit spektralen Summenregeln. Zusätzlich untersuchen wir mehrere Ordnungsparameter der Wiederherstellung der chiralen Symmetrie, mit besonderem Fokus auf die phänomenlogisch relevante Vektor–Axialvektor Korrelatordifferenz, die am Crossover um mehr als eine Größenordnung unterdrückt ist.

Der zweite Teil dieser Arbeit befasst sich mit der Photonemissivität des Quark-Gluon-Plasmas (QGP). Die Abschätzung der vollständigen energieabhängigen Photonemissivität aus der Gitter-QCD erfordert die Lösung eines numerisch ill-poseden inversen Problems. Integrierte Größen—wie Energiemomente—lassen sich jedoch ohne eine solche Inversion extrahieren, indem räumlich transversale euklidische Korrelatoren $H_E(\omega_n)$ bei imaginären räumlichen Impulsen betrachtet werden. Wir berechnen das erste Energiemoment $H_E(\omega_1)$ der thermischen elektromagnetischen Spektralfunktion $\sigma_{\mathrm{em}}(\omega)$ auf denselben drei $N_{\mathrm{f}} = 2 + 1$ Ensemblen, die auch in der Pion-Studie verwendet wurden. Unsere Ergebnisse deuten auf eine beträchtliche Photonemission in späten Stadien von Schwerionenkollisionen hin. Zudem analysieren wir die ersten beiden Energiemomente in der Hochtemperatur-Phase anhand von drei $N_{\mathrm{f}} = 2$ Ensemblen mit Gitterabständen im Bereich von $0{,}033-0{,}049$ fm. Der Einsatz stochastischer „momentum-wall-sources“ verbessert die statistische Genauigkeit der relevanten Korrelatoren um einen Faktor von bis zu ≈ 40 im Vergleich zu unserer früheren Analyse mit Punktquellen. Dies ermöglicht eine kontrollierte Kontinuumsextrapolation der ersten beiden Energiemomente und eine detaillierte Betrachtung systematischer Unsicherheiten im Zusammenhang mit großen Quelle-Senke-Abständen. Unser Ergebnis für die Differenz dieser beiden Momente—sensitiv gegenüber Photonenergien $\omega \gtrsim \pi T$—ist zwar geringer als der aus dem führenden schwach gekoppelten Photonenspektrum bestimmte Wert, aber innerhalb der Fehlergrenzen konsistent. Diese Erkenntnisse tragen zur laufenden Untersuchung des sogenannten „*direct photon puzzles*“ in der HIC-Phänomenologie bei, bei dem aktuelle Modelle Schwierigkeiten haben, gleichzeitig sowohl die Photonenanzahl als auch die azimutale Anisotropie zu reproduzieren.

Abschließend werfen wir einen ersten Blick auf den schwierigen dritten Matsubara-Sektor und liefern eine konservative obere Schranke für das dritte Energiemoment.

Publications

[1] Marco Cè, Tim Harris, Ardit Krasniqi, Harvey B. Meyer, and Csaba Török. "Aspects of chiral symmetry in QCD at T=128 MeV". *Phys. Rev. D* 107 2023, pp. 054509. DOI: 10.1103/PhysRevD.107.054509.

[2] Ardit Krasniqi, Marco Cè, Tim Harris, Harvey B. Meyer, Csaba Török, et al. "A $(2+1)$-flavor lattice study of the pion quasiparticle in the thermal hadronic phase at physical quark masses". *PoS* Lattice2022 2022, pp. 0181. DOI: 10.22323/1.430.0181.

[3] Ardit Krasniqi, Marco Cè, Renwick J. Hudspith, and Harvey B. Meyer. "Hot QCD matter around the chiral crossover: A lattice study with O(a)-improved Wilson fermions". *Phys. Rev. D* 110 2024, pp. 114506. DOI: 10.1103/PhysRevD.110.114506.

[4] Ardit Krasniqi, Marco Cè, Tim Harris, Renwick J. Hudspith, Harvey B. Meyer, et al. "The thermal photon emissivity at the QCD chiral crossover from imaginary momentum correlators". *PoS* LATTICE2023 2024, pp. 180. DOI: 10.22323/1.453.0180.

[5] Marco Cè, Tim Harris, Ardit Krasniqi, Harvey B. Meyer, and Csaba Török. "Photon emissivity of the quark-gluon plasma: A lattice QCD analysis of the transverse channel". *Phys. Rev. D* 106 2022, pp. 054501. DOI: 10.1103/PhysRevD.106.054501.

[6] Marco Cè, Tim Harris, Ardit Krasniqi, Harvey B. Meyer, and Csaba Török. "Probing the photon emissivity of the quark-gluon plasma without an inverse problem in lattice QCD". *Phys. Rev. D* 109 2024, pp. 014507. DOI: 10.1103/PhysRevD.109.014507.

[7] Ardit Krasniqi, Marco Cè, Tim Harris, Renwick J. Hudspith, and Harvey B. Meyer. "Probing how bright the quark-gluon plasma glows in lattice QCD". *Phys. Rev. D* 112 2025, pp. 074503. DOI: 10.1103/8dq9-q62p.

[8] H. C. Lange, A. Krasniqi, and S. Scherer. "Quark-mass and 1/Nc corrections to the vector-meson pseudoscalar-meson photon (VPγ) interaction". *Phys. Rev. D* 105 2022, pp. 054001. DOI: 10.1103/PhysRevD.105.054001.

[9] Csaba Török, Marco Cè, Tim Harris, Ardit Krasniqi, Arianna Toniato, et al. "Estimating the thermal photon production rate using lattice QCD". *PoS* LATTICE2021 2021, pp. 172. DOI: 10.22323/1.396.0172.

[10] Csaba Török, Marco Cè, Tim Harris, Ardit Krasniqi, Harvey B. Meyer, et al. "Estimation of the photon production rate using imaginary momentum correlators". *PoS* LATTICE2022 2023, pp. 193. DOI: 10.22323/1.430.0193.

[11] Harvey B. Meyer, Marco Cè, Tim Harris, Ardit Krasniqi, and Csaba Török. "Photon and dilepton production rate in the quark-gluon plasma from lattice QCD". *PoS* LATTICE2022 2023, pp. 186. DOI: 10.22323/1.430.0186.

Statement of Contributions

Most of the results presented in this thesis have already been published. All projects were carried out under the supervision of Xxxxxx X. Xxxxx, whose scientific guidance and feedback have been invaluable throughout.

For the results published in Refs. [1, 2], a new $N_f = 2 + 1$ gauge ensemble was generated by Xxxxxx Xx, and the measurements of the relevant correlation functions were performed by Xxx Xxxxxx using point sources. I independently carried out all subsequent numerical calculations and prepared the initial drafts of the publications, which were then revised and enriched by Xxxxxx X. Xxxxx. During the peer review process, I served as the corresponding author and responded to the referee reports in close coordination with Xxxxxx X. Xxxxx.

Over the past three years, this project has been extended in two main directions. Xxxxx Xx generated two additional ensembles, enabling a coarse temperature scan around the QCD crossover. On these new ensembles, I performed measurements of both temporal and screening two-point correlation functions using stochastic momentum wall sources, as implemented in Xxxxxxx X. Xxxxxxxx's `Witnesser` code. These measurements were mainly carried out on the *Noctua2* cluster in Paderborn, as part of two successful NHR proposals, which I assisted my supervisor in drafting. I conducted the full numerical analysis and wrote the main draft of the resulting publication, which was again enriched through collaboration with Xxxxxx X. Xxxxx. The results have been published in Ref. [3], and I also co-authored the referee reply. The results of Part II of this thesis are almost entirely based on Ref. [3].

Using the same three ensembles, I measured two-point correlation functions at imaginary spatial momentum to probe the thermal photon emissivity of the quark-gluon plasma (QGP) without encountering a numerically ill-defined inverse problem. These measurements were also performed with the `Witnesser` code. I carried out the numerical calculations, data analysis, and interpretation. Results from one ensemble were published in Ref. [4]. This thesis presents, for the first time, the full set of results from the complete temperature scan.

In parallel, the photon emissivity of the QGP was also investigated using three $N_f = 2$ ensembles at fixed lattice spacing in the high-temperature phase. The transverse channel was analyzed in Ref. [5], which lies outside the scope of this thesis. These ensembles were generated by Xxxxx Xx and other former members of the Mainz group. The correlator measurements (using point sources) were carried out by Xxx Xxxxxx and collaborators. My contribution to this project was limited to performing consistency checks with the Backus-Gilbert method, which I later applied in my own work [Refs. [1, 3]]. The numerical work and drafting of the manuscript were done by Xxxxx Xxxxx, who also initiated the analysis of imaginary momentum correlators. I assisted by cross-checking most aspects of this analysis. The resulting article, selected as an Editor's Suggestion by *Physical Review D*, is Ref. [6].

In the past 18 months, I have taken the lead in significantly improving the statistical precision—up to a factor of approximately 40—of the correlators discussed in Ref. [6] by employing stochastic momentum wall sources in the `Witnesser` framework. These high-precision measurements enabled a more thorough investigation of the systematic uncertainties in the long-distance behavior of the correlators. Xxxxxxx X. Xxxxxxxx independently validated key aspects of the numerical calculations. I wrote the main body of the draft, while the introduction and further improvements were contributed by my supervisor. This work has been published in Ref. [7].

Additionally, I contributed to Refs. [8–11], though the results of those projects are not included in this thesis.

Abbreviations

AMY Arnold, Moore and Yaffe 128, 134

ChPT Chiral Perturbation Theory 1, 8
CLS Coordinated Lattice Simulations 30, 34

EFT Effective Field Theory 8

GOR Gell-Mann–Oakes–Renner 52, 77, 78

HIC Heavy-Ion Collision 13, 17–20
HMC Hybrid Monte Carlo 43, 44
HRG hadron resonance gas 54, 75

KMS Kubo-Martin-Schwinger 22, 24

l.h.s. left hand side 64, 75, 78, 80, 83, 84, 96, 98, 99, XXX, XXXI, LVI, LVII
LGT Lattice Gauge Theory 26, 33
LHC Large Hadron Collider 1, 13, 52, 135, 136
LO leading-order 90, 98, 99, 128, LVIII
LQCD Lattice Quantum Chromodynamics 1–3, 5, 7, 8, 20, 26, 27, 29, 37, 39, 40, 43, 45, 136

NLO next-to-leading-order 129

PCAC partially conserved axial current 54, 55, 58, 60, 62, 63, 65, 69, 77, 78

QCD Quantum Chromodynamics 1–3, 5, 26, 28, 30, 33, LIV
QFT Quantum Field Theory 20, 21, 25, 26, LV
QGP Quark-Gluon Plasma 1, 2, 14, 18
QNS quark number susceptibility 54, 73, 100, 135
QSM Quantum Statistical Mechanics 20

r.h.s. right hand side 64, 80, 84, 99, XXX, XXXI, LVI
RGI renormalization-group-invariant III
RHIC Relativistic Heavy-Ion Collider 1, 13, 52, 135

SBM Statistical Bootstrap Model 15, 17
SHM Statistical Hadronization Model 18
SM Standard Model 1

TFT Thermal Field Theory 20, 21

UV ultraviolet 26

w.r.t. with respect to 6

Contents

Abstract III

Zusammenfassung IV

Statement of Contributions VI

Abbreviations VII

1 Introduction 1

I Theoretical and Phenomenological Background 4

2 Quantum Chromodynamics (QCD) 5
2.1 The Euclidean QCD Lagrangian . . . 5
2.2 QCD in the chiral limit . . . 9
2.2.1 Spontaneous Symmetry Breaking . . . 11

3 Ultrarelativistic Heavy Ion Collisions 13
3.1 Statistical hadronization model . . . 14
3.2 Probes of the QGP . . . 18
3.2.1 Charm Quarks . . . 18
3.2.2 Dilepton Production . . . 19

4 Finite Temperature 20
4.1 Quantum Statistical Mechanics . . . 20
4.2 Thermal Field Theory . . . 21
4.3 Thermal Correlation Functions . . . 22
4.4 Spectral Functions . . . 23

5 Lattice QCD 26
5.1 Basic Concepts . . . 26
5.2 A First Glimpse on Euclidean Two-Point Correlation Functions . . . 28
5.3 Scale Setting and Extrapolations . . . 29
5.4 Discretization of the Euclidean QCD Action . . . 31
5.4.1 Discretization of the Free Fermion Action . . . 31
5.4.2 Gauge Invariance on the Lattice and the Naive Fermion Action . . . 32
5.4.3 Wilson Gauge Action . . . 33
5.4.4 The Fermion Doubling Problem . . . 35

5.4.5 Improvement of the Wilson Fermion Action . . . 37
5.5 Improvement of the Vector Current . . . 39
5.6 The Path Integral on the Lattice . . . 39
5.6.1 Pseudofermions . . . 40
5.6.2 Importance Sampling . . . 41
5.6.3 Markov Chains . . . 41
5.6.4 Metropolis Algorithm . . . 42
5.6.5 Hybrid Monte Carlo Algorithm . . . 43
5.7 Calculation of Propagators . . . 44
5.7.1 Inversion of the Dirac Operator . . . 46
5.7.2 The Truncated Solver Method . . . 49

II Spectral and Chiral Properties of Hot QCD Matter around the Crossover 50

6 Hot QCD Matter Around the Chiral Crossover 51
6.1 Introduction . . . 52
6.2 Preliminaries . . . 54
6.2.1 Definition of Operators and Correlation Functions . . . 54
6.2.2 Pion Properties at Finite Temperature . . . 56
6.2.3 The Pole in the Axial-Charge Correlator above the Chiral Crossover . . . 58
6.2.4 Lattice Implementation of the Correlators . . . 60
6.2.5 Numerical Setup . . . 61
6.3 Results on the Pseudoscalar Sector . . . 62
6.3.1 The PCAC Mass: A Control quantity . . . 62
6.3.2 Static correlators: The Pion Screening Mass and Decay Constant . . . 64
6.3.3 Properties of the Pion Quasiparticle . . . 64
6.3.4 Dependence of the Pion Velocity u_f on a Finite Pion Thermal Width $\Gamma(T)$ . . . 66
6.4 Spectral Function Reconstruction with the Backus-Gilbert Method . . . 66
6.5 Comparison with Results from the Literature . . . 69
6.6 Static Mesonic Screening Masses . . . 70
6.7 Isovector Quark Number Susceptibility . . . 73
6.7.1 Comparison with the Hadron Resonance Gas Model . . . 75
6.8 Order Parameters for Chiral Symmetry Restoration . . . 77
6.8.1 The Gell-Mann–Oakes–Renner Relation . . . 77
6.8.2 The (PA_0)-Correlator . . . 78
6.8.3 Dey-Eletsky-Ioffe Mixing Theorem at Finite Quark Mass . . . 78
6.9 Vacuum Subtracted Vector and Axial-Vector Spectral Functions . . . 82
6.10 Conclusion . . . 84

III Probing The Photon Emissivity of the QGP without an Inverse Problem 86

7 Theoretical Framework 87
7.1 Introduction . . . 87
7.2 Imaginary Momentum Correlators . . . 89
7.2.1 Lattice Subtractions . . . 92
7.2.2 The Virtuality Dependence of H_E . . . 94
7.2.3 Lattice Observables . . . 95
7.3 Modeling the Tail of the Integrand of H_E . . . 96
7.3.1 Fit Ansatz for the Tail of the Screening Correlators . . . 97
7.4 The Thermal Photon Rate . . . 98

8 Temperature Scan of the Thermal Photon Emissivity around the Chiral Crossover 101
8.1 Screening Masses in the First Matsubara Sector . . . 101
8.2 Temperature Scan of $H_E(\omega_1)$ . . . 103
8.2.1 Bounding Method . . . 105
8.3 Temperature Scan of the Q^2 Derivative of $H_E(\omega_1, Q^2)$ at $Q^2 = 0$ . . . 108

9 $N_f = 2$ Continuum Extrapolated Results on the First Three Matsubara Sectors 109
9.1 Simulation Details and Algorithmic Aspects . . . 109
9.2 The Completely Static ω_0-sector . . . 111
9.3 Continuum Extrapolated Observables in the ω_1-Sector . . . 112
9.3.1 Screening Masses in the First Matsubara Sector . . . 112
9.3.2 Continuum Extrapolation of $H_E(\omega_1)$ . . . 115
9.3.3 Continuum Extrapolation of the Q^2 Derivative of $H_E(\omega_1, Q^2)$ at $Q^2 = 0$ . . . 116
9.4 Continuum Extrapolated Observables in the ω_2-Sector . . . 116
9.4.1 Screening Masses in the Second Matsubara Sector . . . 118
9.4.2 Continuum Extrapolation of $H_E(\omega_2)$ . . . 122
9.4.3 Evaluation of the Difference $H_E(\omega_2) - H_E(\omega_1)$ . . . 125
9.5 Comparisons . . . 127
9.6 Continuum Extrapolated Observables in the ω_3-Sector . . . 130
9.6.1 Screening Masses in the Third Matsubara Sector . . . 131
9.6.2 Continuum Extrapolation of $H_E(\omega_3)$ . . . 132
9.7 Conclusion . . . 134
9.8 Outlook . . . 136

IV Appendices VIII
A Derivation of the Spectral Representation of the Euclidean Correlator . . . IX
B Improvement Process . . . XI
C Renormalization Process . . . XII
D Error Analysis . . . XIII
E Chiral Effective Theory Lagrangian of Son and Stephanov . . . XVI
F Alternative Determination of the Screening Pion Decay Constant . . . XVII
G The Influence of the $\mathcal{O}(a)$-Improvement Process on the PCAC Mass . . . XVIII
H Dealing with Outliers . . . XIX
I Determination of Static Screening Properties in the Pseudoscalar Channel . . . XX
J Free Theory Expression for the Spectral Function of the Axial Charge . . . XXIII
K Numerical Values for Temporal Correlators . . . XXIV
L Correlator Fits: Varying the Number of States . . . XXVII
M Lattice Perturbation Theory and Choice of Kernel . . . XXVIII
N Non-Continuum Extrapolated Results at $T \approx 1.4\,\mathrm{GeV}$ . . . XXIX
N.1 The ω_0 Sector . . . XXIX
N.2 The ω_1 Sector . . . XXIX
N.3 The ω_2 Sector . . . XXX

Eigenständigkeitserklärung XXXVI

List of Figures LIV

List of Tables LXIV

Chapter 1

Introduction

According to our current knowledge physical phenomena are governed by four fundamental forces: gravity, and the electromagnetic, weak, and strong interactions. Unlike gravity, the latter three forces are encompassed within the Standard Model (SM) of particle physics and are therein formulated as renormalizable quantum field theories. The strong interaction was initially postulated as a short-range counterforce to account for nuclear stability. Subsequent deep-inelastic scattering experiments revealed that nucleons are not elementary particles but are composed of point-like constituents, namely quarks and gluons [12–14]. By now, quarks and gluons are integral to the SM and are described by an $\mathrm{SU}(3)$ gauge theory known as Quantum Chromodynamics (QCD) [15–17]. Quarks, which carry a so-called color charge, interact through the exchange of gauge bosons, termed gluons, which also carry a color charge. This characteristic gives rise to three- and four-vertex gluon self-interactions. Despite being fundamental constituents of matter, isolated quarks have not been experimentally observed; instead, only color-neutral bound states of quarks and gluons, referred to as hadrons, are observed in nature. The derivation of this phenomenon, known as color confinement [18], from QCD remains an open question. Another notable phenomenon, termed asymptotic freedom, may be related to confinement [15, 18, 19]. It states that the running coupling constant, α_s, of QCD decreases with increasing momentum transfer, permitting a perturbative expansion of QCD in powers of α_s in the high-energy domain. However, in the low-energy domain, where the coupling constant is large, perturbation theory becomes inapplicable. Given the absence of an analytical solution for QCD, alternative methods must be employed to describe QCD dynamics in the low-energy regime, such as Chiral Perturbation Theory (ChPT) or—as explored in this thesis—Lattice Quantum Chromodynamics (LQCD).

Even though confinement implies that individual free quarks or gluons cannot be observed in the physical vacuum, during the early universe—on a microsecond timescale—the strongly interacting constituents existed in a deconfined phase. This hot and dense phase is nowadays referred to as the Quark-Gluon Plasma (QGP). As pointed out by E. Shuryak, although the QGP is often labeled the "exotic phase of QCD", it is in fact the only phase whose quasiparticles directly reflect the quark and gluon fields of the QCD Lagrangian [20]. In contrast, the low-temperature hadronic phase and the QCD vacuum are highly nontrivial, characterized by condensates associated with confinement and chiral symmetry breaking [20, 21].

Following a proposal by T. D. Lee from 1974 to "investigate phenomena by distributing high energy or high nucleon density over a relatively large volume" [22], heavy-ion colliders, such as the Large Hadron Collider (LHC) at CERN and the Relativistic Heavy-Ion Collider (RHIC) at Brookhaven National Laboratory (BNL), enable the recreation of similar conditions in laboratory settings. As a consequence of asymptotic freedom, it is anticipated that the QGP is weakly-coupled at sufficiently high temperatures and/or densities. However, at temperatures relevant to

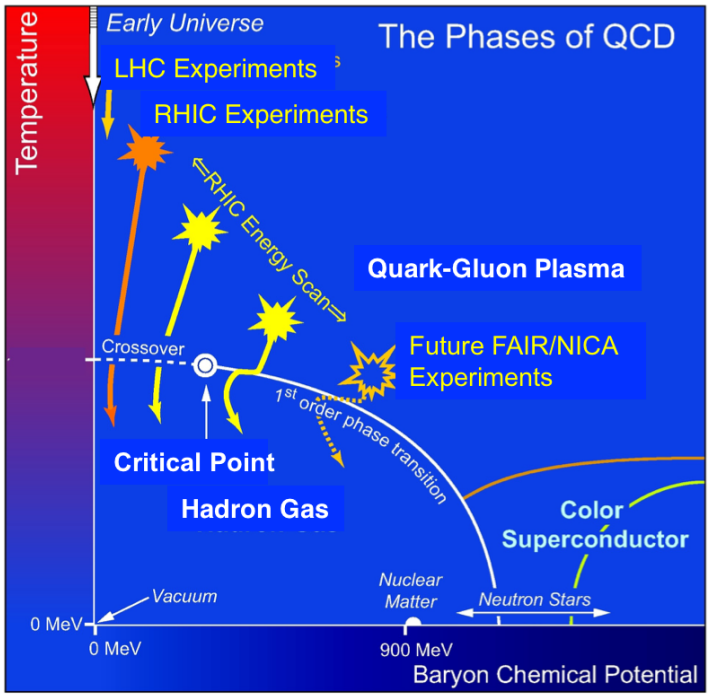

Figure 1.1: A schematic representation of the phase diagram of QCD as a function of temperature T and baryonic chemical potential μ_B. This figure is adapted from Ref. [32].

heavy-ion phenomenology, perturbation theory converges very poorly, and the QGP exhibits unexpected behavior. In the early 2000s, the substantial measured elliptic flow in particle yields [23], along with the pronounced suppression of high-energy jets and heavy quarks [24], implied that the matter produced can be characterized as a strongly-coupled system [25]. Around the same time, utilizing the AdS/CFT correspondence, the shear viscosity to entropy density ratio, $\frac{\eta}{s}$, was determined in the context of strong-coupling [26]. A comparison of RHIC data on elliptic flow with hydrodynamic calculations led to the conclusion that $\frac{\eta}{s}$ must not exceed a few times the lower bound established by strong coupling; otherwise, the elliptic flow would be significantly underestimated [27, 28]. Consequently, the hot quark matter produced in heavy-ion collisions (HICs) has been termed strongly-coupled quark-gluon plasma (sQGP) [29] and is considered as a "nearly-perfect" fluid [27]. In a fluid with very low shear viscosity η, the presence of well-defined quasiparticles (needed for a weak-coupling description) with large mean free paths is not feasible [30]. If such quasiparticles were to exist, they would enable the efficient transport of momentum over significant distances, thereby increasing η [30]. For a hydrodynamic description to be applicable, the medium must achieve approximate local thermal equilibrium, enabling the short-lived "fireball" to be accurately described by fluid dynamics [28] within less than 1 fm after the collision [31].

These observations highlight that the QGP created in HICs occupies an intermediate regime where neither perturbative nor strong-coupling approximations are fully reliable. In this thesis, we explore properties of strongly interacting matter under extreme conditions using LQCD, which offers a non-perturbative first-principles approach. Starting in the QCD vacuum, increasing the temperature initially leads to a dilute gas of pions. Compared to standard hadrons, which are excitations of the QCD vacuum, the excitations of the thermal medium are expected to be quasi-

particles with (to some extent) modified properties. Experimentally measuring thermal modifications of hadrons—such as shifts in their pole masses—is extremely challenging. In HICs, hadrons propagate through a short-lived, strongly interacting medium where numerous effects intertwine: interactions with other hadrons, color screening, (partial) chiral symmetry restoration, and substantial thermal broadening. For instance, in the case of the ρ meson, thermal broadening tends to surpass a distinct mass shift [21, 33]. From a theoretical perspective, the relevant information is encoded in the spectral functions associated with two-point correlation functions, such as those of the electromagnetic current. Of particular interest is the slope of the spectral function at the origin, which determines transport coefficients via Kubo formulas [34]. On the lattice, however, one does not have direct access to spectral functions. Instead, one measures Euclidean two-point correlators, and extracting the corresponding real-time spectral information requires solving an inverse problem that is inherently ill-posed.

Over the past two decades, HICs have created matter at temperatures well above the finite temperature crossover. This initial matter undergoes expansion and gradual cooling, eventually traversing a rapid yet smooth crossover at zero and low chemical potential [35]. This process is characterized by a pseudocritical temperature $T_{pc} = 156.5(1.5)\,\mathrm{MeV}$ [36]. The thermodynamic phases of QCD can be represented in a plane defined by the temperature T and the baryonic chemical potential μ_B. This representation is known as the QCD phase diagram [cf. Fig. 1.1]. A pertinent question arises regarding whether the crossover temperature, as defined by *deconfinement* observables (such as static quark free energy and its temperature derivative), aligns with the crossover temperature determined through *chiral symmetry*, specifically in terms of the chiral condensate $\langle\bar{\psi}\psi\rangle$ and its susceptibility χ. [37] Findings from a recent LQCD study demonstrate that—at infinite volume—the deconfinement crossover temperature is marginally lower than the chiral crossover temperature [37]. At higher baryonic chemical potentials, a variety of models and functional approaches [38–41] predict the existence of a *critical end point* at which the crossover line (dashed line in Fig. 1.1) culminates into a first-order phase transition line (solid white line in Fig. 1.1). The experimental identification of its position within the $T - \mu_B$ plane constitutes a primary objective of relativistic HIC programs [25]. Systematic beam energy scans (BES) are conducted by reducing the beam energy within the range $\sqrt{s_{NN}} = \{200, \ldots, 7.7\}\,\mathrm{GeV}$, which increases μ_B from about 20 MeV up to 420 MeV [42]. It is noteworthy that recent results from a LQCD study suggest that a critical point for $\mu_B < 450\,\mathrm{MeV}$ is excluded at the 2σ confidence level [43]. In this thesis, however, we exclusively examine the scenario of vanishing baryonic chemical potential.

A particularly important property of the QGP is that it emits photons throughout its entire space–time evolution (cf. Secs. 7.1 and 7.4). The emission rate and energy spectrum of these photons provide penetrating probes of the medium, as photons escape the plasma essentially without final-state interactions. Developing theoretical descriptions of relativistic heavy-ion collisions therefore requires two key ingredients. First, one needs estimates of the photon emission rates at the *microscopic* level, using weak-coupling calculations, effective field theories, or, as pursued in this thesis, LQCD. Second, these rates must be implemented into *macroscopic* dynamical simulations, which integrate over the entire space-time history of the collision to yield observable quantities such as the transverse-momentum spectrum of photons [44].

Part I

Theoretical and Phenomenological Background

Chapter 2

Quantum Chromodynamics (QCD)

In this chapter, we briefly introduce QCD as the continuum theory of strong interactions, with quarks and gluons as fundamental degrees of freedom. The theory incorporates an internal color degree of freedom, known as color charge, which forms the basis for the interaction among these particles. QCD is characterized as a non-Abelian gauge theory, with color SU(N_c) serving as the underlying gauge group. The concept of color charge was initially introduced in the 1960s as an additional internal quantum number to ensure that three-quark bound states, such as the $\Delta(1232)$ resonance, comply with the Pauli exclusion principle [45, 46]. An indirect method to determine the number of color charges involves the precise measurement of the R-ratio, which was first proposed in Ref. [47]. It is defined as the ratio

$$R(\sqrt{s}) = \frac{\sigma(e^+e^- \to \text{hadrons})}{\sigma(e^+e^- \to \mu^+\mu^-)}\,, \tag{2.0.1}$$

between the e^+e^- cross-section into hadrons with that into muons and measured as a function of the center-of-mass energy $\sqrt{s}$ of the electrons [cf. Fig. 2.1]. Given that the e^+e^- pair annihilates into a virtual (colorless) photon, which subsequently decays into a quark-antiquark pair of identical color charge, and considering that each color state is produced with equal probability, the R-ratio is proportional to the number of color charges N_c. Additionally, it is necessary to account for a squared charge factor Q_f^2 for each produced quark-antiquark pair of flavor f. Consequently, the R-ratio is approximately expressed as

$$R(\sqrt{s}) \approx N_c \sum_\mathrm{f} Q_\mathrm{f}^2\,, \tag{2.0.2}$$

where the sum runs over all flavors f, which are kinematically accessible at the center-of-mass energy $\sqrt{s}$. Considering all six quark flavors with their respective charges as presented in Table 2.1, one arrives at $R \approx 5/3N_c$. Given that the leading-order hadronic vacuum polarization contributing to the muon anomalous magnetic moment [48] is associated with the R-ratio, this ratio has been determined with high precision. Consequently, the value $N_c = 3$ is now firmly established.

2.1 The Euclidean QCD Lagrangian

We employ the Euclidean metric from the outset to facilitate a straightforward connection to LQCD (cf. Chap. 5). Consequently, the γ-matrices adhere to the Euclidean anti-commutation relations.

$$\{\gamma_\mu, \gamma_\nu\} = 2\delta_{\mu\nu}\mathbb{1}\,. \tag{2.1.1}$$

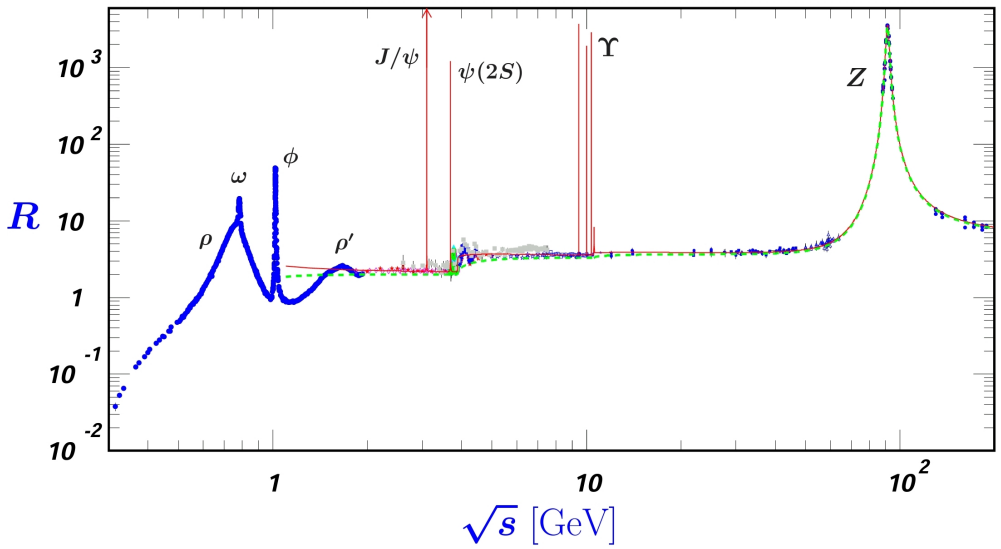

Figure 2.1: World data on the ratio $R(\sqrt{s})$ of the total cross-section of the e^+e^- annihilation into hadrons with that into muons. The plot is taken from Ref. [49].

The QCD matter fields are called quarks and carry spin 1/2. For each quark flavor [50, 51], (u, d, s, c, b, t), a Dirac-spinor quark field,

$$\begin{pmatrix} \psi_f^1(x) \\ \psi_f^2(x) \\ \psi_f^3(x) \end{pmatrix}, \tag{2.1.2}$$

is introduced as a color triplet [cf. Table 2.1].

In addition to quarks, QCD encompasses vector gauge bosons associated with gluons. These are represented by four-vector potentials $A_\mu(x) \equiv A_\mu^a(x)$ and carry spin 1. Unlike quarks, which transform under the fundamental representation of the gauge group SU(3), gluons transform under the adjoint representation of SU(3). Consequently, the color index, a, ranges from 1 to $N_c^2 - 1 = 8$. Neglecting the θ-term and employing matrix/vector notation for the color and Dirac indices, the gauge-invariant continuum Euclidean QCD Lagrangian—divided into fermionic and gluonic contribution—can be expressed as follows:

$$\begin{aligned} \mathcal{L}_E[\bar{\psi}, \psi, A] &= \mathcal{L}_F[\bar{\psi}, \psi, A] + \mathcal{L}_G[A] \\ &= \sum_{f=1}^{6} \bar{\psi}_f(x) \left[\gamma_\mu D_\mu(x) + m_f\right] \psi_f(x) + \frac{1}{2g^2} \mathrm{Tr}\left[F_{\mu\nu}(x) F_{\mu\nu}(x)\right], \end{aligned} \tag{2.1.3}$$

where m_f denotes the quark mass of flavor f, the trace is taken with respect to (w.r.t.) the color indices and g quantifies the strength of the quark-flavor-independent coupling between quark and gluon fields. The gauge fields $A_\mu(x)$ are elements[1] of the Lie algebra $\mathfrak{su}(3)$ and enter the

[1] As will be discussed in Sec. 5.4.2, within the lattice framework, the gauge fields are represented as elements of the corresponding Lie group, rather than the Lie algebra.

Table 2.1: Quark flavors and their charges and masses, taken from Ref. [52]

Flavor	Charge Q_f	Mass
u (up)	$+2/3$	(2.2 ± 0.6) MeV
d (down)	$-1/3$	(4.7 ± 0.5) MeV
s (strange)	$-1/3$	(96 ± 8) MeV
c (charm)	$+2/3$	(1.27 ± 0.03) GeV
b (bottom)	$-1/3$	(4.18 ± 0.04) GeV
t (top)	$+2/3$	(173.21 ± 0.71) GeV

Lagrangian in Eq. (2.1.3) via the covariant derivative[2]

$$D_\mu = \partial_\mu + i \sum_{a=1}^{8} A_\mu^a(x) \frac{\lambda^a}{2} \equiv \partial_\mu + i A_\mu(x) \,, \tag{2.1.4}$$

where $\lambda_a/2$ denote the eight *Gell-Mann matrices*, which are the generators of the Lie algebra $\mathfrak{su}(3)$. Therefore, the commutation relations of these matrices,

$$\left[\frac{\lambda^a}{2}, \frac{\lambda^b}{2}\right] = i f_{abc} \frac{\lambda^c}{2} \,, \tag{2.1.5}$$

encode the structure of the Lie group SU(3) through the totally antisymmetric real structure constants f_{abc}. The corresponding field-strength tensor reads

$$F_{\mu\nu} \equiv F_{\mu\nu}^a \frac{\lambda_a}{2} = \left(\partial_\mu A_\nu^a - \partial_\nu A_\mu^a - g f_{abc} A_\mu^b A_\nu^c\right) \frac{\lambda^a}{2} \,. \tag{2.1.6}$$

To ensure that the continuum QCD Lagrangian is gauge invariant, the quark and gauge fields have to transform under *local* SU(3) transformations $\Omega(x)$ like

$$\psi(x) \mapsto \Omega(x)\psi(x) \,, \qquad \bar{\psi}(x) \mapsto \bar{\psi}(x)\Omega^\dagger(x) \,, \tag{2.1.7}$$

$$A_\mu(x) \mapsto \Omega(x) A_\mu(x) \Omega^\dagger(x) + \mathrm{i} \left(\partial_\mu \Omega(x)\right) \Omega^\dagger(x) \,, \tag{2.1.8}$$

i.e. in the fundamental and adjoint representation, respectively. In accordance with the aforementioned transformations, the covariant derivative in Eq. (2.1.4) is designed to transform in the same manner as the object it acts on, while the field-strength tensor in Eq. (2.1.6) transforms as

$$F_{\mu\nu}(x) \mapsto \Omega(x) F_{\mu\nu} \Omega^\dagger(x) \,. \tag{2.1.9}$$

Given that the kinetic component of the QCD Lagrangian $[\mathcal{L}_G[A]$ in Eq. (2.1.3)] is quadratic in the gluon field-strength tensor, it results in gauge-field self-interactions involving three and four gluon fields. The non-Abelian self-interactions of gluons in QCD are crucial for two of the most

[2] In LQCD, it is common to include $1/g^2$ as an overall factor in the corresponding gauge action, and we adopt this convention from the outset. Following the rescaling $\frac{1}{g} A_\mu(x) \to A_\mu(x)$, the gauge coupling re-emerges in the covariant derivative $\partial_\mu + i g A_\mu(x)$.

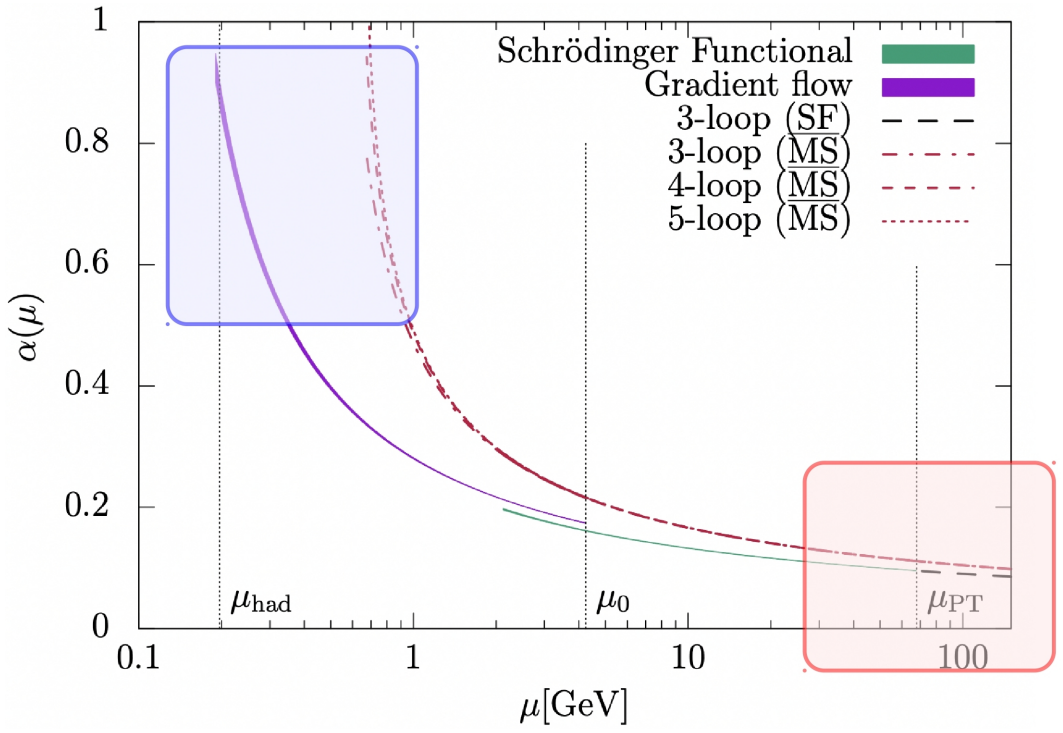

Figure 2.2: Running couplings from $N_f = 3$ QCD. The plot is taken from Ref. [54].

intriguing characteristics of QCD: color confinement and asymptotic freedom. While the confinement of quarks and gluons into hadrons requires a non-perturbative approach to QCD, asymptotic freedom [15, 19] can be examined through perturbation theory. The strong coupling constant [53]

$$\alpha_s(\mu) \equiv \frac{g_R(\mu)^2}{4\pi} = \frac{c}{\ln(\mu/\Lambda_{\rm QCD})} + \cdots, \quad (c \text{ some assessable constant}), \tag{2.1.10}$$

is defined in terms of the renormalized running coupling $g_R(\mu)$ with the property $g_R(\mu \to \infty) \to 0$ and $\Lambda_{\rm QCD}$ denotes the scale at which non-perturbative QCD effects become significant. In Fig. 2.2 the strong coupling constant is shown as a function of the energy-momentum transfer μ. At energy scales $\mu \approx 100\,\text{GeV}$ the strong coupling constant $\alpha_s \approx 0.1$, enabling a perturbative expansion. On the contrary, for small energy-momentum transfers $\mu \approx 1\,\text{GeV}$ the strong coupling constant is of $\mathcal{O}(1)$. Consequently, quarks and gluons are confined into hadrons and a perturbative treatment is no longer feasible.

One potential approach, as pursued in this thesis, is the application of LQCD, which offers numerical solutions to QCD by discretizing space-time [55]. An alternative approach involves the use of an Effective Field Theory (EFT), which serves as a (low-energy) approximation of a more fundamental theory. In this framework, the dynamics are no longer described using fundamental quarks and gluons; instead, the low-energy degrees of freedom of the strong interaction, specifically mesons and baryons, are employed. The EFT of the strong interaction at low energies is referred to as ChPT [56–58]. This theory is predicated on the assumption that QCD, when considered in the so-called *chiral limit*—where the light-quark masses are set to zero and the heavy quarks are excluded—undergoes spontaneous symmetry breaking.

2.2 QCD in the chiral limit

This section is based on Refs. [59, 60]. The six quark flavors are categorized into three light quarks, namely u, d, and s, and three heavy quarks, specifically c, b, and t, as summarized in Table 2.1. The scale of 1 GeV, separating these two groups, is associated with the masses of the lightest hadrons containing light quarks which are not Goldstone bosons, e.g., the ρ meson with a mass of $M_\rho = 770\,\text{MeV}$, and is of the same order of magnitude as the scale associated with spontaneous symmetry breaking [61],

$$\Lambda = 4\pi F_\pi \approx 1170\,\text{MeV}\,. \tag{2.2.1}$$

This indicates that the QCD Lagrangian, in the chiral limit where light-quark masses vanish and heavy quarks are excluded, may serve as a good starting point for describing low-energy QCD. The two projection operators

$$P_R = \frac{1}{2}\left(\mathbb{1} + \gamma_5\right)\,, \qquad \text{and} \qquad P_L = \frac{1}{2}\left(\mathbb{1} - \gamma_5\right)\,, \tag{2.2.2}$$

project the quark fields ψ onto their right-handed, $\psi_R = P_R\psi$, and left-handed, $\psi_L = P_L\psi$, components, respectively. Due to the flavor independence of the covariant derivative, the QCD Lagrangian in the chiral limit exhibits a *global* $\mathrm{U}(3)_L \times \mathrm{U}(3)_R$ symmetry within flavor space, which can be decomposed into

$$\mathrm{SU}(3)_L \times \mathrm{SU}(3)_R \times \mathrm{U}(1)_V \times \mathrm{U}(1)_A\,. \tag{2.2.3}$$

Applying Noether's theorem [62] results in conserved currents associated with the SU(3) transformations of the left-handed or right-handed quarks,

$$\begin{aligned} L^a_\mu &= \bar\psi_L \gamma_\mu \frac{\lambda^a}{2}\psi_L, \quad \partial^\mu L^a_\mu = 0\,, \\ R^a_\mu &= \bar\psi_R \gamma_\mu \frac{\lambda^a}{2}\psi_R, \quad \partial^\mu R^a_\mu = 0\,. \end{aligned} \tag{2.2.4}$$

Instead of these chiral currents one often uses linear combinations,

$$V^a_\mu = R^a_\mu + L^a_\mu = \bar\psi \gamma_\mu \frac{\lambda^a}{2}\psi\,, \tag{2.2.5}$$

$$A^a_\mu = R^a_\mu - L^a_\mu = \bar\psi \gamma_\mu \gamma_5 \frac{\lambda^a}{2}\psi\,, \tag{2.2.6}$$

transforming under parity as vector and axial-vector currents, respectively. Furthermore, a conserved singlet vector current is derived from the transformation of all left-handed and right-handed quark fields by the *same* phase. The singlet axial-vector current, originating from the transformation of all left-handed quark fields with one phase and all right-handed quark fields with the *opposite* phase, however, is only conserved at the *classical* level. On the quantum-level it develops a so-called *anomaly* [63–65]. Consequently, the QCD Lagrangian in the chiral limit, is invariant (only) under global $\mathrm{SU}(3)_L \times \mathrm{SU}(3)_R \times \mathrm{U}(1)_V$ transformations. Due to the conserved currents in Eqs. (2.2.4) corresponding "charge operators" can be defined as the space integrals of

the charge densities,

$$\begin{aligned} Q_L^a(t) &= \int \mathrm{d}^3x\, \psi_L^\dagger(t,\mathbf{x})\frac{\lambda^a}{2}\psi_L(t,\mathbf{x})\,, \\ Q_R^a(t) &= \int \mathrm{d}^3x\, \psi_R^\dagger(t,\mathbf{x})\frac{\lambda^a}{2}\psi_R(t,\mathbf{x})\,, \\ Q_V(t) &= \int \mathrm{d}^3x\, \psi^\dagger(t,\mathbf{x})\psi(t,\mathbf{x})\,. \end{aligned} \tag{2.2.7}$$

Using Eqs. (2.2.5-2.2.6) as a template, we form linear combinations of the right-handed and left-handed charge operators,

$$Q_V^a = Q_R^a + Q_L^a \qquad \text{and} \qquad Q_A^a = Q_R^a - Q_L^a\,, \tag{2.2.8}$$

with opposite parity. It was shown by Vafa and Witten [66] that the ground state in the chiral limit, $|0\rangle$, is necessarily invariant under $\mathrm{SU}(3) \times \mathrm{U}(1)$, i.e., the nine charges Q_V^a and Q_V annihilate the ground state,

$$Q_V^a\,|0\rangle = Q_V\,|0\rangle = 0\,. \tag{2.2.9}$$

If the ground state of QCD was invariant under the full symmetry group[3]

$$\mathrm{SU}(3)_L \times \mathrm{SU}(3)_R \times \mathrm{U}(1)_V =: \mathrm{G} \times \mathrm{U}(1)_V \tag{2.2.10}$$

of the Hamiltonian corresponding to the QCD Lagrangian in the chiral limit, it is expected that hadrons would arrange in approximately degenerate multiplets, corresponding to the dimensionalities of irreducible representations of this symmetry group. Consequently, for each multiplet, a corresponding multiplet of opposite parity would be expected [e.g., $\rho(770) - a_1(1260)$, or $N(940) - N^*(1535)$] [21]. However, the absence of parity doubling, coupled with a typical mass splitting of 500 MeV, implies that the charges Q_A^a do not annihilate the ground state, indicating that the ground state is *not* invariant under the corresponding 'axial' transformations. In conclusion, the ground state is not invariant under the full symmetry group of the Hamiltonian but is only invariant under the subgroup $\mathrm{H} = \mathrm{SU}(3)_V \times \mathrm{U}(1)_V$. Thus, massless QCD experiences *spontaneous symmetry breaking*, with G being spontaneously reduced to the subgroup H. Given that G possesses $n_\mathrm{G} = 16$ generators and H has $n_\mathrm{H} = 8$ generators, the *Goldstone theorem* [67] predicts the emergence of $n_\mathrm{G} - n_\mathrm{H} = 8$ massless Goldstone bosons ϕ^a. These bosons exhibit the same transformation properties under parity as the axial generators Q_A^a:

$$\phi^a(t,\mathbf{x}) \overset{P}{\mapsto} -\phi^a(t,-\mathbf{x})\,. \tag{2.2.11}$$

This elucidates why Goldstone bosons are pseudoscalars and highlights the unique role of the pion among hadrons in the chiral limit. Despite the fact that there is no explicit proof that spontaneous chiral symmetry breaking actually exists in nature, assuming its presence allows for the interpretation of the $\mathrm{SU}(3)_V$ multiplets through Coleman's theorem [68]. This theorem states that the symmetry of the spectrum is determined by the symmetry of the ground state, rather than by

[3] The $\mathrm{U}(1)_V$ symmetry corresponds to the conservation of baryon number B which divides hadrons into mesons with $B = 0$ and baryons with $B = 1$. Further, G is often referred to as the chiral group [60].

the Hamiltonian.

2.2.1 Spontaneous Symmetry Breaking

Following Ref. [69], we introduce the concept of *spontaneous symmetry breaking* through the example of the *Ising model* [70]. We consider a d-dimensional lattice of length N, where spins $s_i = \pm 1$ are positioned at each lattice site N^d. Assuming nearest-neighbor interactions with uniform coupling[4] $J > 0$, the Hamiltonian of the Ising model is expressed as

$$\mathcal{H}_I = -J \sum_{\langle i,j \rangle} s_i s_j - H \sum_i s_i \,, \quad (H: \text{ external field}) \,, \tag{2.2.12}$$

where the notation $\langle i, j \rangle$ indicates that the sum runs over nearest neighbors only. The Ising model possesses as discrete, *global* $\mathbb{Z}_2$-symmetry for $H = 0$, i.e. the Hamiltonian $\mathcal{H}_I$ is invariant under the simultaneous flipping of *all* spins $s_i \to -s_i$. Since the corresponding partition function of the system [69],

$$Z(T, N, H = 0) = \prod_{i=1}^{N^d} \sum_{s_i = \pm 1} \exp\left(-\beta \mathcal{H}_I\right) = \prod_{i=1}^{N^d} \sum_{s_i = \pm 1} \exp\left(\beta J \sum_{\langle i,j \rangle} s_i s_j\right) , \quad \beta = 1/T \,, \tag{2.2.13}$$

preserves the $\mathbb{Z}_2$-symmetry of the Hamiltonian, the same is also true for the thermodynamic quantities derived from it. However, the actual state of the system shares this $\mathbb{Z}_2$-symmetry, with an equal number of up and down spins on average, only for high temperatures above the *Curie temperature* T_C, which for $d = 2$ has the exact solution [71]

$$T_C = \frac{2J}{\ln(1 + \sqrt{2})} \,. \tag{2.2.14}$$

On the contrary, below T_C spontaneous symmetry breaking occurs: On average, there are either more up or more down spins. However, the $\mathbb{Z}_2$-symmetry is still respected to the extent that both possibilities are equally likely. A suitable *order parameter* for spontaneous symmetry breaking is given by the magnetization [69],

$$m(T, N, H = 0) = \frac{1}{Z(T, N, H = 0)} \prod_{i=1}^{N^d} \sum_{s_i = \pm 1} \left[\frac{\sum_i s_i}{N^d}\right] \exp\left(\beta J \sum_{\langle i,j \rangle} s_i s_j\right) , \tag{2.2.15}$$

which describes the average value of the spin over the entire lattice. Thus, the Curie temperature T_C marks the point at which the system transitions from an ordered state, characterized by spontaneous magnetization ($m(T) \neq 0$), to a state where magnetization disappears ($m(T) = 0$). We note that for $H \neq 0$ the magnetization never vanishes, as in this case the $\mathbb{Z}_2$-symmetry is always broken by the external field and, consequently, the spins will always be partially aligned.

The phenomenon of spontaneous symmetry-breaking[5] in a ferromagnet bears resemblance to

[4] The scenario where $J > 0$ is termed *ferromagnetic* interaction, whereas the scenario where $J < 0$ is termed *antiferromagnetic* interaction. For $J > 0$ and $H = 0$, the system's energy is minimized when neighboring spins are aligned in the same direction ($s_i s_j = 1$).

[5] Furthermore, chiral symmetry is *explicitly* broken by the finite light quark masses $m_{u,d} \ll |\langle \bar{\psi}\psi \rangle|^{1/3} \approx 250\,\text{MeV}$ [21]. Thus, the quark masses in QCD are the equivalent of the external field H in the Ising model.

QCD in the chiral limit, where the symmetry of the Hamiltonian $\mathrm{SU}(3)_L \times \mathrm{SU}(3)_R$, is spontaneously broken the ground state to $\mathrm{SU}(3)_V$. The analogous observable to magnetization $m(T)$ is the quark condensate $\langle\bar{\psi}\psi\rangle(T) = \langle\bar{u}u + \bar{d}d + \bar{s}s\rangle(T)$, which thus serves as an order parameter for chiral symmetry. We note that a non-zero vacuum expectation value of the quark condensate is a sufficient but *not* a necessary condition for spontaneous symmetry breaking in QCD[6] [60]. Gradually increasing the temperature, at some point the elevated thermal energy breaks the binding of quark-antiquark pairs, effectively "evaporating" the quark condensate $\bar{\psi}\psi$ and restoring chiral symmetry [21]. In Sec. 6.8.1, we analyze the temperature-dependence of an 'effective chiral condensate' based on the Gell-Mann–Oakes–Renner relation.

Utilizing lattice QCD methods, it has been demonstrated that at a vanishing baryon chemical potential μ_B, the restoration of chiral symmetry occurs slightly subsequent to the deconfinement transition [37]. This transition is characterized as an analytical crossover rather than a genuine phase transition, meaning that thermodynamic quantities increase rapidly yet continuously and smoothly, as opposed to abruptly, around the pseudo-critical temperature.

[6] A non-zero value of the pion decay constant in the chiral limit, on the other hand, is a necessary *and* sufficient condition [60].

Chapter 3

Ultrarelativistic Heavy Ion Collisions

In a relativistic Heavy-Ion Collision (HIC) viewed in the center of mass system, the approaching nuclei are accelerated to ultrarelativistic ($v \approx c$) speeds before they crash into each other. Consequently, they experience significant Lorentz contraction as indicated in the lower panel of Fig. 3.1. This relativistic effect compresses the longitudinal inter-nucleon spacings along the direction of motion, transforming them from spherical shapes into much thinner, pancake-like structures[1]. Thus, the elementary inelastic nucleon-nucleon collisions occur nearly simultaneously and within a very limited spatial region. A nucleon from one nucleus can collide with multiple nucleons in the other nucleus (*Glauber model* [72] of multiple-collision processes). Consequently, a substantial amount of energy is deposited in a small spatial region over a brief period of time, which favors the formation of extreme states of matter [73]. In a reaction, kinematic quantities along the direction of the incident beam, designated as the longitudinal axis or z-axis, exhibit properties that differ from those along the transverse directions, which are perpendicular to the beam axis. We can represent a particle's four-momentum as

$$p = (p_0, \mathbf{p}_\mathrm{T}, p_z)\,, \tag{3.0.1}$$

where p_0 is the energy, $\mathbf{p}_\mathrm{T}$ is the transverse momentum, and p_z is the longitudinal momentum. At the center-of-mass energies available at RHIC and the LHC, the colliding nuclei typically pass through each other rather than coming to a complete stop [74], i.e. the incoming nucleons retain a substantial fraction of the collision energy ("*leading particle effect*" [69]). This interaction produces matter characterized by extremely high energy densities and temperatures, while maintaining relatively low baryon densities [75]. These droplets then undergo rapid expansion and cooling, producing a multitude of hadrons [76].

A comprehensive depiction of these processes is summarized in Fig. 3.1, which demonstrates the space-time evolution of two heavy ions colliding at the coordinates $(z, t) = (0, 0)$. The figure includes a separation distance b, known as the *impact parameter*, between the centers of the colliding nuclei. Immediately following the collision, in the initial stages, the matter produced primarily consists of non-equilibrium gluons [69]. During the early stages, the initial hard gluons generate numerous soft gluons. These soft gluons then rapidly thermalize, forming a heat bath that absorbs energy from the remaining hard gluons, ultimately leading to complete thermalization [77]. Due to the high gluon occupation number, this matter is strongly interacting and evolves towards both kinetic and chemical equilibrium, with quark-antiquark pairs being created in the process [78].

[1] The interaction region will be circular only when the impact parameter approaches zero. Generally, as the impact parameter increases, the 'ellipticity' of the interaction region will also increase, resulting in an almond-shaped interaction region [28].

In the subsequent stages, the bulk evolution of the system is well-described by nearly ideal relativistic hydrodynamics. As the system expands, it cools down, ultimately forming the QGP, a phase in which most of the energy is concentrated in quarks and gluons, but the color charges cannot yet be associated with individual hadrons [69]. As the temperature decreases further (but still $T > T_{pc}$) the system reaches a "*mixed phase*", where heavy charmed hadrons continue to coexist within the QGP phase. In Refs. [79, 80] the authors claim that the relevant charm degrees of freedom are categorized as meson-like, baryon-like, and quark-like. Notably, charm quarks only become the dominant degree of freedom at temperatures exceeding 175 MeV [80]. Eventually, the QGP reaches the confinement temperature and the *hadronization* [73] to a hot hadron gas, including also lighter hadrons, like pions takes place. Within the hydrodynamic framework, the confinement transition is seamlessly integrated into the equation of state, as long as the system remains near equilibrium [78]. As the system continues to dilute, the mean free path of the particles increases, making a kinetic theory description more suitable than hydrodynamics. Once hadrons emerge from quarks and gluons, the energy density may still be sufficiently high to permit inelastic interactions. These interactions lead to changes in the 'chemical' composition of the system, affecting the relative abundances of different particle species. Loosely bound states like deuterons (d), illustrated in the bottom panel of Fig. 3.1, are especially sensitive to these interactions and can be readily formed or destroyed [81]. In this context, the termination of various reactions is governed by their respective cross-sections: inelastic processes cease first, marking the *chemical freezeout* and fixing the particle composition. Nonetheless, elastic interactions may persist (as illustrated by the $\pi - K$ interaction in the bottom panel of Fig. 3.1) until *kinetic freezeout* takes place, which is defined as the point when the mean free path of the hadrons becomes larger than the size of the fireball [33]. Subsequently, the system becomes too dilute to sustain further momentum-exchanging interactions. Consequently, the momenta of the particles become fixed, and they propagate along straight-line trajectories with constant velocities to the detectors [78]. Among the produced particles, those with transverse momentum $|\mathbf{p}_\mathrm{T}|$ significantly below 1 GeV are classified as *'soft'* particles, whereas those with transverse momentum well above 1 GeV are classified as *'hard'* particles. These two categories arise from distinct production mechanisms: the generation of soft particles is governed by nonperturbative QCD processes, while the production of hard particles can be described using perturbative QCD [73].

3.1 Statistical hadronization model

The phenomenon of multiparticle production in high-energy collisions involving strongly interacting particles has captivated physicists for almost a century. As Heisenberg [82] anticipated in 1939, these '*little bangs*' result in an increasing production of mesons and baryons in various quantum states as the collision energy escalates. The initial statistical approach was formulated in 1950 by Fermi [83], who proposed that collisions concentrate a substantial amount of energy in a small region surrounding the interacting particles. This energy, referred to as the *fireball*, is subsequently distributed among the emitted hadrons in accordance with statistical laws.

Experimental evidence indicates that the secondary particles are not emitted isotropically; their average transverse momenta $|\mathbf{p}_\mathrm{T}|$ remains constant irrespective of the incident energy, whereas their average longitudinal momenta p_z increases with the collision energy [69]. An explanatory

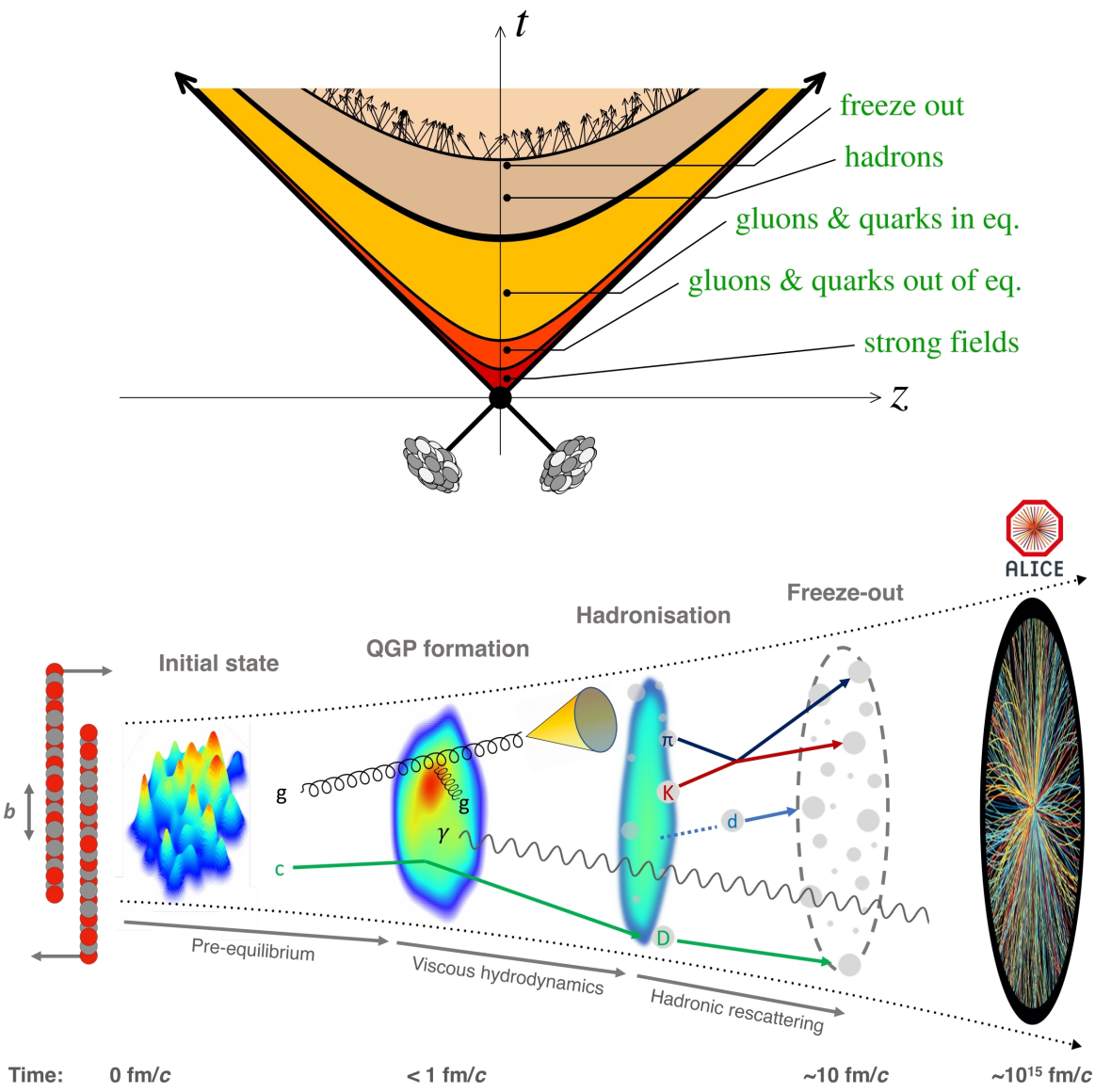

Figure 3.1: A sketch of the space-time evolution of the matter produced in a heavy-ion collision. The upper plot is taken from Ref. [78], the lower from Ref. [81].

framework for the observed anisotropy was formulated using a hydrodynamical model by Landau [84], assuming that the created medium behaves like a fluid confined within the interaction region. Within such a fluid, the pressure increase resulting from Lorentz contraction along the collision axis induces a more pronounced flow in that direction. Consequently, the secondary particles emitted exhibit greater longitudinal momenta relative to their transverse momenta [69]. Although different varieties of secondary particles exhibited distinct (energy-independent) transverse momentum distributions, their *transverse masses* m_{T}^i follow a universal pattern,

$$\frac{\mathrm{d}N_i}{\mathrm{d}m_{\mathrm{T}}^i} \sim \mathrm{e}^{-\lambda m_{\mathrm{T}}^i}, \qquad m_{\mathrm{T}}^i = \sqrt{\left|\mathbf{p}_{\mathrm{T}}^i\right|^2 + (m^i)^2}, \tag{3.1.1}$$

where i labels the different types of secondary particles (with masses m_i), $\mathbf{p}_{\mathrm{T}}^i$ denotes the transverse momentum of species i and λ is a universal parameter. An explanation for this universality was given by R. Hagedorn in 1965 within the *Statistical Bootstrap Model (SBM)* [85] based on a self-

similar resonance spectrum [86]. To elucidate the argument, it is sufficient to consider a simplified model employing a non-relativistic approximation in conjunction with Boltzmann statistics. For the exact relativistic version incorporating Bose and Fermi statistics, see Ref. [85]. The partition function of a mixture of ideal gases with point-like constituents of species i with particle masses m_i (including resonances) contained in a volume V at temperature T is given by [87],

$$\begin{aligned}\ln[Z(T,V)] = \sum_i \ln[Z_i] &= \frac{V}{(2\pi)^3}\sum_i \int \mathrm{d}^3p\, \mathrm{e}^{-\sqrt{|\mathbf{p}|^2+m_i^2}/T} \\ &= \frac{VT}{2\pi^2}\sum_i m_i^2 K_2\left(\frac{m_i}{T}\right) \approx V\left(\frac{T}{2\pi}\right)^{3/2}\sum_i m_i^{3/2}\mathrm{e}^{-m_i/T}\,, \end{aligned} \tag{3.1.2}$$

where the asymptotic behavior for large arguments of the involved modified Bessel function of the second kind, $K_2(x) = [\pi/(2x)]^{1/2}e^{-x}[1+\mathcal{O}(4/x^2)]$, was used in the approximation [69]. Since the sum over i goes over all hadron species including resonances, it is convenient to introduce a *mass spectrum* $\rho(m)$ [85], such that $\rho(m)\mathrm{d}m$ denotes the variety of hadron states of possible constituents of fireballs in the interval $[m, m+\mathrm{d}m]$. Let m_0 denote the lightest mass in the spectrum (i.e. the pion mass). The partition function in Eq. (3.1.2) can be rewritten as [87]

$$Z(T,V) = \exp\left[V\left(\frac{T}{2\pi}\right)^{3/2}\int_{m_0}^{\infty}\mathrm{d}m\,\rho(m)m^{3/2}\mathrm{e}^{-m/T}\right] \tag{3.1.3}$$

$$\equiv \int_{m_0}^{\infty}\mathrm{d}m\,\sigma(m,V_0)\mathrm{e}^{-m/T}\,, \tag{3.1.4}$$

where $\sigma(m,V_0)\,\mathrm{d}m$ denotes the diversity of fireball states of volume V_0 [86]. Hagedorn's decisive consideration was now that heavy resonances, which are included in $\rho(m)$ possess numerous decay channels, some of which include other resonances. Consequently, heavy resonances are composed (statistically) of particles and lighter resonances, similar to the composition of fireballs [85, 86]. Based on this argument Hagedorn formulated a weak requirement [85],

$$\frac{\ln[\sigma(m,V_0)]}{\ln[\rho(m)]} \quad \underset{m\to\infty}{\longrightarrow} \quad 1\,, \tag{3.1.5}$$

known as the '*bootstrap condition*'. In words: "Fireballs consist of fireballs, which consist of fireballs, which..." [85]. Thus, fireballs are simultaneously the objects being described and the constituents of this object [86]. As a consequence of the bootstrap condition, Eq. (3.1.5), Hagedorn was able to prove that the mass spectrum $\rho(m)$ has to grow exponentially for large m [85],

$$\rho(m) \quad \underset{m\to\infty}{\longrightarrow} \quad \frac{\text{const.}}{m^a}\,\mathrm{e}^{+m/T_0}\,. \tag{3.1.6}$$

Incorporating specific refinements, W. Nahm [88] demonstrated the condition in Eq. (3.1.5) could be tightened, resulting in the power of the denominator in Eq. (3.1.6) being $a = 3$. An interesting observation can be made by inserting the asymptotic behavior of the mass spectrum in Eq. (3.1.3): The partition function diverges for

$$T > T_0 \equiv T_H \approx 155(5)\,\text{MeV [86]} \quad \text{(Hagedorn temperature)}\,. \tag{3.1.7}$$

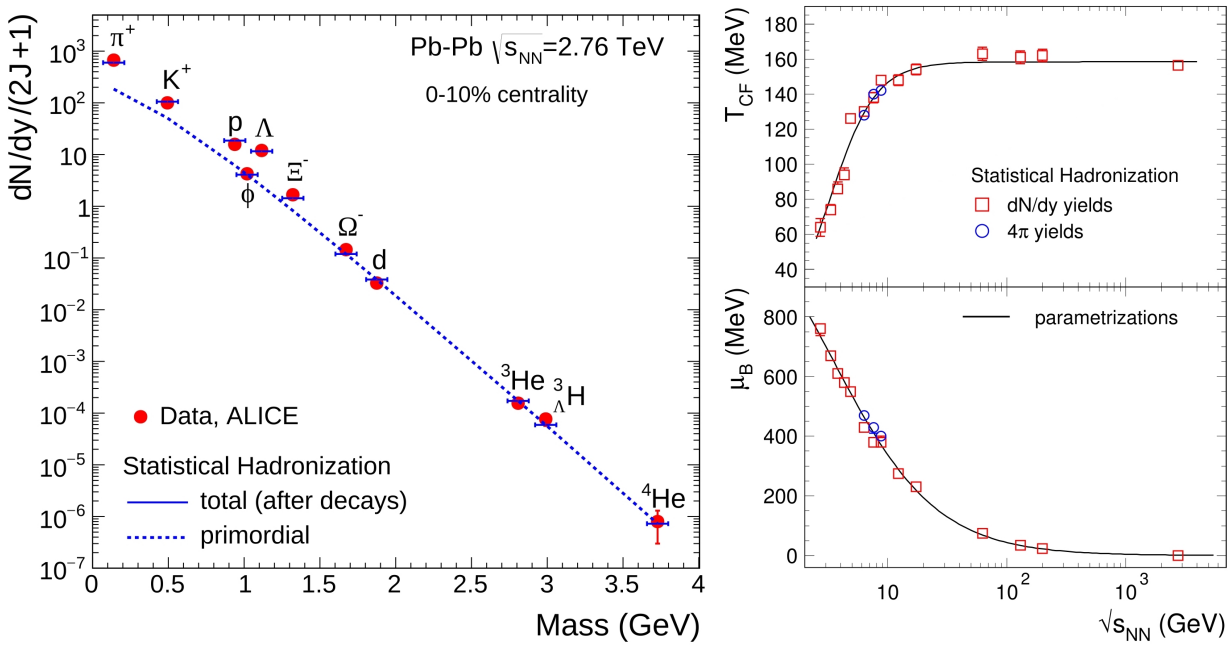

Figure 3.2: **Left panel**: Mass dependence of light flavor hadron yields normalized by the spin degeneracy factor $(2J+1)$ obtained from central Pb-Pb collisions at $\sqrt{s_{NN}} = 2.76\,\text{TeV}$ of the ALICE-collaboration. The data is compared to the statistical hadronization model with a chemical freezeout temperature $T_{\text{cf}} = 156.5(1.5)$ MeV, baryon chemical potential $\mu_B = 0.7(3.8)$ MeV and a volume $V = 5280(410)\,(\text{fm})^3$. **Right panel**: Chemical freeze-out temperature T_{cf} (top) and baryon chemical potential μ_B (bottom) as a function of center-of-mass energies per nucleon pair $\sqrt{s_{NN}}$. The plots are taken from Ref. [91].

As a consequence, T_H represents the "boiling point of hadronic matter" [89]. In some sense "hadron thermodynamics defines its own limits" [90]. Near this temperature, particle creation becomes so intense that the temperature cannot rise any further, regardless of the beam energy. Instead, a greater variety of more massive hadrons is produced [69]. Consequently, the momentum spectra adopt the form of Eq. (3.1.1) with the identification of the universal parameter λ as the inverse Hagedorn temperature $\frac{1}{T_H}$.

In the original SBM, hadrons were treated as point particles. However, with the advent of quark theory, a subtle modification was necessary: hadrons composed of quarks must be assigned a finite volume that increases with their mass [86]. The extension of the SBM was developed in the late 1970s [92]. It was found found that at T_H, finite-size hadrons dissolve into a quark-gluon liquid. This new state of matter can also reach temperatures above T_H. It is interesting to note that the production yields of light flavor hadrons from a chemically equilibrated[2] fireball can be predicted using a 'statistical hadronization approach' [91], which creates a connection between hadron production yields from ultrarelativistic HICs and the QCD partition function [see Fig. 3.2]. These models generally follow the relationship $\mathrm{d}N/\mathrm{d}y \sim \exp(-m/T_{\text{cf}})$, where T_{cf} agrees remarkably within error limits with the pseudocritical deconfinement transition temperature T_{pc} as well as with the Hagedorn temperature T_H [cf. Eq. (3.1.7) and right plot of Fig. 3.2]. It should also be stressed that light flavor hadron yields over nine orders of magnitude can be described with the

[2]Chemical equilibration is characterized by the *chemical freezeout temperature* $T_{\text{cf}} = 156.5(1.5)$ MeV, i.e. the point from which all hadron yields are frozen [91] and the fireball attains its ultimate particle composition [33].

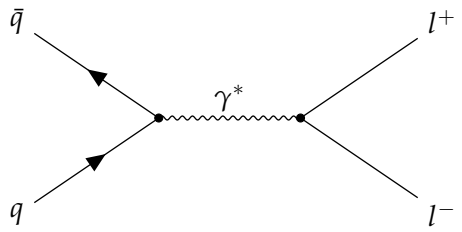

Figure 3.3: Dilepton production via quark-antiquark annihilation for the reaction $q\bar{q} \to l^- l^+$.

Statistical Hadronization Model (SHM) [see left plot of Fig. 3.2].

3.2 Probes of the QGP

Despite significant progress in HIC experiments and theoretical understanding, a definitive and unique signal for identifying the QGP phase is still not universally agreed upon. However, various signatures are employed in the search for the QGP. Thus, in this section we briefly discuss probes of the QGP, i.e. particles arising from the interactions between constituents of the QGP, thus providing information about the state of the plasma [73]. For many of these probes the Lorentz-invariant differential yield of final state particles [81],

$$E\frac{\mathrm{d}^3N}{\mathrm{d}^3p} = \frac{1}{2\pi p_\mathrm{T}}\frac{\mathrm{d}^2N}{\mathrm{d}p_\mathrm{T}\mathrm{d}y}\,, \tag{3.2.1}$$

is related to the transverse momentum p_T and the rapidity [73]

$$y = \frac{1}{2}\ln\left(\frac{p_0 + p_z}{p_0 - p_z}\right)\,, \tag{3.2.2}$$

which is the ratio of the forward light-cone momentum and the backward light-cone momentum.

3.2.1 Charm Quarks

Charm quarks are approximately 200-500 times heavier than up or down quarks [cf. Table 2.1], leading to a strong Boltzmann suppression in their thermal production. Their overall yield is determined by the charm production cross section rather than the temperature of the fireball [93]. Due to their significant mass ($m_c \gg T_{pc}$), charm quarks are produced predominantly in the initial hard collisions. However, they subsequently interact strongly within the hot fireball, leading to their thermalization. The interactions with numerous lighter quarks impart sufficient momentum to charm quarks, enabling their participation in the expansion of the QGP. This characteristic, coupled with the fact that they are produced in the early stages of the collision allows charm quarks to experience the full time evolution of the QGP. Thus, they serve as a perfect tool for investigating phenomena such as diffusion, recombination, and energy loss, thereby providing valuable insights into the medium's properties.

3.2.2 Dilepton Production

In the QGP phase a quark q may interact with an antiquark $\bar{q}$ forming a virtual photon γ^*, which subsequently decays into a lepton-antilepton pair $l^- l^+$ [see Fig. 3.3]. This pair is called *dilepton* and is characterized by a dilepton invariant mass squared $M^2 = (l^- + l^+)^2$ as well as a dilepton transverse momentum $\mathbf{p}_\mathrm{T} = \mathbf{l}_\mathrm{T}^- + \mathbf{l}_\mathrm{T}^+$ [cf. Eq. (3.0.1)]. During a relativistic HIC, photons and dileptons are produced throughout the entire spacetime evolution, from the initial stage where the colliding nuclei pass through each other, to the stage where they are produced by decaying hadrons that have decoupled from the QGP [94]. After their production, dileptons pass the collision region interacting only via the electromagnetic[3] interaction [73]. Consequently, dileptons have a large mean-free path and pass through the detector without scattering via strong interaction, thereby probing the entire spacetime history of the QGP.

The invariant pair mass M_{ll} helps to isolate different sources in dilepton spectra leading to an experimental advantage of a superior signal to background ratio compared to real photons, which lack this additional discriminating variable [33]. More information on photon production can be found in Secs. 7.1 and 7.4.

[3]The cross section is of the order $(\alpha_\mathrm{em}/\sqrt{s})^2$, where $\alpha_\mathrm{em} \approx 1/137$ is the electromagnetic coupling constant and $\sqrt{s}$ the center-of-mass energy [73].

Chapter 4

Finite Temperature

Thermal Field Theory (TFT) serves as the framework for addressing Quantum Field Theory (QFT) at finite temperature. It is predominantly utilized in cosmology and in the theoretical description of HIC experiments. Given the relevance of the latter context to this thesis, we provide a concise overview of TFT in this chapter, primarily based on Refs. [34, 95, 96].

4.1 Quantum Statistical Mechanics

Given that this thesis deals with systems interacting with a thermal reservoir at a constant temperature T, we briefly introduce the basic concepts of Quantum Statistical Mechanics (QSM) in this section. In equilibrium statistical mechanics, the *grand canonical ensemble* describes a system that is in contact with a reservoir allowing the exchange of both energy and particles, while the thermodynamic variables temperature $T = \frac{1}{\beta}$, volume V, and chemical potential μ [1] remain fixed. The statistical properties of the system are represented by the density matrix[2]

$$\hat{\rho} = \exp\left[-\beta\left(H - \mu_i \hat{N}_i\right)\right] , \tag{4.1.1}$$

where $\hat{N}_i$ represents a set of conserved number operators and H denotes the Hamiltonian characterizing the system. The thermal average of an observable A is determined as follows:

$$A = \langle A \rangle = \frac{1}{Z} \mathrm{Tr}[\hat{\rho} A] , \tag{4.1.2}$$

which represents an average over an ensemble of states constituting the corresponding Hilbert space with the partition function of the *canonical* ensemble defined as

$$Z = Z(T, V) = \mathrm{Tr}\, \mathrm{e}^{-\beta H} = \sum_n \langle n | \, \mathrm{e}^{-\beta H} \, | n \rangle , \tag{4.1.3}$$

where a complete set of eigenstates of the Hamiltonian H has been inserted. From the partition function $Z(T, V)$ all the thermodynamic properties may be determined via standard relations, e.g. the entropy S in the infinite-volume limit is given by $\frac{\partial (T \log Z)}{\partial T}$.

[1] In the remainder of the thesis, we will consider the case of a vanishing chemical potential, corresponding to zero baryon density. At $\mu \neq 0$ LQCD actions become complex and Monte-Carlo importance sampling is no longer feasible with standard techniques due to the sign problem.

[2] We employ a "hat" symbol on the density matrix to clearly distinguish it from the spectral function ρ, which will be introduced in Sec. 4.4.

4.2 Thermal Field Theory

The connection to TFT can be established through a functional integral representation of the canonical partition function. Within this framework, the partition function (4.1.3) can be evaluated by inserting a complete set of eigenstates of the Schrödinger-picture field operator,

$$Z(T,V) = \int \mathcal{D}[\phi]\, \langle\phi|\mathrm{e}^{-\beta H}|\phi\rangle\,, \qquad \mathcal{D}[\phi] \equiv \prod_{\mathbf{x}\in\mathbb{R}^3} \mathrm{d}\phi(\mathbf{x})\,, \tag{4.2.1}$$

where $|\phi\rangle$ denotes an eigenstate of the operator $\hat{\phi}(0,\mathbf{x})$. The action of the operator is defined by

$$\hat{\phi}(0,\mathbf{x})\,|\phi\rangle = \phi(\mathbf{x})\,|\phi\rangle\ , \tag{4.2.2}$$

and these eigenstates satisfy the completeness and orthogonality relations

$$\int \mathcal{D}[\phi]\ |\phi\rangle\,\langle\phi| = \mathbb{1}\,, \tag{4.2.3}$$

$$\langle\phi_a|\,\phi_b\rangle = \prod_{\mathbf{x}\in\mathbb{R}^3} \delta(\phi_a(\mathbf{x}) - \phi_b(\mathbf{x}))\,. \tag{4.2.4}$$

Analogous expressions apply to the eigenstates of the conjugate momentum operator $\hat{\pi}(0,\mathbf{x})$. At this stage, the functional integration over $\phi(\mathbf{x})$ merely represents the evaluation of the trace in a continuous basis of field eigenstates at a fixed time slice. It should therefore not be confused with the Euclidean path-integral measure introduced in Eq. (4.2.5), which integrates over full field configurations at imaginary time.

Upon examining Eq. (4.2.1), it becomes evident that the transition matrix element $\langle\phi|\mathrm{e}^{-\beta H}|\phi\rangle$ can be derived from the transition matrix element in QFT by performing a Wick rotation $t \to -i\tau$ of the time-evolution operator $U(t) = \mathrm{e}^{-\mathrm{i}Ht}$. This procedure restricts the imaginary time τ to the interval $[0,\beta]$, where the upper bound β is identified as the inverse temperature $1/T$. An evaluation of the resulting functional integral for a scalar field theory yields the expression [96]

$$Z(T,V) = \mathcal{C} \int_{\phi(\beta,\mathbf{x})=\phi(0,\mathbf{x})} \mathcal{D}[\phi]\ \exp\left[-\int_0^\beta \mathrm{d}\tau \int \mathrm{d}^3x\, \mathcal{L}_E(\phi,\partial\phi)\right]\,, \tag{4.2.5}$$

where $\mathcal{L}_E$ denotes the Euclidean Lagrange density. The factor $\mathcal{C}$ represents an overall normalization constant that emerges from the integration over the conjugate momenta $\hat{\pi}(0,\mathbf{x})$ and does not contain any dynamical information. Notably, this constant typically drops out in practical calculations, e.g. two-point correlation functions. It should be noted that for fermion fields ψ, the boundary condition specified in Eq. (4.2.5) is modified to be antiperiodic, specifically $\psi(\beta,\mathbf{x}) = -\psi(0,\mathbf{x})$. This is a consequence of the trace operation appearing in Eq. (4.2.5). To clarify this concept, we introduce fermionic thermal Green's functions as follows:

$$G_F(\tau_1,\tau_2;\mathbf{x},\mathbf{y}) = Z^{-1}\,\mathrm{Tr}\big\{\hat{\rho}\,T_\tau\left[\hat{\psi}(\tau_1,\mathbf{x})\,\hat{\psi}(\tau_2,\mathbf{y})\right]\big\}\ , \tag{4.2.6}$$

where T_τ denotes the time ordering operator in imaginary time τ defined by:

$$T_\tau\left[\hat{\psi}(\tau_1,\mathbf{x})\,\hat{\psi}(\tau_2,\mathbf{y})\right] = \hat{\psi}(\tau_1,\mathbf{x})\,\hat{\psi}(\tau_2,\mathbf{y})\,\theta(\tau_1-\tau_2) - \hat{\psi}(\tau_2,\mathbf{y})\,\hat{\psi}(\tau_1,\mathbf{x})\,\theta(\tau_2-\tau_1)\,. \tag{4.2.7}$$

Starting from Eq. (4.2.6) and applying the cyclic property of the trace, we derive

$$\begin{aligned} G_F(\tau,0;\mathbf{x},\mathbf{y}) &= Z^{-1}\,\mathrm{Tr}\left[\mathrm{e}^{-\beta H}\,\mathrm{e}^{\beta H}\,\hat{\psi}(0,\mathbf{y})\,\mathrm{e}^{-\beta H}\,\hat{\psi}(\tau,\mathbf{x})\right] \\ &= Z^{-1}\,\mathrm{Tr}\left[\mathrm{e}^{-\beta H}\,\hat{\psi}(\beta,\mathbf{y})\,\hat{\psi}(\tau,\mathbf{x})\right] \\ &= -Z^{-1}\,\mathrm{Tr}\left[\rho_T\,T_\tau\,\hat{\psi}(\tau,\mathbf{x})\,\hat{\psi}(\beta,\mathbf{y})\right] = -G_F(\tau,\beta;\mathbf{x},\mathbf{y})\,, \end{aligned} \tag{4.2.8}$$

where we used $e^{\beta H}\,\hat{\psi}(0,\mathbf{y})\,e^{-\beta H} = \hat{\psi}(\beta,\mathbf{y})$, which is the analogue of the Heisenberg time-evolution in real time, $\mathrm{e}^{\mathrm{i}Ht}\,\hat{\psi}(0,\mathbf{y})\,\mathrm{e}^{-\mathrm{i}Ht} = \hat{\psi}(t,\mathbf{y})$. In the context of bosonic Green's functions, the time ordering operator (4.2.7) is characterized by a positive sign between the terms. Consequently, we obtain

$$G_B(\tau,0;\mathbf{x},\mathbf{y}) = G_B(\tau,\beta;\mathbf{x},\mathbf{y})\,. \tag{4.2.9}$$

In concluding this section, we quote the expansion of the fields in Fourier modes in imaginary time τ [96]

$$\phi(\tau,\mathbf{x}) = T\sum_{\omega_n}\frac{1}{V}\sum_{\mathbf{k}}\tilde{\phi}(\omega_n,\mathbf{k})\mathrm{e}^{\mathrm{i}(\omega_n\tau+\mathbf{k}\mathbf{x})}\,. \tag{4.2.10}$$

In the following sections, we will provide a concise examination of various forms of thermal Green's functions and their relationship to spectral functions, which constitute a central element of this thesis.

4.3 Thermal Correlation Functions

Given the significance of this topic for the thesis, we shall present several key relationships between Euclidean and retarded correlators in the presence of a thermal bath, restricting to the case of zero chemical potential. The subsequent relations closely adhere to the presentation and notation found in Ref. [34]. We define the structure of a general time-ordered thermal correlator for two arbitrary composite operators, A and B. It is assumed that the density matrix is normalized. To simplify the notation, we project both operators to zero momentum, thereby integrating over the spatial dependence. The two potential contributions can be expressed as follows:

$$G^{AB}_{>}(t) = \mathrm{Tr}\{\hat{\rho}\,A(t)B(0)\}\,, \tag{4.3.1}$$

$$G^{AB}_{<}(t) = \mathrm{Tr}\{\hat{\rho}\,B(0)A(t)\}\,, \tag{4.3.2}$$

where A is an operator in the Heisenberg picture, i.e., $A(t) = e^{\mathrm{i}Ht}A(0)e^{-\mathrm{i}Ht}$. By utilizing Eq. (4.3.1), it can be shown that

$$G^{AB}_{>}(t) = G^{BA}_{>}(-t-\mathrm{i}\beta)\,, \tag{4.3.3}$$

which is recognized as the Kubo-Martin-Schwinger (KMS) relation. This property uniquely characterizes the equilibrium density matrix [34]. In practical calculations one inserts a complete set

of eigenstates of the Hamiltonian H, i.e.,

$$G_{>}^{AB}(t) = \frac{1}{Z}\sum_{m,n} \mathrm{e}^{-\beta E_m}\, \mathrm{e}^{\mathrm{i}t(E_m - E_n)} \langle m|A(0)|n\rangle\langle n|B(0)|m\rangle = G_{<}^{AB}(-t)\,. \tag{4.3.4}$$

Equations (4.3.1) and (4.3.2) can be combined into a commutator,

$$G^{AB}(t) = \mathrm{i}\,\mathrm{Tr}\{\hat{\rho}[A(t), B(0)]\} = \mathrm{i}\left(G_{>}^{AB}(t) - G_{<}^{AB}(t)\right)\,, \tag{4.3.5}$$

which vanishes outside the light-cone[3].

The Fourier transform over the positive half axis defines the retarded correlator

$$G_R^{AB}(\omega) = \int_0^\infty \mathrm{d}t\, \mathrm{e}^{\mathrm{i}\omega t}\, G^{AB}(t)\,, \tag{4.3.6}$$

which plays an important role in linear response theory [34] and is also closely related to the time-ordered correlator, $G_T^{AB}(\omega)$, familiar from perturbation theory, via

$$G_R^{AB}(\omega) = \begin{cases} \mathrm{i}\, G_T^{AB}(\omega)\,, & \mathrm{Re}\,\omega > 0, \\ (\mathrm{i}\, G_T^{B^\dagger A^\dagger}(\omega))^*\,, & \mathrm{Re}\,\omega < 0\,. \end{cases} \tag{4.3.7}$$

4.4 Spectral Functions

In thermal equilibrium, it turns out that all the correlation functions delineated in the previous section 4.3 are interrelated. Specifically, they can be expressed in terms of the *spectral function* [96],

$$\rho^{AB}(\omega) = \frac{1}{2\pi\mathrm{i}}\int_{\mathbb{R}} \mathrm{d}t\, \mathrm{e}^{\mathrm{i}\omega t}\, G^{AB}(t) \tag{4.4.1}$$

$$= \frac{1}{2\pi}\int_{\mathbb{R}} \mathrm{d}t\, \mathrm{e}^{\mathrm{i}\omega t}\left(G_{>}^{AB}(t) - G_{<}^{AB}(t)\right) \tag{4.4.2}$$

$$= G_{>}^{AB}(\omega) - G_{<}^{AB}(\omega)\,, \tag{4.4.3}$$

where in the first step we employed Eq. (4.3.5). By comparing with Eq. (4.3.6), we obtain

$$G_R^{AB}(t) = 2\pi\mathrm{i}\,\theta(t)\,\rho^{AB}(t)\,, \quad \text{with } \theta(t) = \int_{\mathbb{R}} \frac{\mathrm{d}\omega}{2\pi}\mathrm{e}^{-\mathrm{i}\omega t}\frac{\mathrm{i}}{\omega + \mathrm{i}\epsilon}\,. \tag{4.4.4}$$

Performing the Fourier transform of (4.4.4) we arrive at

$$\begin{aligned} G_R^{AB}(\omega) &= 2\pi\mathrm{i}\int_{\mathbb{R}} \mathrm{d}t\, \mathrm{e}^{\mathrm{i}\omega t}\left[\theta(t)\int_{\mathbb{R}} \mathrm{d}\omega' \frac{\mathrm{e}^{-\mathrm{i}\omega' t}}{2\pi}\rho^{AB}(\omega')\right] \\ &= \mathrm{i}\int_{\mathbb{R}} \mathrm{d}\omega' \rho^{AB}(\omega') \underbrace{\int_{\mathbb{R}} \mathrm{d}t\, \theta(t)\, \mathrm{e}^{\mathrm{i}(\omega-\omega')t}}_{=\mathrm{i}\,/\,[\omega-\omega'+\mathrm{i}\epsilon]} \\ &= \int_{\mathbb{R}} \mathrm{d}\omega' \frac{\rho^{AB}(\omega')}{\omega' - \omega - \mathrm{i}\epsilon} \end{aligned} \tag{4.4.5}$$

[3] This is a reflection of the causality of the underlying theory [97].

a dispersion relation for the retarded correlator G_R. Employing Eq. (4.4.1) together with $G^{AB}(-t) = -G^{BA}(t)$ we derive another important relation[4]

$$\rho^{AA^\dagger}(\omega) = \frac{1}{\pi}\,\mathrm{Im}\,G_R^{AA^\dagger}(\omega) \;\in \mathbb{R}\,, \tag{4.4.6}$$

relating the spectral function to the imaginary part of the retarded correlator.

The Euclidean correlator is a crucial component in the lattice formulation, as it is this particular form of the correlator that can be determined through Monte Carlo simulations at imaginary times[5] $it = \tau \in [0, \beta]$. It is connected to the previously defined quantities as follows:

$$G_E^{AB}(\tau) = G_>^{AB}(-\mathrm{i}\tau)\,, \tag{4.4.7}$$

For the Euclidean G_E correlator, the KMS relation (4.3.3) implies that

$$G_E^{BA}(\beta - \tau) = G_E^{AB}(\tau)\,. \tag{4.4.8}$$

Expanding in a Fourier series, we obtain at finite temperature

$$G_E(\tau) = \frac{1}{\beta}\sum_n \mathrm{e}^{-\mathrm{i}\omega_n\tau}\,G_E(\omega_n)\,, \tag{4.4.9}$$

$$G_E(\omega_n) = \int_0^\beta \mathrm{d}\tau\,\mathrm{e}^{\mathrm{i}\omega_n\tau}\,G_E(\tau)\,, \tag{4.4.10}$$

where $\beta = \frac{1}{T}$ denotes the inverse temperature. Note that in transitioning to frequency space, the Euclidean propagator is assessed at discrete Matsubara frequencies,

$$\omega_n = \frac{2\pi n}{\beta} \quad \text{for bosons,} \qquad \omega_n = \frac{(2n+1)\pi}{\beta} \quad \text{for fermions.} \tag{4.4.11}$$

Furthermore, by analyticity, the Euclidean correlator satisfies a dispersion relation (4.4.5) that mirrors that of the retarded correlator, i.e. [98],

$$G_E(\omega_n) = \int_{\mathbb{R}} \mathrm{d}\omega'\,\frac{\rho(\omega')}{\omega' - \mathrm{i}\omega_n} = \int_{\mathbb{R}} \mathrm{d}\omega'\,\frac{\omega'}{(\omega')^2 + \omega_n^2}\rho(\omega')\,, \tag{4.4.12}$$

where $\rho(-\omega) = -\rho(\omega)$ has been used. Consequently, we can relate the retarded correlator to the Euclidean correlator in the following way,

$$G_R(\omega) \;=\; G_E(\mathrm{i}\omega_n \;\to\; \omega + \mathrm{i}\epsilon)\,. \tag{4.4.13}$$

For an analytically known Euclidean correlator, the spectral function can in principle be derived by following the sequence [98]

$$G_E(\tau) \;\longrightarrow\; G_E(\omega_n) \;\longrightarrow\; G_R(\omega) \;\longrightarrow\; \rho(\omega)\,. \tag{4.4.14}$$

[4] Alternatively one can use Eq. (4.4.5) together with the identity $\frac{1}{x-\mathrm{i}\epsilon} - \frac{1}{x+\mathrm{i}\epsilon} = \frac{2\mathrm{i}\epsilon}{x^2+\epsilon^2} \xrightarrow[\epsilon\to 0]{} 2\mathrm{i}\pi\delta(x)$.

[5] Let $\mathcal{X} = (t, \mathbf{x})$ and $\mathcal{K} = (\omega, \mathbf{k})$ represent coordinates and momenta in Minkowskian spacetime, with their Euclidean counterparts denoted as $X = (\tau, \mathbf{x})$ and $K = (\omega_n, \mathbf{k})$. These are related through Wick rotations, specifically $\tau \leftrightarrow \mathrm{i}t$ and $\omega_n \leftrightarrow -\mathrm{i}\omega$ [96].

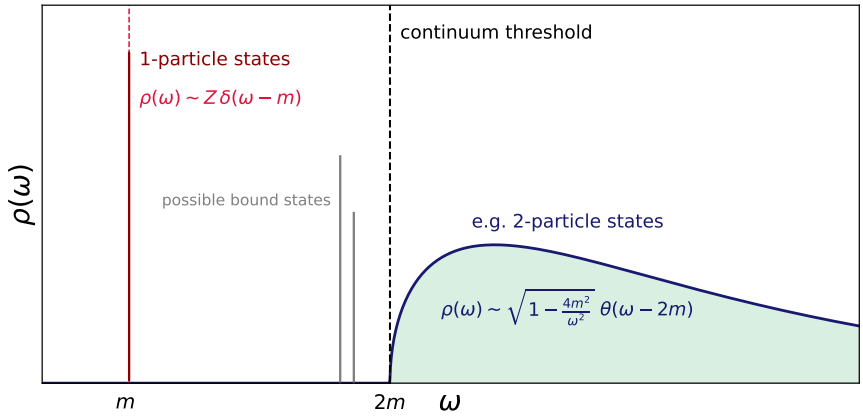

Figure 4.1: The spectral function $\rho(\omega)$ in a typical interacting QFT is characterized as follows: The contribution from one-particle states is represented by a delta function at $\omega = m$, where m denotes the particle's mass, and $Z = |\langle 1|\, A(0)^\dagger\, |0\rangle|^2$ is the field-strength renormalization factor quantifying the overlap strength of the operator with that single-particle state. In contrast, multiparticle states generate a continuous spectrum starting at a threshold of $2m$. Additionally, bound states may be present in the system. At finite temperature, energy can be exchanged with the heat bath; consequently, the discrete peaks broaden into Breit-Wigner type curves. This figure is inspired by Ref. [97].

In typical lattice simulations, the Euclidean correlator at finite temperature, $G_E(\tau)$, is typically determined at $\mathcal{O}(10)$ discrete points along the temporal direction. In contrast, the spectral function $\rho(\omega)$ is generally a continuous function w.r.t. ω. As a result, spectral reconstruction methods are required, for which a particular representation of the Euclidean correlator, expressed through a generalized Laplace transform, has been found to be beneficial [see Eq. (6.2.15) and Appendix A].

In the following we want to motivate a simple physical interpretation of the spectral function. For the sake of simplicity, we assume $B = A^\dagger = A$ and focus on the zero temperature limit, where $\beta \to \infty$. As a result, in the expression $\sum_m \mathrm{e}^{-\beta E_m}$ in Eq. (4.3.4), only the vacuum state $|0\rangle$ survives. By employing Eq. (4.4.2) with $E_0 \equiv 0$, we derive the following:

$$\rho^{AA}(\omega) = \frac{1}{2\pi} \sum_n |\langle 0|\, A(0)\, |n\rangle|^2 \int_{\mathbb{R}} \mathrm{d}t\, \left(\mathrm{e}^{-\mathrm{i}t(E_n - \omega)} - \mathrm{e}^{+\mathrm{i}t(E_n + \omega)} \right) \tag{4.4.15}$$

$$= \sum_n |\langle n|\, A(0)^\dagger\, |0\rangle|^2 \left[\delta(E_n - \omega) - \delta(E_n + \omega) \right]. \tag{4.4.16}$$

In this representation, it is apparent that the spectral function ρ is an odd function of ω. Moreover, ρ characterizes a density of states, meaning that the factor $|\langle n|\, A(0)^\dagger\, |0\rangle|^2$ represents the probability of generating a state with energy $E_n = \omega$ from the vacuum state $|0\rangle$. This situation is depicted in Fig. 4.1. At finite temperatures, this straightforward model undergoes modification as the system is capable of exchanging energy with the heat bath. Consequently, the Dirac-Delta peaks broaden, and the localization of the poles may also shift, necessitating a description with more sophisticated distributions to account for finite thermal widths, such as those of a Breit-Wigner type as in (6.3.7). The outcome of the spectral function reconstruction method for the pion quasiparticle mass in the low-temperature phase of QCD is presented in Fig. 6.6.

Chapter 5

Lattice QCD

Lattice Gauge Theory (LGT), introduced by Kenneth Wilson in 1974 [55], represents a formulation of QFT on a discrete space-time lattice. Wilson's pioneering work, which earned him the 1982 Nobel Prize in Physics, offers a non-perturbative framework for the study of gauge theories, such as QCD. A significant advantage of the lattice discretization is its ability to preserve gauge invariance precisely at finite lattice spacing. Furthermore, it has been demonstrated that LQCD serves as a valid ultraviolet (UV) regularization of QCD to all orders of perturbation theory [99]. By employing only a finite number of degrees of freedom, this formulation enables numerical simulations through Monte Carlo methods.

In this chapter, we present a concise overview of LQCD, primarily drawing upon Ref. [100]. Additional introductory textbooks on LGT include Refs. [53, 101–104]. Portions of the current chapter are influenced by the PhD theses [105–110].

5.1 Basic Concepts

The path integral found in the definition of the partition function (4.2.5) is an entity of infinite dimension. To achieve a finite number of degrees of freedom, Euclidean four-dimensional space-time is discretized on a lattice

$$\Lambda = \left\{ x \in \mathbb{R}^4 \,|\, x_\mu = a n_\mu;\; n_i = 0, \ldots, N_s - 1;\; n_0 = 0, \ldots, N_\tau - 1 \right\} , \tag{5.1.1}$$

with a lattice spacing a, which establishes the minimal distance between points and naturally acts as a regulator for UV divergences. An often misunderstood yet significant aspect is that the lattice spacing a is not an input parameter in LQCD simulations. Instead, it must be determined a posteriori through a procedure known as *scale setting* [cf. Sec. 5.3].

Throughout this thesis, we are always dealing with isotropic lattices, i.e. $a_s = a_\tau$. However, it is often beneficial to have a huge resolution in temporal direction, e.g. in spectral reconstruction problems [see Sec. 6.4]. The `FASTSUM` collaboration has developed a robust program utilizing anisotropic lattices, where $a_\tau < a_s$. This approach has been effectively applied to various studies, including electrical conductivity [111, 112], heavy quark physics [113–117], and the phenomenon of parity doubling in baryons [117–120]. Recent findings have been reported concerning a lattice with a temporal lattice spacing of $a_\tau = 15\,\mathrm{am}$ [121].

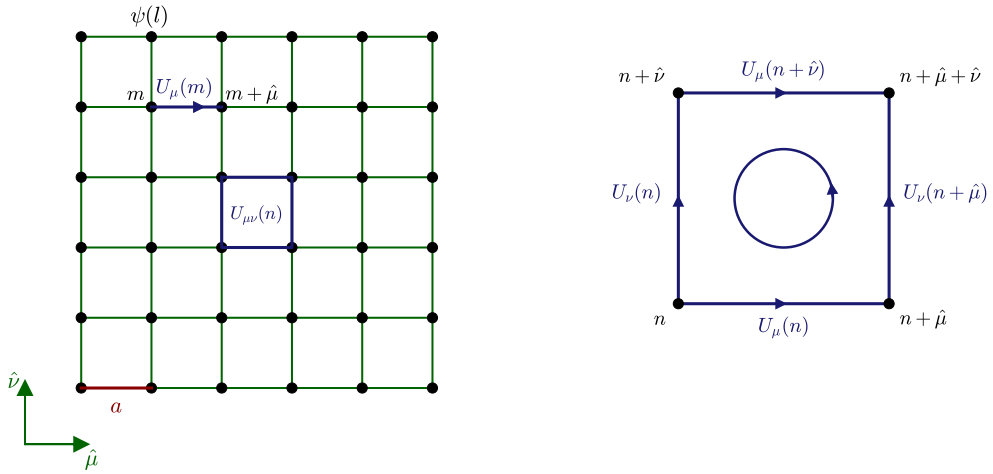

Figure 5.1: Schematic representation of a two-dimensional Euclidean lattice with lattice spacing a. The fermion fields are positioned at the lattice site n, while the link variable $U_\mu(n)$ connects adjacent sites n and $n+\hat{\mu}$. The plaquette variable $U_{\mu\nu}(n)$ is defined as the oriented product of four link variables encircling an elementary square in the $(\hat{\mu}$-$\hat{\nu})$–plane. The circle indicates the direction in which the link variables are traversed.

The physical volume of LQCD boxes is given by $V = \frac{L^3}{\beta}$, where

$$L = aN_s\,, \tag{5.1.2}$$

$$\beta = \frac{1}{T} = aN_\tau\,. \tag{5.1.3}$$

Consequently, the *inverse temperature* β[1] is defined as the imaginary time extent of the box and can be adjusted either by modifying the number of lattice points or by altering the lattice spacing, whereby the vacuum theory is obtained in the limit $\beta \to \infty$. The quantity $\frac{L}{\beta}$ is independent of the lattice spacing and is referred to as the *aspect ratio*.

The discretization of space-time has significant implications for the momentum resolution[2] on the lattice. By transitioning to momentum space, we can define the reciprocal lattice as the set [100]

$$\tilde{\Lambda}_{\mathcal{B}} = \left\{ p \in \mathbb{R}^4 \;\middle|\; p_\mu = \frac{2\pi}{an_\mu}(k_\mu + \theta_\mu) \;\middle|\; k_\mu = -\frac{n_\mu}{2}+1, \cdots, \frac{n_\mu}{2} \right\}, \tag{5.1.4}$$

where the boundary phase θ_μ must be incorporated into the definition of the momenta to ensure they adhere to the same boundary conditions as functions

$$f(x + aN_\mu) = \mathrm{e}^{\mathrm{i}2\pi\theta_\mu} f(x) \tag{5.1.5}$$

[1] This should not be confused with the *inverse coupling* $\beta = \frac{2N_c}{g^2}$. Unfortunately, both are standard notation and it should be clear from the context what is meant.

[2] In the special case of quark-connected observables it is feasible to attain continuous momentum values by utilizing partially twisted boundary conditions. For more details, see Ref. [122]. This is relevant for instance if the lattice possesses a non-integer aspect ratio as demonstrated by the `E250Nt20` ensemble [cf. Table 6.2] and there is a need to inject momenta of identical magnitude in both spatial and temporal directions of two-point functions.

defined on the lattice. In the spatial directions ($\mu \in \{1,2,3\}$), periodic boundary conditions are imposed [$\theta_i = 0$ in Eq. (5.1.5)], whereas in the temporal direction, antiperiodic boundary conditions are applied, corresponding to $\theta_0 = \frac{1}{2}$. The associated values $\omega_k \equiv p_0$ are referred to as *Matsubara frequencies*.

As a subsequent step, the continuum QCD action corresponding to the Euclidean Lagrangian (2.1.3) must be discretized, ensuring that in the limit $a \to 0$, the continuum version is accurately reproduced. During this procedure, challenges such as the loss of chiral symmetry and the emergence of fermion doublers are encountered and there is no unique prescription for constructing the lattice action. The degrees of freedom living on the lattice (5.1.1) are classical field variables. We will see that fermionic degrees of freedom live on the lattice sites n. In order to make the fermionic action gauge-invariant, matrix-valued *link variables* $U_\mu(n)$ need to be introduced connecting the lattice sites n and $n+\hat{\mu}$ [cf. Fig. 5.1]. The expectation value of a general observable O is then computed as [100]

$$\langle O \rangle = \frac{\int [\mathrm{d}\bar{\psi}]\,[\mathrm{d}\psi]\,\mathcal{D}[U]\;\mathrm{e}^{-S_{\mathrm{LQCD}}[\bar{\psi},\psi,U]}\;O[\bar{\psi},\psi,U]}{\int [\mathrm{d}\bar{\psi}]\,[\mathrm{d}\psi]\,\mathcal{D}[U]\;\mathrm{e}^{-S_{\mathrm{LQCD}}[\bar{\psi},\psi,U]}}\,. \tag{5.1.6}$$

In this expression, S_{LQCD} denotes the discretized version of the Euclidean action that will be discussed in Sec. 5.4 and the denominator corresponds to the partition function Z. We emphasize that in Eq. (5.1.6), the symbols $\bar{\psi}, \psi$, and U do not represent operators; rather, they have been replaced by functionals corresponding to their respective classical lattice field variables. Euclidean correlation functions are computed as integrals over all lattice field configurations, wherein the functionals are weighted by the Boltzmann factor $\mathrm{e}^{-S_{\mathrm{LQCD}}}$.

5.2 A First Glimpse on Euclidean Two-Point Correlation Functions

Euclidean two-point correlation functions are the central quantities of this thesis. They are defined as the expectation value $\langle O_2 O_1^\dagger \rangle$ of an operator $O_1^\dagger(\tau_1, \mathbf{x}_1)$, which creates a tower of states carrying the quantum numbers specified by O_1 at the space-time point $(\tau_1, \mathbf{x}_1)$, and an operator $O_2(\tau_2, \mathbf{x}_2)$, which annihilates states specified by the operator O_2 at space-time point $(\tau_2, \mathbf{x}_2)$. Exploiting translation invariance, we can fix one operator at the origin $(\tau_1, \mathbf{x}_1) = (0, \mathbf{0})$, and the other at $(\tau_2, \mathbf{x}_2) = (\tau, \mathbf{x})$. Utilizing Eqs. (4.1.2) and (4.1.3) as well as Heisenberg time-evolution for O_2 leads to [100]

$$\begin{aligned}
\langle O_2(\tau,\mathbf{x}) O_1^\dagger(0)\rangle &= \frac{\mathrm{Tr}\left[\mathrm{e}^{-(\beta-\tau)H} O_2(0,\mathbf{x}) \mathrm{e}^{-\tau H} O_1^\dagger(0)\right]}{\sum_m \langle m|\mathrm{e}^{-\beta H}|m\rangle} \\
&= \frac{\sum_{m,n} \langle m|\,\mathrm{e}^{-(\beta-\tau)H} O_2(0,\mathbf{x})\,|n\rangle\,\langle n|\,\mathrm{e}^{-\tau H} O_1^\dagger(0)\,|m\rangle}{\mathrm{e}^{-\beta E_0} + \mathrm{e}^{-\beta E_1} + \mathrm{e}^{-\beta E_2} + \cdots} \\
&= \frac{\sum_{m,n} \mathrm{e}^{-(\beta-\tau)E_m}\,\mathrm{e}^{-\tau E_n}\,\langle m|\,O_2(0,\mathbf{x})\,|n\rangle\,\langle n|\,O_1^\dagger(0)\,|m\rangle}{\mathrm{e}^{-\beta E_0}\left(1 + \mathrm{e}^{-\beta(E_1-E_0)} + \mathrm{e}^{-\beta(E_2-E_0)} + \cdots\right)} \\
&= \frac{\sum_{m,n} \mathrm{e}^{-(\beta-\tau)\Delta E_m}\,\mathrm{e}^{-\tau \Delta E_n}\,\langle m|\,O_2(0,\mathbf{x})\,|n\rangle\,\langle n|\,O_1^\dagger(0)\,|m\rangle}{1 + \mathrm{e}^{-\beta\Delta E_1} + \mathrm{e}^{-\beta\Delta E_2} + \cdots}\,,
\end{aligned} \tag{5.2.1}$$

where $\Delta E_m = E_m - E_0$ represents the energy differences relative to the ground-state energy, which are measurable in physical experiments. In the limit as $\beta = N_\tau a \to \infty$ and with the normalization of the vacuum energy E_0 to zero, only the terms with $|m\rangle = 0$ remain in the numerator of Eq. (5.2.1), leading to the important expression

$$\lim_{\beta\to\infty} \langle O_2(\tau, \mathbf{x}) O_1^\dagger(0)\rangle = \sum_n \mathrm{e}^{-\beta E_n} \langle 0| O_2(0, \mathbf{x}) |n\rangle \langle n| O_1^\dagger(0) |0\rangle \ . \tag{5.2.2}$$

To illustrate the usefulness of the spectral representation (5.2.2), we show how to extract the pion mass and its matrix element on the lattice. For this purpose we need to construct an interpolator[3] with the pion's quantum numbers from quark and antiquark fields. A standard choice is the pseudoscalar density $P = \bar{u}\gamma_5 d$. We then consider the corresponding two-point function G_P. By projecting to vanishing momentum $\mathbf{p} = 0$, we obtain

$$\begin{aligned} G_P(an_\tau, \mathbf{p} = 0) &= \sum_{\mathbf{x}} \sum_n \mathrm{e}^{-n_\tau a E_n} \langle 0| P(0, \mathbf{x}) |n\rangle \langle n| P^\dagger(0) |0\rangle \\ &= L^3 \sum_n \mathrm{e}^{-n_\tau a E_n} |\langle n|P^\dagger(0, \mathbf{p} = 0)|0\rangle|^2 \qquad (5.2.3) \\ &= L^3 |\langle \pi|P(0, \mathbf{0})|0\rangle|^2 \, \mathrm{e}^{-n_\tau a m_\pi} \left[1 + \mathcal{O}(\mathrm{e}^{-n_\tau a \Delta E})\right] , \qquad (5.2.4) \end{aligned}$$

where an_τ denotes the Euclidean time in lattice units and ΔE is the mass gap to the first excited state, such as the first radial pion excitation π^* [123]. In the spectral decomposition (5.2.3), multi-pion states (e.g. $|\pi(\mathbf{p})\pi(-\mathbf{p})\pi(\mathbf{0})\rangle$) also contribute since they have a non-vanishing overlap with $P^\dagger(0, \mathbf{p} = 0)|0\rangle$. However, at sufficiently large Euclidean time separations an_τ, these excited states are exponentially suppressed, and the correlator becomes dominated by the lightest state $|\pi\rangle$ with ground-state energy m_π.

5.3 Scale Setting and Extrapolations

All observables calculated in LQCD are dimensionless, i.e. expressed in terms of powers of the lattice spacing a. The *Callan-Symanzik equations* [100]

$$\frac{\mathrm{d}O(g, m_l, m_s, a)}{\mathrm{d}\log a} = \left(\frac{\mathrm{d}}{\mathrm{d}\log a} + \frac{\partial g}{\partial \log a}\frac{\partial}{\partial g} + \frac{\partial m_l}{\partial \log a}\frac{\partial}{\partial m_l} + \frac{\partial m_s}{\partial \log a}\frac{\partial}{\partial m_s}\right) O(g, m_l, m_s, a) = 0 \,, \tag{5.3.1}$$

describe how the bare lattice parameters depend on the lattice spacing a, such that the lattice observable $O(g(a), m_l, m_s, a)$ has a well-defined continuum limit. The coefficient function of the second term in Eq. (5.3.1)

$$\beta(g) = -\frac{\partial g}{\partial \log a} \overset{g\to 0}{=} -\beta_0 g^3 - \beta_1 g^5 + \mathcal{O}(g^7) \tag{5.3.2}$$

plays a special role. It encodes how the bare coupling g depends on the lattice spacing a. The first two terms of the expansion (β_0 and β_1) are simple functions of the number of quark flavors N_f and

[3] Interpolators are functionals of the lattice fields with the quantum numbers of the physical state in question [100].

the number of colors N_c. The solution of Eq. (5.3.2) is given by [100]

$$a(g) = \frac{1}{\Lambda_{\mathrm{L}}}(\beta_0 g^2)^{-\frac{\beta_1}{2\beta_0^2}} \exp\left(-\frac{1}{2\beta_0 g^2}\right)\left[1 + O(g^2)\right], \tag{5.3.3}$$

where Λ_{L} denotes an integration constant. From Eq. (5.3.3), it can be deduced that the continuum limit $a \to 0$ is associated with $g \to 0$, a property referred to as *asymptotic freedom*.

To establish a connection with the "real world", it is necessary to select a quantity that can be easily computed on the lattice with high precision and for which the corresponding dimensionful quantity can be determined experimentally. In practice, this process of *setting the scale* is hampered by the fact that the lattice observable is often measured at an unphysical quark mass and requires separate chiral extrapolations to its physical value for each value of the lattice spacing. Additionally, the ensembles utilized by the Coordinated Lattice Simulations (CLS) initiative are generated in the isospin-symmetric limit, complicating direct comparisons with experimental data.

A commonly utilized hadronic reference length in lattice QCD is the Sommer parameter, denoted as r_0. It is defined by the relation [124]

$$r^2 F(r)\big|_{r=r_0} = 1.65\,, \tag{5.3.4}$$

where $F(r) = \frac{\mathrm{d}V(r)}{\mathrm{d}r}$ represents the force derived from the static quark potential $V(r)$. The constant value of 1.65 is chosen to ensure that $r_0 \simeq 0.5\,\mathrm{fm}$, aligning with phenomenological data from bottomonium and charmonium spectra [125]. Initially, the scale was established using the Sommer parameter r_0 for our two-flavor CLS ensembles, which are employed in Part III of this thesis. Subsequently, the scale setting was refined by utilizing the kaon-decay constant f_k with a quenched strange quark [126].

In Part II of this thesis, measurements are performed on CLS ensembles in $N_{\mathrm{f}} = 2 + 1$ flavor QCD [127]. Also in this framework, effects from electromagnetism, isospin breaking, and heavy sea quarks are omitted.

Consider a lattice observable $a^n O(a, am_l, am_s, \frac{L}{a})$, where n is selected such that $a^n O$ is dimensionless. The input parameters, specifically the light and strange quark masses, require chiral extrapolation to reach their physical values. Additionally, simulations must be performed for varying spatial lattice sizes $\frac{L}{a}$ to quantify the so-called *finite size effects*. By fitting the dependence on L, it is possible to perform the infinite volume limit as $L \to \infty$. The dimensionless parameters

$$\phi_2 = 8\frac{t_0}{a^2}(aM_\pi)^2 \quad \propto \quad (m_u + m_d)\,, \tag{5.3.5}$$

$$\phi_4 = 8\frac{t_0}{a^2}\left[(aM_K)^2 + \frac{1}{2}(aM_\pi)^2\right] \quad \propto \quad (m_u + m_d + m_s)\,, \tag{5.3.6}$$

are used to define a target point in the (m_l, m_s)-plane. In this context, $\frac{t_0}{a^2}$ represents the Wilson flow time parameter [128], which serves to define an intermediate scale. This parameter is only accessible through lattice simulations. It cannot be measured experimentally [127]. On the other hand, due to its nature as a purely gluonic observable, $\frac{\sqrt{t_0}}{a}$ can be determined with high precision on the lattice. The process of scale setting starts with the selection of an initial value of $\sqrt{t_0}$ in physical units [129], thereby defining a target point in the (ϕ_2, ϕ_4)-plane. To establish a connection

with experimental data, the lattice observable O is selected as a linear combination of the pion and kaon decay constants [129]

$$af_{\pi K}\left(a, am_l, am_s\right) = \frac{2}{3}a\left(f_K + \frac{1}{2}f_\pi\right), \tag{5.3.7}$$

and measured on the lattice alongside the product $\frac{\sqrt{t_0}}{a}af_{\pi K}$ for various values of a. Subsequently, the observable $\sqrt{t_0}f_{\pi K}$ is extrapolated to the "physical" point within the (ϕ_2, ϕ_4)-plane. Finally, the ratio

$$\frac{[\sqrt{t_0}f_{\pi K}]_{\text{phys.}}}{[f_{\pi K}]_{\text{experim.}}}, \tag{5.3.8}$$

is constructed using the experimental value and compared to the initial value of $\sqrt{\tilde{t}_0}$. Should a discrepancy be observed, the entire procedure is repeated until concordance is achieved.

Instead of the linear combination of decay constants (5.3.7), one can utilize an observable with minimal sensitivity to isospin-breaking effects, such as the Ω-baryon [130, 131], which is composed of three valence strange quarks. Consequently, every lattice spacing determination is affected by lattice artifacts itself.

5.4 Discretization of the Euclidean QCD Action

In this section, we aim to present the discretization of the continuum Euclidean QCD action $S_E = \int \mathrm{d}^4x\, \mathcal{L}_E$, where $\mathcal{L}_E$ is defined in Eq. (2.1.3). When fermions are placed on the lattice, the naive discretization of the fermionic action S_F requires augmentation with an additional term to eliminate lattice artifacts. Furthermore, we will see that the gauge fields must be incorporated as elements of the gauge group, rather than the algebra, for S_F to become gauge invariant.

5.4.1 Discretization of the Free Fermion Action

The continuum version of the free fermion action reads [100]

$$S_F^0[\bar{\psi}, \psi] = \int \mathrm{d}^4x\, \bar{\psi}(x)\left[\gamma_\mu\partial_\mu + m\right]\psi(x), \tag{5.4.1}$$

where matrix/vector notation is employed, suppressing color and Lorentz indices. In the discretization procedure the spinors $\bar{\psi}(x)$ and $\psi(x)$ are placed at the sites n of the lattice (5.1.1) such that $x_\mu = an_\mu$. This arrangement is visualized in Fig. 5.1. The next step involves substituting the integral $\int \mathrm{d}^4x$ with the discretized sum $a^4\sum_{x\in\Lambda}$ and discretizing the derivative by replacing

$$\partial_\mu\psi(x) \longrightarrow \frac{1}{2a}\left[\psi(x + a\hat{\mu}) - \psi(x - a\hat{\mu}) + \mathcal{O}(a^2)\right]. \tag{5.4.2}$$

For further technical details on lattice derivatives, see Appendix B. This leads to the lattice formulation of the free fermion action:

$$S_F^0[\bar{\psi}, \psi] = a^4\sum_{x\in\Lambda}\bar{\psi}(x)\left(\sum_\mu \gamma_\mu\frac{\psi(x + a\hat{\mu}) - \psi(x - a\hat{\mu})}{2a} + m\psi(x)\right). \tag{5.4.3}$$

Already in the straightforward case of the free fermion action, it is evident that one has the flexibility to select an alternative discretized version of the derivative, thereby approaching the continuum version (5.4.1) differently as $a \to 0$. It is also important to note that by employing these discretized derivatives the action (5.4.3) loses its local character, raising the question of how gauge invariance is maintained on the lattice.

5.4.2 Gauge Invariance on the Lattice and the Naive Fermion Action

As we have seen in Sec. 2.1, the requirement of gauge invariance for the Euclidean continuum Lagrangian necessitates that the fermion transform under local SU(3) transformations $\Omega(x)$ in the fundamental representation [cf. Eq. (2.1.7)]. Consequently, on the lattice we require an independent SU(3) rotation $\Omega(x)$ for each lattice site $n = \frac{x}{a}$

$$\psi(x) \longrightarrow \psi'(x) = \Omega(x)\psi(x)\,, \qquad \bar{\psi}(x) \longrightarrow \bar{\psi}'(x) = \bar{\psi}(x)\Omega^\dagger(x)\,, \tag{5.4.4}$$

and it is observed that the mass term in Eq. (5.4.3) remains gauge invariant. However, the derivative term is non-local as it couples nearest neighbors resulting in the expression

$$\bar{\psi}(x)\psi(x+a\hat{\mu}) \;\longrightarrow\; \bar{\psi}'(x)\psi'(x+a\hat{\mu}) = \bar{\psi}(x)\,\Omega^\dagger(x)\,\Omega(x+a\hat{\mu})\,\psi(x+a\hat{\mu})\,, \tag{5.4.5}$$

which is obviously not gauge invariant. To preserve gauge invariance link variables with a directional index μ need to be introduced, which connect the lattice points $x \in \Lambda$ and $(x+a\hat{\mu}) \in \Lambda$ and need to transform as elements of the gauge group SU(3), i.e.

$$U_\mu(x) \longrightarrow U'_\mu(x) = \Omega(x)U_\mu(x)\Omega^\dagger(x+a\hat{\mu})\,, \tag{5.4.6}$$

in order to restore gauge invariance for the nearest neighbor term (5.4.5). This transformation ensures that the expression

$$\bar{\psi}(x)U_\mu(x)\psi(x+a\hat{\mu}) \longrightarrow \bar{\psi}'(x)U'_\mu(x)\psi'(x+a\hat{\mu}) \tag{5.4.7}$$

remains gauge invariant. The nearest neighbor coupling also necessitates the need of a link variable $U_{-\mu}(x) \equiv U^\dagger_\mu(x-a\hat{\mu})$ connecting the point x and $x-a\hat{\mu}$. Now we are ready to formulate the generalization of the free fermion action (5.4.3), called the naive fermion action

$$S_F[\bar{\psi},\psi,U] = a^4 \sum_{x\in\Lambda} \bar{\psi}(x)\left(\sum_\mu \gamma_\mu \frac{U_\mu(x)\psi(x+a\hat{\mu}) - U_{-\mu}(x)\psi(x-a\hat{\mu})}{2a} + m\psi(x)\right). \tag{5.4.8}$$

This action now, by construction, is gauge invariant satisfying $S_F[\bar{\psi}',\psi',U'] = S_F[\bar{\psi},\psi,U]$.

Next, we want to make the connection between the link variable $U_\mu(x)$ and the continuum gauge fields $A_\mu(x)$, which are elements of the Lie algebra $\mathfrak{su}(3)$ and transform in the adjoint representation under local SU(3) transformations [cf. Eq. (2.1.8)]. The connection to the continuum is made via a transformation called the *gauge transporter* [100],

$$W(x,y) = \mathcal{P}\exp\left(\mathrm{i}\int_x^y A_\mu \cdot \mathrm{d}z_\mu\right), \tag{5.4.9}$$

which connects the points y and x along a path Γ_{xy}, with $\mathcal{P}$ denoting path ordering. In non-Abelian gauge theories such QCD the gauge fields $A^a_\mu(x)\frac{\lambda^a}{2}$ do not commute at different points along the path. Therefore, to properly define the exponential of the line integral, path ordering is required. The gauge transporter (5.4.9) shares the same transformation properties under SU(3) transformations as the link variable U_μ, specifically

$$W(x,y) \longrightarrow \Omega(x)W(x,y)\Omega^\dagger(y)\,. \tag{5.4.10}$$

In order to establish the connection between the link variable and the gauge transporter it is necessary to expanded it in terms of the algebra-valued gauge fields A_μ

$$U_\mu(x) = \exp\left(\mathrm{i}aA^a_\mu(x)\frac{\lambda^a}{2}\right) = 1 + \mathrm{i}aA^a_\mu(x)\frac{\lambda^a}{2} + \mathcal{O}(a^2) = W(x, x+a\hat{\mu}) + \mathcal{O}(a)\,, \tag{5.4.11}$$

where the line integral $\int_x^{x+a\hat{\mu}} A_\mu \cdot \mathrm{d}z_\mu$ has been approximated by the product of the path length, a, and the value of the gauge field at the initial point x. By incorporating these expanded link variables into the naive fermion action (5.4.8), we derive

$$S_F[\bar{\psi},\psi,U] = S_F^{(0)}[\bar{\psi},\psi] + S_F^{(I)}[\bar{\psi},\psi,A], \tag{2.41}$$

where $S_F^{(0)}$ represents the free component of the fermionic action (5.4.3), and the interaction component is expressed as

$$\begin{aligned} S_F^{(I)}[\bar{\psi},\psi,A] &= \mathrm{i}a^4 \sum_{x\in\Lambda}\sum_\mu \bar{\psi}(x)\gamma_\mu \frac{1}{2}\left[A_\mu(x)\psi(x+a\hat{\mu}) + A_\mu(x-a\hat{\mu})\psi(x-a\hat{\mu})\right] \\ &= \mathrm{i}a^4 \sum_{x\in\Lambda}\sum_\mu \bar{\psi}(x)\gamma_\mu A_\mu(x)\psi(x) + \mathcal{O}(a)\,, \end{aligned} \tag{5.4.12}$$

where we have used $\psi(x \pm a\hat{\mu}) = \psi(x) + \mathcal{O}(a)$ and $A_\mu(x \pm a\hat{\mu}) = A_\mu(x) + \mathcal{O}(a)$. Consequently, in the limit as $a \to 0$, the continuum action

$$S_F^0[\bar{\psi},\psi] = \int \mathrm{d}^4x\, \bar{\psi}(x)\left[\gamma_\mu(\partial_\mu + iA_\mu(x) + m\right]\psi(x) \tag{5.4.13}$$

is recovered.

5.4.3 Wilson Gauge Action

In this section we present the discretization of the gauge action originally proposed by Wilson [55] as the first formulation of LGT in 1974. It consists of four link variables U_μ arranged in a gauge-invariant closed loop, called *plaquette* [cf. right part of Fig. 6.1]

$$\begin{aligned} U_{\mu\nu}(x) &= U_\mu(x)U_\nu(x+a\hat{\mu})U_{-\mu}(x+a\hat{\mu}+a\hat{\nu})U_{-\nu}(x+a\hat{\nu}) \\ &= U_\mu(x)U_\nu(x+a\hat{\mu})U_\mu(x+a\hat{\nu})^\dagger U_\nu(x)^\dagger. \end{aligned} \tag{5.4.14}$$

The Wilson gauge action is expressed as a sum over all plaquettes [100]

$$S_G^W[U] = \frac{2}{g^2} \sum_{x\in\Lambda} \sum_{\mu<\nu} \mathrm{Re\,Tr}\left[\mathbb{1} - U_{\mu\nu}(x)\right] = \frac{\beta}{3} \sum_{x\in\Lambda} \sum_{\mu<\nu} \mathrm{Re\,Tr}\left[\mathbb{1} - U_{\mu\nu}(x)\right] , \tag{5.4.15}$$

where the inverse coupling β has been introduced. In this expression, each plaquette is considered only once with a single orientation, and the factor $\frac{2}{g^2}$ is incorporated to reproduce the continuum counterpart as $a \to 0$. Moreover, the real part of the plaquette is taken to account for both orientations, given that $\mathrm{Re}[U_{\mu\nu}] = \frac{1}{2}(U_{\mu\nu} + U_{\mu\nu}^\dagger)$ and $U_{\mu\nu}^\dagger = U_{\nu\mu}$. Using a Taylor expansion of U_μ together with the Baker–Campbell–Hausdorff formula, one finds that [100]

$$S_G^W[U] = \frac{\beta}{3} \sum_{x\in\Lambda} \sum_{\mu<\nu} \mathrm{Re\,Tr}\left[1 - U_{\mu\nu}(x)\right] = \frac{a^4}{2g^2} \sum_{x\in\Lambda} \mathrm{Tr}\left[F_{\mu\nu}^2(x)\right] + \mathcal{O}(a^2) , \tag{5.4.16}$$

which has dimension 4. Replacing $a^4 \sum_{x\in\Lambda}$ by $\int \mathrm{d}^4x$ and taking the limit $a \to 0$

$$\lim_{a\to 0} S_G^W[U] = \frac{1}{2g^2} \int \mathrm{d}^4x\, F_{\mu\nu}^a(x) F_{\mu\nu}^a(x) = S_G[A] , \tag{5.4.17}$$

the continuum version of the gluon action is reproduced [cf. Eq. (2.1.3)].

In most lattice simulations, the primary source of systematic uncertainty arises from discretization effects, specifically due to the finite lattice spacing a at which simulations are performed. As we have already seen in the straightforward case of the free fermion action in Sec. 5.4.1, there exists a certain freedom in how the continuum limit $a \to 0$ is approached. For instance, discretization errors can be reduced by employing improved derivatives. As simulations with increasingly finer lattice spacings become feasible, it is necessary to increase the number of lattice points to maintain a constant physical volume of the box. Consequently, it is advantageous to accelerate the approach to the continuum limit. This can be systematically achieved through the *Symanzik improvement program* [132, 133]. To develop an improved version of the Wilson gauge action (5.4.15), it is essential to first identify correction terms of higher dimension (greater than four) that share the same symmetries, such as gauge invariance and parity, as the original action [134, 135]. These terms should then be organized according to their dimension [100, 108]. It turns out that, additionally to the plaquette (5.4.14), there are three independent elementary loops $\mathcal{S}_k$ of dimension six that comply with the imposed symmetry constraints leading to the *Lüscher-Weisz gauge action* [134, 135],

$$S_G^{LW} = \frac{\beta}{3} \sum_{k=0}^{3} c_k(g^2) \sum_{\mathcal{C}\in\mathcal{S}_k} \mathrm{Re\,Tr}\{1 - U(\mathcal{C})\} . \tag{5.4.18}$$

To determine the coefficients $c_k(g^2)$ in Ref. [135] an on-shell improvement condition was specified. The choice for the $N_\mathrm{f} = 2 + 1$ simulations of the CLS consortium is

$$c_0(0) = 3, \quad c_1(0) = 12, \quad c_2(0) = c_3(0) = 0 . \tag{5.4.19}$$

Consequently, only (1×1) plaquettes (already present in the Wilson gauge action (5.4.15)) as well

as (2×1) rectangles

$$\begin{aligned} R_{\mu\nu}(x) &= U_\mu(x)U_\mu(x+a\hat{\mu})U_\nu(x+2a\hat{\mu})U_{-\mu}(x+2a\hat{\mu}+a\hat{\nu})U_{-\mu}(x+a\hat{\mu}+a\hat{\nu})U_{-\nu}(x+a\hat{\nu}) \\ &= U_\mu(x)U_\mu(x+a\hat{\mu})U_\nu(x+2a\hat{\mu})U_\mu^\dagger(x+a\hat{\mu}+a\hat{\nu})U_\mu^\dagger(x+a\hat{\nu})U_\nu^\dagger(x)\,, \end{aligned} \tag{5.4.20}$$

contribute to (5.4.18) [136].

5.4.4 The Fermion Doubling Problem

In Sec. 5.4.2, the naive fermion action was motivated, demonstrating its ability to reproduce the correct continuum limit. As a next step, we will analyze the Dirac operator derived from this action, encountering the so-called *Fermion doubling problem*. To this end, we express the action (5.4.8) in a quadratic form

$$S_F[\bar{\psi},\psi,U] = a^4 \sum_{x,y\in\Lambda} \bar{\psi}(x)D(x,y)\psi(y)\,, \tag{5.4.21}$$

where the summation over quark flavors, as well as spin and color indices, is implied and the naive Dirac operator [100] is introduced as

$$D(x,y) = \frac{1}{2a}\sum_\mu \gamma_\mu \left[U_\mu(x)\,\delta_{x+a\hat{\mu},y} - U_{-\mu}(x)\,\delta_{x-a\hat{\mu},y}\right] + m\,\delta_{x,y}\,. \tag{5.4.22}$$

In the following, we focus on the free theory, wherein all link variables U_μ are equivalent to the identity matrix. The free propagator of a quark with mass m is given by the inverse of the Dirac operator (5.4.22) in momentum space. Let us denote the matrix elements of the operator $D(x,y)$ by $\langle x|D|y\rangle$. The Fourier transform of (5.4.22) is then expressed as

$$\begin{aligned} D(p,q) = \frac{1}{N_\tau N_s^3}\langle p|D|q\rangle &= \frac{1}{N_\tau N_s^3}\sum_{x,y\,\in\Lambda}\langle p|x\rangle\langle x|D|y\rangle\langle y|q\rangle \\ &= \frac{1}{N_\tau N_s^3}\sum_{x,y\,\in\Lambda} \mathrm{e}^{-\mathrm{i}p\cdot x}D(x,y)\mathrm{e}^{\mathrm{i}q\cdot y} \\ &= \frac{1}{N_\tau N_s^3}\sum_{x\,\in\Lambda} \mathrm{e}^{-\mathrm{i}(p-q)\cdot x}\left(\sum_\mu \gamma_\mu \frac{\mathrm{e}^{\mathrm{i}aq\cdot\hat{\mu}}-\mathrm{e}^{-\mathrm{i}aq\cdot\hat{\mu}}}{2a} + m\mathbb{1}\right) \\ &= \delta_{p,q}\,D(p)\,, \end{aligned} \tag{5.4.23}$$

and we identify the Fourier transform of the naive free Dirac operator, as well as the corresponding propagator as [100]

$$D(p) = m + \frac{\mathrm{i}}{a}\sum_\mu \gamma_\mu \sin(ap_\mu)\,, \tag{5.4.24}$$

$$D^{-1}(p) = \frac{m - \frac{\mathrm{i}}{a}\sum_\mu \gamma_\mu \sin(ap_\mu)}{m^2 + \frac{1}{a^2}\sum_\mu \sin^2(ap_\mu)} \quad \xrightarrow[a\to 0]{m=0} \quad \frac{-\mathrm{i}\sum_\mu \gamma_\mu p_\mu}{p^2}\,. \tag{5.4.25}$$

Thus, in the massless $a \to 0$ limit, (5.4.25) reproduces the continuum propagator. However, while the continuum propagator in the massless case has a single pole at $p = (0,0,0,0)$, the lattice

propagator exhibits 15 additional poles at the corners of the Brillouin zone,

$$p = \left(\tfrac{\pi}{a},0,0,0\right),\ \left(0,\tfrac{\pi}{a},0,0\right),\ \cdots,\left(\tfrac{\pi}{a},\tfrac{\pi}{a},\tfrac{\pi}{a},\tfrac{\pi}{a}\right), \tag{5.4.26}$$

the so-called *doublers*. Consequently, the action (5.4.8) describes the propagation of 15 additional fermion species, and these unphysical poles need to be removed. To address this issue, Wilson [137] proposed the inclusion of an additional term—now referred to as the *Wilson term*—to the naive action, thereby modifying the Dirac operator as follows [100]

$$D(p) = m + \frac{\mathrm{i}}{a}\sum_{\mu}\gamma_\mu \sin(ap_\mu) + \frac{1}{a}\sum_{\mu}\left[1-\cos(ap_\mu)\right]. \tag{5.4.27}$$

The Wilson term vanishes for the physical pole at $p_\mu = 0$. However, for the unwanted doublers, it functions as an additional mass term, resulting in an increase in their total mass. Consequently, in the continuum limit as $a \to 0$, these doublers ultimately decouple from the theory. To identify the Wilson term in position space one needs to perform an inverse Fourier transformation for the last term in (5.4.27), leading to [100]

$$\begin{aligned} D^W(x,y) &= \frac{1}{N_s^3 N_\tau\, a}\sum_{p\in\tilde{\Lambda}_{\mathcal{B}}}\sum_{\mu} \mathrm{e}^{\mathrm{i}p\cdot(x-y)}\left[1-\cos(ap_\mu)\right], \\ &= \frac{4}{a}\,\delta_{x,y} - \frac{1}{2a}\sum_{\mu}\left(U_\mu(x)\,\delta_{x+a\hat{\mu},y} + U_{-\mu}(x)\,\delta_{x-a\hat{\mu},y}\right) \qquad (5.4.28) \\ &= -\frac{a}{2}\sum_{\mu}\frac{1}{a^2}\left(U_\mu(x)\,\delta_{x+a\hat{\mu},y} - 2\,\delta_{x,y} + U_{-\mu}(x)\,\delta_{x-a\hat{\mu},y}\right), \qquad (5.4.29) \end{aligned}$$

where the link variables are needed to make $D^W(x,y)$ gauge invariant. Note that Eq. (5.4.29) corresponds to the naive gauge-invariant discretized Laplacian operator. The associated Wilson term in the fermion action is then obtained as

$$\begin{aligned} S^W[\bar{\psi},\psi,U] &= a^4\sum_{x,y\in\Lambda}\bar{\psi}(x)D^W(x,y)\psi(y) \\ &= -a^5\sum_{x\in\Lambda}\bar{\psi}(x)\sum_{\mu}\left(\frac{U_\mu(x)\psi(x+a\hat{\mu}) - 2\psi(x) + U_{-\mu}(x-a\hat{\mu})\psi(x-a\hat{\mu})}{2a^2}\right). \end{aligned} \tag{5.4.30}$$

This term must be incorporated into the naive fermion action (5.4.8) to construct the complete Wilson fermion action for fermions with mass m,

$$\begin{aligned} &S_F^W[\bar{\psi},\psi,U] = S_F[\bar{\psi},\psi,U] + S^W[\bar{\psi},\psi,U] \\ &= a^4\sum_{x\in\Lambda}\bar{\psi}(x)\left[\left(m+\frac{4}{a}\right)\psi(x) - \sum_{\mu}\frac{(\mathbb{1}-\gamma_\mu)U_\mu(x)\psi(x+a\hat{\mu}) + (\mathbb{1}+\gamma_\mu)U_{-\mu}(x)\psi(x-a\hat{\mu})}{2a}\right]. \end{aligned} \tag{5.4.31}$$

It is crucial to emphasize that the initial term in Eq. (5.4.28) explicitly breaks chiral symmetry at finite lattice spacing, even in the chiral limit where the quark mass approaches zero, which can be

expressed as

$$\{D_W, \gamma_5\} \neq 0\,, \tag{5.4.32}$$

as the identity $\mathbb{1}$ in Eq. (5.4.31) does not anticommute with γ_5. Consequently, there is no symmetry protecting the quark mass from additive renormalization (cf. Appendix C). In practical LQCD simulations with Wilson fermions, the *hopping parameter* is employed as the input parameter, rather than the bare quark mass. This parameter is defined as

$$\kappa_q = \frac{1}{2am + 8}\,. \tag{5.4.33}$$

A broader conceptualization of this issue is described by the *Nielsen–Ninomiya "no-go" theorem* [138–140], which establishes that it is impossible to eliminate the fermion doubling problem while simultaneously maintaining exact chiral symmetry in the continuum sense. For the sake of completeness, we briefly mention some alternative formulations for fermions on the lattice. Notably, there are *staggered* or *Kogut-Susskind* [141] fermions, which allow for the reduction of the 16-fold fermion species degeneracy to four, while retaining a (remnant) chiral symmetry. Additionally, *twisted mass* [142–144] fermions—a variant of Wilson fermions—employ an isospin breaking mass term to achieve an $\mathcal{O}(a)$-improved lattice formulation. An elegant method of defining chiral symmetry on the lattice was proposed by Ginsparg and Wilson in 1982. Instead of requiring that the Dirac operator D anticommutes with γ_5 they proposed [145]

$$\{D, \gamma_5\} = aD\gamma_5 D\,. \tag{5.4.34}$$

In 1997 (1998), the Ginsparg-Wilson equation (5.4.34) was implemented on the lattice using *overlap* [146] (*fixed point* [147]) fermions. Another type of fermions that satisfy (5.4.34) are *domain wall* fermions, as introduced by Kaplan [148]. These fermions are formulated on a $(4+1)$ dimensional lattice, where the fifth dimension serves to exponentially suppress chirality-breaking effects [100]. However, a significant limitation of these fermions is their computational expense [149].

5.4.5 Improvement of the Wilson Fermion Action

So far lattice artifacts for the fermion action start at $\mathcal{O}(a)$ [cf. Eq. (5.4.12)], while the discretization of the gauge action introduces only $\mathcal{O}(a^2)$ lattice artifacts [cf. Eq. (5.4.16)]. As already mentioned in Sec. 5.4.3, the Symanzik improvement program can be utilized to remove $\mathcal{O}(a)$ discretization effects by incorporating higher-dimensional operators to an effective action [100]

$$S_{\text{eff}} = \int \mathrm{d}^4x \left(\mathcal{L}^{(0)}(x) + a\mathcal{L}^{(1)}(x) + a^2\mathcal{L}^{(2)}(x) + \cdots \right)\,. \tag{5.4.35}$$

In this context, $\mathcal{L}^{(0)}$ represents the continuum Lagrangian (2.1.3), while $\mathcal{L}^{(k)}$, $k \geq 1$ denotes correction terms of dimension $4+k$, which must exhibit the same symmetries as the original Lagrangian $\mathcal{L}^{(0)}$. For the case where $k = 1$, a set of five operators of dimension 5 can be formulated [150]. Utilizing the continuum field equations, it is demonstrated that only three of these operators are

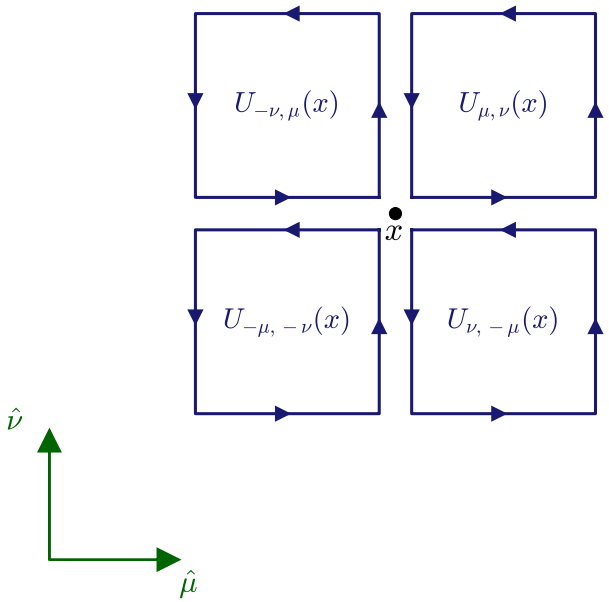

Figure 5.2: Visualization of the clover term $Q_{\mu\nu}(x)$ on the lattice, given by the sum of four plaquettes in the $(\hat{\mu},\hat{\nu})$-plane, [cf. Eq. (5.4.41)].

linearly independent. They are expressed as [151]

$$\mathcal{L}^{(1)} = \bar{\psi}(x)\,\sigma_{\mu\nu}F_{\mu\nu}\,\psi(x)\,, \tag{5.4.36}$$

$$\mathcal{L}^{(2)} = m\,\mathrm{Tr}\big[F_{\mu\nu}F_{\mu\nu}\big]\,, \tag{5.4.37}$$

$$\mathcal{L}^{(3)} = m^2\,\bar{\psi}(x)\,\psi(x)\,, \tag{5.4.38}$$

where $\sigma_{\mu\nu} = -\frac{1}{2}[\gamma_\mu,\gamma_\nu]$. The terms $\mathcal{L}^{(2)}$ and $\mathcal{L}^{(3)}$ are already present within the Wilson gauge action and the original fermion action. These can be addressed through the redefinition of the bare gauge coupling g and the bare quark mass m [151]. Consequently, $\mathcal{O}(a)$-improvement can be achieved by adding the *Sheikholeslami-Wohlert* or *clover* term $\mathcal{L}^{(1)}$ into the Wilson fermion action (5.4.31):

$$S_F^{SW,\mathrm{imp}}[\bar{\psi},\psi,U] = S_F^{W}[\bar{\psi},\psi,U] + c_{\mathrm{sw}}(g^2)a^5\sum_{x\in\Lambda}\sum_{\mu<\nu}\bar{\psi}(x)\,\frac{1}{2}\sigma_{\mu\nu}F_{\mu\nu}(x)\,\psi(x)\,, \tag{5.4.39}$$

where the coefficient $c_{\mathrm{sw}}(g^2)$ needs to be determined non-perturbatively [151, 152] to achieve $\mathcal{O}(a)$-improvement. The field-strength tensor $F_{\mu\nu}$ is discretized according to [151]

$$\hat{F}_{\mu\nu}(x) = -\frac{1}{8a^2}\left(Q_{\mu\nu}(x) - Q_{\nu\mu}(x)\right)\,, \tag{5.4.40}$$

$$Q_{\mu\nu}(x) = U_{\mu,\nu}(x) + U_{\nu,-\mu}(x) + U_{-\mu,-\nu}(x) + U_{-\nu,\mu}(x)\,. \tag{5.4.41}$$

For a graphical representation of the clover term, we refer to Fig. 5.2.

5.5 Improvement of the Vector Current

In the previous section, we have discussed the $\mathcal{O}(a)$-improvement of the Wilson Fermion action. The next logical progression involves the improvement (and also renormalization) of composite operators, such as the vector current

$$V_\mu^{(f,f')}(x) = \bar{\psi}_f(x)\gamma_\mu\psi_{f'}(x)\,, \tag{5.5.1}$$

which is of central interest in this thesis. This step is essential to ensure that the matrix elements of these composite operators converge to the correct continuum values. The vector current (5.5.1) has mass dimension three. As discussed in the context of the improvement of the fermion action, we need to add a linear combination of dimension-4 terms that share the same symmetry properties as the underlying composite operator (5.5.1). For the vector current, it turns out that there is only one dimension-4 operator, resulting in the improved current [153, 154]

$$(V_\mu^{\text{imp}})^{(f,f')}(x) = V_\mu^{(f,f')}(x) - ac_V(g^2)\partial_\nu\bar{\psi}_f(x)\frac{1}{2}[\gamma_\mu,\gamma_\nu]\psi_{f'}(x)\,, \tag{5.5.2}$$

where the improvement coefficient c_V is determined non-perturbatively. For more details, we refer to Appendix B.

5.6 The Path Integral on the Lattice

After completing the discretization of the LQCD action in Sec. 5.4, we now move on to briefly outline the practical computation of LQCD observables. As previously mentioned in Eq. (5.1.6) and repeate here for clarity, the expectation value of an observable O in numerical simulations is calculated using the path integral.

$$\langle O\rangle = \frac{\int[\mathrm{d}\bar{\psi}][\mathrm{d}\psi]\,\mathcal{D}[U]\;\mathrm{e}^{-S_{\text{LQCD}}[\bar{\psi},\psi,U]}\;O[\bar{\psi},\psi,U]}{\int[\mathrm{d}\bar{\psi}][\mathrm{d}\psi]\,\mathcal{D}[U]\;\mathrm{e}^{-S_{\text{LQCD}}[\bar{\psi},\psi,U]}}\,,$$

where the denominator represents the LQCD partition function Z_{LQCD}, and the path integral over the link variables $U_\mu(x)$ is defined as the product measure

$$\int\mathcal{D}[U] = \prod_{x\in\Lambda}\prod_{\mu=0}^{3}\int\mathrm{d}U_\mu(x)\,. \tag{5.6.1}$$

The individual measures $\mathrm{d}U_\mu(x)$ are given by the *Haar measure* [100]. Additionally, the product measure for the Grassmann number valued fermionic fields is given by $\int[\mathrm{d}\bar{\psi}][\mathrm{d}\psi]$. We reiterate that the discretized LQCD action S_{LQCD} is expressed as [cf. Eqs. (5.4.18) and (5.4.39)]

$$S_{\text{LQCD}} = S_G^{LW} + S_F^{SW,\text{imp}}\,. \tag{5.6.2}$$

Given that the Fermion action is quadratic in the fields, as indicated in Eq. (5.4.21), it is feasible to compute the fermionic path integral analytically. Specifically,

$$\begin{aligned}\langle O\rangle = \langle\langle O\rangle_F\rangle_G &= \frac{1}{Z_{\mathrm{LQCD}}}\int \mathcal{D}[U]\,\mathrm{e}^{-S_G^{LW}[U]}O[U]\prod_{f=1}^{N_f}\int[\mathrm{d}\bar{\psi}_f][\mathrm{d}\psi_f]\mathrm{e}^{-\sum_{x,y}\bar{\psi}_f(x)D_f^{SW,\mathrm{imp}}[U](x,y)\,\psi_f(y)} \\ &= \frac{1}{Z_{\mathrm{LQCD}}}\int \mathcal{D}[U]\,\mathrm{e}^{-S_G^{LW}[U]}O[U]\prod_{f=1}^{N_f}\det\left(D^{SW,\mathrm{imp}}[U]\right)\,, \end{aligned} \tag{5.6.3}$$

where $\langle\cdots\rangle_F$ and $\langle\cdots\rangle_G$ denote the fermionic and the gauge field part of the expectation value, respectively [100] and we have included the product over quark flavors for clarity. Historically[4], LQCD simulations have been performed using the so-called *quenched approximation* ($N_\mathrm{f} = 0$), wherein the determinants were manually set to unity. Physically, this approach disregards vacuum quark loops, wherein quark-antiquark pairs are generated and annihilated within a fermionic background. These quarks are termed *sea quarks*. Conversely, the quark fields involved in the Wick contractions, as defined in the quark propagator (5.7.1), are referred to as *valence quarks*.

In order to generate appropriately distributed gauge configurations, the fermion determinant is utilized as a probability weight factor,

$$\mathrm{d}p[U] = \frac{\mathcal{D}[U]\prod_{f=1}^{N_f}\det(D_f^{SW,\mathrm{imp}}[U])\,\mathrm{e}^{-S_G^{LW}[U]}}{Z_{\mathrm{LQCD}}}\,, \tag{5.6.4}$$

which requires it to be both real and positive. The first condition is fulfilled due to the γ_5-hermiticity property (5.7.6) of the Wilson Dirac operator. It can be readily verified that

$$\det[D^{SW,\mathrm{imp}}]^* = \det[(D^{SW,\mathrm{imp}})^\dagger] = \det(\gamma_5 D^{SW,\mathrm{imp}}\gamma_5) = \det(D^{SW,\mathrm{imp}})\,.$$

Nevertheless, the determinant may still be negative [100]. This issue can be addressed by utilizing two (or, more generally, an even number of) mass-degenerate *dynamical* quark flavors, allowing the determinant to factorize into an even number of identical fermion determinants. This setup is referred to as $N_\mathrm{f} = 2$ and is employed in Chap. 9. The projects discussed in Chaps. 6 and 8 utilize $N_\mathrm{f} = 2+1$ dynamical quarks, which additionally includes the strange quark in the sea. However, the simulations are again performed in the isospin-symmetric limit of equal light quark masses and effects from heavier quarks are neglected.

5.6.1 Pseudofermions

The computation of the configuration-dependent fermion determinant is not computationally feasible (for further details, please refer to the beginning of Sec. 5.7). As a consequence, the concept of *pseudofermions* was developed in Ref. [156]. For this purpose, complex bosonic scalar fields $\phi = \mathrm{Re}\,\phi + \mathrm{i}\,\mathrm{Im}\,\phi$ with the same number of degrees of freedom as the fermionic variables are introduced [100]. For two mass-degenerate quark flavors u and d the fermion determinant can

[4] In Ref. [155], lattice constraints on the thermal photon rate were obtained using the quenched approximation less than a decade ago.

thus be expressed as [156]

$$\det[DD^\dagger] = \int [\mathrm{d}\,\mathrm{Re}\,\phi][\mathrm{d}\,\mathrm{Im}\,\phi]\,\mathrm{e}^{-\phi^\dagger[DD^\dagger]^{-1}\phi}\,, \tag{5.6.5}$$

up to an overall irrelevant normalization factor [100]. Employing Eq. (5.6.5), the integration over the fermionic Grassmann variables $\bar{\psi}_{u/d}$ and $\psi_{u/d}$ can be replaced by

$$\int [\mathrm{d}\bar{\psi}][\mathrm{d}\psi]\,\mathrm{e}^{-\bar{\psi}_u D\psi_u - \bar{\psi}_d D\psi_d} = \int [\mathrm{d}\,\mathrm{Re}\,\phi][\mathrm{d}\,\mathrm{Im}\,\phi]\,\mathrm{e}^{-\phi^\dagger[DD^\dagger]^{-1}\phi}\,. \tag{5.6.6}$$

Due to the appearance of the inverse $(DD^\dagger)^{-1}$ this interaction is highly nonlocal [100], in contrast to the gauge action S_G^{LW}, which is local. If the observable in question also depends on the fermion fields, it is necessary to first apply Wick's theorem in order to express their expectation value in terms of propagators. This topic will be discussed in Sec. 5.7. To conclude this section, we remark that it is common to define a so-called *effective fermion action* S_F^{eff} by rewriting [157, 158]

$$\det[DD^\dagger] = \exp\left(\mathrm{Tr}[\ln(DD^\dagger)]\right) \equiv \exp\left(-S_F^{\mathrm{eff}}\right)\,, \tag{5.6.7}$$

such that dynamical fermions are incorporated in the combined Boltzmann factor [100]

$$\mathrm{e}^{-S[U]} \quad \text{with} \quad S[U] = S_G^{LW}[U] + S_F^{\mathrm{eff}}[U]\,. \tag{5.6.8}$$

5.6.2 Importance Sampling

To calculate expectation values, we have to evaluate the path integral defined in Eq. (5.6.3). On the lattice this is a high-dimensional yet finite integral that can be computed employing stochastic *Monte-Carlo* techniques. Due to the Boltzmann factor (5.6.8) a substantial number of *gauge configurations*

$$C_n \equiv \{[U_\mu(x)]_n \,|\, x \in \Lambda,\, 0 \leq \mu \leq 3\}\,, \quad n \in \{1, \cdots, N_{\mathrm{con}}\}\,, \tag{5.6.9}$$

will contribute only marginally to the path integral. Rather than generating N_{con} random gauge configurations C_n of a certain *ensemble*, the process can be significantly optimized by generating configurations in accordance with their probability density distribution (5.6.4). This method is referred to as *importance sampling* and ensures that $\mathcal{O}(1000)$ gauge configurations—sampled with the appropriate Boltzmann weight factor—are sufficient to reliably sample the path integral (5.6.3) by the ensemble average

$$\langle O \rangle = \frac{1}{N_{\mathrm{con}}} \sum_{n=1}^{N_{\mathrm{con}}} O[C_n]\,. \tag{5.6.10}$$

In accordance with the central limit theorem, the statistical error scales with $\frac{1}{\sqrt{N_{\mathrm{con}}}}$ [100].

5.6.3 Markov Chains

To generate a series of configurations $\{C_n\}$ in accordance with the probability density distribution (5.6.4), one begins with an initial configuration C_0 and subsequently constructs a so-called

Markov chain

$$C_0 \longrightarrow C_1 \longrightarrow C_2 \longrightarrow \cdots , \tag{5.6.11}$$

that eventually follows a target equilibrium probability distribution [100]. The initial configuration C_0 may be either a randomly generated gauge field or one derived from a prior simulation with similar bare parameters.

To attain the desired equilibrium probability distribution, *thermalization* runs have to be performed. By closely examining the Monte-Carlo time evolution of specific observables, such as the average plaquette, one must ensure that thermalization effects are gone and exclude all gauge configurations prior to this stage. The length of these runs is influenced by the bare parameters, the lattice volume, and the particular observable being studied [100, 106].

An important property of a Markov chain is that the transition probability $T(C'|C)$ to update to configuration C' when starting in configuration C is solely dependent on the immediate preceding state and is unaffected by the chain's Monte-Carlo history. Additionally, in order to sample the entire configuration space the transition probability needs to obey

$$0 \leq T(C'|C) \leq 1, \quad \sum_{C'} T(C'|C) = 1 , \tag{5.6.12}$$

i.e. positivity and a normalization. Furthermore it is required that

$$\forall\, C, C' \;\exists\, m : T^m(C'|C) > 0 . \tag{5.6.13}$$

Thus, in principle, any configuration C' in configuration space can be attained from any other configuration C after a finite number of updates m with non-vanishing probability [100]. This requirement is called *ergodicity*. However, in practice, at fine lattice spacing and/or high temperature the probability of connecting non-trivial topological sectors is strongly suppressed, and standard Monte Carlo methods may inadequately sample those sectors [159]. The Markov chain reaches equilibrium when the probability distribution of the gauge configurations, $P(C)$, satisfies the *balance equation* [100]

$$\sum_C T(C'|C)P(C) = \sum_C T(C|C')P(C') \overset{(5.6.13)}{=} P(C') , \tag{5.6.14}$$

indicating that the Markov process cannot exhibit sinks or sources of probability [100].

In concluding this section, we emphasize that the generated configurations $\{C_n\}$ are not statistically independent. The updating process is heavily reliant on the previously generated configuration, resulting in a Markov chain of configurations that exhibits autocorrelation effects. These effects must be appropriately taken into account to ensure an accurate error estimate (cf. Appendix D).

5.6.4 Metropolis Algorithm

The Metropolis algorithm [160] is a simple method for transitioning a Markov chain from one configuration $C = C_{n-1}$ to another C'. Assuming $P(C) \propto \exp(-S[C])$ in Eq. (5.6.14), the algorithm

involves three steps [100]:

1. Select a candidate configuration C' with an initial symmetric selection probability $T_0(C'|C) = T_0(C|C')$.
2. Adopt the suggested configuration C' as the new configuration C_n with an acceptance probability given by

$$T_A(C'|C) = \min(1, e^{-\Delta S}) \quad \text{with} \quad \Delta S = S[C'] - S[C]\,. \tag{5.6.15}$$

   In case of rejection, the original configuration C remains in the Markov chain and is included in the measurements.
3. Restart the procedure from the beginning.

The total transition probability is then given by

$$T(C'|C) = T_A(C'|C)T_0(C'|C)\,, \tag{5.6.16}$$

and satisfies the *detailed balance condition* [100]

$$T(C'|C)\exp(-S[C]) = T(C|C')\exp(-S[C'])\,. \tag{5.6.17}$$

The Metropolis algorithm is designed to update only a small number of variables, or sometimes just a single link variable at a time. This approach is effective for local actions, such as the pure Wilson gauge action (5.4.15). However, when fermions are included, the fermion determinant introduces nonlocal couplings. As a result, computing the change of the action requires the consideration of all link variables [100], which makes the update process costly. In such scenarios, global update algorithms, that modify numerous variables in one step are used instead.

5.6.5 Hybrid Monte Carlo Algorithm

The Hybrid Monte Carlo (HMC) algorithm [161–163] is the most commonly employed method for producing gauge field configurations in LQCD simulations that include dynamical fermions. For a comprehensive explanation of this algorithm, we refer readers to Refs. [100, 164] and provide only a brief overview of the main concept in this section. The key idea of the HMC algorithm is to introduce a "fictitious" Markov time (or computer time) $\mathcal{T}$ that parametrizes the evolution of the fields along a Markov chain. In this section we assume two flavors of mass-degenerate fermions. Expressing the gauge links as $U_\mu(x) = e^{iQ^a_\mu(x)\frac{\lambda^a}{2}}$ and identifying the parameters $Q^a_\mu(x)$ as the generalized coordinates, one can define an Hamiltonian of the molecular dynamics [100]

$$H[Q,P] = \frac{1}{2}\sum_{x,\mu,a}[P^a_\mu(x)]^2 + S^{LW}_G[U(Q)] + \phi^\dagger[D[U(Q)]D^\dagger[U(Q)]]^{-1}\phi\,. \tag{5.6.18}$$

Here $P_\mu(x) = P^a_\mu(x)\frac{\lambda^a}{2}$ denotes the momentum variables conjugate to $Q^a_\mu(x)$, and ϕ represents the pseudofermion fields introduced in Sec. 5.6.1. The "fictitious" Hamilton equations of motion

$$\begin{aligned} \frac{\mathrm{d}}{\mathrm{d}\mathcal{T}} P &= -\frac{\partial H}{\partial Q}\,, \\ \frac{\mathrm{d}}{\mathrm{d}\mathcal{T}} Q &= \frac{\partial H}{\partial P}\,, \end{aligned} \tag{5.6.19}$$

describe how the system evolves in Markov time [100]. The HMC algorithm consists of the following steps:

1. **Initialization:** Start with a gauge configuration $C_n \equiv C(n\Delta\mathcal{T})$. Each link variable $U_\mu(x)$ is associated with coordinates $Q(n\Delta\mathcal{T}) \equiv Q_\mu(x|n\Delta\mathcal{T})$. The conjugate momenta $P(n\Delta\mathcal{T}) \equiv P_\mu(x|n\Delta\mathcal{T})$ are drawn for every link variable from a Gaussian distribution proportional to $\exp(-\frac{1}{2}\sum_{x,\mu,a}[P^a_\mu(x)]^2)$ [100].
2. **Pseudofermions:** Create a complex vector η with pseudofermionic degrees of freedom, according to a probability distribution $\propto \mathrm{e}^{-\eta^\dagger\eta}$. The pseudofermion fields ϕ are obtained by applying the Dirac operator $D[U]\eta = \phi$, and can be kept constant throughout the molecular dynamics step 3 [165].
3. **Molecular dynamics trajectory:** Evolve the initial configuration (Q, P) to a candidate configuration $(Q', P') = (Q((n+1)\Delta\mathcal{T}), P((n+1)\Delta\mathcal{T}))$ by numerically integrating Eqs. (5.6.19) over a distance $\Delta\mathcal{T}$, utilizing the initial values $Q(n\Delta\mathcal{T})$ and $P(n\Delta\mathcal{T})$. A reversible and area-preserving integrator is employed in this step to ensure compliance with the detailed balance condition (5.6.17). This process introduces numerical errors such that $H[Q,P] \neq H[Q',P']$, which can be rectified by an accept/reject step.
4. **Metropolis accept/reject step:** Compute the variation $\Delta H = H[Q',P'] - H[Q,P]$ and accept $C_{n+1} \equiv C((n+1)\Delta\mathcal{T})$ as a new configuration with an acceptance probability of $\min(1, \mathrm{e}^{-\Delta H})$.

Otherwise, the configuration C_{n+1} is rejected and the whole procedure is restarted with the initial configuration C_n.

So far, we have focused on the case of two mass-degenerate quark flavors. For a single flavor (or other odd numbers of flavors), the HMC algorithm is generalized to the Rational Hybrid Monte Carlo (RHMC) algorithm [166, 167], which represents fractional powers of the fermion determinant using a rational approximation. Since the approximation is not exact, expectation values can be corrected by reweighting to account for the difference between the true and approximate actions [168, 169].

5.7 Calculation of Propagators

Although the Dirac matrix D may itself be sparse, containing numerous zero entries, its inverse, the propagator D^{-1}, is generally too large to be stored in computer memory. For a two-point correlation function, it typically comprises $(4 \times 3 \times N_s^3 \times N_\tau)^2$ complex entries. Consider, for instance, the `E250Nt24` box (cf. Table 6.2). Storing $(12 \times 96^3 \times 24)^2 = \mathcal{O}(10^{16})$ entries would necessitate approximately 1 Exabyte of memory. Each element $D^{-1}(y,x)^{ba}_{\beta\alpha}$ connects a source point (x,α,a) to a sink point (y,β,b). As is customary, Greek letters denote Dirac indices, while Latin

letters represent color indices.

In Sec. 5.2, the formal spectral decomposition of Euclidean two-point functions has been established. We now proceed to examine their implementation within LQCD. In numerical simulations, the evaluation of expectation values in Eq. (5.2.2) necessitates the computation of (light) quark propagators D_f^{-1}. These propagators are defined as the Wick contractions of a quark and an antiquark of the same flavor f, i.e.,

$$\overbrace{\psi_f(x)^a_\alpha\,\bar{\psi}_f(y)^b_\beta} = D_f^{-1}(x,y)^{ab}_{\alpha\beta}\,, \qquad f \in \{u,d\}\,. \tag{5.7.1}$$

We now discuss this procedure in more detail.

In this thesis, we focus exclusively on Euclidean two-point correlation functions, both at zero momentum and when projected to a specific momentum, i.e.

$$G^{\text{2pt.}}_{O_2O_1^\dagger}(\tau_f,\tau_i,\mathbf{p}_f,\mathbf{p}_i) = \frac{1}{N_s^3}\sum_{\mathbf{x}_f,\mathbf{x}_i} \mathrm{e}^{\mathrm{i}\mathbf{p}_f\cdot\mathbf{x}_f}\mathrm{e}^{-\mathrm{i}\mathbf{p}_i\cdot\mathbf{x}_i}\langle O_2(\tau_f,\mathbf{x}_f)O_1^\dagger(\tau_i,\mathbf{x}_i)\rangle\,. \tag{5.7.2}$$

Using translational invariance, we are free to perform a shift by the source position $x_f \to x_f - x_i$ resulting in the more familiar form

$$G^{\text{2pt.}}_{O_2O_1^\dagger}(\tau,\mathbf{p}) = \frac{1}{N_s^3}\sum_{\mathbf{x}_f,\mathbf{x}_i} \mathrm{e}^{\mathrm{i}\mathbf{p}\cdot(\mathbf{x}_\mathrm{f}-\mathbf{x}_\mathrm{i})}\langle O_2(\tau,\mathbf{x}_f-\mathbf{x}_i)O_1^\dagger(0,\mathbf{0})\rangle\,, \tag{5.7.3}$$

where we have defined $\mathbf{p}_f \equiv \mathbf{p}$, and $\tau \equiv \tau_f - \tau_i$.

Next, we want to evaluate Eq. (5.7.2) for two general operators $O_2(x_f) = \bar{\psi}_{f_1}(x_f)\Gamma_2\psi_{f_2}(x_f)$ and

$$\begin{aligned} O_1^\dagger(x_i) &= \left[\bar{\psi}_{f_1}(x_i)\Gamma_1\psi_{f_2}(x_i)\right]^\dagger = \psi_{f_2}(x_i)^\dagger\mathbb{1}\Gamma_1^\dagger\left(\psi_{f_1}^\dagger(x_i)\gamma_0\right)^\dagger \\ &= \psi_{f_2}(x_i)^\dagger\gamma_0\gamma_0\Gamma_1^\dagger\gamma_0\psi_{f_1}(x_i) = \pm\bar{\psi}_{f_2}(x_i)\Gamma_1\psi_{f_1}(x_i)\,, \end{aligned} \tag{5.7.4}$$

where Γ_i represents a monomial of Euclidean gamma matrices. Note that the daggered operator can pick up a minus sign, depending on the Dirac structure of Γ_1. We obtain

$$\begin{aligned} N_s^3\,G^{\text{2pt.}}_{O_2O_1^\dagger}(\tau,\mathbf{p}) &= \sum_{\mathbf{x}_f,\mathbf{x}_i}\mathrm{e}^{\mathrm{i}\mathbf{p}\cdot(\mathbf{x}_\mathrm{f}-\mathbf{x}_\mathrm{i})}\left\langle\bar{\psi}_{f_1}(x_f)\Gamma_2\psi_{f_2}(x_f)\,\bar{\psi}_{f_2}(x_i)(\gamma_0\Gamma_1^\dagger\gamma_0)\psi_{f_1}(x_i)\right\rangle \\ &= \sum_{\mathbf{x}_f,\mathbf{x}_i}\mathrm{e}^{\mathrm{i}\mathbf{p}\cdot(\mathbf{x}_\mathrm{f}-\mathbf{x}_\mathrm{i})}\left\langle\overbrace{\bar{\psi}_{f_1}(x_f)^a_\alpha\,(\Gamma_2)^{ab}_{\alpha\beta}\,\psi_{f_2}(x_f)^b_\beta\,\bar{\psi}_{f_2}(x_i)^c_\gamma\,(\gamma_0\Gamma_1^\dagger\gamma_0)^{cd}_{\gamma\delta}\,\psi_{f_1}(x_i)^d_\delta}\right\rangle^{\text{conn.}} \\ &= -\sum_{\mathbf{x}_f,\mathbf{x}_i}\mathrm{e}^{\mathrm{i}\mathbf{p}\cdot(\mathbf{x}_\mathrm{f}-\mathbf{x}_\mathrm{i})}\left\langle(\Gamma_2)^{ab}_{\alpha\beta}\,D_{f_2}^{-1}(x_f,x_i)^{bc}_{\beta\gamma}\,(\gamma_0\Gamma_1^\dagger\gamma_0)^{cd}_{\gamma\delta}\,D_{f_1}^{-1}(x_i,x_f)^{da}_{\delta\alpha}\right\rangle^{\text{conn.}} \\ &= -\sum_{\mathbf{x}_f,\mathbf{x}_i}\mathrm{e}^{\mathrm{i}\mathbf{p}\cdot(\mathbf{x}_\mathrm{f}-\mathbf{x}_\mathrm{i})}\,\mathrm{Tr}\left[\Gamma_2 D_{f_2}^{-1}(x_f,x_i)\gamma_0\Gamma_1^\dagger\gamma_0 D_{f_1}^{-1}(x_i,x_f)\right]\,, \end{aligned} \tag{5.7.5}$$

where the negative sign emerges from the reordering of two fermionic fields before performing the Wick contraction for flavor f_1, and "conn." stands for "connected". An important aspect is that only quarks of equal flavor can be contracted. However, after applying Wick's theorem—assuming exact isospin symmetry—we can set $D_u^{-1} = D_d^{-1}$ and, hence, suppress the flavor index in the following when not explicitly needed.

For iso-scalar operators such as $\frac{1}{\sqrt{2}}(\bar{u}\Gamma u + \bar{d}\Gamma d)$, it is the case that $f_1 = f_2$, resulting in an additional disconnected contribution, expressed as $+\delta_{f_1 f_2}\mathrm{Tr}[\Gamma_2 D^{-1}_{f_1}(x_f, x_f)]\mathrm{Tr}[\gamma_0\Gamma_1^\dagger\gamma_0 D^{-1}_{f_2}(x_i, x_i)]$. Throughout this thesis, we neglect disconnected contributions; for further details, we refer to Sec. 7.2). The Wilson Dirac operator has the property [100]

$$D^{-1}(x,y) = \gamma_5 \left(D^{-1}(y,x)\right)^\dagger \gamma_5 \,. \tag{5.7.6}$$

Consequently, the backward propagator does not need to be calculated explicitly and we end up with

$$G^{\mathrm{2pt.}}_{O_2 O_1^\dagger}(\tau, \mathbf{p}) = -\frac{1}{N_s^3}\sum_{\mathbf{x}_f, \mathbf{x}_i} \mathrm{e}^{\mathrm{i}\mathbf{p}\cdot(\mathbf{x}_\mathrm{f}-\mathbf{x}_\mathrm{i})}\,\mathrm{Tr}\left[\Gamma_2 D^{-1}(x_f, x_i)\gamma_0\Gamma_1^\dagger\gamma_0\gamma_5 \left(D^{-1}(x_f, x_i)\right)^\dagger \gamma_5\right] . \tag{5.7.7}$$

5.7.1 Inversion of the Dirac Operator

Given that the propagator describes propagation within a single background gauge field configuration [100], its entries exhibit significant correlation, making it sufficient to compute only portions of the matrix. The idea behind so-called *point sources*

$$S^{(x_0,\alpha_0,a_0)}(x)^a_\alpha = \delta_{x x_0}\,\delta_{\alpha\alpha_0}\,\delta_{a a_0}\,, \tag{5.7.8}$$

is to focus on the propagator from a fixed source point (x_0, α_0, a_0) to any site on the lattice. This object represents a single column of the inverse Dirac operator, i.e. we can write [100]

$$D^{-1}(y, x_0)^{b a_0}_{\beta\alpha_0} = \sum_{x,\alpha,a} D^{-1}(y,x)^{ba}_{\beta\alpha}\, S^{(x_0,\alpha_0,a_0)}(x)^a_\alpha \,. \tag{5.7.9}$$

Equation (5.7.8) clearly indicates that a point source is confined to a single spin-color component at a specific lattice point[5]. Consequently, it is sensitive to local fluctuations in the background gauge field. To extract information from the background gauge field more efficiently, stochastic methods can be employed, which fundamentally rely on the use of randomly generated sources [170].

$$\{\eta^{(n)}(x)^a_\alpha \in \mathcal{D} \,|\, n = 1, \cdots, N_{\mathrm{hits}}\}\,, \tag{5.7.10}$$

drawn from a distribution $\mathcal{D}$ and are referred to as *stochastic sources* [171]. The index n labels the different samples for each gauge configuration. In the large sample limit, $N_{\mathrm{hits}} \to \infty$, the resulting average satisfies [170, 171]

$$\begin{aligned}\lim_{N_{\mathrm{hits}}\to\infty} \frac{1}{N_{\mathrm{hits}}}\sum_{n=1}^{N_{\mathrm{hits}}} \eta^{(n)}(x)^a_\alpha \eta^{(n)}(y)^b_\beta \equiv \left\langle \eta^{(n)}(x)^a_\alpha \eta^{(n)}(y)^b_\beta \right\rangle_n = 0\,, \\ \left\langle \eta^{(n)}(x)^a_\alpha [\eta^{(n)}(y)^b_\beta]^\dagger \right\rangle_n = \delta_{xy}\delta_{\alpha\beta}\,\delta_{ab}\,,\end{aligned} \tag{5.7.11}$$

[5] As a result, the explicit summation over the source position $\mathbf{x}_i$ in Eq. (5.7.3) is absent. For a fixed source position, the Dirac inversions are performed once, and the two-point correlators can be projected onto any allowed lattice momentum $\mathbf{p}$ in the Fourier sum over the sink coordinates $\mathbf{x}_f$. To complete the Fourier transform, one multiplies the correlator by the complex conjugate phase factor $\mathrm{e}^{\mathrm{i}\mathbf{p}\cdot\mathbf{x}_i}$, corresponding to the fixed source position. In contrast to wall sources, which require additional Dirac inversions for each momentum, point sources thus allow access to all lattice momenta without further inversions.

independent of the noise choice. It was suggested in Ref. [172] that the optimal choice is

$$\mathcal{D} = \mathbb{Z}_2 \otimes \mathbb{Z}_2 = \left\{ \frac{1}{\sqrt{2}} (\pm 1 \pm \mathrm{i}) \right\} , \tag{5.7.12}$$

i.e. random $\mathbb{Z}_2$ numbers for the real and imaginary part [170]. Solving the linear system $D\phi = \eta$ is necessary to invert the lattice Dirac operator. For every sample n of the stochastic source η and for each gauge configuration this process corresponds to [171]

$$\phi^{(n)}(y)^a_\alpha = \sum_{z,\gamma,c} \left[D^{(n)}(y,z)^{ac}_{\alpha\gamma} \right]^{-1} \eta^{(n)}(z)^c_\gamma \, . \tag{5.7.13}$$

Averaging over the n samples and utilizing Eq. (5.7.13) together with Eq. (5.7.11) yields

$$\begin{aligned} \lim_{N_{\text{hits}} \to \infty} \frac{1}{N_{\text{hits}}} \sum_{n=1}^{N_{\text{hits}}} \left[\eta^{(n)}(x)^b_\beta \right]^\dagger \phi^{(n)}(y)^a_\alpha &= \left\langle \left[\eta^{(n)}(x)^b_\beta \right]^\dagger \left[D^{(n)}(y,z)^{ac}_{\alpha\gamma} \right]^{-1} \eta^{(n)}(z)^c_\gamma \right\rangle_n \\ &= \left[D^{(n)}(y,x)^{ab}_{\alpha\beta} \right]^{-1} . \end{aligned} \tag{5.7.14}$$

In practical simulations, the sample size N_{hits} is limited, meaning that the relation (5.7.14) is only approximately satisfied due to the presence of stochastic noise. Denoting the source degrees of freedom (spin, color, space-time) by V_s, the signal in the stochastic estimator is of $\mathcal{O}(1)$, whereas the noise scales as $\frac{\sqrt{V_s}}{\sqrt{R}}$ [171]. Consequently, variance reduction methods are necessary.

A particularly useful variance reduction technique is the so-called *one-end trick* [171–173]. Upon inspecting Eq. (5.7.7) one notices that we need to compute the product of two quark propagators. Instead of applying Eq. (5.7.14) two times, i.e.

$$\eta^\dagger \phi (\eta^\dagger \phi)^\dagger = ((D^{-1})^\dagger + \text{stochastic noise}) \times (D^{-1} + \text{stochastic noise}) \, ,$$

one defines stochastic sources that have support only on a single time-slice τ_i [170]

$$\eta^{(n)}(\tau, \mathbf{x}_i | \tau_i) \in \mathcal{D} \quad \text{for} \quad \tau = \tau_i \, , \tag{5.7.15}$$

and are zero for $\tau \neq \tau_i$. This time-slice source satisfies

$$\left\langle \eta^{(n)}(\tau_i, \mathbf{x}_i | \tau_i)^c_\gamma [\eta^{(n)}(\tau_i, \mathbf{z} | \tau_i)^e_\epsilon]^\dagger \right\rangle_n = \delta_{\mathbf{x}_i \mathbf{z}} \delta_{\gamma\epsilon} \delta_{ce} \, , \tag{5.7.16}$$

and its location is changed randomly as one proceeds to the next gauge configuration [174]. Insert-

ing the orthonormality condition (4.2.4) into Eq. (5.7.7) projected to vanishing momentum gives:

$$
\begin{aligned}
&N_s^3\, G^{\text{2pt.}}_{O_2 O_1^\dagger}(\tau, \mathbf{p}=\mathbf{0}) = -\sum_{\mathbf{x}_f,\mathbf{x}_i,\mathbf{z}} \times \\
&\Big\langle (\gamma_5\Gamma_2)^{ab}_{\alpha\beta}\, D^{-1}_{(n)}(x_f,x_i)^{bc}_{\beta\gamma} \Big\langle \eta^{(n)}(\tau_i,\mathbf{x}_i|\tau_i)^c_\gamma [\eta^{(n)}(\tau_i,\mathbf{z}|\tau_i)^e_\epsilon]^\dagger \Big\rangle_n (\gamma_0\Gamma_1^\dagger\gamma_0\gamma_5)^{ed}_{\epsilon\delta}\, (D^{-1}_{(n)})^\dagger(x_f,z)^{da}_{\delta\alpha} \Big\rangle^{\text{conn.}} \\
&= -\sum_{\mathbf{x}_f} \Bigg\langle (\gamma_5\Gamma_2)^{ab}_{\alpha\beta}\, \phi_2^{(n)}(\tau_f,\mathbf{x}_f|\tau_i)^b_\beta \Bigg[\sum_{\mathbf{x}_i} D^{-1}_{(n)}(x_f,x_i)^{ad}_{\alpha\delta} \left((\gamma_0\Gamma_1^\dagger\gamma_0\gamma_5)^{de}_{\delta\epsilon} \right)^\dagger \eta^{(n)}(\tau_i,\mathbf{x_i}|\tau_i)^e_\epsilon \Bigg]^\dagger \Bigg\rangle_n \\
&= -\sum_{\mathbf{x}_f} \Bigg\langle \Big(\gamma_5\Gamma_2\, \phi_2^{(n)}(\tau_f,\mathbf{x}_f|\tau_i) \Big)^a_\alpha \Bigg[\sum_{\mathbf{x}_i} \Big(D^{-1}_{(n)}(x_f,x_i)\, \left(\gamma_0\Gamma_1^\dagger\gamma_0\gamma_5 \right)^\dagger \eta^{(n)}(\tau_i,\mathbf{x_i}|\tau_i) \Big)^a_\alpha \Bigg]^\dagger \Bigg\rangle_n \\
&\equiv -\sum_{\mathbf{x}_f} \Big\langle \Big(\gamma_5\Gamma_2\, \phi_2^{(n)}(\tau_f,\mathbf{x}_f|\tau_i) \Big) \cdot \Big(\phi^{(n)}_{1,\Gamma}(\tau_f,\mathbf{x}_f|\tau_i) \Big)^\dagger \Big\rangle_n \,, \qquad (5.7.17)
\end{aligned}
$$

with

$$
\phi_2^{(n)}(\tau_f,\mathbf{x}_f|\tau_i)^b_\beta \equiv \sum_{\mathbf{x}_i} D^{-1}_{(n)}(x_f,x_i)^{bc}_{\beta\gamma}\, \eta^{(n)}(\tau_i,\mathbf{x}_i|\tau_i)^c_\gamma \,, \qquad (5.7.18)
$$

$$
\phi^{(n)}_{1,\Gamma}(\tau_f,\mathbf{x}_f|\tau_i)^a_\alpha \equiv \sum_{\mathbf{x}_i} D^{-1}_{(n)}(x_f,x_i)^{ad}_{\alpha\delta} \left((\gamma_0\Gamma_1^\dagger\gamma_0\gamma_5)^{de}_{\delta\epsilon} \right)^\dagger \eta^{(n)}(\tau_i,\mathbf{x}_i|\tau_i)^e_\epsilon \,. \qquad (5.7.19)
$$

Consequently, the two-point correlation function at vanishing momentum is given by the product of two "solution vectors" $\phi_2^{(n)}$ and $\phi^{(n)}_{1,\Gamma}$ contracted at the sink-position. Currently, $\phi^{(n)}_{1,\Gamma}$ has to be calculated for each of the 16 combinations[6] of gamma-matrices, requiring 16 inversions for every $n \in \{1,\cdots,N_{\text{hits}}\}$ [170]. However, the signal-to-noise ratio becomes now of $\mathcal{O}(1)$ instead of $\mathcal{O} = \frac{\sqrt{N_{\text{hits}}}}{\sqrt{V_s}}$ without employing the one-end-trick [171].

It is possible to reduce to four inversions per stochastic hit [170] by employing spin-explicit (*SEM*) sources [175]. Independent stochastic noise vectors in color space, $\eta^{(n)}(\mathbf{x})$, are assigned at each spatial point of the selected time slice τ_i, while the spin structure is fixed explicitly through a Kronecker delta. The resulting time-slice source—dubbed `Z2SEMWall` in Ref. [170]—has the form

$$
\eta^{(n)}(\tau,\mathbf{x}\,|\,\tau_i,\beta,\mathbf{p})^c_\alpha = \delta_{\beta\alpha}\, \zeta^{(n)}(\mathbf{x})^c\, \mathrm{e}^{\mathrm{i}\mathbf{p}\cdot\mathbf{x}} \,, \quad \text{with} \quad \langle \zeta^{(n)}(\mathbf{x})^b\, \zeta^{(n)}(\mathbf{y})^{c\,\dagger} \rangle_n = \mathrm{e}^{\mathrm{i}\mathbf{p}\cdot\mathbf{x}}\, \mathrm{e}^{-\mathrm{i}\mathbf{k}\cdot\mathbf{y}}\, \delta_{\mathbf{xy}}\delta_{bc} \,. \qquad (5.7.20)
$$

We have defined the source (5.7.20) as a *momentum source*, in accordance with Ref. [176]. Note that the complex phase factor is not part of the orthonormality condition. Furthermore, since the source has only support when the Dirac index equals β, it is also termed a *linked source* or *spin diluted source* [171]. Consequently, the solution vectors $\phi^{(n)}$ satisfy [177]

$$
\sum_{y,b,\beta} D^{(n)}(x,y)^{ab}_{\alpha\beta}\, \phi^{(n)}(\tau_y,\mathbf{y}|\tau_i,\mathbf{p})^b_{\beta\gamma} = \zeta^{(n)}(\mathbf{x})^a \delta_{\alpha\gamma}\delta_{\tau_y,\tau_i}\, \mathrm{e}^{\mathrm{i}\mathbf{p}\cdot\mathbf{x}} \,. \qquad (5.7.21)
$$

Note, that the spin-explicit source ζ carries no spin index. Performing similar steps that led to

[6] Note that for $\Gamma_1 = \gamma_5$ the solution vectors $\phi_2^{(n)}$ and $\phi^{(n)}_{1,\Gamma}$ are identical, differing only by a factor of (-1).

Eq. (5.7.17), the two-point correlation function at finite momentum is given by

$$N_s^3\, G^{\text{2pt.}}_{O_2 O_1^\dagger}(\tau, \mathbf{p}) = -\sum_{\mathbf{x}_f} \mathrm{e}^{\mathrm{i}\mathbf{p}\cdot\mathbf{x}_f} \left\langle \left(\gamma_5 \Gamma_2\, \phi_2^{(n)}(\tau_f, \mathbf{x}_f | \tau_i, \mathbf{p})\right)^a_{\alpha\gamma} \left(\phi^{(n)}_{1,\Gamma}(\tau_f, \mathbf{x}_f | \tau_i, \mathbf{p}=0)^a_{\gamma\alpha}\right)^\dagger \right\rangle_n . \quad (5.7.22)$$

We emphasize that both solution vectors, $\phi_2^{(n)}$ and $\phi^{(n)}_{1,\Gamma}$, satisfy Eq. (5.7.21). It is necessary to perform two distinct inversions on the same stochastic noise source: one with zero momentum and the other with finite momentum $\mathbf{p}$. Consequently, for the projects outlined in Part III of this thesis, $4 \times N_p$ inversions are required per stochastic hit, where N_p represents the number of momentum sources and 4 corresponds to the number of spin indices. Specifically, we require a zero momentum propagator, one with momentum in the temporal direction, and one with momentum in a spatial direction.

5.7.2 The Truncated Solver Method

In the computation of two-point correlation functions, the most expensive part is the inversion of the Dirac operator. A computational speedup of roughly a factor of three can be achieved by employing the so-called *truncated solver method* [178–180]. The basic idea of this method is rather simple: Instead of solving the Dirac equation with high precision for all stochastic sources one performs a large number N_{LP} of "low-precision" solves. The resulting bias is then corrected by performing additional $N_{\text{HP}} \approx [\frac{1}{100}, \frac{1}{50}]\, N_{\text{LP}}$ "high-precision" measurements such that an unbiased estimator of the final expectation value $\langle O \rangle$ is obtained as the source average

$$\langle O \rangle = \left\langle \frac{1}{N_{\text{LP}}} \sum_{j=1}^{N_{\text{LP}}} O_i^{\text{LP}} \right\rangle + \underbrace{\left\langle \frac{1}{N_{\text{HP}}} \sum_{j=1}^{N_{\text{HP}}} \left(O_i^{\text{HP}} - O_i^{\text{LP}}\right) \right\rangle}_{\equiv \langle O_{\text{bias}} \rangle} . \quad (5.7.23)$$

Part II

Spectral and Chiral Properties of Hot QCD Matter around the Crossover

Chapter 6

Hot QCD Matter Around the Chiral Crossover

In this chapter, we explore the characteristics of thermal QCD matter at the temperatures $T = \{128, 154, 192\}$ MeV. We utilize $N_f = 2 + 1$ lattice QCD simulations with $\mathcal{O}(a)$-improved Wilson quarks and physical quark masses, maintaining a fixed lattice spacing $a = 0.064$ fm and volume $V = (6.1\,\text{fm})^3$. Our findings indicate that the pion quasiparticle, identified as the low-energy pole in the two-point function of the axial charge, becomes lighter as the temperature increases. We provide a hydrodynamics-based argument explaining why this pole transitions to a purely diffusive state above the chiral crossover. We examine the thermal alterations in the isovector vector spectral function using the Backus-Gilbert method, observing an enhancement at low energies and a depletion at approximately 1 GeV. A similar analysis of the axial-vector channel reveals a more pronounced enhancement at energies below 1 GeV, and we demonstrate that these observations align with rigorous spectral sum rules. The difference between the vector and axial-vector correlators—serving as an order parameter for chiral symmetry—is suppressed by more than an order of magnitude at the crossover.

This chapter has been adapted, with minor modifications, from the following references:

Authors:	**Ardit Krasniqi**, Marco Cè, Renwick J. Hudspith, Harvey B. Meyer
Title	Hot QCD matter around the chiral crossover: A lattice study with $\mathcal{O}(a)$-improved Wilson fermions
Year:	2024
Journal:	*Physical Review D*
Volume/Issue:	110, 11
DOI:	10.1103/PhysRevD.110.114506

Authors:	**Ardit Krasniqi**, Marco Cè, Tim Harris, Harvey B. Meyer, Csaba Török
Title	Aspects of chiral symmetry in QCD at $T = 128$ MeV
Year:	2023
Journal:	*Physical Review D*
Volume/Issue:	107, 5
DOI:	10.1103/PhysRevD.107.054509

6.1 Introduction

Quark matter under extreme conditions of temperature and density is of significant interest from both experimental and theoretical perspectives. In the early universe, within a timescale of microseconds, the strongly interacting constituents, quarks and gluons, existed in a hot and dense phase known as the Quark-Gluon Plasma (QGP). Heavy-ion colliders, such as the LHC at CERN and the RHIC at BNL, enable the re-creation of similar conditions under laboratory settings. As the universe expanded, it gradually cooled, undergoing a transition to the hadronic phase in which we currently reside. Notably, at physical quark masses, this transition is a crossover [35], characterized by a pseudocritical temperature $T_{\rm pc} = 156.5(1.5)\,\text{MeV}$ [36]; see also the earlier results of Ref. [181].

In the limit of massless quarks, the QCD Lagrangian exhibits a global $\mathrm{SU}(N_\mathrm{f})_L \times \mathrm{SU}(N_\mathrm{f})_R$ symmetry, corresponding to independent rotations of the left- and right-handed components of the Dirac fields. This symmetry is spontaneously broken to $\mathrm{SU}(N_\mathrm{f})_V$ at low temperatures and is restored in the high-temperature phase, a phenomenon known as chiral symmetry restoration. A non-zero value of the scalar density $\langle\bar\psi\psi\rangle(T)$ in the chiral limit characterizes the low-temperature phase, with T_c approximately in the range of $130 - 135\,\text{MeV}$ [182, 183]. Conversely, $\langle\bar\psi\psi\rangle(T) = 0$ for $T > T_\mathrm{c}$, indicating the restoration of chiral symmetry. Thus, the quark condensate $\langle\bar\psi\psi\rangle$ serves as an order parameter for chiral symmetry breaking.

The most immediate consequence of a broken chiral symmetry is the presence of light pions, as indicated by Goldstone's theorem. Consequently, starting with the QCD vacuum, an initial increase in temperature results in a dilute gas of pions. With further temperature elevation, additional hadron species start to contribute. Concurrently, it is anticipated that the medium's excitations will manifest as quasiparticles with properties somewhat altered compared to standard hadrons, which are excitations of the vacuum. A natural starting point in investigating the medium's quasiparticles is to examine the properties of the pion within the thermal environment [184, 185]. The pion mass and decay constant have been analyzed to one loop in a thermal chiral perturbation theory (ChPT) approach [186]. Furthermore, the energy density, pressure, and quark condensate have been explored up to $\mathcal{O}(p^8)$ in a chiral expansion below the phase transition [187]. In Ref. [188], the shift in the pion pole was calculated as a function of temperature up to second order in the density. Toublan [189] also calculated the pion decay constant within thermal ChPT to two loops and examined the validity of the Gell-Mann–Oakes–Renner (GOR) relation at finite temperature. It is not *a priori* clear how far this expansion is applicable as temperature increases, since the partition function is certainly no longer dominated by pions for $T \gtrsim 100\,\text{MeV}$ [184, 187]. However, the Goldstone-boson nature of pions ensures the existence of a divergent static correlation length for vanishing quark masses [190].

In conventional thermal ChPT, both the quark mass and temperature are considered small parameters, leading to an expansion around $m_q = 0$ and $T = 0$. However, in Refs. [191, 192], Son and Stephanov explored perturbations solely around $m_q = 0$, while maintaining the temperature T at any value within the chirally broken phase. Although this approach precludes an explicit relationship between parameters such as the quark condensate and the pion decay constant with their $T = 0$ counterparts, it extends the applicability of their findings to a regime in which neither ChPT nor perturbative Quantum Chromodynamics (pQCD) is applicable. Given that lattice

simulations employ the imaginary-time formalism, deriving real-time observables, such as "pole masses," from lattice quantities (e.g. Euclidean correlators) generally presents a significant challenge. Nonetheless, at small u, d quark masses, the real part of the dispersion relation of soft pions can be extracted from static Euclidean correlators, with corrections that tend to zero in the chiral limit. Our investigation focuses on the behavior of the pion pole as the system transitions into the chirally restored phase, utilizing both numerical analysis and insights from hydrodynamics.

In the low-temperature phase, the dispersion relation of the pion quasiparticle can be characterized at low momenta by a renormalization-group invariant (RGI) parameter $u(T)$. This temperature-dependent parameter $u(T)$ is directly measurable on the lattice from screening quantities and serves a dual function: it not only predicts the modified dispersion relation but also connects the *static* pion screening mass to the (*dynamic*) pole mass. This analysis was conducted in Refs. [193, 194] and Refs. [1, 2] for the $N_f = 2$ and $N_f = 2 + 1$ cases, respectively. In this study, we extend these investigations to encompass physical quark masses and achieve higher statistical precision.

In a broader context, changes in the spectrum of QCD excitations constitute a significant aspect of the phenomenology associated with heavy-ion collisions In particular, the strongly interacting matter can produce lepton pairs via timelike photons, and the invariant-mass spectrum of the latter gives access to the vector spectral function of the thermal medium [195] via a Kubo-Martin-Schwinger relation. Within the hadronic phase, dileptons are predominantly produced through the decay of vector mesons [33, 196]. At sufficiently high temperatures, it is anticipated that the vector spectral function can be computed using QCD weak-coupling methods [197]. However, it remains uncertain over which temperature range mesonic excitations, analogous to the ρ, ω, and ϕ, disappear from the medium. Here we address this issue within the isovector vector channel.

We note that, via a timelike Z boson, dileptons can in principle also be produced through the axial current [197], albeit at a very low rate for $T \lesssim 1\,\text{GeV}$. This process would probe the axial-vector spectral function of the thermal medium. A restored chiral symmetry implies the vanishing of the difference of the isovector vector and axial-vector spectral functions, denoted as $V - A$. One of the objectives of this thesis is to determine the temperature range within which this occurs for physical quark masses. Notably, we observe more significant thermal effects in the axial-vector spectral function compared to the vector case. Several other probes of chiral symmetry restoration can be examined: in Refs. [118, 119], the implications of chiral symmetry restoration have been explored in the baryonic sector within the context of parity doubling. The authors find that the ground state masses of light baryons in the hadronic phase remain nearly stable in the positive-parity sector, while the negative-parity ground state masses exhibit temperature dependence, leading to approximate degeneracy as the deconfinement transition is approached.

Thus, by investigating the observables described in the preceding paragraphs, this thesis aims to provide a comprehensive depiction of strongly interacting matter across the chiral crossover. Part II of this thesis is structured as follows: In Section 6.2 we introduce some basic definitions that play a key role in the description of the pion quasiparticle. We continue with the implementation of the relevant lattice correlators, followed by a brief description of the numerical setup. Our results in the pseudoscalar sector are presented in Sec. 6.3. First, we extract the mass and decay constant of the screening pion (6.3.1-6.3.2) and use them to define an "effective chiral con-

densate" (6.8.1). Next, we determine the pion velocity u and examine the extent to which its extraction depends on a finite thermal width of the pion $\Gamma(T)$ (Secs. 6.3.3 and 6.3.4). Subsequently, we reconstruct a smeared version of the spectral function associated with the two-point function of the axial charge and compare our results with those in the literature (Secs. 6.4 and 6.5). We provide the static pseudoscalar, vector and axial-vector screening masses along our temperature scan in Sec. 6.6. Thereafter, we compare our lattice estimate for the isovector quark number susceptibility (QNS) with the prediction of the hadron resonance gas (HRG) model in Sec. 6.7. In that section, we also investigate the effect of a modified dispersion relation for the pion in the HRG model. We examine several order parameters for chiral symmetry restoration in Sec. 6.8, including the '$V - A$' difference. Section 6.9 contains our results on the thermal modification of vector and axial-vector spectral functions. Finally, we present our conclusions in Sec. 6.10.

6.2 Preliminaries

In this chapter we introduce the notation and some basic definitions as well as the key quantities characterizing the pion quasiparticle that we will use throughout the paper. Furthermore, the lattice implementation of the correlators and the numerical setup are described.

6.2.1 Definition of Operators and Correlation Functions

The notations and conventions used in this study are adapted from Ref. [1]. Our framework is the up, down, and strange quark sector of Euclideanized QCD on the space $S^1 \times \mathbb{R}^3$, where S^1 denotes the Matsubara cycle of length $\beta \equiv 1/T$. We define the (isovector) pseudoscalar density, the vector current and the axial-vector current [see also Eqs. (2.2.5-2.2.6)] as

$$P^a(x) = \bar{\psi}(x)\gamma_5\frac{\tau^a}{2}\psi(x)\,, \quad V^a_\mu(x) = \bar{\psi}(x)\gamma_\mu\frac{\tau^a}{2}\psi(x)\,, \quad A^a_\mu(x) = \bar{\psi}(x)\gamma_\mu\gamma_5\frac{\tau^a}{2}\psi(x)\,, \tag{6.2.1}$$

where $a \in \{1,2,3\}$ is an adjoint $\mathrm{SU}(2)_{\mathrm{isospin}}$ index, τ^a is a Pauli matrix and $\bar{\psi}(x) = (\bar{u}(x)\ \bar{d}(x))$ is a Dirac field flavor doublet. The partially conserved axial current (PCAC) relation is an operator identity that holds in Euclidean space when inserted into expectation values. It relates the divergence of the axial vector current $A^a_\mu(x)$ to the pseudoscalar density $P^a(x)$,

$$\partial_\mu A^a_\mu(x) = 2m_{\mathrm{PCAC}}\, P^a(x)\,. \tag{6.2.2}$$

In the path integral formulation, this relation results from performing a chiral rotation $\delta^a_A\psi(x) = \frac{\tau^a}{2}\gamma_5\psi(x)$ of the fields (see Ref. [198]). Applying the pseudoscalar density operator on both sides and taking the expectation value one can obtain the bare PCAC quark mass,

$$2m_{\mathrm{PCAC}}\langle P^b(x)P^b(0)\rangle = \partial_\mu\langle A^a_\mu(x)P^a(0)\rangle\,. \tag{6.2.3}$$

It is convenient to integrate over three space-time directions, leaving only one direction in which the derivative acts on the axial current. Since the PCAC relation is an operator identity, we are free to choose this direction; any dependence on the direction must therefore amount to a discretization error. In our thermal system, the spatial direction is at least four times larger than the temporal

direction. Consequently, measurements along the spatial direction resulted in a longer plateau and, thus, smaller errors. Therefore, we will extract the PCAC quark mass from the relation

$$m_{\mathrm{PCAC}}(x_3) = \frac{1}{2}\frac{\int \mathrm{d}\tau \mathrm{d}^2x_\perp \, \langle \widetilde{\partial}_3 A_3^a(x) P^a(0)\rangle}{\int \mathrm{d}\tau \mathrm{d}^2x_\perp \, \langle P^b(x) P^b(0)\rangle}, \qquad x_\perp = (x_1, x_2)\,. \tag{6.2.4}$$

Wilson fermions explicitly break chiral symmetry at finite lattice spacing a, leading to $\mathcal{O}(a)$ lattice artifacts.

We introduce the static screening axial correlator, given by

$$\delta^{ab} G_A^s(x_3, T) = \int \mathrm{d}\tau \mathrm{d}^2x_\perp \langle A_3^a(x) A_3^b(0)\rangle \overset{|x_3|\to\infty}{=} \delta^{ab} \frac{f_\pi^2 m_\pi}{2} \mathrm{e}^{-m_\pi |x_3|}\,, \tag{6.2.5}$$

where we have specified the asymptotic form of the correlator, which defines the pion screening mass m_π and decay constant f_π. Analogously, we define[1] the following static screening correlators:

$$\delta^{ab} G_P^s(x_3, T) = \int \mathrm{d}\tau \mathrm{d}^2x_\perp \langle P^a(x) P^b(0)\rangle\,, \tag{6.2.6}$$

$$\delta^{ab} G_{AP}^s(x_3, T) = \int \mathrm{d}\tau \mathrm{d}^2x_\perp \langle A_3^a(x) P^b(0)\rangle\,, \tag{6.2.7}$$

$$\delta^{ab} G_V^s(x_3, T) = -\frac{1}{2}\sum_{i=1,2} \int \mathrm{d}\tau \mathrm{d}^2x_\perp \langle V_i^a(x) V_i^b(0)\rangle\,, \tag{6.2.8}$$

$$\delta^{ab} G_A^s(x_3, T) = -\frac{1}{2}\sum_{i=1,2} \int \mathrm{d}\tau \mathrm{d}^2x_\perp \langle A_i^a(x) A_i^b(0)\rangle\,. \tag{6.2.9}$$

To probe the dynamical properties of the thermal system, we define time-dependent correlators projected onto a definite spatial momentum as follows:

$$\delta^{ab} G_{A_0}(\tau, T) = \int \mathrm{d}^3x \, \langle A_0^a(x) A_0^b(0)\rangle \tag{6.2.10}$$

$$\delta^{ab} G_P(\tau, T) = \int \mathrm{d}^3x \, \langle P^a(x) P^b(0)\rangle \tag{6.2.11}$$

$$\delta^{ab} G_{PA_0}(\tau, T) = \int \mathrm{d}^3x \, \langle P^a(x) A_0^b(0)\rangle = -\int \mathrm{d}^3x \, \langle A_0^a(x) P^b(0)\rangle \tag{6.2.12}$$

$$\delta^{ab} G_A(\tau, \mathbf{p}, T) = -\frac{1}{3}\sum_{i=1}^{3} \int \mathrm{d}^3x \, \mathrm{e}^{i\mathbf{p}\cdot\mathbf{x}} \, \langle A_i^a(x) A_i^b(0)\rangle \tag{6.2.13}$$

$$\delta^{ab} G_V(\tau, \mathbf{p}, T) = -\frac{1}{3}\sum_{i=1}^{3} \int \mathrm{d}^3x \, \mathrm{e}^{i\mathbf{p}\cdot\mathbf{x}} \, \langle V_i^a(x) V_i^b(0)\rangle\,. \tag{6.2.14}$$

The time-dependent correlators are related to the corresponding spectral function (see e.g. the review [34]) via

$$G_J(\tau, \boldsymbol{p}, T) = \int_0^\infty \mathrm{d}\omega \, \rho_J(\omega, \mathbf{p}, T) \, \frac{\cosh(\omega(\beta/2 - \tau))}{\sinh(\omega\beta/2)}\,, \quad J = A_0, P, A, V. \tag{6.2.15}$$

A close examination of Eq. (6.2.15) reveals that the Euclidean correlators exhibit a dual depen-

[1] Please note that in the case of identical operators at source and sink, we do not use double labels for the correlators, for example $G_P^s(x_3, T)$, instead of $G_{PP}^s(x_3, T)$.

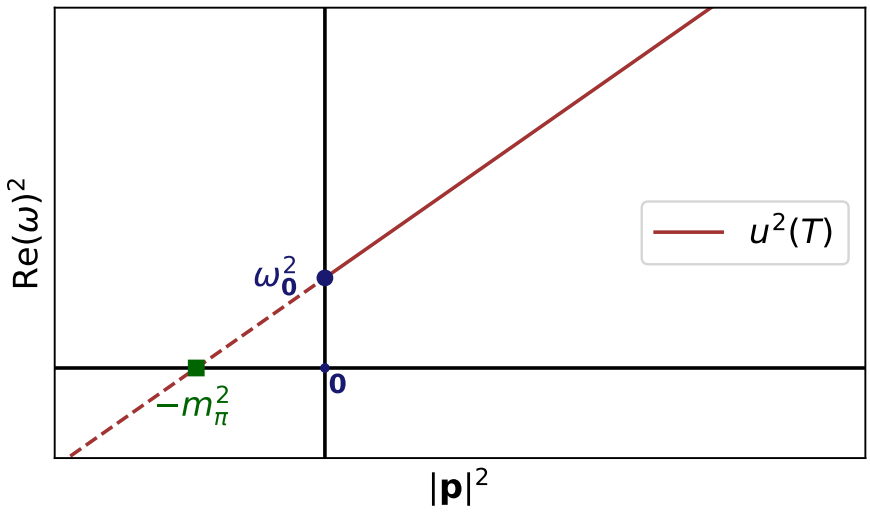

Figure 6.1: A sketch of the trajectory of the pion pole within the pseudoscalar retarded correlator $G_P^R(\omega, \mathbf{p}, T)$ is illustrated on the $(\omega, \mathbf{p})$-plane, whereby the slope corresponds to the squared pion velocity $u^2(T)$. The figure is inspired by Ref. [199].

dence on temperature: *implicitly*, through the presence of the inverse temperature β in the kernel function $\cosh(\omega(\beta/2-\tau))/\sinh(\omega\beta/2)$, as well as through the *explicit* temperature dependence of the spectral function. The former effect induces a temperature dependence in the Euclidean correlator even in the absence of changes in the spectral function. Therefore, it is crucial to isolate this effect from a genuine temperature dependence arising from alterations in the thermal medium, such as the QGP. Consequently, discrepancies between the thermal and reconstructed [cf. Eq. (6.8.9)] correlators can be attributed to modifications in the spectral function, and thus the physical picture. The converse, however, is not necessarily true [98].

In Sec. 6.4, we will conduct an analysis of the axial spectral function [$J = A_0$ in Eq. (6.2.15)] utilizing the Backus-Gilbert method. Subsequently, in Sec. 6.9, this reconstruction method will be applied to the vacuum-subtracted vector and axial-vector spectral functions. Throughout the remainder of this thesis, the temperature argument of the correlators and spectral functions will not always be explicitly stated.

6.2.2 Pion Properties at Finite Temperature

It has been established within several frameworks [191, 192] that at temperatures below the chiral phase transition a pion quasiparticle persists, with the real part of the dispersion relation of sufficiently soft pions given by

$$\omega_{\mathbf{p}} = u(T)\sqrt{m_\pi^2 + |\mathbf{p}|^2}\,, \quad \text{for any } T \lesssim T_c\,, \tag{6.2.16}$$

$$\Rightarrow \quad u(T) = \left.\frac{\mathrm{d}\omega_{\mathbf{p}}}{\mathrm{d}|\mathbf{p}|}\right|_{m_\pi^2=0}\,. \tag{6.2.17}$$

Consequently, the parameter $u(T)$ can be interpreted as the group velocity of a massless pion excitation in the chiral limit. While the quasiparticle mass $\omega_{\mathbf{0}}$ is the real-part of a pole of the retarded correlator $G_P^R(\omega, \mathbf{p} = 0, T)$ of the pseudoscalar density in the frequency variable, the

screening mass m_π is a pole of $G_P^R(\omega = 0, \mathbf{p}, T)$ in the spatial momentum $|\mathbf{p}|$ and represents an inverse spatial correlation length [see Fig. 6.1]. Note that $T = 0$, the SO(4) Euclidean symmetry implies that $m_\pi = \omega_{\mathbf{0}}$, and u is assigned the value of 1 [199]. A simple interpretation of the dispersion relation (6.2.16) was given in Ref. [194] in terms of the poles of screening and time-dependent correlators. Son and Stephanov [191, 192] showed that the pion velocity u in the chiral limit is given by the ratio of f_π^2 to the axial charge susceptibility $\int_0^\beta \mathrm{d}\tau\, G_{A_0}(\tau, T)$:

$$u^2 = \frac{f_\pi^2}{\int_0^\beta \mathrm{d}\tau\, G_{A_0}(\tau, T)}\,. \tag{6.2.18}$$

However, the latter contains an ultraviolet divergence at any non-vanishing quark mass [193] and is therefore not practical for lattice calculations. As an alternative, in Refs. [193, 194] the parameter u was determined using lattice correlation functions at vanishing spatial momentum via two independent estimators,

$$u_m = \left[-\frac{4m_q^2}{m_\pi^2} \frac{G_P(\tau, T)}{G_{A_0}(\tau, T)}\bigg|_{\tau=\beta/2} \right]^{1/2}, \tag{6.2.19}$$

$$u_f = \frac{f_\pi^2 m_\pi}{2G_{A_0}(\beta/2, T)\sinh(u_f m_\pi \beta/2)}\,, \tag{6.2.20}$$

that agree in the chiral limit. In the present study, we adopt these estimators. In doing so, for the estimator u_m, the parametric dominance of the pion in the time-dependent Euclidean axial as well as the pseudoscalar density correlator at small quark masses is exploited. The estimator u_f only exploits the pion dominance in the axial correlator; however, it relies on the residue determined from the static screening correlator. Note that in the estimators (6.2.19) and (6.2.20), only the contribution at the midpoint of the Euclidean correlators is considered, thus circumventing the issues associated with the short-distance UV contribution.

The pion contribution to the spectral function ρ_{A_0} is expected to take the form of a sharp peak,

$$\rho_{A_0}(\omega, T) = \mathrm{sgn}(\omega)\mathrm{Res}(\omega_{\mathbf{0}})\delta(\omega^2 - \omega_{\mathbf{0}}^2) + \dots\,, \tag{6.2.21}$$

where in Ref. [192] (see also Ref. [194]) the residue was predicted to have the form

$$\mathrm{Res}(\omega_{\mathbf{0}}) \equiv (f_\pi^t)^2 \omega_0^2 = f_\pi^2 m_\pi^2\,, \tag{6.2.22}$$

such that we can access the quasiparticle decay constant via $f_\pi^t = f_\pi / u_m$.

We note that the equations of this subsection unambiguously define the observables $\omega_{\mathbf{0}}$, u_m, u_f, m_π and f_π, even for temperatures above the chiral crossover, although the notation reflects their interpretation in the chirally broken phase. In the next subsection, we elaborate on the expected pole structure at low energies in the axial-charge correlator.

6.2.3 The Pole in the Axial-Charge Correlator above the Chiral Crossover

From the static pseudoscalar correlator, we define the overlap G_s onto the (screening) ground state,

$$\int_0^\beta \mathrm{d}\tau \, \langle P^a(x) \, P^b(0) \rangle \stackrel{|\boldsymbol{x}|\to\infty}{=} -\delta^{ab} \, G_s^2 \, \frac{\mathrm{e}^{-m_s|\boldsymbol{x}|}}{4\pi|\boldsymbol{x}|}. \tag{6.2.23}$$

Note that the engineering dimension of G_s is GeV^2. In this and the subsequent two paragraphs, we use Minkowski-space notation with mostly minus metric $\eta^{\mu\nu}$ and $\{\gamma^\mu, \gamma^\nu\} = 2\eta^{\mu\nu}$. In Ref. [192], the spectral functions of the operators $A^{0,a}$ and P^a were determined in the chirally broken phase. Both are hydrodynamic fields at small quark masses, A^0 because it is the density of the almost conserved axial charge and P because $\varphi^a = 2i\frac{P^a}{\langle\bar{\psi}\psi\rangle}$ corresponds to the phase of the condensate [see e.g. Ref. [200], Sec. 2.2], which as a Goldstone mode should be included in the list of hydrodynamic fields [192].

Here we are concerned with the chirally symmetric phase. Our main goal is to determine the form of the spectral function of the axial charge density, which is a hydrodynamic field at low frequencies and momenta. The corresponding current, up to higher-order terms, can be expressed via Fick's law,

$$\boldsymbol{A}^a = -D_A \nabla A^0 + \ldots \tag{6.2.24}$$

In the chirally restored phase, the pseudoscalar density is no longer a hydrodynamic field. Thus, it should be expressed in terms of the axial charge density and its spatial gradients. To leading order, we have the constitutive equation

$$\phi^a \equiv iP^a = -\frac{\bar{\lambda}}{2} m_q G_s^2 A^{0,a} + \ldots, \tag{6.2.25}$$

where the suppression by the quark mass reflects the fact that P and A^0 belong to different chiral multiplets and as such decouple in the chiral limit at the linear level. Note that $\bar{\lambda}$ is a hydrodynamic coefficient and $(T^5\bar{\lambda})$ is renormalization-group invariant.

The PCAC relation can then be interpreted as an equation of motion for the axial charge density,

$$\partial_0 A^{0,a} = -\nabla \cdot \boldsymbol{A}^a + 2m_q\phi^a = D_A \triangle A^{0,a} - \bar{\lambda} m_q^2 G_s^2 A^{0,a} + \ldots. \tag{6.2.26}$$

Linear response theory then leads to a prediction for the form of the spectral function for the axial charge density (see e.g. Ref. [34]),

$$\frac{\rho_A(\omega,\boldsymbol{k})}{\omega} = \frac{\chi_A(\boldsymbol{k})}{\pi} \, \frac{\bar{\lambda} m_q^2 G_s^2 + D_A \boldsymbol{k}^2}{\omega^2 + (\bar{\lambda} m_q^2 G_s^2 + D_A \boldsymbol{k}^2)^2}. \tag{6.2.27}$$

Close to the chiral limit, $\chi_A(\boldsymbol{k}) \simeq \chi_s$ is close to the isospin susceptibility corresponding to the vector current. Similarly, $D_A = D_I$ corresponds to the diffusion coefficient of isospin. Thus, in the chiral regime, the only new and independent transport coefficient is $\bar{\lambda}$. The qualitative difference in the spectral functions of the broken phase and the restored phase at $\boldsymbol{k} = 0$ is illustrated in Fig. 6.2. We also note that for non-interacting quarks, $\bar{\lambda} = 0$; see Appendix J.

From the result (6.2.27), one deduces the spectral funtions for the $\langle A^0 P\rangle$ and $\langle PP\rangle$ correlators

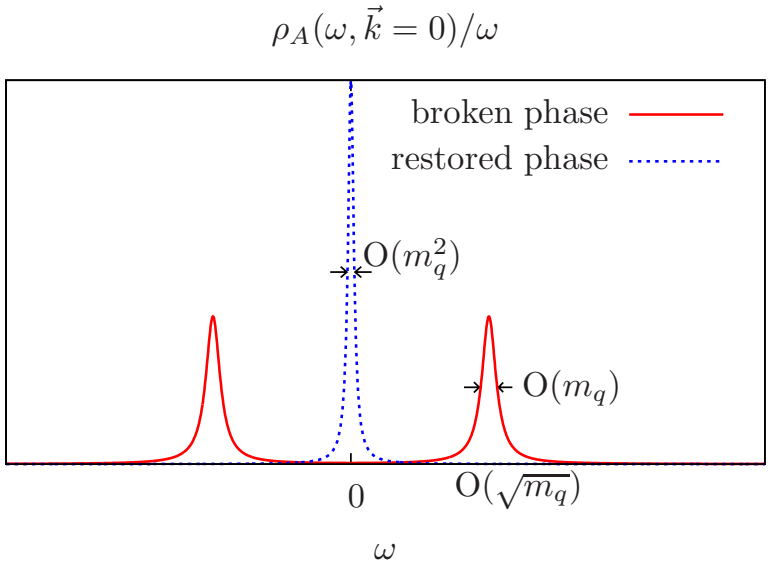

Figure 6.2: Qualitative features of the low-energy poles in the spectral function of the axial charge, in the broken and in the restored phase.

at vanishing spatial momentum,

$$\rho_{AP}(\omega, \mathbf{0}) = \frac{\omega}{2m_q}\rho_A(\omega, \mathbf{0}) = \frac{\chi_A(0)}{2\pi}\,\frac{\bar{\lambda} m_q G_s^2 \omega^2}{\omega^2 + (\bar{\lambda} m_q^2 G_s^2)^2}, \tag{6.2.28}$$

$$\frac{\rho_P(\omega, \mathbf{0})}{\omega} = -\frac{1}{2m_q}\rho_{AP}(\omega, \mathbf{0}) = -\frac{\chi_A(0)}{4\pi}\,\frac{\bar{\lambda} G_s^2 \omega^2}{\omega^2 + (\bar{\lambda} m_q^2 G_s^2)^2}. \tag{6.2.29}$$

We note that in the chiral limit,

$$\lim_{\omega\to 0}\frac{\rho_P(\omega, \mathbf{0})}{\omega} = -\frac{\chi_s}{4\pi}\,\bar{\lambda}\, G_s^2. \tag{6.2.30}$$

By contrast, at large frequencies we have $\frac{\rho_P(\omega,\mathbf{0})}{\omega} \overset{|\omega|\to\infty}{\sim} -\frac{N_c}{16\pi^2}|\omega|$. Eq. (6.2.30) represents a Kubo formula for the transport coefficient $\bar{\lambda}$.

Finally, it is useful to record the parametric size of the Euclidean correlators G_{A_0} and G_P at $\tau = \beta/2$; see Table 6.1. This information determines whether the real part of the pole can be determined without addressing an inverse problem. Clearly, this is possible in the broken phase near the chiral limit, because both G_{A_0} and G_P are dominated by the pole contribution. However, in the restored phase, the pseudoscalar correlator is not dominated by this contribution.

In Ref. [201], a real-time simulation of the dynamics of "Model G" [202] is performed. This model lies in the same dynamic universality class as QCD. The authors study the scaling properties of real-time correlation functions of an $O(4)$ critical system. The left panel of Fig. 4 of Ref. [201] shows results in the chirally symmetric phase. The statistical correlators for the σ, π, and axial channels are plotted against time. The (by orders of magnitude) slower decay in the axial channel is clearly visible, whereas the σ and π channels are nearly degenerate and dissipate on a much shorter timescale. Furthermore, the authors find that at the pseudocritical temperature, the axial charge correlator still exhibits purely dissipative behavior. However, the peak becomes noticeably

Table 6.1: Parametric size, in terms of the average up-down quark mass m_q, of the low-energy contribution vs. the rest in the axial charge density and in the pseudoscalar density Euclidean-time dependent correlators at zero spatial momentum and $\tau = \beta/2$. The left part of the table concerns the chirally broken phase, and the right-hand part the restored phase.

	pion pole	rest	diffusion pole	rest
G_{A_0}	$\mathcal{O}(1)$	$\mathcal{O}(m_q^2)$	$\mathcal{O}(1)$	$\mathcal{O}(m_q^2)$
G_P	$\mathcal{O}(m_q^{-1})$	$\mathcal{O}(1)$	$\mathcal{O}(1)$	$\mathcal{O}(1)$

broader than that of the unbroken phase. This suggests that the approximate conservation of the axial charge, which is valid in the unbroken phase, breaks down in this regime. In addition, in Refs. [203, 204], the authors have recently investigated universal non-equilibrium properties of Goldstone modes in Model G, focusing on their behavior during quenches from the symmetric (restored) phase to the symmetry-broken phase. Although in the "real world" chiral symmetry is explicitly broken due to the presence of finite quark masses, lattice QCD results for the quark mass dependence of the chiral condensate reveal that the chiral crossover follows the qualitative—and partly quantitative—behavior predicted by the investigated static $O(4)$ scaling [182, 205].

6.2.4 Lattice Implementation of the Correlators

In this study, we exclusively employ the local discretizations of the operators introduced in the previous subsection. Consequently, the expressions for the bare operators in the lattice theory remain consistent with those in Eq. (6.2.1). These bare operators undergo $\mathcal{O}(a)$-improvement followed by renormalization. While the bare pseudoscalar density is automatically $\mathcal{O}(a)$-improved, the specifics of the improvement process for the vector and axial-vector currents are detailed in Appendix B.

The finite renormalization of the vector and axial-vector currents is conducted using non-perturbatively determined renormalization factors $Z_V(g_0^2)$ and $Z_A(g_0^2)$, supplemented by a quark-mass dependent factor to fully achieve $\mathcal{O}(a)$-improvement; further details are provided in Appendix C.

The pseudoscalar density $P^a(x)$ acquires scale (and scheme) dependence through the renormalization process. The renormalization factor is denoted as $Z_P(g_0^2, a\mu)$. In this context, we renormalize $P^a(x)$ within the (non-perturbative) gradient-flow (GF) scheme at the renormalization scale μ, where the corresponding coupling $\bar{g}^2_{\mathrm{GF}} = 9.25$; this corresponds to a low scale of $\mu \approx 230$ MeV [206]. Although none of our physics applications depend on the selection of a specific scheme, it is noteworthy that in the aforementioned publication, the scale dependence of the renormalization factor has been computed up to perturbative scales μ; thus, the connection to the RGI operator is established.

The chosen renormalization of the PCAC mass preserves the axial Ward identity in Eq. (6.2.2). Consequently, all renormalization scale-dependent quantities in this study are reported in the aforementioned gradient-flow scheme. Specifically, the PCAC mass is renormalized by multiplying it with Z_A/Z_P, and the combination $m_\pi^2 f_\pi^2/m_{\mathrm{PCAC}}$ considered in Sec. 6.8.1 is renormalized via the factor $Z_A Z_P$. The numerical values of the renormalization factors are listed in Appendix C.

Table 6.2: Parameters and lattice spacing of the ensembles analyzed in this study. The lattice spacing has been determined in Ref. [129].

N_τ/a	L/a	$6/g_0^2$	κ_l	κ_s	a [fm]	N_{conf}	$\frac{\text{MDUs}}{\text{conf}}$	Label
24	96	3.55	0.137232867	0.136536633	0.06426(76)	1200	4	`E250Nt24`
20	96	3.55	0.137232867	0.136536633	0.06426(76)	1000	4	`E250Nt20`
16	96	3.55	0.137232867	0.136536633	0.06426(76)	1500	4	`E250Nt16`

6.2.5 Numerical Setup

Our study utilizes three $N_{\text{f}} = 2+1$ ensembles, employing the tree-level $\mathcal{O}(a^2)$-improved Lüscher-Weisz gauge action alongside non-perturbatively $\mathcal{O}(a)$-improved Wilson fermions [136]. This choice is consistent with the Coordinated Lattice Simulations (CLS) initiative [127], and the bare parameters are identical with those of the CLS zero-temperature ensemble `E250` [207]. These parameters, along with the lattice spacing as determined in Ref. [129], are presented in Table 6.2. The spatial dimension is uniformly $N_s = 96$ across all ensembles, while the temporal dimension is subject to thermal boundary conditions with $N_\tau \in \{24, 20, 16\}$, marking the only variation from the zero-temperature ensemble. This setup yields the following temperatures:

$$T_{24} = \frac{1}{24a} = 127.9(1.5)\,\text{MeV}\,, \tag{6.2.31}$$

$$T_{20} = \frac{1}{20a} = 153.5(1.8)\,\text{MeV}\,, \tag{6.2.32}$$

$$T_{16} = \frac{1}{16a} = 191.9(2.3)\,\text{MeV}\,. \tag{6.2.33}$$

The value of the pseudocritical temperature[2] $T_{\text{pc}} = 156.5(1.5)\,\text{MeV}$, as obtained in $(2+1)$-flavor QCD [36], implies our temperature range $\{T_{24}, T_{20}, T_{16}\}/T_{\text{pc}} \approx \{0.82, 0.98, 1.23\}$ spans the hadronic phase, the chiral crossover, and the high-temperature or quark-gluon plasma phase.

For reference, we also quote the zero-temperature pseudoscalar masses and pion decay constant, determined in Ref. [208],

$$T = 0: \qquad m_\pi^0 = 130.0(0.7)(1.5)\,\text{MeV}, \qquad m_K^0 = 489.36(0.25)(5.8)\,\text{MeV}, \tag{6.2.34}$$

$$f_\pi^0 = 87.1(0.3)(1.0)\,\text{MeV}\,, \tag{6.2.35}$$

where the first error arises from the corresponding quantity in lattice units, and the second from the determination of the lattice spacing in Ref. [129].

The ensembles were generated utilizing version 2.0 of the `openQCD` package [209], by introducing a small twisted mass to the light-quark doublet to ensure algorithmic stability. The correct QCD expectation values are derived by incorporating the reweighting factors for the twisted mass and the rational approximation of the propagator employed to simulate the strange quark [167, 209–211]. Error estimation was conducted using the Γ method [212–214] as implemented in the `pyerrors` package [215]. For further details, refer to Appendix D.

[2] In Ref. [36], the kaon decay constant f_K is used to determine the lattice spacing a, whereas Ref. [129] employs the linear combination (5.3.7) for converting lattice measurements to physical units. The scale-setting procedures are thus quite similar.

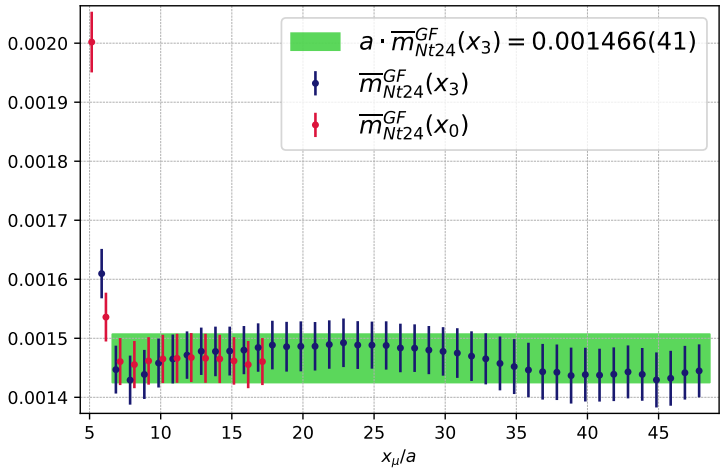

Figure 6.3: Renormalized PCAC mass in the `E250Nt24` ensemble along the τ and x_3 direction. The final result—obtained from a fit along the x_3 direction—is also shown with a $1-\sigma$ band. We have used the improved axial current together with the symmetrized derivative [see Eqs. (B.3-B.5)].

Measurements were performed using stochastic wall sources within the framework of Renwick J. Hudspith's `Witnesser` code. An improvement in this calculation compared to our previous work [1] is the use of stochastic wall sources for the two-point functions. In this context, we utilize $Z_2 \otimes Z_2$ noise [172], inverting solely on the spin indices. These sources, also referred to as "`Z2SEMWall`" [170] or "linked" sources [171], necessitate only 4 inversions of the Dirac matrix, as opposed to the typical 12 for a point source. Given that the wall source has support on a large volume, it exhibits reduced sensitivity to local fluctuations of the gauge field and generally yields a smaller variance for two-point functions at a fixed cost compared to point sources. Additionally, we extensively applied the Truncated Solver Method [178] with a substantial number of low-precision solves, rendering the calculations presented here relatively cost-effective.

The results for the `E250Nt24` ensemble presented in Ref. [1] were obtained using point sources. When comparing the result for the pion screening decay constant, $f_\pi/T = 0.559(11)$, from that study to our result reported here, $f_\pi/T = 0.569(4)$, we have achieved an approximate eightfold increase in statistical precision [see Sec. 6.3.2].

6.3 Results on the Pseudoscalar Sector

In this section, we present our lattice results concerning observables within the pseudoscalar sector, specifically those related to pion properties. As a crucial reference point, we initiate our discussion with the determination of the light-quark doublet PCAC masses.

6.3.1 The PCAC Mass: A Control quantity

The process of extracting the PCAC masses, as specified in Eq. (6.2.4), involves fitting a constant over the interval where a plateau is discernible; see Figs. 6.3 and 6.4. This approach takes

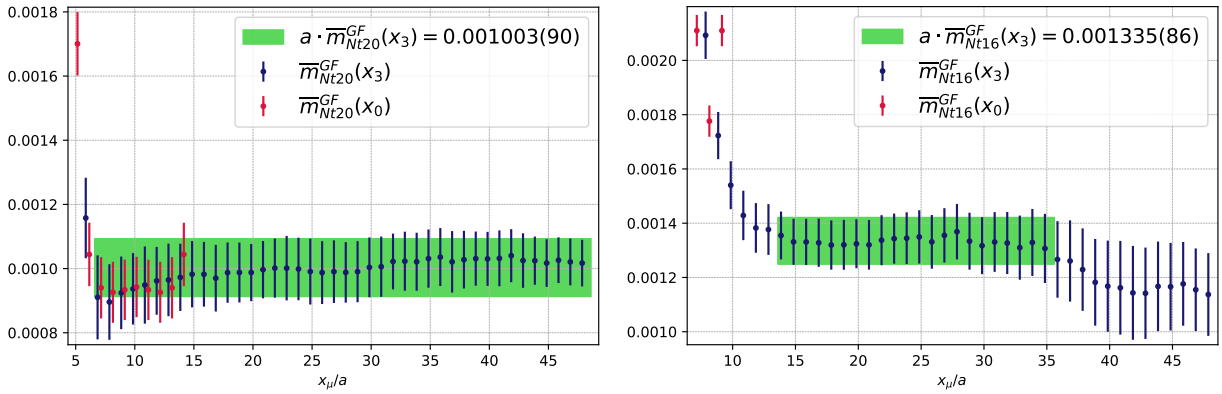

Figure 6.4: Renormalized PCAC masses in the `E250Nt20` ensemble (**left**) and `E250Nt16` ensemble (**right**) along the τ and x_3 direction. For the `E250Nt20` ensemble we used $\mathcal{O}(a)$-improvement of the axial current and the symmetrized derivative [see Eqs. (B.3-B.5)]. In contrast, the PCAC mass on `E250Nt16` (**right**) was determined using the unimproved version of the axial current.

advantage of the extensive plateaus observed in the $\hat{x}_3$ direction. We obtain

$$\begin{aligned} a \cdot m^{vac}_{\text{PCAC}} &= 0.001428(16)\,, \\ a \cdot m^{N_t 24}_{\text{PCAC}} &= 0.001466(41)\,, \\ a \cdot m^{N_t 16}_{\text{PCAC}} &= 0.001335(86)\,. \end{aligned} \tag{6.3.1}$$

In the hadronic phase and at the chiral phase transition, the extracted PCAC masses from the $\hat{x}_0$ direction are consistent with those obtained from the $\hat{x}_3$ direction, indicating minimal cut-off effects at this lattice spacing. However, the temporal extent[3] of the high-temperature `E250Nt16` box is insufficient to align with the PCAC mass value derived from the spatial direction. Additionally, for the `E250Nt16` ensemble, the improved axial current was not utilized. The AP-correlator serves as an order parameter for chiral symmetry restoration and thus approaches zero in the chirally symmetric phase. Consequently, the correction term proportional to c_A in Eq. (B.5) becomes comparable in magnitude to the correlator itself in the chirally restored phase. For further details, we refer to Sec. G.

The PCAC mass, derived from an operator identity, is expected to remain invariant with respect to temperature. Nevertheless, in lattice units, the measured value of the PCAC mass, $a \cdot m^{N_t 20}_{\text{PCAC}} = 0.001003(90)$, deviates by a factor of approximately 1.5 compared to the corresponding vacuum box. Given that the PCAC mass is linked to the derivative of the AP-correlator, we compared the integrated autocorrelation time τ_{int} at a fixed source-sink separation $x_3/a = 10$ between the `E250Nt20` and `E250Nt24` boxes. As illustrated in Fig. 6.5, we encounter significant autocorrelation in this observable at the chiral crossover (further details are provided in Appendix D). Consequently, we will utilize the value of the $\mathcal{O}(a)$-improved PCAC mass derived from the `E250Nt24` ensemble in our subsequent analysis, as it is consistent within errors with the PCAC mass obtained from the vacuum ensemble.

[3] Due to periodic boundary conditions, we effectively have eight points in the time direction.

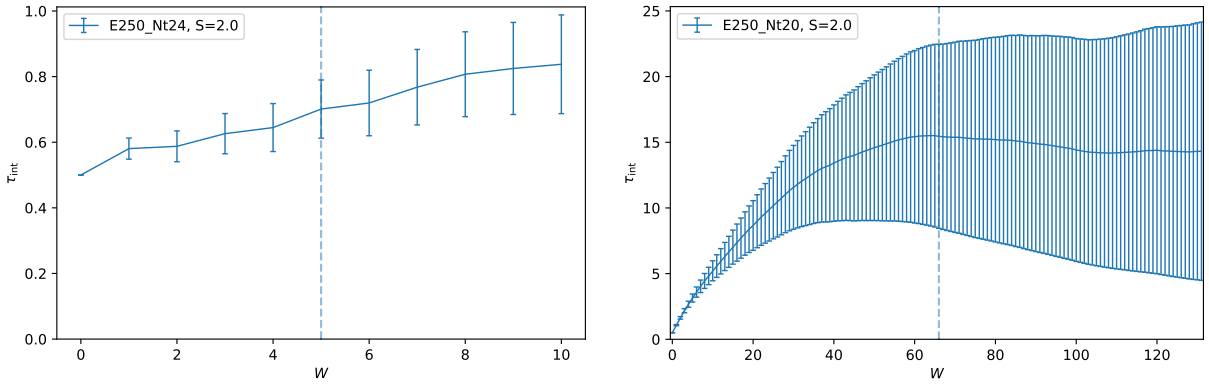

Figure 6.5: Comparison of the integrated autocorrelation times τ_{int} for the AP-correlator at fixed source-sink separation $x_3/a = 10$. The left hand side (l.h.s.) shows the correlator on the hadronic `E250Nt24` ensemble and the right hand side (r.h.s.) shows the correlator on the chiral crossover ensemble `E250Nt20`.

6.3.2 Static correlators: The Pion Screening Mass and Decay Constant

The pion screening decay constant, denoted as f_π, and the screening mass, represented by m_π, are defined through Eq. (6.2.5). To determine these parameters, we perform a simultaneous fit of the static screening pseudoscalar and the axial-pseudoscalar correlator, as detailed in Eq. (I.5). Appendix I elaborates on the calculation process, including effective mass plots.

The results are presented in Table 6.3 in units of the respective temperature. In physical units, they correspond to

$$\begin{aligned} m_\pi^{N\tau 24} &= 145(2)\,\text{MeV}\,, \\ m_\pi^{N\tau 20} &= 196(4)\,\text{MeV}\,, \\ m_\pi^{N\tau 16} &= 555(8)\,\text{MeV}\,. \end{aligned} \tag{6.3.2}$$

The pion screening decay constant is significantly reduced on all three ensembles compared to the decay constant $f_\pi^0 = 87.4(1.0)\,\text{MeV}$ on the corresponding zero-temperature ensemble [see Eq. (6.2.35)]. The values obtained are:

$$\begin{aligned} f_\pi^{N\tau 24} &= 73(1)\,\text{MeV}\,, \\ f_\pi^{N\tau 20} &= 26(2)\,\text{MeV}\,, \\ f_\pi^{N\tau 16} &= 5.9(4)\,\text{MeV}\,. \end{aligned} \tag{6.3.3}$$

The observables characterizing the properties of the pion quasiparticle across the chiral phase transition are summarized in Table 6.3.

6.3.3 Properties of the Pion Quasiparticle

The results for the estimators u_m and u_f, as defined in Eqs. (6.2.19) and (6.2.20), along with those of the screening quantities, are presented in Table 6.3. Good agreement is found between the two independent estimators u_f and u_m of the pion velocity, both in the hadronic and high-

Table 6.3: Summary of the results of the E250 thermal ensembles with $N_\tau \in \{24, 20, 16\}$. The static screening quantities m_π and f_π are defined by Eq. (6.2.5), and in practice have been computed according to Eq. (I.5). The two estimators u_f and u_m for the pion velocity parameter are defined in Eqs. (6.2.19)- and (6.2.20) and should agree in the broken phase up to higher-order effects in the chiral expansion. The pion quasiparticle mass $\omega_\mathbf{0}$ is calculated using $\omega_\mathbf{0} = u_m m_\pi$ and the corresponding decay constant using $f_\pi^t = f_\pi / u_m$.

Ensemble	E250Nt24	E250Nt20	E250Nt16
m_π/T	1.136(16)	1.250(24)	2.891(43)
f_π/T	0.569(4)	0.172(12)	0.0305(21)
u_f	0.831(3)	0.274(11)	0.0462(31)
u_m	0.807(9)	0.425(13)	0.0462(16)
u_f/u_m	1.028(10)	0.644(28)	1.001(76)
$\omega_\mathbf{0}/T$	0.917(15)	0.531(16)	0.133(4)
f_π^t/T	0.705(7)	0.405(18)	0.661(50)
$\mathrm{Res}(\omega_\mathbf{0})/T^4$	0.418(14)	0.0463(60)	0.0078(11)

temperature phases. Notably, both estimators deviate significantly from unity, indicating a clear violation of Lorentz invariance due to thermal effects. However, in the chirally restored phase, the interpretation of u as the pion velocity becomes invalid. Nevertheless, the ratio u_f/u_m is anticipated to remain finite in the chiral limit, as both u_f and u_m are proportional to the quark mass[4]. At the chiral crossover, u_f and u_m exhibit a significant discrepancy, with $u_f/u_m \approx 0.64$; for this estimate, we utilize the PCAC mass obtained from E250Nt24, as it is deemed more reliable. Thus, the interpretation as a pion velocity is already questionable at the chiral crossover, and we lack an explanation for the ratio u_f/u_m approaching unity in the high-temperature ensemble.

Furthermore, it was observed that the zero-temperature pion mass, as given in Eq. (6.2.34), 'splits' into a lower pion quasiparticle mass and a higher pion screening mass. For the former, we derive from the estimator $\omega_\mathbf{0} = u_m\, m_\pi$.

$$\omega_\mathbf{0}^{N_\tau 24} = 117(2)\,\mathrm{MeV}\,, \tag{6.3.4}$$

$$\omega_\mathbf{0}^{N_\tau 20} = 81(2)\,\mathrm{MeV}\,, \tag{6.3.5}$$

$$\omega_\mathbf{0}^{N_\tau 16} = 26(1)\,\mathrm{MeV}\,. \tag{6.3.6}$$

These values can be compared to the pion screening masses, as specified in Eq. (6.3.2). Notably, the decrease in $\omega_\mathbf{0}$ is particularly pronounced between the crossover point and our ensemble in the high-temperature phase.

The quasiparticle decay constant in the hadronic phase, $f_\pi^t = f_\pi/u_m = 90(1)\,\mathrm{MeV}$, is significantly closer to the vacuum decay constant $f_\pi^0 = 87(1)\,\mathrm{MeV}$ than to $f_\pi^{N\tau 24}$. At the chiral crossover, we determine $f_\pi^t = 62(3)\,\mathrm{MeV}$ ($f_\pi^t = 96(3)\,\mathrm{MeV}$ when using u_m derived from the PCAC mass on the E250Nt20 ensemble), and in the high-temperature phase, $f_\pi^t = 127(10)\,\mathrm{MeV}$.

[4]Indeed, m_π is of order unity, but f_π is of order m_q. In this context, we correct an erroneous statement made in Ref. [193].

Table 6.4: Dependence of the pion velocity estimator u_f on a finite pion thermal width $\Gamma(T)$ [see Eq. (6.3.7)] on the E250 thermal ensembles with $N_\tau \in \{24, 20, 16\}$.

$\Gamma(T)$ [MeV]	E250Nt24	E250Nt20	E250Nt16
5			0.0454(31)
10			0.0426(33)
15	0.825(3)	0.262(20)	0.0375(38)
20	0.819(3)	0.251(21)	0.0289(50)
30	0.806(3)	0.224(23)	
40	0.785(3)	0.177(28)	
80	0.626(6)		
100	0.472(10)		

6.3.4 Dependence of the Pion Velocity u_f on a Finite Pion Thermal Width $\Gamma(T)$

Son and Stephanov [191, 192] concluded that, at temperatures below the chiral phase transition, the imaginary part of the pion pole is parametrically small compared to its real part. In this subsection, we examine the sensitivity of our findings regarding the pion quasiparticle mass and the velocity parameter u to the assumption of a negligible thermal width of this quasiparticle. To assess the implications of a finite thermal pion width on the pion velocity u, we substitute the δ-distribution in Eq. (6.2.21) with a Breit-Wigner peak of width $\Gamma(T)$, resulting in

$$\rho_{A_0}(\omega, T) = f_\pi^2 m_\pi^2 \frac{\Gamma(T)}{\pi} \frac{1}{2\omega_\mathbf{0}} \left(\frac{1}{(\omega - \omega_\mathbf{0})^2 + \Gamma(T)^2} - \frac{1}{(\omega + \omega_\mathbf{0})^2 + \Gamma(T)^2} \right) + \dots , \tag{6.3.7}$$

where the second term is necessary to ensure the antisymmetry of the spectral function in ω [34]. By expressing the correlator midpoint of the time-dependent Euclidean correlator $G_{A_0}(\beta/2, T)$ in terms of the spectral function ρ_{A_0} using Eq. (6.2.15) and employing $\omega_\mathbf{0} = u_f m_\pi$, one can extract the pion velocity u_f for various thermal pion widths. The results are presented in Table 6.4.

Our analysis reveals that the extracted estimator of the pion velocity in the hadronic phase, $u_f = 0.831(3)$, assuming the presence of a discrete delta term in the spectral function, aligns with the Breit-Wigner approach up to pion thermal widths $\Gamma(T) \approx 15\,\text{MeV}$. At the chiral crossover, the estimate assuming a vanishing width, $u_f = 0.274(11)$, is consistent with the estimation of u_f assuming a pion thermal width of up to $\approx 20\,\text{MeV}$.

6.4 Spectral Function Reconstruction with the Backus-Gilbert Method

To extract the spectral function $\rho_{A_0}(\omega)$ at zero momentum from the corresponding temporal Euclidean correlator, $G_{A_0}(\tau_i, T)$, $\tau \equiv \tau$, it is necessary to invert the analogue for G_{A_0} of Eq. (6.2.15) with a kernel $K(\tau_i, \omega) = \cosh(\omega(\beta/2 - \tau_i))/\sinh(\omega\beta/2)$. This process presents a numerically ill-posed problem. One potential solution to this challenge is the Backus-Gilbert method [216]. We utilize the notation from Ref. [194], where this method was first applied to lattice QCD. Notably, this approach does not require a specific ansatz for the spectral function. The Backus-Gilbert method provides an estimator for the smeared axial spectral function, $\hat{\rho}$. It is advantageous to introduce a rescaling function $f(\omega)$, with $\lim_{\omega\to 0} f(\omega)/\omega$ finite and $f(\omega) > 0$ for $\omega > 0$, and to express $K^f(\tau, \omega) = f(\omega)K(\tau, \omega)$. The values of $\hat{\rho}$ are then constructed linearly from the lattice

correlator data $G(\tau_i)$,

$$\frac{\hat{\rho}(\bar{\omega})}{f(\bar{\omega})} = \sum_{i=1}^{N_p} q_i(\bar{\omega}) G(\tau_i) = \int_0^\infty \mathrm{d}\omega\, \hat{\delta}(\bar{\omega},\omega)\frac{\rho(\omega)}{f(\omega)}\,. \tag{6.4.1}$$

It is important to note that the coefficients q_i are contingent upon a reference value $\bar{\omega}$, around which the resolution function is concentrated, as expressed in the following equation:

$$\hat{\delta}(\bar{\omega},\omega) = \sum_{i=1}^{N_\tau} q_i(\bar{\omega}) K^f(\tau_i,\omega)\,. \tag{6.4.2}$$

The coefficients q are selected such that the resolution function is normalized according to the condition:

$$\int_0^\infty \mathrm{d}\omega\, \hat{\delta}(\bar{\omega},\omega) = 1\,. \tag{6.4.3}$$

Although the final coefficients q are affected by the choice of f, and the functions $\hat{\rho}$ and $\hat{\delta}$ are similarly dependent, this dependence is not explicitly indicated to avoid overcluttering the notation. The optimal resolution function is ideally represented by a Dirac delta distribution centered at $\bar{\omega}$. To achieve a resolution function that is as sharply centered around $\bar{\omega}$ as possible, we employ the strategy of minimizing the second moment of its square, in compliance with the constraint specified in Eq. (6.4.3). To prevent the emergence of widely oscillating coefficients $q_i(\bar{\omega})$, the quadratic form to be minimized is regulated by the covariance matrix $\mathrm{Cov}[G]$ of the Euclidean correlator. We define the following expressions:

$$R_i = \int_0^\infty \mathrm{d}\omega\, K^f(\tau_i,\omega), \tag{6.4.4}$$

$$W_{ij}(\bar{\omega}) = \int_0^\infty \mathrm{d}\omega\, K^f(\tau_i,\omega)(\omega-\bar{\omega})^2 K^f(\tau_j,\omega), \tag{6.4.5}$$

$$W^{\mathrm{reg}}(\bar{\omega}) = \lambda W(\bar{\omega}) + (1-\lambda)\mathrm{Cov}[G]\ , \tag{6.4.6}$$

where $0 < \lambda < 1$. The function to be minimized is given by $\mathcal{F}_\alpha(q) = (q, W^{\mathrm{reg}} q) - \alpha((q,R)-1)$, leading to the result

$$q(\bar{\omega}) = \frac{1}{(R, W^{\mathrm{reg}}(\bar{\omega})^{-1}R)}\, W^{\mathrm{reg}}(\bar{\omega})^{-1}R\,. \tag{6.4.7}$$

In the analysis of $\hat{\rho}_{A_0}$, we select the function

$$f(\omega) := \tanh(\beta\omega/2). \tag{6.4.8}$$

The values of λ mentioned below are expressed in units where all dimensionful quantities are made dimensionless through appropriate powers of the temperature. Some examples for the resolution function $T\hat{\delta}(\bar{\omega},\omega)$ for different values of λ are presented in the left panel of Fig. 6.6. The right panel of Fig. 6.6 illustrates the smeared and rescaled axial spectral function $\frac{\hat{\rho}_{A_0}(\bar{\omega},T)}{f(\omega)\,T^2}$ with $\lambda = 10^{-3}$ for the hadronic `E250Nt24` ensemble. In addition, Fig. 6.7 illustrates the results on the `E250Nt20` (left panel) and `E250Nt16` ensemble (right panel). These findings demonstrate, in a model-independent manner, that the axial-charge correlator is predominantly influenced by low

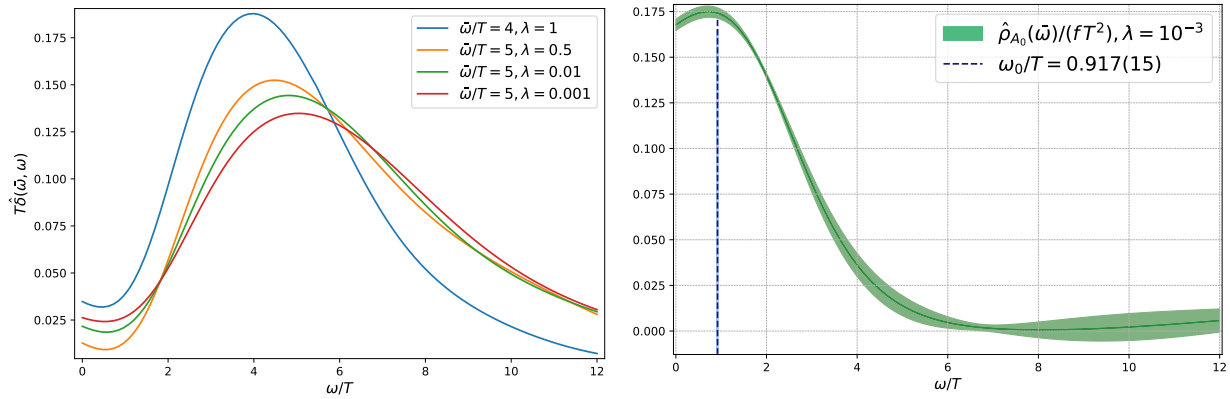

Figure 6.6: **Left panel**: Examples of resolution functions for different values of λ, centered around $\bar{\omega}/T$. **Right panel**: Estimator of the spectral function $\hat{\rho}_{A_0}(\omega, T = 128\,\mathrm{MeV})/(f\,T^2)$. The blue dashed line corresponds to the location of the expected position of the pole ω_0 according to Eq. (6.2.16). The temporal $G_{A_0}(\tau, T)$-correlator is $\mathcal{O}(a)$-improved.

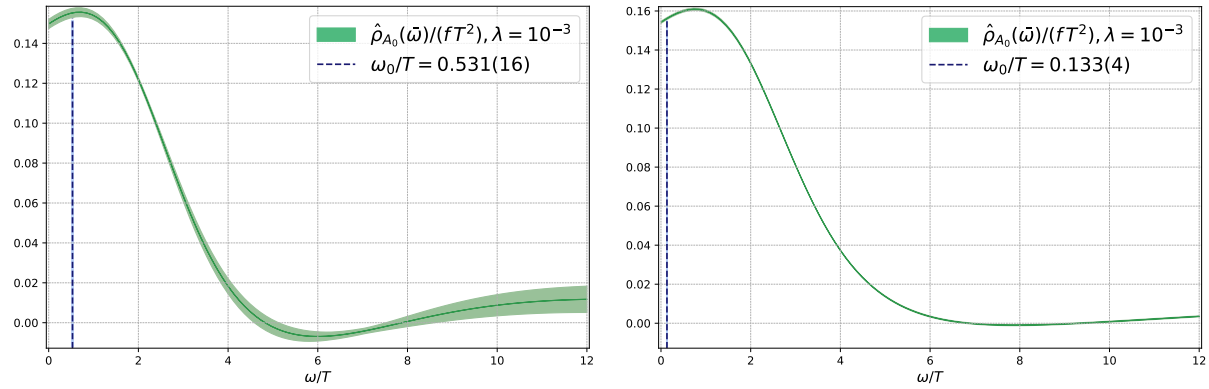

Figure 6.7: **Left panel**: Estimator of the spectral function $\hat{\rho}_{A_0}(\omega, T = 154\,\mathrm{MeV})/(f\,T^2)$. The blue dashed line corresponds to the location of the expected position of the pole ω_0 according to Eq. (6.2.16). The temporal $G_{A_0}(\tau, T)$-correlator is $\mathcal{O}(a)$-improved. **Right panel**: Estimator of the spectral function $\hat{\rho}_{A_0}(\omega, T = 192\,\mathrm{MeV})/(f\,T^2)$. The blue dashed line corresponds to the location of the expected position of the pole ω_0 according to Eq. (6.2.16).

frequencies. Furthermore, the predicted position of the quasiparticle mass ω_0 is close to the peak of the smeared spectral function in the hadronic regime.

Until now, we have indirectly determined the pion quasiparticle mass, denoted as ω_0, utilizing screening quantities and subsequently compared it to the pion pole position within the smeared axial spectral function $\hat{\rho}_{A_0}$. Our next objective is to predict the temporal axial correlator $G_{A_0}(\tau, T = 128\,\mathrm{MeV})$ using the screening quantities f_π and m_π. By employing Eqs. (6.2.15) and (6.2.21)-(6.2.22), we derive:

$$G_{A_0}(\tau, T) = \frac{\mathrm{Res}(\omega_0)}{2\omega_0} \frac{\cosh(\omega_0(\beta/2 - \tau))}{\sinh(\omega_0\beta/2)} + \cdots . \tag{6.4.9}$$

The outcome of this prediction, alongside the lattice data of the temporal $G_{A_0}(x_0, T)$-correlator and its corresponding fit result, is illustrated in the right panel of Fig. 6.8. Notably, the pre-

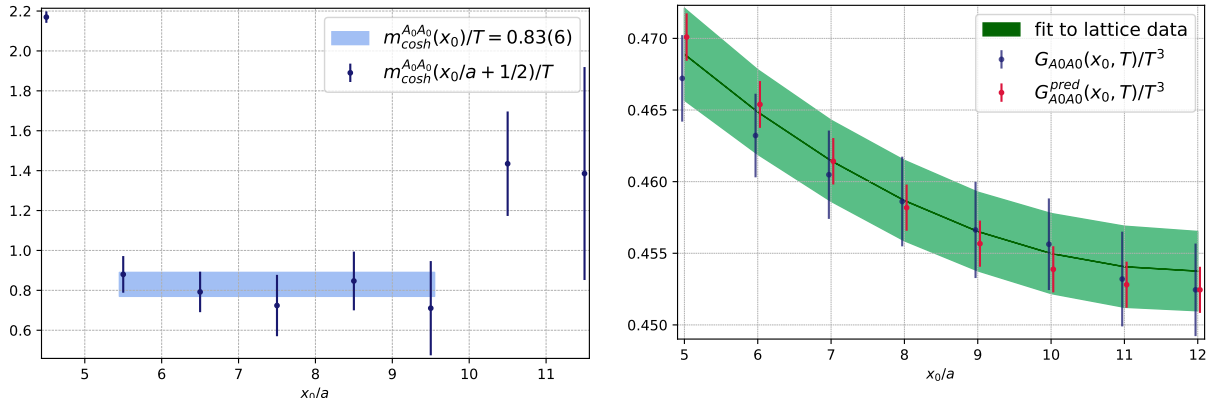

Figure 6.8: Both plots show results from the hadronic `E250Nt24` ensemble. **Left panel**: Effective mass plot for the cosh mass $m_{\cosh}(x_0)/T$ as a function of the x_0-coordinate in temperature units, obtained from the temporal axial correlation function at zero spatial momentum $G_{A_0}(x_0, T)$. **Right panel**: The blue bars correspond to the lattice data of the temporal $G_{A_0}(x_0, T)$-correlator in the hadronic phase, while the red bars represent the prediction of the aforementioned correlator in terms of the screening quantities f_π and m_π. The green band represents the result of a direct one-state fit to the temporal correlator. From this fit we obtain $\omega_\mathbf{0}/T = 0.91(9)$.

diction demonstrates excellent agreement with the lattice data, not only at the midpoint $\frac{\beta}{2}$ but across the entire range $x_0/a \geq 7$. The direct fit yields $\omega_\mathbf{0}/T = 0.91(9)$. As an additional verification, we directly determined the effective cosh mass from the temporal correlator, resulting in $m_{\cosh}(x_0)/T = 0.83(6)$ [see left panel of Fig. 6.8].

We want to emphasize that the three estimators for the pion pole mass in the hadronic phase, specifically:

- $\omega_\mathbf{0} = u_m m_\pi = 117(2)\,\text{MeV}$, obtained from the PCAC relation,
- $\omega_\mathbf{0} = 116(12)\,\text{MeV}$, obtained from a direct fit of the temporal correlator,
- $m_{\cosh}(x_0)/T = 106(8)\,\text{MeV}$, obtained as the effective mass of the temporal correlator,

are consistent with each other within errors. These estimators yield values that are significantly lower than the *in vacuo* pion mass value of $m_\pi^0 = 130(2)\,\text{MeV}$.

6.5 Comparison with Results from the Literature

In comparing our pion quasiparticle mass $\omega_\mathbf{0}(T)$ and quasiparticle decay constant $f_\pi^t(T)$ at $T = 128\,\text{MeV}$ with the corresponding quantities at zero temperature, we find $\omega_\mathbf{0}(T)/m_\pi^0 = 0.892(14)$ and $f_\pi^t(T)/f_\pi^0 = 1.023(10)$. This indicates a decrease in the quasiparticle mass at finite temperature, while the quasiparticle decay constant exhibits a slight increase. This behavior is consistent with findings from a ChPT calculation [see Ref. [189], Fig. 3 and Fig. 4] at two loops, where the reduction in the quasiparticle mass is approximately 0.9, and the quasiparticle decay constant increases by a factor of about 1.03. The decrease in the pion pole mass with temperature is further supported by a recent lattice-improved soft-wall AdS/QCD model study [217]. On the chiral crossover ensemble, we get $\omega_\mathbf{0}(T)/m_\pi^0 = 0.63(2)$ and $f_\pi^t(T)/f_\pi^0 = 0.69(3)$. In the high-temperature phase, the values are $\omega_\mathbf{0}(T)/m_\pi^0 = 0.17(1)$ and $f_\pi^t(T)/f_\pi^0 = 1.57(5)$.

Regarding the screening pion mass m_π, it is observed to increase with temperature relative to m_π^0, with a ratio of $m_\pi/m_\pi^0 = 1.105(14)$ at $T = 128\,\text{MeV}$. This increase is also qualitatively supported by the study of Son and Stephanov near the chiral phase transition [191]. On the chiral crossover ensemble, we find $m_\pi/m_\pi^0 = 1.460(27)$, while in the high-temperature phase ensemble, the ratio is $m_\pi/m_\pi^0 = 4.218(63)$.

In Ref. [218], the authors examined the pion damping width and the pion spectral function within the framework of a SU(2) Nambu-Jona-Lasinio (NJL) model for a few temperatures below the critical temperature $T_c^{\text{NJL}} = 190\,\text{MeV}$. They report that the peak position of the pion spectral function at vanishing momentum $\mathbf{p}$ shifts to the right with increasing temperatures $T/T_c^{\text{NJL}} \in \{0, 0.79, 0.89, 0.97\}$ [see Fig. 3 in Ref. [218]]. This finding contradicts our observation of a reduced pion pole mass at finite temperature. Utilizing a two-flavor effective field theory (EFT) inspired by the NJL model near the chiral crossover, the authors note that the parameter u [see Eqs. (6.2.19)-(6.2.20)] decreases with temperature below T_{pc}. Consequently, the pion pole mass decreases as the temperature increases below the crossover [see Fig. 4 in Ref. [219]]. However, they observe that above the crossover, the pion pole mass increases rapidly. The formalism for this finite temperature EFT was developed in Ref. [220].

In recent studies, as referenced in Refs. [203, 204] a superfluid effective theory has been formulated as a limit of "Model G". Starting in thermal equilibrium in the symmetric phase at $T > T_c$ the system is rapidly quenched into the broken phase at $T < T_c$. In doing so, the authors investigate the non-equilibrium dynamics of Goldstone bosons, finding a parametric enhancement over the equilibrium expectation of low-momentum pions due to a separation of scales, that is, due to ballistic transport before dissipative effects dominate. In this regime, the parameters of the superfluid are the pion screening decay constant and the axial isospin susceptibility, linked by the pion velocity.

6.6 Static Mesonic Screening Masses

In addition to the pseudoscalar screening mass m_π discussed in Sec. 6.3.2 we examine the static screening masses associated with the transverse vector and axial-vector correlators as defined in Eqs. (6.2.8)-(6.2.9). In particular, the difference between these correlators serves as an order parameter for chiral symmetry restoration. Furthermore, it is interesting to investigate the temperature above which the asymptotic exponential decay of these correlators corresponds to an isolated pole rather than a multi-pion continuum.

Thus, in this section, we present our findings on the screening masses in the pseudoscalar, vector, and axial-vector channels and compare them with those reported by the HotQCD collaboration [221]. The latter results were obtained using the highly improved staggered quark (HISQ) action, with a continuum extrapolation performed from a range of lattice spacings corresponding to $N_\tau = 6 - 16$. In contrast to Ref. [221], our results are limited to mesons of the type $u\bar{d}$. A direct comparison of the numerical values across the three channels is summarized in Table 6.5.

At $T = 128\,\text{MeV}$, we determine a pseudoscalar screening mass of $145(2)\,\text{MeV}$, which represents an increase of approximately 12 % compared to the pion mass in the corresponding vacuum ensemble [see Eq. (6.2.34)] and also relative to the HotQCD result of $129(5)\,\text{MeV}$, obtained at a slightly higher temperature of $T = 132\,\text{MeV}$. The HotQCD collaboration's results for the

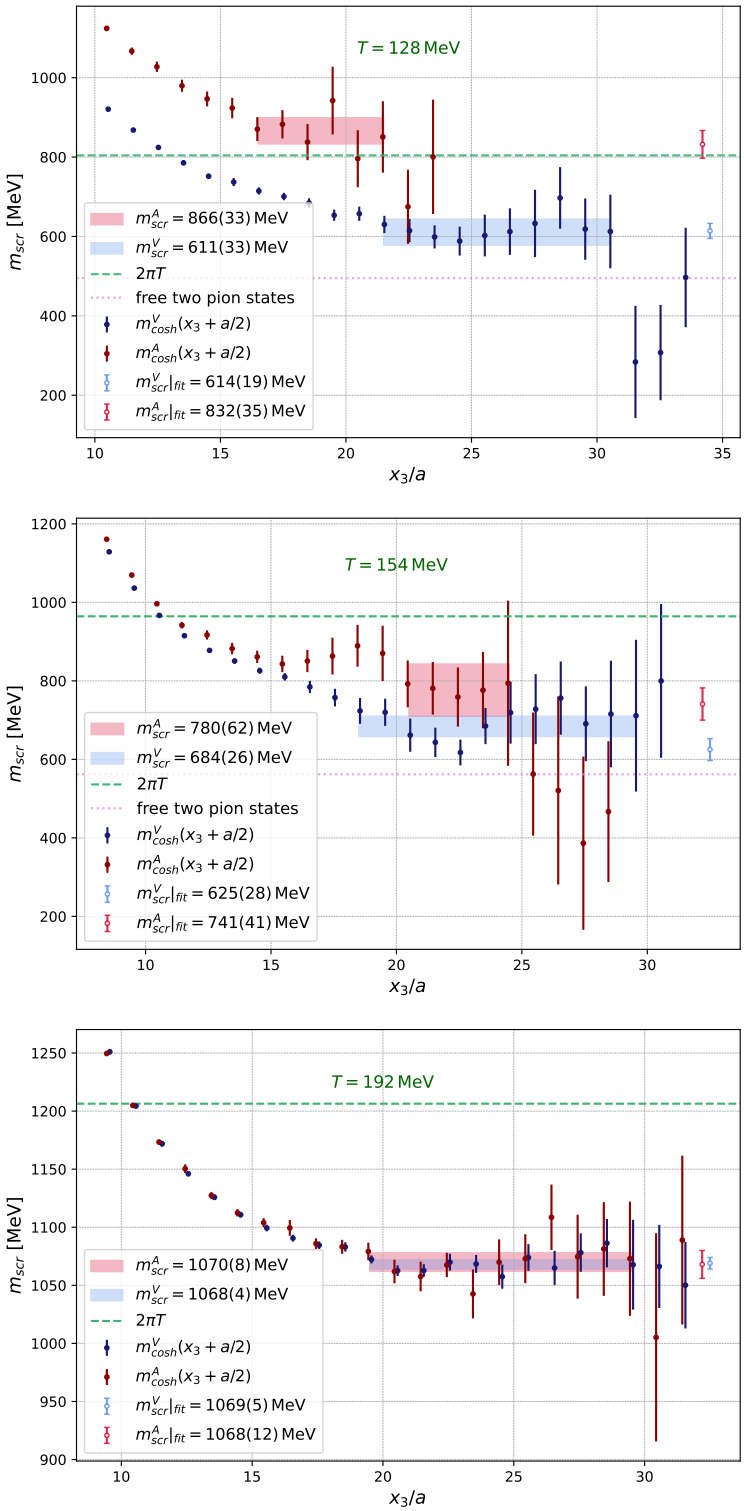

Figure 6.9: **Top panel**: Screening vector and axial-vector effective masses at $T = 128$ MeV. **Middle panel**: Screening vector and axial-vector effective masses at $T = 154$ MeV. **Bottom panel**: Screening vector and axial-vector effective masses at $T = 192$ MeV. The bands represent correlated fits to the plateau, while the green dashed line represents the $2\pi T$ limit. Furthermore, the values for the screening masses obtained from a direct fit of the axial-vector and vector correlators are also included and represented by a single light bar. The violet dotted line represents the free two-pion states (for $T = 128$ MeV and $T = 154$ MeV).

Table 6.5: Comparison of the screening masses in the $u\bar{d}$ channel extracted at temperatures $T \in \{128, 154, 192\}$ MeV to the continuum-extrapolated results obtained by the HotQCD collaboration [see Ref. [221], Table X].

	m^P_{scr} [MeV]		m^V_{scr} [MeV]		m^A_{scr} [MeV]	
Temperature [MeV]	HotQCD	this work	HotQCD	this work	HotQCD	this work
128	—	145(2)	—	614(19)	—	832(35)
132	129(5)	—	700(200)	—	1000(200)	—
152	187(2)	—	730(50)	—	850(40)	—
154	—	196(4)	—	625(28)	—	741(41)
156	202(3)	—	750(60)	—	830(60)	—
192	540(10)	555(8)	1020(40)	1069(5)	1040(30)	1068(12)

vector and axial-vector screening masses at the aforementioned temperature are 0.7(2) GeV and 1.0(2) GeV, respectively, and are consistent within errors with our results of 614(19) MeV and 832(35) MeV, respectively. The lightest vector and axial-vector mesons with $u\bar{d}$ valence quarks are the ρ meson, with a physical mass of 775 MeV, and the a_1 meson, with a physical mass of 1.23 GeV. It is noteable that both masses are significantly larger $[m_\rho / m^V_{scr} \approx 1.26, m_{a_1} / m^A_{scr} \approx 1.48]$ than the screening masses extracted from our $N_\tau = 24$ ensemble at $T = 128$ MeV in the hadronic phase. However, since the vector and axial-vector screening spectra commence with a continuum rather than an isolated pole, we also present the energies of free two-pion states.

$$E_{\pi\pi} = 2\sqrt{[m^P_{scr}(T)]^2 + \left(\frac{2\pi}{L}\right)^2}, \tag{6.6.1}$$

with a violet dotted line in Fig. 6.9.

Next, we compare our screening mass results obtained from the $N_\tau = 20$ ensemble near the pseudocritical temperature with the continuum-extrapolated results from the HotQCD collaboration. Regarding the pseudoscalar screening mass, our result $m^P_{scr}(T = 154\,\text{MeV}) = 196(4)$ MeV is in very good agreement with the HotQCD results of 187(2) MeV and 202(3) MeV at temperatures $T = 152$ MeV and $T = 156$ MeV, respectively. However, our vector screening mass $m^V_{scr}(T = 154\,\text{MeV}) = 625(28)$ MeV deviates by approximately 2σ from the HotQCD results of 730(50) MeV and 750(60) MeV at $T = 152$ MeV and $T = 156$ MeV, respectively. Furthermore, it is comparable within errors with our result obtained in the hadronic phase. Our axial-vector screening mass $m^A_{scr}(T = 154\,\text{MeV}) = 741(41)$ MeV also differs by approximately 2σ from the HotQCD result and is reduced by a factor of approximately 1.12 compared to our result at $T = 128$ MeV. Consequently, the ratio of the axial-vector to vector screening mass decreases from approximately 1.36 at $T = 128$ MeV to approximately 1.19 at $T = 154$ MeV.

Subsequently, we examine the screening masses extracted from the $N_{\tau=16}$ ensemble in the chirally-symmetric phase against the HotQCD collaboration's results. The pseudoscalar screening mass $m^P_{scr}(T = 192\,\text{MeV}) = 555(8)$ MeV is consistent within errors with the HotQCD result of 540(10) MeV at the same temperature. For the vector and axial-vector screening masses, we obtain 1069(5) MeV and 1068(12) MeV, respectively. Both screening masses are consistent within

errors with the HotQCD results of 1020(40) MeV and 1040(30) MeV, and their ratio is precisely one. Upon examining the effective mass plots presented in the lower panel of Fig. 6.9, we observe that the degeneracy of the vector and axial-vector screening masses at $T = 192\,\text{MeV}$ is evident not only in the plateau region but also individually (within errors) over an extended range of source-sink separations. However, at this temperature, the vector and axial-vector screening masses remain approximately 11% below the $2\pi T$ limit of screening masses. This high-temperature limit corresponds to the propagation of two quark quasiparticles in the thermal medium, each carrying a "mass" of πT corresponding to the first Matsubara mode.

Overall, while there is room for improvement in precision, the agreement between our calculation of static screening masses and that of the HotQCD collaboration is satisfactory, with the exception of the pion screening mass m_π in the low-temperature phase, where we find a value larger by about three standard deviations.

6.7 Isovector Quark Number Susceptibility

The QNS measures the response of the net quark number density to an infinitesimal change in the quark chemical potential. At vanishing chemical potential, it can be equivalently understood as representing the mean square fluctuation of the net quark number around zero per unit volume. It thus provides a measure of the number of degrees of freedom carrying a specific quantum number, specifically the third component of isospin in the context of this thesis.

On the lattice, we determine the QNS via

$$\delta^{ab}\chi_q(\tau,T) = 2Z_V^2(g_0^2)\,\beta \int \mathrm{d}^3x\,\langle V_0^a(\tau,\mathbf{x})\,V_0^b(0,\mathbf{0})\rangle\,, \qquad \tau \neq 0\,. \tag{6.7.1}$$

It is important to note that for the QNS, there is no need for any additive improvement of the vector current.

The results are presented in Fig. 6.10 in units of temperature. It is important to note that computing the isospin susceptibility does not involve contributions from disconnected diagrams. In Ref. [222] (see Table I) the QNS was determined as a function of temperature using 2+1 dynamical staggered quark flavors, and a continuum extrapolation was also performed. Their findings indicate that $\chi_q(T)/T^2 = 0.432(92)$ and $\chi_q(T)/T^2 = 0.481(87)$ for temperatures $T = 125\,\text{MeV}$ and $T = 130\,\text{MeV}$, respectively [see Table I of Ref. [222]]. Our result,

$$\chi_q(T)/T^2 = 0.485(7)\,, \qquad (T = 128\,\text{MeV}) \tag{6.7.2}$$

is consistent with both of these findings. At the crossover, our estimation of the QNS

$$\chi_q(T)/T^2 = 0.744(7)\,, \qquad (T = 154\,\text{MeV}) \tag{6.7.3}$$

exceeds their value, $\chi_q(T)/T^2 = 0.669(47)$ at a temperature $T = 155\,\text{MeV}$, by approximately 1.6σ. Furthermore, in the high-temperature phase, our estimate

$$\chi_q(T)/T^2 = 0.856(3)\,, \qquad (T = 192\,\text{MeV}) \tag{6.7.4}$$

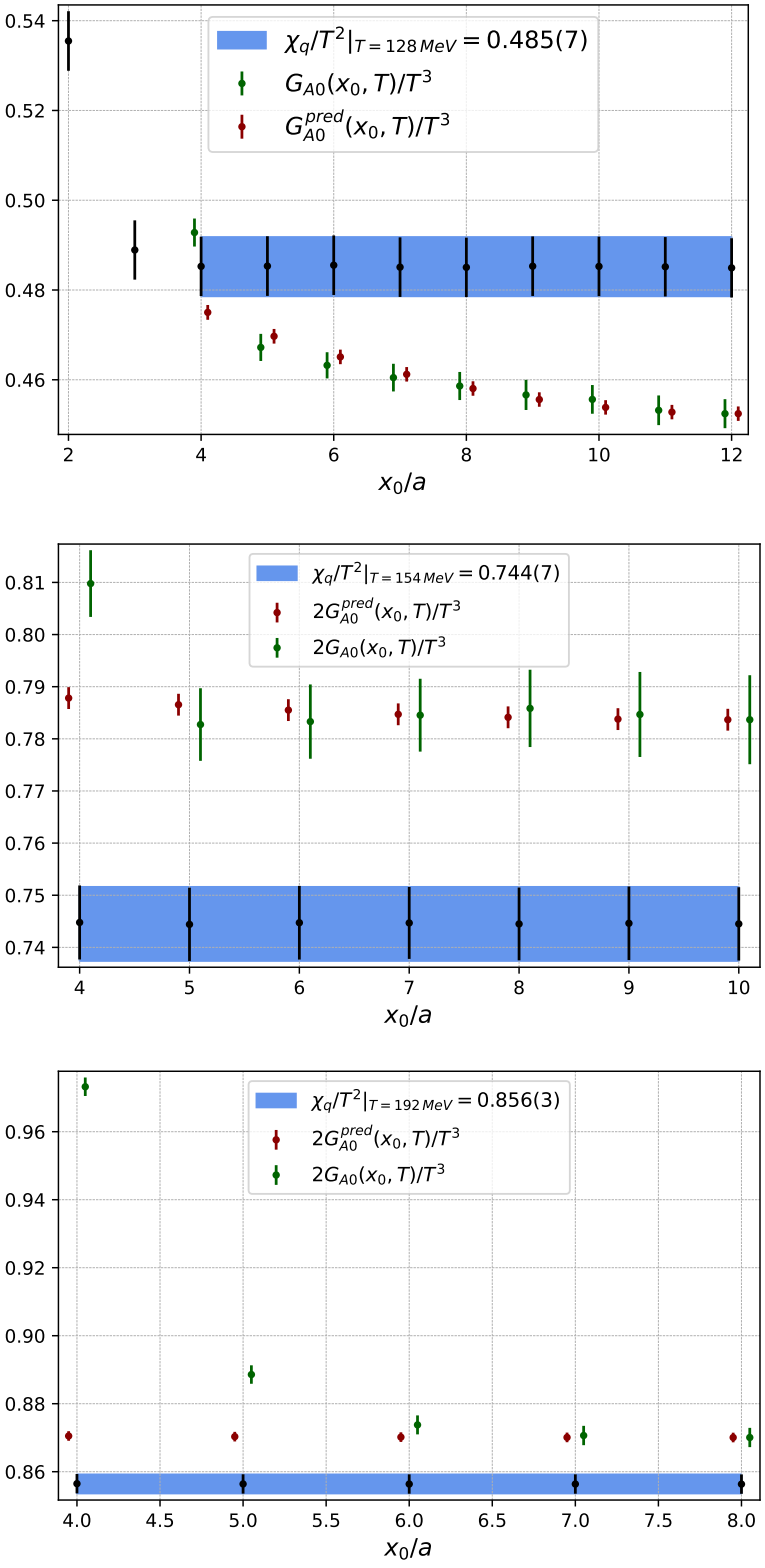

Figure 6.10: QNS extracted from the local vector current correlator, Eq. (6.7.1). For comparative purposes, $G_{A_0}(\tau, T)$ and its theoretical prediction based on screening quantities are presented. The top panel illustrates the QNS at a temperature of $T = 128\,\text{MeV}$, the middle panel at $T = 154\,\text{MeV}$, and the bottom panel at $T = 192\,\text{MeV}$. The correlators depicted in these figures follow the normalization specified in Eq. (6.7.1), which introduces an additional factor of 2, except for $G_{A_0}(\tau, T = 128\,\text{MeV})$, as noted in the legend, to enhance visibility.

lies above their result of $0.810(17)$ by approximately 2.7σ. However, note that our results have not been extrapolated to the continuum limit. For comparative purposes, the axial charge correlator $G_{A_0}(\tau, T)$ is also depicted in the plots. At $T = 128\,\text{MeV}$, the correlator exhibits a relatively flat profile; yet its magnitude is approximately twice that of the isospin charge correlator. Near the crossover at $T = 154\,\text{MeV}$, the axial charge correlator exceeds the isospin charge correlator by only 6%. Ultimately, at $T = 192\,\text{MeV}$, the two correlators are nearly indistinguishable. Although a continuum extrapolation was not conducted, our lattice spacing is approximately $2/3$ of the finest lattice spacing utilized in Ref. [222]. Consequently, in addition to the larger errors reported in Ref. [222], the presence of only small cut-off effects may also account for this observed agreement.

Next, we will compare our lattice estimate for the QNS with the HRG model and evaluate an alternative 'quasiparticle gas' model, which employs our modified dispersion relation for the pion quasiparticle.

6.7.1 Comparison with the Hadron Resonance Gas Model

The HRG model [87, 223] effectively characterizes the thermodynamic properties and the QNSs of the low-temperature phase. It assumes that the system's thermodynamic properties are determined by the aggregate of the partial contributions from non-interacting hadron species, as expressed by the following equation:

$$\ln[Z(T,V)] = -\frac{V}{2\pi^2}\sum_i \int_0^\infty \mathrm{d}p\, p^2 \ln[1 - \eta_i\, \mathrm{e}^{-\sqrt{m_i^2+\mathbf{p}^2}/T}]\,, \tag{6.7.5}$$

where $\eta_i = \pm 1$ accounts for bosons and fermions, respectively. The summation encompasses all resonances with masses up to 2.0 GeV, as for most of them, the width is not large compared to the temperature.

The QNS can be expressed as the sum [224]

$$\chi_q(T) = (\chi_q)_{\text{mesons}} + (\chi_q)_{\text{baryons}}\,, \tag{6.7.6}$$

where

$$\frac{(\chi_q)_{\text{mesons}}}{T^2} = \frac{2\beta^3}{3}\sum_{\text{multiplets}} (2J+1)I(I+1)(2I+1)\int \frac{\mathrm{d}^3\mathbf{p}}{(2\pi)^3}\, f_{\mathbf{p}}^B(1+f_{\mathbf{p}}^B)\,, \tag{6.7.7}$$

$$\frac{(\chi_q)_{\text{baryons}}}{T^2} = \frac{2\beta^3}{3}\sum_{\text{multiplets}} (2J+1)I(I+1)(2I+1)\int \frac{\mathrm{d}^3\mathbf{p}}{(2\pi)^3}\, f_{\mathbf{p}}^F(1-f_{\mathbf{p}}^F)\,, \tag{6.7.8}$$

and $f_{\mathbf{p}}^{B/F} = 1/[\mathrm{e}^{\beta\omega_{\mathbf{p}}} \mp 1]$ represent the Bose-Einstein and Fermi-Dirac distributions, respectively. The summations are conducted over all multiplets of spin J and isospin I that are distinct. Especially, particles and antiparticles must be considered separately, resulting in an additional factor of two in the baryon case and for mesons with strange quark constituents.

Utilizing Eqs. (6.7.7)-(6.7.8) within the HRG model and summing all resonances up to a mass of 2 GeV, we derive $\chi_q(T)/T^2 = 0.486$, which aligns precisely with our lattice estimate, Eq. (6.7.2). The relative composition of the total QNS is depicted on the l.h.s. of Fig. 6.11. The inclusion of resonances such as the $K_0^*(700)$, which possesses a full Breit-Wigner width of $(478 \pm 50\,\text{MeV})$,

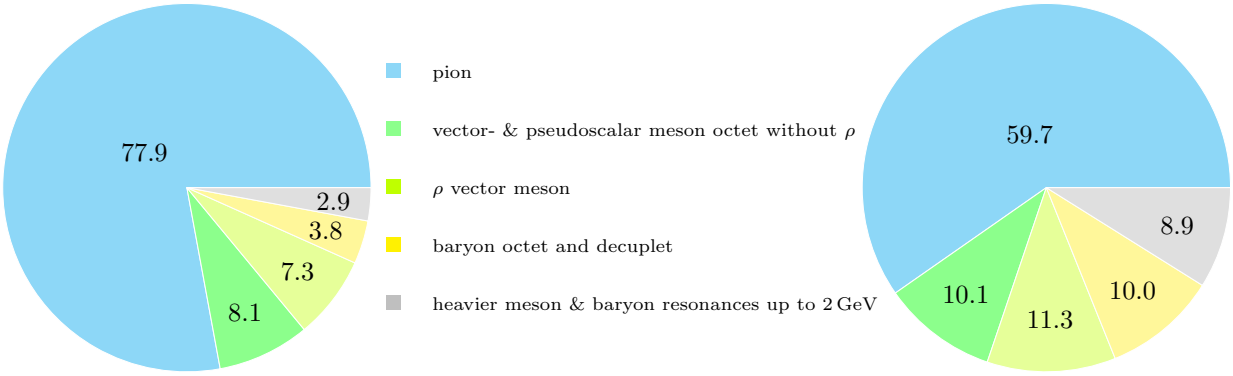

Figure 6.11: Relative composition of the total QNS predicted by the HRG model in the hadronic phase (**left panel**) and at the chiral crossover (**right panel**).

exceeding the temperature under consideration, remains questionable.

An alternative approach to the HRG model involves considering solely the pion contribution, while accounting for the modified dispersion relation (6.2.16) at low momenta:

$$\frac{\chi_q}{T^2} = 4\beta^3 \int_{|\mathbf{p}|<\Lambda_p} \frac{\mathrm{d}^3\mathbf{p}}{(2\pi)^3} f^B_{\mathbf{p}}(\omega_{\mathbf{p}})(1 + f^B_{\mathbf{p}}(\omega_{\mathbf{p}}))\,. \tag{6.7.9}$$

At this point, we only integrate up to the momentum cut-off $\Lambda_p = 400\,\mathrm{MeV}$ because it is not clear if the thermal width of the pion is still negligible for $|\mathbf{p}| > \Lambda_p$. Consequently, including contributions from higher momenta may not be justified. In Ref. [194] the authors have performed fits to the axial-charge density correlator at non-vanishing momenta. They then have compared the residue obtained from the fit parameters to the chiral prediction

$$\mathrm{Res}(\omega_{\mathbf{p}}) = f_\pi^2(m_\pi^2 + \mathbf{p}^2)(1 + b(\mathbf{p}))\,. \tag{6.7.10}$$

For $|\mathbf{p}| \approx 400\,\mathrm{MeV}$, a small value of $b = -0.08(3)$ was obtained, suggesting that the chiral effective theory description remains valid. To estimate our error, we present results for $\Lambda_p \in \{400, 500\}\,\mathrm{MeV}$. Utilizing Eq. (6.7.9) with $u_m = 0.807$, a screening pion mass $m_\pi = 145\,\mathrm{MeV}$, and $\Lambda_p = 400\,\mathrm{MeV}$, we derive $\chi_q(T)/T^2 = 0.402$, which is approximately 17% below the lattice estimate. Conversely, for $\Lambda_p = 500\,\mathrm{MeV}$, we obtain $\chi_q(T)/T^2 = 0.512$, which is approximately 5% above the lattice estimate. Notably, the sum over resonances is absent in this model. The contributions of other hadrons are indirectly accounted for via the modified dispersion relation, as the interactions of pions with themselves and other hadrons result in the modified pion dispersion relation.

Applying the HRG for the ensemble at the chiral crossover, we obtain $\chi_q(T)/T^2 = 0.701$, a result that is 5.8% below the lattice estimate. The relative composition of the total QNS predicted by the HRG model in this scenario is shown on the right part of Fig. 6.11. At both temperatures, the pion evidently dominates the contribution to the total QNS.

6.8 Order Parameters for Chiral Symmetry Restoration

In this section, several order parameters for chiral symmetry restoration are investigated. Based on the pion screening quantities m_π^2 and f_π^2 presented in Sec. 6.3, we initially evaluate an 'effective chiral condensate' based on the GOR relation. Additionally, we explore two Euclidean-time dependent thermal correlation functions that serve as order parameters for chiral symmetry and compare them to their zero-temperature equivalents. We begin with the (PA_0)-correlator, which encompasses the pion pole previously analyzed in Sec. 6.3. Subsequently, we consider the difference between the (isovector) vector and axial-vector correlators. In the QCD vacuum, the corresponding spectral functions are experimentally measured in τ decays [225]. These functions become degenerate in the chirally restored phase of QCD. Their temperature dependence in the chirally broken phase has been extensively studied within the framework of hadronic models augmented by sum rules [33, 226, 227].

6.8.1 The Gell-Mann–Oakes–Renner Relation

In accordance with Ref. [193], we introduce an 'effective chiral condensate' based on the GOR relation, expressed as follows:

$$C_{\mathrm{GOR}}^{\mathrm{GF}} \equiv -\frac{f_\pi^2 m_\pi^2}{m_\mathrm{q}}\,. \tag{6.8.1}$$

In the chiral limit, it is observed that $C_{\mathrm{GOR}}^{\mathrm{GF}} \to \langle\bar{\psi}\psi\rangle$. Furthermore, above the critical temperature T_c, where $m_\pi \sim T$ and $f_\pi \sim m_\mathrm{q}$, the expression $C_{\mathrm{GOR}}^{\mathrm{GF}}$ is of the order $\mathcal{O}(m_\mathrm{q}\,T^2)$. Consequently, it serves as an order parameter for chiral symmetry. By employing $m_\mathrm{q} = m_{\mathrm{PCAC}}$ [see Eq. (6.2.4)] and the screening quantities of Table 6.3 we derive the following results:

$$\begin{aligned}
\left|C_{\mathrm{GOR}}^{\mathrm{GF}}\right|^{1/3}_{T=128\,\mathrm{MeV}} &= 291(3)\,\mathrm{MeV}\,,\\
\left|C_{\mathrm{GOR}}^{\mathrm{GF}}\right|^{1/3}_{T=154\,\mathrm{MeV}} &= 180(8)\,\mathrm{MeV}\,,\\
\left|C_{\mathrm{GOR}}^{\mathrm{GF}}\right|^{1/3}_{T=192\,\mathrm{MeV}} &= 133(6)\,\mathrm{MeV}\,.
\end{aligned} \tag{6.8.2}$$

The value of the chiral condensate has been extracted in the gradient flow scheme analogous to the PCAC mass (cf. Sec. 6.2.4). By comparing this to the chiral condensate on the corresponding zero-temperature ensemble [208], we obtain

$$\begin{aligned}
\left[\frac{C_{T\approx 128\,\mathrm{MeV}}}{C_{T\approx 0\,\mathrm{MeV}}}\right]_{\mathrm{GOR}} &\equiv \frac{(f_\pi^2 m_\pi^2)_{T\approx 128\,\mathrm{MeV}}}{(f_\pi^2 m_\pi^2)_{T\approx 0\,\mathrm{MeV}}} = 0.84(3)\,,\\
\left[\frac{C_{T\approx 154\,\mathrm{MeV}}}{C_{T\approx 0\,\mathrm{MeV}}}\right]_{\mathrm{GOR}} &\equiv \frac{(f_\pi^2 m_\pi^2)_{T\approx 154\,\mathrm{MeV}}}{(f_\pi^2 m_\pi^2)_{T\approx 0\,\mathrm{MeV}}} = 0.21(3)\,,\\
\left[\frac{C_{T\approx 192\,\mathrm{MeV}}}{C_{T\approx 0\,\mathrm{MeV}}}\right]_{\mathrm{GOR}} &\equiv \frac{(f_\pi^2 m_\pi^2)_{T\approx 192\,\mathrm{MeV}}}{(f_\pi^2 m_\pi^2)_{T\approx 0\,\mathrm{MeV}}} = 0.08(1)\,.
\end{aligned} \tag{6.8.3}$$

The reduction in the hadronic phase corresponds to a 16% decrease. Notably, as the temperature increases from $T = 128\,\mathrm{MeV}$ to $T = 154\,\mathrm{MeV}$, the effective chiral condensate (normalized to its zero-temperature equivalent) decreases by a factor of four, reaching $0.21(3)$. At a temperature of

$T = 192\,\text{MeV}$, the effective chiral condensate attains a value of approximately 8% of its vacuum value. The reduction observed in the low-temperature phase is consistent, within the margin of error, with the three-loop result of Gerber and Leutwyler [see Ref. [187], Fig. 5].

6.8.2 The (PA_0)-Correlator

Reference [193] demonstrates that the temporal (PA_0)-correlator can be exactly predicted in the chiral limit.

$$G_{PA_0}(\tau, T) = \frac{\langle\bar{\psi}\psi\rangle}{2\beta}\left(\tau - \frac{\beta}{2}\right) . \tag{6.8.4}$$

Equation (6.8.4) demonstrates that the (PA_0)-correlator exhibits antisymmetry around $\beta/2$. Consequently, we assign the value zero to the point $\tau = \beta/2$. In our analysis, we have averaged the (PA_0)- and (A_0P)-correlators. The latter is derived by interchanging the source and sink.[5] Our findings indicate that the estimator based on the final expression of Eq. (6.2.12) exhibits a superior signal-to-noise ratio. Given that this correlator is proportional to the chiral condensate $\langle\bar{\psi}\psi\rangle$, it can also function as an order parameter for chiral symmetry restoration. Examining the ratio of the thermal to the reconstructed correlator, as obtained via Eq. (6.8.9), we observe that the reductions of the (PA_0) correlator align satisfactorily with the reductions obtained for the chiral condensate using the GOR relation [cf. Eq. (6.8.3)] across all three temperatures, specifically:

$$\lim_{\tau\to\beta/2}\frac{G_{PA_0}(\tau,T)}{G^{\text{rec}}_{PA_0}(\tau,T)} = \begin{cases} 0.817(21)\,, & N_\tau = 24 \\ 0.276(23)\,, & N_\tau = 20 \\ 0.088(5)\,, & N_\tau = 16. \end{cases} \tag{6.8.5}$$

The corresponding plots are presented in Fig. 30 in Appendix K.

6.8.3 Dey-Eletsky-Ioffe Mixing Theorem at Finite Quark Mass

In Refs. [228–230], it was demonstrated, utilizing PCAC current algebra, that near the chiral limit, the finite-temperature vector and axial-vector correlators can be described with the aid of their vacuum counterparts. In terms of the corresponding spectral functions, this assumption can be expressed as follows:

$$\rho_V(\omega,\mathbf{p},T) - \rho_A(\omega,\mathbf{p},T) = (1-2\epsilon(T))\left[\rho_V(\omega,\mathbf{p},T=0) - \rho_A(\omega,\mathbf{p},T=0)\right] , \tag{6.8.6}$$

while the sum $(\rho_V + \rho_A)$ does not receive a thermal correction at this order. The coefficient

$$\epsilon(T) \equiv \frac{T^2}{6(f_\pi^0)^2} , \tag{6.8.7}$$

is a temperature-dependent expansion parameter in powers of the pion density. More generally, based solely on symmetry arguments [see, for instance, Ref. [231]], the difference on the l.h.s. of Eq. (6.8.6) serves as an order parameter for chiral symmetry restoration. An estimate of the tem-

[5] This holds true exclusively for our vacuum correlators, which are derived from point-sources. For our finite temperature correlators, obtained from stochastic wall-sources, these are equivalent due to the symmetric source-sink setup employed.

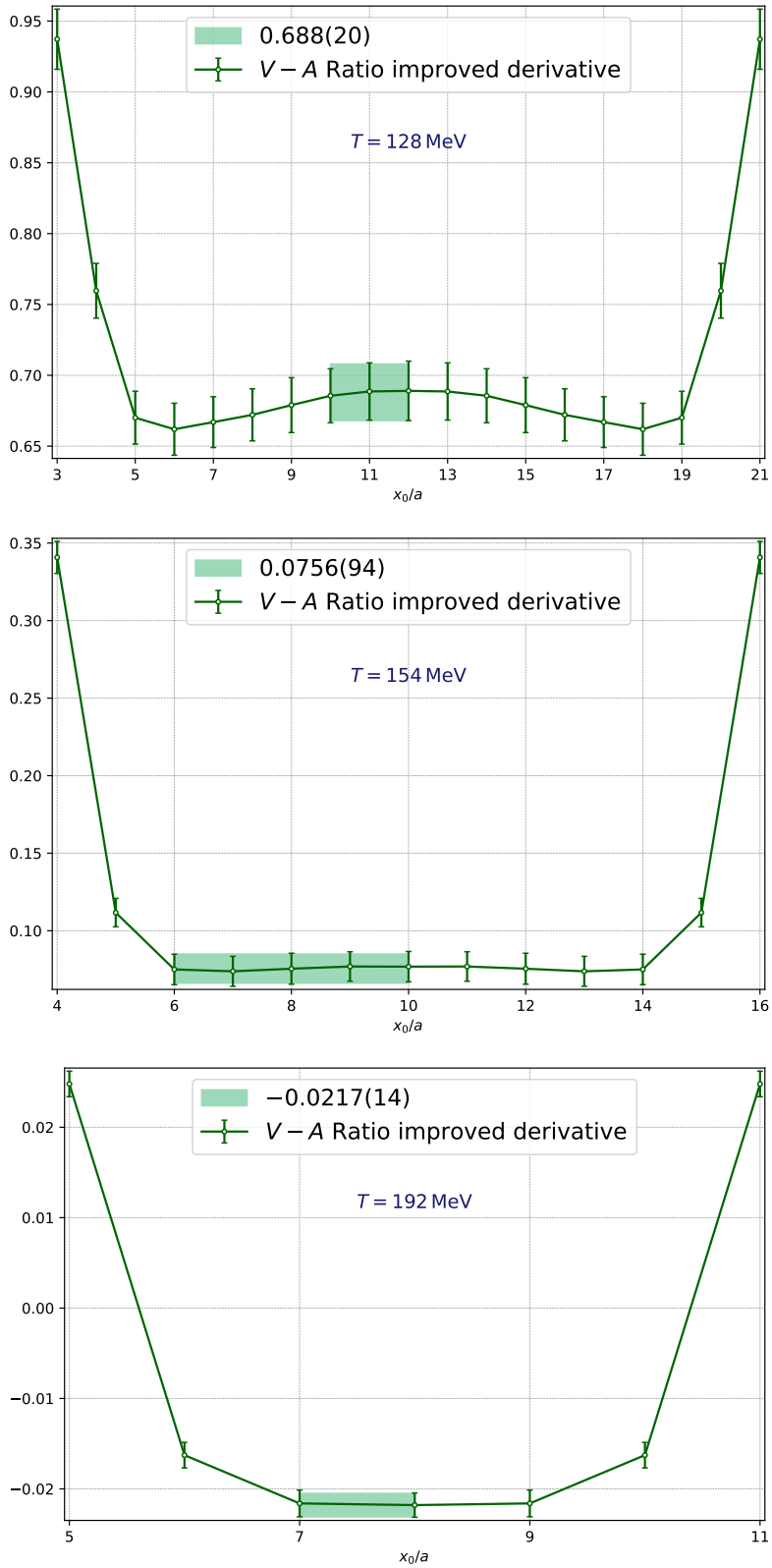

Figure 6.12: **Top panel**: Ratio of the difference '$V - A$' [see Eqs. (6.2.13)-(6.2.14)] and the difference of the reconstructed correlator '$(V - A)_{\text{rec}}$' [see Eq. (6.8.9)] at $T = 128$ MeV. **Middle panel**: Same quantity at $T = 154$ MeV. **Bottom panel**: Same quantity at $T = 192$ MeV. The green band shows the result of a correlated fit to the plateau.

perature for chiral symmetry restoration can be obtained by examining Eq. (6.8.6). For $\epsilon(T) = 1/2$, the ratio of the difference of the spectral function at finite temperature to the difference of the spectral function at zero temperature vanishes. This corresponds to the case of maximal mixing of the vacuum spectral functions. Using $\epsilon(T) = 1/2$ in Eq. (6.8.7), we derive a rough estimate of the chiral symmetry restoration temperature,

$$T_r = \sqrt{3} f_\pi^0 \,, \tag{6.8.8}$$

in terms of the pion decay constant. Employing the pion decay constant measured on the `E250Nt192` vacuum box [see Eq. (6.2.35)], we obtain $T_r \approx 151\,\text{MeV}$, while using $f_\pi^0 \approx 93\,\text{MeV}$ [97] yields $T_r \approx 161\,\text{MeV}$. Both estimates are remarkably close to the pseudocritical temperature $T_{pc} = 156.5(1.5)\,\text{MeV}$ [36].

Inspired by the Dey-Eletsky-Ioffe mixing theorem [228–230], we examine the difference $[G_V(\tau, \mathbf{p} = 0, T) - G_A(\tau, \mathbf{p} = 0, T)]$ at zero spatial momentum [see Eqs. (6.2.13)-(6.2.14)]. Utilizing the quasi zero-temperature `E250` ensemble with dimensions 192×96^3, we compute the 'reconstructed' correlator $G_V^{\text{rec}} - G_A^{\text{rec}}$ for this difference. This correlator can be interpreted as the thermal Euclidean correlator that would be realized if the spectral function remained unaffected by thermal effects during the transition from $T \approx 0$ to $T \in \{128, 154, 192\}\,\text{MeV}$. Following the methodology initially proposed in Ref. [232], we derive the reconstructed correlator as

$$G_J^{\text{rec}}(\tau, T, \mathbf{p}) = \sum_{m \in \mathbb{Z}} G_J(|\tau + m\beta|, 0, \mathbf{p}) \qquad (J = \{V, A, \dots\}). \tag{6.8.9}$$

It is based on the identity of the kernel function

$$\frac{\cosh(\omega(\beta/2 - \tau))}{\sinh(\omega\beta/2)} = \sum_{m \in \mathbb{Z}} \mathrm{e}^{-\omega|\tau + m\beta|} \,. \tag{6.8.10}$$

The difference '$V - A$' for the thermal ensembles is depicted on the l.h.s. of Fig. 31 in Appendix K, while the r.h.s. illustrates the corresponding reconstructed correlators derived from the $T \approx 0$ ensemble employing Eq. (6.8.9). In both cases, renormalization factors are incorporated in accordance with Eqs. (C.4)-(C.5). Additionally, the vector current has been $\mathcal{O}(a)$-improved[6] using the improved derivative defined in Eq. (B.4). The top two panels present the relevant correlator difference '$V - A$' at $T = 128\,\text{MeV}$, the middle panels at $T = 154\,\text{MeV}$, and the bottom panels at $T = 192\,\text{MeV}$. Notably, we are completely dominated by the error on the corresponding vacuum ensemble. The ratios of the thermal and reconstructed correlators are illustrated in Fig. 6.12. It is immediately evident that the ratio significantly deviates from unity at all three temperatures, despite the expectation that the ratio should approach unity as $\tau \to 0$ for $m_q \neq 0$. Considering the physical interpretation of the reconstructed correlator provided above Eq. (6.8.9), we can infer that the corresponding spectral function must also have undergone changes during the transition from $T \approx 0$ to $T \in \{128, 154, 192\}\,\text{MeV}$.

As Eq. (6.8.6) is obtained in the chiral limit, one would not necessarily expect to see a drop to a constant value in the ratio even for finite quark masses. However, as shown in Fig. 6.12, we

[6] The axial-vector current is inherently $\mathcal{O}(a)-$improved as the spatially integrated improvement term vanishes in this case. Conversely, for the vector current, the term $\propto T_{i0}$ contributes in the improvement process [cf. Eqs. (B.5)-(B.6)].

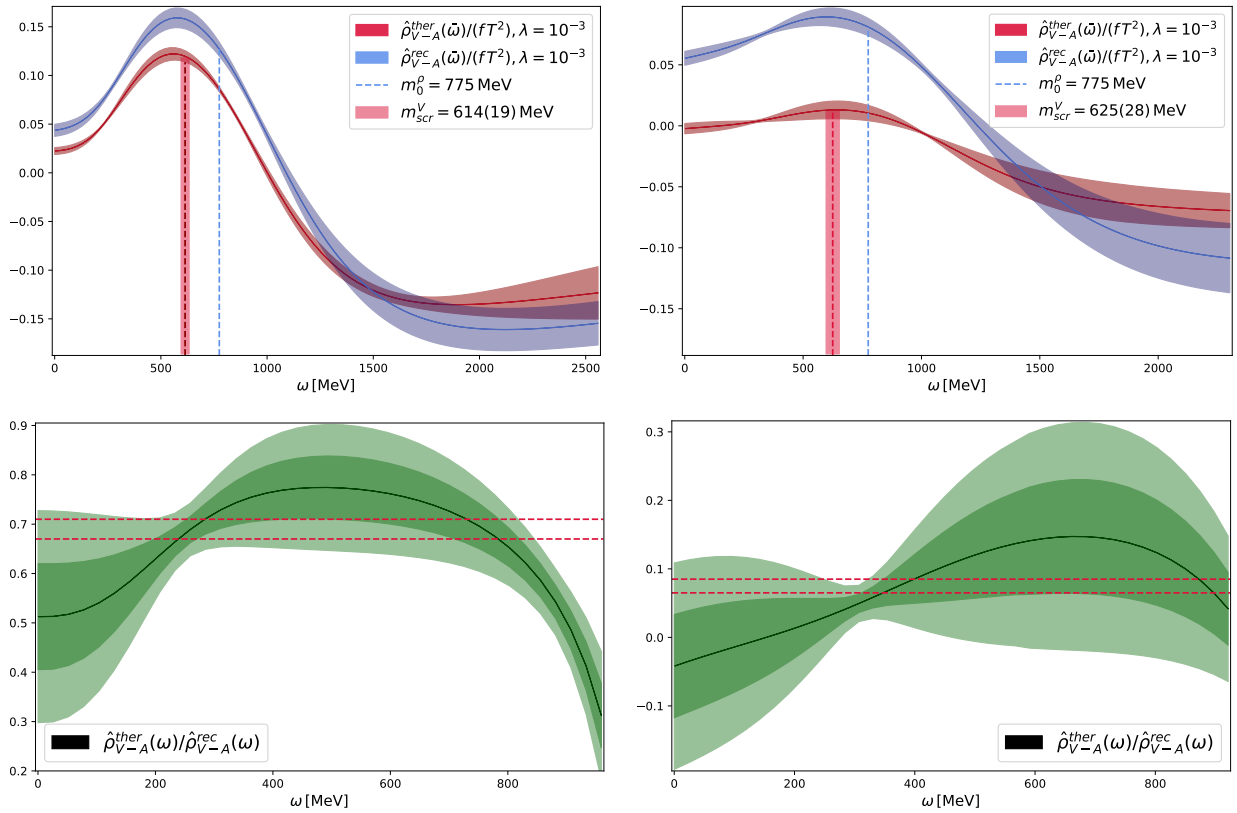

Figure 6.13: **Top panel**: The Backus-Gilbert analysis of the difference between the vector and axial-vector channels, as defined in Eqs. (6.2.13)-(6.2.14), is presented. The Backus-Gilbert spectral function $\hat{\rho}^{\text{rec}}_{V-A}(\omega)/(f\,T^2)$, derived from the reconstructed '$V-A$' correlator, is depicted as a blue band at temperatures of $T = 128\,\text{MeV}$ and $154\,\text{MeV}$ for the left and right panels, respectively. The corresponding estimator of the thermal spectral function $\hat{\rho}^{\text{ther}}_{V-A}(\omega)/(f\,T^2)$ is illustrated as a red band. For reference, the blue vertical line indicates the physical mass of the ρ meson, while the red vertical line denotes the vector screening mass at the respective temperature [see Table 6.5]. The underlying temporal vector correlators are $\mathcal{O}(a)$-improved.
Bottom panel: The ratio of the estimators of the thermal and reconstructed spectral functions is shown, accompanied by the $1-\sigma$ band (dark green) and the $2-\sigma$ band (light green). The red horizontal dashed line represents the $1-\sigma$ band at the correlator level [see top and middle panel of Fig. 6.12].

observe a flat behavior around the midpoint[7] at $T = 128\,\text{MeV}$ and $T = 154\,\text{MeV}$. In particular in the $N_\tau = 20$ ensemble the ratio is almost constant in the range $6 \leq \tau/a \leq 10$. In the hadronic phase, we read off a reduction to a factor $0.69(2)$ indicating that chiral symmetry restoration is already at an advanced stage in the hadronic phase [see top panel of Fig. (6.12)]. During the transition from $T = 128\,\text{MeV}$ to $T = 154\,\text{MeV}$ the ratio in the '$V-A$' channel drops drastically by a factor of ≈ 9 down to a reduction factor of $\approx 0.08(1)$. This is confirmed by inspecting the smoothed '$V-A$' spectral function obtained from the Backus-Gilbert method in Fig. 6.13. Increasing the temperature further to $T = 192\,\text{MeV}$, well in the chirally symmetric phase, the ratio even becomes slightly negative (≈ -0.02). In consequence of the short extent in the time direction,

[7] Given that chiral symmetry restoration is a long-distance phenomenon, it is anticipated that for physical quark masses, the suppression of the '$V-A$' spectral function predominantly occurs at low energies. This corresponds to the longest accessible (Euclidean) time.

cut-off effects could be responsible for this behavior.

In summarizing our findings, we observe that at temperatures $T \in \{128, 154, 192\}$ MeV, the 'effective chiral condensate', derived from static screening quantities, is reduced to $\{0.84(3), 0.21(3), 0.08(1)\}$ times the value at the corresponding vacuum ensemble. These values are consistent within errors with the reduction to $\{0.817(21), 0.276(23), 0.088(5)\}$ times the value at the corresponding vacuum ensemble observed in the temporal (PA_0)-correlator, which, in the chiral limit, is proportional to the chiral condensate. Notably, in both the low- and high-temperature phases, these two predictions exhibit strong agreement. These reduction factors can be compared to the reduction in the temporal '$V - A$' sector. While the reduction to 0.69(2) times the vacuum value at $T = 128$ MeV is comparable, we find that during the transition to the crossover region, chiral symmetry restoration appears to occur more rapidly. At $T = 154$ MeV, the reduction factor in the '$V - A$' sector is smaller by a factor of approximately 4. As the temperature increases further to $T = 192$ MeV, the ratio in the PA_0-channel decreases to approximately 0.09, while the ratio in the temporal '$V - A$' channel is consistent with zero.

The varying rates at which different order parameters of chiral symmetry breaking approach zero are already evident in predictions from chiral perturbation theory at vanishing quark masses. Specifically, the suppression of the chiral condensate to leading order in T^2 follows the relation $1 - \frac{T^2}{8(f_\pi^0)^2}$ [see Ref. [187, 233]] and is therefore less pronounced relative to Eq. (6.8.6) with $1 - 2\epsilon = 1 - \frac{T^2}{3(f_\pi^0)^2}$ [228].

6.9 Vacuum Subtracted Vector and Axial-Vector Spectral Functions

Utilizing the Backus-Gilbert method as delineated in Sec. 6.4, we present an estimator for the smeared spectral function, which represents the difference between the finite temperature and reconstructed zero-temperature temporal vector correlators, projected to zero momentum. For the analysis of vacuum-subtracted spectral functions, we employ the rescaling function defined as

$$f_2(\omega) := \omega. \tag{6.9.1}$$

The outcomes of the smeared and rescaled spectral functions are depicted in Fig. 6.14.

The difference

$$\Delta\rho_V(\omega, \boldsymbol{p}, T) \equiv \rho_V(\omega, \boldsymbol{p}, T) - \rho_V(\omega, \boldsymbol{p}, T = 0)\,, \tag{6.9.2}$$

between the spatial components of the finite and zero-temperature spectral functions satisfies the sum rule [234]

$$\int_0^\infty \frac{\mathrm{d}\omega}{\omega}\, \Delta\rho_V(\omega, \mathbf{0}, T) = 0\,, \tag{6.9.3}$$

in the thermodynamic limit. According to the operator-product expansion (OPE), the difference in Eq. (6.9.2) falls off as $1/\omega^2$ for large frequencies ω [235]. Applying the sum rule to our smeared spectral function derived from the Backus-Gilbert method, Eq. 6.9.3 evaluates to $-0.30(29)$ at $T = 128$ MeV, $-0.46(37)$ at $T = 154$ MeV, and 0.44(1) at $T = 192$ MeV. Consequently, the sum rule is satisfied within the substantial errors at the lower two temperatures. In the high-temperature phase, the sum rule is not satisfied. However, it is important to emphasize that owing to the limited temporal extent of the `E250Nt16` ensemble, we were restricted to using $4 \leq \tau/a \leq 8$ for

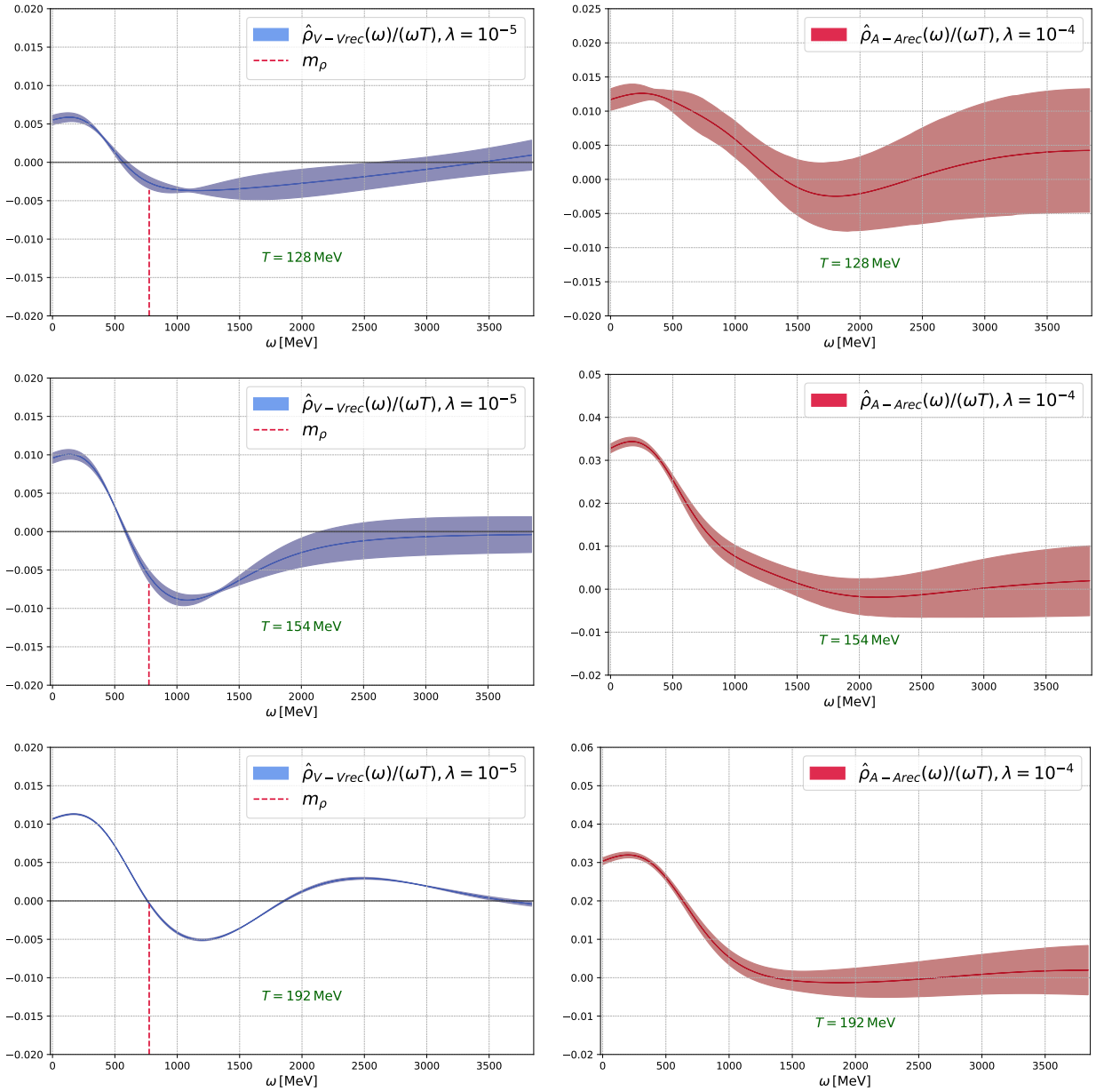

Figure 6.14: **Top panels**: The l.h.s. shows the smeared spectral function of the difference between the finite temperature and reconstructed zero-temperature temporal vector correlators [defined in Eq. (6.2.14))] projected to zero momentum at a temperature $T = 128$ MeV. The r.h.s shows the same quantity for the temporal axial-vector correlators [defined in Eq. (6.2.13)] projected to zero momentum. **Middle panels**: The same quantities at a temperature $T = 154$ MeV. **Bottom panels**: Again the same quantities at a temperature $T = 192$ MeV.

the spectral function reconstruction. Therefore, this result should be taken with a grain of salt.

For the thermal modification of the axial-vector channel, we have the spectral representation

$$2\int_0^\infty \frac{\mathrm{d}\omega}{\omega}\,\Delta\rho_A(\omega,\boldsymbol{p},T) = \int_0^\beta \mathrm{d}\tau\, G_A(\tau,\boldsymbol{p},T) - \int_{-\infty}^\infty \mathrm{d}\tau\, G_A(\tau,\boldsymbol{p},0). \tag{6.9.4}$$

Close to the chiral limit, we can saturate the correlation functions on the r.h.s. at the zero four-momentum by the screening pion, leading to the sum rule

$$2\int_0^\infty \frac{\mathrm{d}\omega}{\omega}\,\Delta\rho_A(\omega,\boldsymbol{0},T) = f_\pi^2(T=0) - f_\pi^2(T) + \mathcal{O}(m_q^2). \tag{6.9.5}$$

This bears resemblance to the first Weinberg sum rule [236] and its finite-temperature generalization [226]; however the integral on the l.h.s. of Eq. (6.9.5) remains convergent even when $m_q \neq 0$. We have observed that $f_\pi^2(T)$ is already considerably diminished at $T = 128\,\mathrm{MeV}$ and is of $\mathcal{O}(m_q^2)$ in the chirally restored phase. Consequently, the r.h.s. of Eq. (6.9.5) soon exhibits only a weak dependence on temperature. This qualitative behavior is corroborated by the numerical data presented in the right panels of Fig. 6.14. Given that $\Delta\rho(\omega,\boldsymbol{p},T) \sim 1/\omega^2$ at large ω, the sum rule implies that thermal effects contribute to the accumulation of spectral weight below the mass of the vacuum $a_1(1260)$ meson.

6.10 Conclusion

Utilizing lattice simulations at physical (u,d,s) quark masses, we have demonstrated that the real component of the low-energy pole in the two-point function of the axial charge diminishes as the temperature rises throughout the hadronic phase of QCD. We interpret this phenomenon as a reduction of the pion quasiparticle mass within the thermal medium. At our lowest temperature of 128 MeV, this effect corresponds to a ten percent reduction [cf. Eq. (6.3.4)]. This finding is obtainable because the pole representing the pion quasiparticle parametrically dominates both the Euclidean two-point functions of the axial charge and the pseudoscalar density at $\tau = \beta/2$ [cf. Fig. 6.8].

Above the crossover temperature, the pole in the axial-charge correlator is anticipated to exhibit a diffusive nature, wherein its imaginary part dominates over the real part. As the curvature in the Euclidean correlator of the axial charge is not parametrically dominated by the pole in the chirally restored phase, an inverse problem arises when attempting to ascertain the precise position of the pole. It is certain, however, that the pole approaches the origin, $\omega = 0$, in the chiral limit. Indeed, our calculations in the high-temperature phase indicate that the axial-charge correlator is nearly degenerate with the (temporally constant) isospin-charge correlator [cf. bottom panel of Fig. 6.10].

Our findings further indicate that the static pseudoscalar correlation length, denoted as m_π^{-1}, consistently decreases with increasing temperature, as corroborated by Eq. (6.3.2) and in alignment with prior lattice calculations. The corresponding 'decay constant' f_π, defined in Eq. (6.2.5) as the coupling of the spatial longitudinal axial current to this correlation length, also exhibits a steady decline with increasing temperature [cf. Eq.(6.3.3)]. Parametrically, it is of order of the quark mass in the chirally restored phase. Additionally, we have calculated the spatially trans-

verse vector and axial-vector static screening lengths, which largely concur with the findings of the HotQCD collaboration [see Sec. 6.6].

The combination $f_\pi^2 m_\pi^2 / m_\mathrm{q}$ serves as an estimator for the condensate $\langle -\bar{\psi}\psi \rangle$ in the chiral limit. We have calculated the ratio of $f_\pi^2 m_\pi^2$ to its vacuum value as an indicator of the 'melting' of the chiral condensate [cf. Eq. (6.8.3)]. This ratio was compared with an alternative estimator derived from the temporal correlation function of the axial-charge with the pseudoscalar density, and the results were found to be consistent [cf. Eq. (6.8.5)].

We have constrained the thermal modification of the vector and axial-vector spectral functions by constructing the difference between the thermal and the 'reconstructed' correlator, i.e., the correlator that would be realized at finite temperature if no change occurred in the spectral function [see Sec. 6.9]. This approach has been previously employed in a two-flavor calculation with $m_\pi \simeq 270\,\mathrm{MeV}$ [224]; however, the present study is the first to operate at physical quark masses around the crossover temperature. Utilizing the Backus-Gilbert method to directly analyze the thermal change in the spectral function, we conclude that in the vector channel, there is an increase in spectral weight at low frequencies, while a depletion is observed around energies of 1 GeV. Such a change is consistent with the sum rule (6.9.3). In the axial-vector case, we observe a significant increase in thermal spectral weight up to 1 GeV; see Fig. 6.14.

Finally, we have investigated the difference of the thermal correlators for the spatial components of the vector and axial-vector currents at zero spatial momentum [see Sec. 6.8.3]. Phenomenologically, it is frequently studied in the context of dilepton production by the thermal medium [227]. This observed correlator difference serves as an order parameter for chiral symmetry as well and offers additional insights into its restoration. Notably, this correlator is already reduced by approximately two-thirds compared to its vacuum counterpart at our lowest temperature, $T \simeq 128\,\mathrm{MeV}$, and by more than an order of magnitude at the crossover temperature, $T \simeq 154\,\mathrm{MeV}$. The consistent behavior of this ratio aligns with an overall suppression factor of the '$V - A$' spectral function extending to relatively high energies [cf. Fig. 6.12]. This qualitative behavior was initially predicted at low temperatures in the chiral limit [228], and our findings confirm its validity as a good approximation at the correlator level up to the crossover.

Overall, our simulations, conducted at physical quark masses using $\mathcal{O}(a)$-improved Wilson fermions, have proven entirely feasible with current algorithmic techniques. We have observed extended autocorrelation times for the two-point correlation function of the axial-current with the pseudoscalar density at the chiral crossover [cf. Fig. 6.5], which is expected for an order parameter near a phase transition. Future simulations could be performed at finer lattice spacings to facilitate continuum extrapolations of the most important observables, such as the pion quasiparticle mass.

Part III

Probing The Photon Emissivity of the QGP without an Inverse Problem

Chapter 7

Theoretical Framework

In this chapter, we present the imaginary-momentum correlators required for the second part of the thesis, together with their lattice implementation. We also introduce the notation and provide basic definitions relevant to the photon emissivity of the QGP. Note that, in contrast to Part II, we denote the correlator decay direction by x_1 rather than x_3.

7.1 Introduction

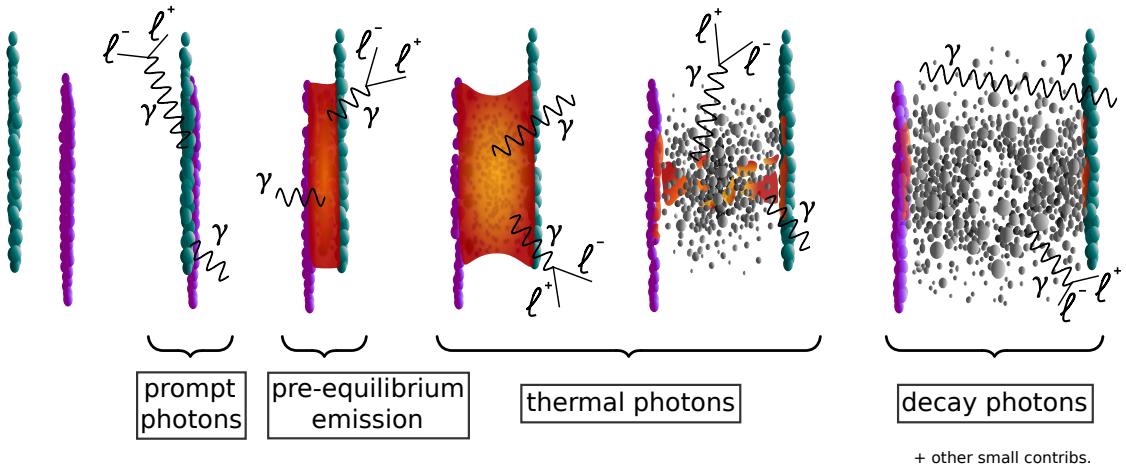

Figure 7.1: Sources of photons in a relativistic heavy ion collision. Figure is taken from Ref. [4] and was created by Csaba Török.

The radiation spontaneously emitted by a thermal medium provides valuable insights into its composition and dynamics. In the field of astronomy, for example, the spectral lines of interstellar gas serve as the primary source of information regarding its constituents and overall motion [237]. At asymptotically high temperatures, within a plasma of quasi-free quarks and gluons, photon emission occurs only when a quark undergoes a collision, rendering photon emissivity directly sensitive to interactions within the medium. In the context of relativistic heavy-ion collisions (RHIC), the system's brief lifespan prevents photon equilibration, allowing them to escape the QGP without re-scattering. Photons are emitted throughout the entire space-time evolution of the system, with the highest abundance occurring when the medium is at its hottest, complicating the task of disentangling their various sources [44].

Experimentally [238], photons are categorized into **decay photons**, which originate from the electromagnetic decays of long-lifetime final-state hadrons, and **direct photons**, produced at any stage of the collision prior to hadron freeze-out [see Fig. 7.1]. Among the latter, **prompt photons** are real photons generated directly in hard scattering processes between partons during the initial

stage of the collision, whereas **pre-equilibrium photons** arise from quarks and gluons that have scattered only a few times and have not yet reached a thermal distribution, i.e., before the system achieves thermalization. At transverse momenta[1] $1 < p_T/\text{GeV} < 3$, a significant contribution is anticipated from **thermal photons**, which are radiated both in the QGP and during the hadronic phase.

Transverse momentum-dependent yields and azimuthal anisotropies of direct photons have been extensively investigated in several RHIC experiments [239–248]. These observables are sensitive to photon production throughout the spacetime evolution of the matter produced in the collision, necessitating complex modeling of the system's expansion and cooling for accurate predictions. While data from the STAR experiment [246] generally align with theoretical models, measurements by the PHENIX and ALICE collaborations indicate an excess of direct photons at low transverse momenta, below a few GeV [242, 244, 247, 249]. In addition, these collaborations report a photon anisotropy, v_2, w.r.t. the reaction plane that exceeds hydrodynamic predictions [240, 243, 248]. Photons emitted during the later stages of the collision can acquire the collective flow of the strongly interacting medium from which they are emitted. Consequently, an increased emission rate in this regime could enhance the resulting anisotropy [250]. The persistent challenge for most models to simultaneously describe yields and anisotropies is commonly referred to as the *direct photon puzzle* [238, 249, 251].

These model predictions depend on theoretical estimates of the thermal photon emissivity, which is directly linked to the photon spectral function $\sigma(\omega)$. In the high-temperature phase, current phenomenological models rely on the weak-coupling calculation by Arnold, Moore, and Yaffe (AMY) [252, 253], whereas for the low-temperature phase, relativistic kinetic theory calculations within a hot meson gas have been utilized [254, 255]. The precise method of connecting these predictions near the pseudo-critical temperature T_{pc} remains uncertain, leading to the use of interpolations between these two regimes. This uncertainty in the vicinity of the transition motivates lattice QCD studies, which can provide non-perturbative input directly relevant for heavy-ion phenomenology.

In this thesis, we aim to shed light on this problem from two complementary directions. After presenting the theoretical framework, we first perform a temperature scan around the crossover region at fixed lattice spacing a in $N_f = 2+1$ QCD with physical quark masses, computing screening masses as well as $H_E(\omega_1)$, the first energy moment of $\sigma(\omega)$. This observable is directly accessible in lattice QCD via spatially transverse Euclidean correlators evaluated at imaginary spatial momentum, which realizes light-like kinematics in Euclidean space [256]. Our results indicate a pronounced enhancement around the crossover, suggesting larger photon yields in the late stages of heavy-ion collisions than typically assumed.

Second, we present a continuum-extrapolated determination of the first two energy moments, $H_E(\omega_{1,2})$, in $N_f = 2$ QCD at $T \approx 254\,\text{MeV}$. Here, we achieve percent-level precision for $H_E(\omega_1)$, enabling in-depth tests of weak-coupling predictions [253]. In contrast to previous lattice QCD studies of the photon emissivity [5, 155, 257, 258], the results presented in this thesis do not involve tackling a numerically ill-posed inverse problem. They significantly improve upon our recent works [6, 10] through superior statistical precision on the current-current correlation func-

[1] In this thesis, we focus on the scale set by $\omega_n = 2n\pi T, \quad n \in \{1, 2, 3\}$.

tions, thereby allowing us to more stringently probe the emission of the phenomenologically most relevant photons, $\omega \gtrsim \pi T$. We find evidence for a non-zero photon emissivity in this regime at the $2.6\,\sigma$ level.

7.2 Imaginary Momentum Correlators

We define the spectral function of the electromagnetic current as [257]

$$\rho^{\mathrm{em}}_{\mu\nu}(\omega,\mathbf{k},T) = \int \mathrm{d}^4x\, \mathrm{e}^{\mathrm{i}(\omega x_0 - \mathbf{k}\mathbf{x})}\, \mathrm{Tr}\left\{ \frac{\mathrm{e}^{-\beta H}}{Z(\beta)} [j^{\mathrm{em}}_\mu(x_0,\mathbf{x}), j^{\mathrm{em}}_\nu(0,\mathbf{0})^\dagger] \right\}, \tag{7.2.1}$$

where $j^{\mathrm{em}}_\mu(x) = \sum_{\mathrm{f}} Q_{\mathrm{f}} \bar{\psi}_{\mathrm{f}}(x)\gamma_\mu\psi_{\mathrm{f}}(x)$ is the electromagnetic current, $Q_{\mathrm{f}} \in \{2/3, -1/3\}$ denotes the charge of a quark with flavor f and γ_μ are the Euclidean Dirac matrices satisfying $\{\gamma_\mu,\gamma_\nu\} = 2\delta_{\mu\nu}$. Expectation values are taken w.r.t. the thermal density matrix $\mathrm{e}^{-\beta H}/Z(\beta)$, where Z is the grand canonical partition function, H is the QCD Hamiltonian and $\beta = 1/T$ denotes the inverse temperature.

The spectral function $\rho^{\mathrm{em}}_{\mu\nu}$ encodes the response of a medium to electromagnetic perturbations. At finite temperature, Lorentz invariance is violated. Consequently, $\rho^{\mathrm{em}}_{\mu\nu}$ can be decomposed into a longitudinal and transverse piece,

$$\rho^{\mathrm{em}}_{\mathrm{L}}(\omega,k) = \frac{k^i k^j}{k^2}\rho^{\mathrm{em}}_{ij} - \rho^{\mathrm{em}}_{00}\,, \tag{7.2.2}$$

$$\rho^{\mathrm{em}}_{\mathrm{T}}(\omega,k) = \frac{1}{2}\left(\delta^{ij} - \frac{k^i k^j}{k^2}\right)\rho^{\mathrm{em}}_{ij}\,, \tag{7.2.3}$$

such that

$$2\rho^{\mathrm{em}}_{\mathrm{T}} + \rho^{\mathrm{em}}_{\mathrm{L}} = -\rho^{\mu,\mathrm{em}}_{\ \ \mu}\,. \tag{7.2.4}$$

In the following, we consider the correlator of the isospin current[2]

$$j_\mu := \frac{1}{\sqrt{2}}\left(\bar{u}\gamma_\mu u - \bar{d}\gamma_\mu d\right), \tag{7.2.5}$$

and drop the superscript "em" on the vector current. The isospin current j_μ is related to the (light part) of the electromagnetic current

$$j^{\mathrm{em}}_\mu = \sum_{\mathrm{f}} Q_{\mathrm{f}}\,\bar{q}_{\mathrm{f}}\gamma_\mu q_{\mathrm{f}} = \frac{2}{3}\bar{u}\gamma_\mu u - \frac{1}{3}\bar{d}\gamma_\mu d + \cdots, \tag{7.2.6}$$

which can be decomposed into a sum of isovector and isoscalar components [224]

$$j^{\mathrm{em}}_\mu = \frac{1}{\sqrt{2}} j_\mu + \frac{1}{2} j^B_\mu\,, \tag{7.2.7}$$

[2]Note the different normalization of isospin current compared to Eq. (6.2.1). As a result, the two-point functions of the vector current considered in Part III are larger by a factor of 2 compared to their counterparts in Part II.

where we have introduced the baryon current as

$$j_\mu^{\mathrm{B}} = \frac{1}{3}\left(\bar{u}\gamma_\mu u + \bar{d}\gamma_\mu d\right) . \tag{7.2.8}$$

In the context of the connected contribution, the sum of the squares of the charges is typically represented as follows [98]:

$$C_{\mathrm{em}} = \sum_{\mathrm{f}} (Q_{\mathrm{f}})^2 = \begin{cases} \frac{5}{9} & (\text{for } u, d), \\ \frac{6}{9} & (\text{for } u, d, s). \end{cases}$$

Conversely, in the disconnected contribution, the expression involves the square of the sum of the charges [98]:

$$C_{\mathrm{em}}^{\mathrm{disc}} = \Big(\sum_{\mathrm{f}} Q_{\mathrm{f}}\Big)^2 = \begin{cases} \frac{1}{9} & (\text{for } u, d), \\ 0 & (\text{for } u, d, s). \end{cases}$$

The disconnected contribution, which is characterized by significant noise, becomes negligible at very high temperatures, as it is of order $\mathcal{O}(\alpha_s^3)$ at leading-order (LO) in perturbation theory [98]. Consequently, neglecting quark-line disconnected contributions to the two-point function of the electromagnetic current j_μ^{em}, we have [224, 259]

$$\rho_{\mu\nu}^{\mathrm{em}}(\omega, \mathbf{k}, T) \simeq \sum_{\mathrm{f=u,d,(s)}} Q_{\mathrm{f}}^2 \, \rho_{\mu\nu}(\omega, \mathbf{k}, T) = C_{\mathrm{em}} \, \rho_{\mu\nu}(\omega, \mathbf{k}, T) . \tag{7.2.9}$$

Additionally, in Ref. [260], the author investigated the flavor dependence of the vector current two-point function on a single $N_{\mathrm{f}} = 2+1$ ensemble at $T \approx 1.7\, T_{\mathrm{pc}}$. The study revealed only a slight dependence on the (valence) quark mass when comparing the light-light and strange-strange correlators. Consequently, in the high-temperature phase, neglecting SU(3)-flavor breaking effects, we treat the strange quark s as an additional light quark [$C_{\mathrm{em}} = \frac{2}{3}$ in Eq. (7.2.9)], whereas in the low-temperature phase, it is disregarded [$C_{\mathrm{em}} = \frac{5}{9}$].

Let us now look at the Euclidean vector screening correlators

$$G_{E,\mu\nu}(\omega_n, p_2, p_3, x_1) = \int_0^\beta \mathrm{d}x_0 \, \mathrm{e}^{\mathrm{i}\omega_n x_0} \int \mathrm{d}^2 x_\perp \mathrm{e}^{\mathrm{i}(p_2 x_2 + p_3 x_3)} \langle j_\mu(x_0, x_1, x_2, x_3) j_\nu^\dagger(0, \mathbf{0}) \rangle , \quad x_\perp = (x_2, x_3) , \tag{7.2.10}$$

with $\omega_n = 2\pi T n$ being the n-th Matsubara frequency. In an interacting theory, the low-energy part of the spectral function corresponding to Eq. (7.2.10) no longer forms a continuum. Instead it gives rise to a discrete spectrum with a non-zero energy gap in the low-frequency region. This structure leads to an exponential decay of the correlator $G_{E,\mu\nu}(\omega_n, p_2, p_3, x_1)$ as a function of the *spatial decay direction* $\hat{x}_1$.

In a thermally equilibrated medium, the rate of photon emission is governed by the imaginary part of the retarded correlator of the electromagnetic current, specifically its component transverse to the photon's spatial momentum. Consequently, we focus on the transverse channel and define

the Euclidean correlator

$$G_E^{\mathrm{T}}(\omega_n, p_2, x_1) \equiv G_{E,33}(\omega_n, p_2, 0, x_1) = \int_0^\beta \mathrm{d}x_0\, \mathrm{e}^{\mathrm{i}\omega_n x_0} \int \mathrm{d}^2 x_\perp \mathrm{e}^{\mathrm{i}p_2 x_2} \langle j_3(x_0, \mathbf{x}) j_3^\dagger(0, \mathbf{0}) \rangle \,. \tag{7.2.11}$$

In the following, we consider two special cases of Eq. (7.2.11), corresponding to different momentum insertions: the *non-static* (ns),

$$G_{\mathrm{ns}}^{\mathrm{T}}(\omega_n, x_1) \equiv G_E^{\mathrm{T}}(\omega_n, p_2 = 0, x_1) \,, \tag{7.2.12}$$

where momentum is inserted in the time direction, and the *static* (st) case,

$$G_{\mathrm{st}}^{\mathrm{T}}(p, x_1) \equiv G_E^{\mathrm{T}}(\omega_n = 0, p_2 = p, x_1) \,, \tag{7.2.13}$$

where momentum is inserted into a spatial direction. The correlators in Eqs. (7.2.12) and (7.2.13) have a representation [256]

$$G_i^{\mathrm{T}}(\omega_n, x_1) \overset{x_1 \neq 0}{=} \sum_{l=0}^{\infty} |A_{i,n}^l|^2 \, \mathrm{e}^{-m_{i,n}^l \cdot |x_1|} \,, \quad i \in \{\mathrm{ns}, \mathrm{st}\} \,, \tag{7.2.14}$$

in terms of the lth energies (screening masses) $m_{i,n}^l$ and corresponding amplitudes $A_{i,n}^l$ of screening states. For a given Matsubara sector ω_n the asymptotic ($x_1 \to \infty$) is dominated by the lowest screening mass $m_{i,n}^0$. The energies associated with this decay—known as *screening masses*—provide important information about the medium and have been investigated in both weak-coupling frameworks and lattice simulations in Ref. [261].

Next, we define the Fourier transform of the non-static screening correlator,

$$\tilde{G}_{\mathrm{ns}}^{\mathrm{T}}(\omega_n, k) = \int_{\mathbb{R}} \mathrm{d}x_1 \mathrm{e}^{\mathrm{i}kx_1} G_{\mathrm{ns}}^{\mathrm{T}}(\omega_n, x_1) \overset{k=\mathrm{i}\omega_n}{\equiv} H_E(\omega_n) \,, \tag{7.2.15}$$

evaluated at Matsubara frequency ω_n and *imaginary spatial momentum* $k = \mathrm{i}\omega_n$. This choice satisfies the on-shell condition $\omega^2 - k^2 = 0$ in Euclidean space, which requires the spatial momentum to be imaginary to access light-like kinematics relevant for thermal photon emission. Previous approaches [5, 155, 257, 258] used correlation functions at fixed real spatial momentum involving contributions from all photon virtualities when related to the photon production rate. In contrast, the spatially transverse Euclidean correlators in Eq. (7.2.15) are evaluated at imaginary spatial momentum, allowing access to energy-integrated information on the photon emissivity. This makes them particularly well-suited for determining the photon emissivity on the lattice without confronting an inverse problem.

Making use of Eq. (7.2.11), we finally define [256]

$$H_E(\omega_n) = \int_0^\beta \mathrm{d}x_0 \int \mathrm{d}^3 x\, \mathrm{e}^{\mathrm{i}\omega_n x_0} \mathrm{e}^{-\omega_n x_1} \langle j_3(x) j_3^\dagger(0) \rangle \,. \tag{7.2.16}$$

The introduction of an imaginary spatial momentum in the Euclidean correlator significantly enhances the sensitivity to the low-lying screening spectrum in each non-static Matsubara sector.

This follows upon inserting Eq. (7.2.14) into Eq. (7.2.15):

$$\begin{aligned} H_E(\omega_n) &= \sum_{l=0}^{\infty} |A^l_{\mathrm{i},n}|^2 \int_{\mathbb{R}} \mathrm{d}x_1 \, \mathrm{e}^{-m^l_{\mathrm{i},n}\cdot|x_1|-\omega_n x_1} \\ &= \sum_{l=0}^{\infty} |A^l_{\mathrm{i},n}|^2 \int_{-\infty}^{0} \mathrm{d}x_1 \, \mathrm{e}^{(m^l_{\mathrm{i},n}-\omega_n)x_1} + \int_{0}^{\infty} \mathrm{d}x_1 \, \mathrm{e}^{-(m^l_{\mathrm{i},n}+\omega_n)x_1} + \text{c.t.} \\ &= \sum_{l=0}^{\infty} |A^l_{\mathrm{i},n}|^2 \left[\frac{1}{m^l_{\mathrm{i},n}-\omega_n} + \frac{1}{m^l_{\mathrm{i},n}+\omega_n} \right] + \text{c.t.} \\ &= 2\sum_{l=0}^{\infty} |A^l_{\mathrm{i},n}|^2 \frac{m^l_{\mathrm{i},n}}{(m^l_{\mathrm{i},n})^2-\omega_n^2} + \text{c.t.}\,, \end{aligned} \tag{7.2.17}$$

where c.t. denotes contact terms arising from the vicinity of $x_1 = 0$ [256]. Consequently, a precise determination of the low-lying screening states is essential for a proper understanding of the correlator's asymptotic behavior.

7.2.1 Lattice Subtractions

Within the continuum theory, $H_E(\omega_n)$ vanishes in the vacuum [256]. This property is lost at finite lattice spacing owing to the explicit breaking of Lorentz symmetry. However, it can be restored by subtracting a correlator that shares the same short-distance behavior and—crucially—vanishes in the continuum limit, thereby preserving the correct continuum behavior. In principle, the vacuum lattice correlator computed using the same bare parameters provides such a subtraction. This procedure was proposed in the foundational work that developed the underlying theoretical framework [256]. The drawback of this approach is the need for additional costly simulations at $T = 0$.

Motivated by free lattice perturbation theory (Appendix E of Ref. [6]), we have explored alternative subtraction schemes based on thermal correlators. These exhibit improved behavior in practical lattice calculations, particularly in terms of reduced discretization effects. Therefore, already in Ref. [262], it has been proposed to subtract the static screening correlator (7.2.13), with the momentum $p_2 = p$ inserted into a spatial direction $\hat{x}_2$ orthogonal to the decay direction $\hat{x}_1$ as well as the direction corresponding to the Lorentz index of the isospin current, $\hat{x}_3$.

$$\begin{aligned} H_{E,\,p}(\omega_n) &= \int_0^{\beta} \mathrm{d}x_0 \int \mathrm{d}^3x \, \left(\mathrm{e}^{\omega_n(\mathrm{i}x_0-x_1)} - \mathrm{e}^{p(\mathrm{i}x_2-x_1)} \right) \langle j_3(x) j_3^{\dagger}(0) \rangle \\ &= \int_{\mathbb{R}} \mathrm{d}x_1 \, \left[G^T_{\mathrm{ns}}(\omega_n, x_1)\mathrm{e}^{-\omega_n x_1} - G^T_{\mathrm{st}}(p, x_1)\mathrm{e}^{-p x_1} \right] . \end{aligned} \tag{7.2.18}$$

The key observation is that—in the continuum limit—the Fourier transform of a static screening correlator evaluated at light-like momentum vanishes (for more details see Ref. [6]). However, on the lattice it helps reduce discretization errors. The case $p = \omega_n$ exhibits a remarkable feature: the function $H_{E,\,\omega_n}(\omega_n)$ vanishes identically at zero temperature, in exact agreement with the continuum expectation that $H_E(\omega_n) = 0$ in the vacuum. This exact cancellation at $T = 0$ significantly suppresses discretization effects at finite temperature—a behavior that is explicitly confirmed by lattice perturbation theory (see Appendix E of Ref. [6]).

In addition, we define $\Omega_n = \omega_n(1 - \mathcal{O}(a^2))$ to further suppress discretization artifacts [262].

A one-parameter family of such kernel regularizations is given by

$$\Omega_n(k) = \frac{k}{a}\sin\left(\frac{a\omega_n}{k}\right), \quad k \in \mathbb{R}\,. \tag{7.2.19}$$

This choice effectively reduces the Matsubara frequency ω_n that appears in the exponent of Eq. (7.2.18), replacing it with a slightly smaller value $\omega_n \to \omega_n - \mathcal{O}(a^2)$, thereby mitigating leading-order lattice artifacts. We are now prepared to define the *standard subtracted* H_E-quantity as follows:

$$\begin{aligned} H_{E,p=\omega_n}(\omega_n) &= \int_0^\beta \mathrm{d}x_0 \int_{\mathbb{R}^3} \mathrm{d}^3x \, \left(\mathrm{e}^{\mathrm{i}\omega_n x_0} - \mathrm{e}^{\mathrm{i}\omega_n x_2}\right) \mathrm{e}^{-\Omega_n x_1} \langle j_3(x) j_3^\dagger(0)\rangle \\ &= \int_0^\infty \mathrm{d}x_1 \, h_E(\omega_n, x_1)\,, \end{aligned} \tag{7.2.20}$$

where we have defined

$$h_E(\omega_n, x_1) = 2\cosh(\Omega_n x_1) \cdot \left[G^{\mathrm{T}}_{\mathrm{ns}}(\omega_n, x_1) - G^{\mathrm{T}}_{\mathrm{st}}(\omega_n, x_1)\right], \tag{7.2.21}$$

as the integrand of $H_{E,p=\omega_n}(\omega_n)$. We emphasize again that the spatial momentum is inserted in $\hat{x}_2-$direction, that is, transverse to the decay direction $\hat{x}_1$ as well as the direction of the Lorentz index. In our conventions both $G^{\mathrm{T}}_{\mathrm{ns}}$ and $G^{\mathrm{T}}_{\mathrm{st}}$ are positive and we find $G^{\mathrm{T}}_{\mathrm{ns}} < G^{\mathrm{T}}_{\mathrm{st}}$. Consequently, the standard-subtracted quantity $H_{E,p=\omega_n}(\omega_n)$ is negative.

Evaluating $H_{E,p=\omega_2}(\omega_2)$ using point sources was not feasible in Ref. [6] owing to limited statistics. In this study, we found $|H_{E,p=\omega_2}(\omega_2)| < |H_{E,p=\omega_1}(\omega_1)|$ for the central values, which violates[3] the positivity of the transverse channel spectral function $\sigma(\omega)$. To address this issue and obtain results consistent with physical expectations, alternative subtraction schemes have been proposed [6]:

$$H_{E,\,\mathbf{p},\boldsymbol{\alpha}}(\omega_n) = \int_{\mathbb{R}} \mathrm{d}x_1 \left[G^{\mathrm{T}}_{\mathrm{ns}}(\omega_n, x_1)\,\mathrm{e}^{-\omega_n x_1} - \sum_i \alpha_i G^{\mathrm{T}}_{\mathrm{st}}(p_i, x_1)\,\mathrm{e}^{-p_i x_1}\right]. \tag{7.2.22}$$

Within these schemes a general linear combination of static transverse screening correlators with momenta p_i is subtracted. The coefficients α_i determine the relative weights of each subtraction term. The standard subtraction (7.2.20) is recovered as the special case $p_1 = \omega_n$, $\alpha_1 = 1$ and $\alpha_{i>1} = 0$. It is important to note that while the values of $H_{E,\,\mathbf{p},\boldsymbol{\alpha}}(\omega_n)$ depend on the choice of $\mathbf{p}$ and $\boldsymbol{\alpha}$ at finite lattice spacing, they must converge to a unique result in the continuum limit. However, by employing stochastic wall sources, we have significantly increased the statistics compared to our previous draft Ref. [6] making the evaluation of the second Matsubara sector feasible with the standard subtraction, Eq. (7.2.20). In the continuum limit, both the static and non-static screening correlators, $G^T_{\mathrm{st}}(\omega_n, x_1)$ and $G^T_{\mathrm{ns}}(\omega_n, x_1)$, exhibit identical leading singular behavior as $x_1 \to 0$ [6]:

$$G^T_{\mathrm{st}}(\omega_n, x_1), \quad G^T_{\mathrm{ns}}(\omega_n, x_1) \overset{x_1\to 0}{\sim} \left(\omega_n^2 - \frac{\partial^2}{\partial x_1^2}\right)\delta(x_1)\,, \tag{7.2.23}$$

with the same prefactor in both cases. As a result, the integrand in the standard subtraction is par-

[3] The expected hierarchy of H_E across different Matsubara sectors can be inferred from Eq. (7.4.6).

ticularly smooth and shows no singular behavior around $x_1 = 0$ [see Fig. 9.14]. Furthermore, free lattice perturbation theory shows that the standard subtraction exhibits the smallest discretization effects compared to the alternative schemes (see Table V in Ref. [6]). Therefore, we focus exclusively on the standard subtraction scheme in this thesis. Accordingly, we drop the additional indices and denote the subtracted quantity simply as $H_E(\omega_n)$, with the understanding that it refers to the standard subtraction defined in Eq. (7.2.20).

7.2.2 The Virtuality Dependence of H_E

Up to this point, we have investigated the H_E-quantity in the special case of vanishing virtuality Q^2, which is the relevant kinematics for photon emissivity. However, the Euclidean correlator H_E can also be evaluated at finite virtuality $Q^2 \leq \omega_n^2$, providing insight into the behavior of the low-mass dilepton rate [263]. To study the impact of a small but finite virtuality Q^2, we consider the derivative of H_E w.r.t. Q^2, evaluated at $Q^2 = 0$. Following the definition in Ref. [263], the Euclidean correlator $H_E(\omega_n, Q^2)$ is given by

$$\begin{aligned} H_E(\omega_n, Q^2) &= \int_0^\beta \mathrm{d}x_0 \int_{\mathbb{R}^3} \mathrm{d}^3x\, \mathrm{e}^{\mathrm{i}\omega_n x_0}\, \mathrm{e}^{\sqrt{\omega_n^2 - Q^2}\, x_1}\, \langle j_3(x) j_3^\dagger(0)\rangle \\ &= \int_{\mathbb{R}} \mathrm{d}x_1\, G_{\mathrm{ns}}^{\mathrm{T}}(\omega_n, x_1)\, \mathrm{e}^{\sqrt{\omega_n^2 - Q^2}\, x_1}. \end{aligned} \tag{7.2.24}$$

Expanding around $Q^2 = 0$ for $\omega_n > 0$, we obtain

$$\begin{aligned} H_E(\omega_n, Q^2) &= H_E(\omega_n, 0) + Q^2 \left.\frac{\mathrm{d}H_E(\omega_n, Q^2)}{\mathrm{d}Q^2}\right|_{Q^2=0} + \mathcal{O}(Q^4) \\ &= H_E(\omega_n, 0) - \frac{Q^2}{2\omega_n} \int_0^\beta \mathrm{d}x_0 \int_{\mathbb{R}^3} \mathrm{d}^3x\ \ \mathrm{e}^{\omega_n x_1}\, \mathrm{e}^{\mathrm{i}\omega_n x_0}\, x_1\, \langle j_3(x) j_3^\dagger(0)\rangle + \mathcal{O}(Q^4) \\ &= H_E(\omega_n, 0) - \frac{Q^2}{2\omega_n} \int_{\mathbb{R}} \mathrm{d}x_1\, x_1 \sinh(\omega_n x_1)\, G_{\mathrm{ns}}^{\mathrm{T}}(\omega_n, x_1) + \mathcal{O}(Q^4)\,. \end{aligned} \tag{7.2.25}$$

In transitioning from the second to the third line, we have utilized the property that the vector correlator is symmetric under the transformation $x_1 \to -x_1$, resulting in the product $x_1 \langle j_3(x) j_3^\dagger(0)\rangle$ being antisymmetric. Consequently, only the antisymmetric component of the exponential weight function contributes to the integral over $\mathbb{R}$.

To ensure that the definition remains ultraviolet (UV) finite, we eliminate the divergence occurring at finite Q^2 by subtracting the zero-frequency contribution $H_E(0, Q^2)$. This subtraction does not alter the value of the Taylor expansion in Eq. (7.2.25) at $Q^2 = 0$, given that $H_E(0, 0) = 0$ [6]. Upon evaluating the derivative of the subtracted term, we obtain

$$\begin{aligned} \frac{\mathrm{d}H_E(0, Q^2)}{\mathrm{d}Q^2} &= \frac{1}{2Q} \frac{\mathrm{d}H_E(0, Q^2)}{\mathrm{d}Q} \\ &= \frac{1}{2Q} \int_0^\beta \mathrm{d}x_0 \int_{\mathbb{R}^3} \mathrm{d}^3x\, \mathrm{e}^{\mathrm{i}Qx_1}(\mathrm{i}x_1) \langle j_3(x) j_3^\dagger(0)\rangle \\ &= \frac{1}{2Q} \int_0^\beta \mathrm{d}x_0 \int_{\mathbb{R}^3} \mathrm{d}^3x\, (\mathrm{i}x_1)[\mathrm{i}(x_1 Q + \mathcal{O}(Q^3))] \langle j_3(x) j_3^\dagger(0)\rangle \\ &= -\frac{1}{2} \int_{\mathbb{R}} \mathrm{d}x_1\, (x_1)^2\, G_{\mathrm{st}}^{\mathrm{T}}(p = 0, x_1)\,, \end{aligned} \tag{7.2.26}$$

where in going from the second to the third line, the symmetry of the correlator under $x_1 \to -x_1$ was used again. Here $G^{\mathrm{T}}_{\mathrm{st}}(p=0,x_1)$ denotes the completeley static (zero momentum) screening correlator. Subtracting this contribution from Eq. (7.2.25) yields a UV-finite expression:

$$\begin{aligned}&\frac{\mathrm{d}}{\mathrm{d}Q^2}\Big[H_E(\omega_n,Q^2)-H_E(0,Q^2)\Big]_{Q^2=0}\\&\qquad=-\int_0^\infty \mathrm{d}x_1\left[\frac{x_1}{\omega_n}\sinh(\omega_n x_1)\,G^{\mathrm{T}}_{\mathrm{ns}}(\omega_n,x_1)-x_1^2\,G^{\mathrm{T}}_{\mathrm{st}}(0,x_1)\right],\end{aligned}\tag{7.2.27}$$

where the factors of $\frac{1}{2}$ have cancelled as the integration is now performed solely over the positive real axis.

7.2.3 Lattice Observables

This section introduces the lattice observables that will be examined in this thesis. Unlike Ref. [6], we exclusively employ the *local* discretization of the vector current,

$$V^{\mathrm{L}}_\mu(x)\equiv V_\mu(x)=\bar\psi(x)\gamma_\mu\frac{\tau^3}{\sqrt{2}}\psi(x)\,,\tag{7.2.28}$$

which has support on a single lattice site. The local vector current is renormalized by a multiplicative factor $Z_V(g_0^2)$, with renormalization constants taken from Ref. [264]. We emphasize again that in this normalization, the two-point functions of the vector current are larger by a factor of two compared to those in Eq. (6.2.1). In our analysis, we consider the isovector flavor combination, with the current normalized such that $\sum_f Q_{\mathrm{f}}^2 = 1$. The results for $H_E(\omega_n)$ are presented in this normalization. To obtain an estimate of the physical photon emissivity, neglecting SU(3)-flavor breaking effects, one must include the factor $\sum_f Q_{\mathrm{f}}^2 = (2/3)^2+(-1/3)^2+(-1/3)^2 = 2/3$. We define the bare non-static (ns) screening correlator as[4]

$$G_{\mathrm{ns},\mu\nu}(\omega_n,x_i)=a^3\sum_{\substack{x_j\\ j\in\{0,1,2,3\},\,j\neq i}}\mathrm{e}^{\mathrm{i}\omega_n x_0}\,\langle V_\mu(x)V_\nu^\dagger(0)\rangle\,,\tag{7.2.29}$$

where $i\in\{1,2,3\}$ labels the spatial direction of the source–sink separation (i.e. the decay direction), and the momentum is inserted in the Euclidean time direction. Analogously, when the momentum is injected into a spatial direction k, perpendicular to the decay direction x_i, we obtain the bare, static (st) screening correlator at finite momentum,

$$G_{\mathrm{st},\mu\nu}(\omega_n,x_i)=a^3\sum_{\substack{x_j\\ j\in\{0,1,2,3\},\,j\neq i}}\mathrm{e}^{\mathrm{i}\omega_n x_k}\,\langle V_\mu(x)V_\nu^\dagger(0)\rangle\,,\qquad i,k\in\{1,2,3\}\,,\qquad i\neq k\,.\tag{7.2.30}$$

In both cases, we choose $\mu=\nu$, orthogonal to the decay direction x_i, which projects onto the transverse channel.

Therefore, there are six potential combinations of decay direction and Lorentz indices for the non-static screening correlator, as well as six combinations for the static correlator, which account for the selection of decay and momentum-insertion directions. In Ref. [6], the non-static corre-

[4] We denote the continuum screening correlators, Eqs. (7.2.12) and (7.2.13), by the same capital G.

lator in the second Matsubara sector—particularly the ground state screening mass $m^0_{\mathrm{ns},2}(\omega_2)$—exhibited relatively large statistical uncertainties. Consequently, we computed the non-static correlator for all six possible choices of decay direction and Lorentz index and averaged the results. In contrast, for the static correlator, we injected momentum in only one spatial direction but averaged over the three decay directions. For the temperature scan of $H_E(\omega_1)$ in $N_\mathrm{f} = 2+1$ flavor QCD, however, measurements were conducted with only one fixed decay direction. Additionally, in both the $N_\mathrm{f} = 2$ and the $N_\mathrm{f} = 2+1$ projects, we performed measurements with negative injected momenta and averaged over both signs, as the averaged correlator is approximately $\sqrt{2}$ times more precise than the individual measurements in the region $x_i T > 1/2$.

As emphasized in Sec. 7.2.1, particular attention must be given when constructing a lattice estimator for H_E. A straightforward discretization of Eq. (7.2.16) can introduce an ultraviolet divergence. Specifically, at small source-separations x_1, it is crucial to subtract the x_1-independent contribution[5] that multiplies the current-current correlator $\langle j_3(x) j_3^\dagger(0)\rangle$ in Eq. (7.2.16) to obtain a well-defined result. Implementing the continuum version of the standard subtraction, Eq. (7.2.20), where the static correlator evaluated at the same spatial momentum is subtracted, leads on the lattice to [6]

$$H_E(\omega_n)/T^2 = \frac{a}{\beta}\sum_{x_1=a}^{L/2-a} h_E(\omega_n, x_1)/T^3 + \frac{a}{2\beta}\Big(h_E(\omega_n, 0)/T^3 + h_E(\omega_n, L/2)/T^3\Big)\,, \tag{7.2.31}$$

where L and $\beta = \frac{1}{T}$ denote the spatial and temporal extents of the lattice, respectively. In the discretization of Eq. (7.2.20), we employed the trapezoidal rule. The integrand $h_E(\omega_n, x_1)$ is defined in Eq. (7.2.21). Similar to the correlators in Eqs. (7.2.29) and (7.2.30), we do not distinguish between the continuum and lattice observables, that is, we use $H_E(\omega_n)$ also for the lattice quantity.

Following the same procedure as for $H_E(\omega_n)$, a lattice expression for the derivative of $H_E(\omega_n, Q^2)$ can be obtained by applying the trapezoidal rule to Eq. (7.2.27). This proceeds as in Eq. (7.2.31), but with the integrand $h(\omega_n, x_1)$ replaced by [6]

$$h_{Q^2}(\omega_n, x_1) = -\left(\frac{x_1 T}{\omega_n/T}\sinh(\omega_n x_1)\, G^\mathrm{T}_\mathrm{ns}(\omega_n, x_1) - (x_1 T)^2\, G^\mathrm{T}_\mathrm{st}(0, x_1)\right). \tag{7.2.32}$$

We note that this subtraction involves the completely static (i.e. zero-momentum) screening correlator, $G^\mathrm{T}_\mathrm{st}(p = 0, x_1)$.

7.3 Modeling the Tail of the Integrand of H_E

The computation of $H_E(\omega_n)$ becomes increasingly challenging for larger n, primarily because of the enhanced contributions from large spatial separations x_1, where the correlator exhibits an exponential deterioration in the signal-to-noise ratio. This issue is exacerbated by the exponential enhancement of the tail by the "cosh-kernel" in Eq. (7.2.20), leading to an exponentially growing uncertainty of the integrand at large source-sink separations. Additionally, the inserted momenta are of $\mathcal{O}(1\text{–}3\,\mathrm{GeV})$, further worsening the signal-to-noise problem, [see e.g. the l.h.s. of Fig. 9.14].

[5] This is the leading term when Taylor expanding the exponential weight function multiplying the position space vector correlator, Eq. (7.2.16), around $x_1 = 0$.

Figure 7.2: Sketch of the different kinematic regimes relevant for the electrical conductivity, and for photon and dilepton production rates. The four-momentum of the (virtual) photon is denoted by $\mathcal{K} = (\omega, \mathbf{k})$, which is measured in the rest frame of the thermal medium. The figure is adapted from Ref. [265].

Therefore, we have employed a simple model—based on fits to the screening correlators—to describe the asymptotic behavior of the integrand [cf. Sec. 7.3.1].

7.3.1 Fit Ansatz for the Tail of the Screening Correlators

It is established that both correlators G_i^{T}, where $i \in \{\mathrm{ns}, \mathrm{st}\}$, are characterized at long distances (and in infinite volume) by a sum of exponentials with positive prefactors [see Eq. (7.2.14)]. Considering the periodic boundary conditions in our simulations, we utilize the fit ansatz[6]

$$G_i^{\mathrm{T}}(\omega_n, x_1) = \sum_{l=0}^{2} |A_{i,n}^l|^2 \cosh[(x_1 - L/2)\, m_{i,n}^l(\omega_n)]\,. \tag{7.3.1}$$

To better control the noisy long-distance (ld) contribution $h_{E,\mathrm{ld}}$ of the integrand $h_E(\omega_n, x_1)$ and simultaneously correct for finite-volume effects, we insert the infinite-volume version of the fit ansatz, Eq. (7.3.1), into Eq. (7.2.21):

$$\begin{aligned} h_{E,\mathrm{ld}}(\omega_n, x_1) &= 2\sum_{l=0}^{2} \cosh(\Omega_n x_1) \left[|A_{\mathrm{ns},n}^l|^2 \cosh[(x_1 - L/2)\, m_{\mathrm{ns},n}^l(\omega_n)] \right] - (\mathrm{ns}\leftrightarrow\mathrm{st}) \\ &= \cosh(\Omega_n x_1) \sum_{l=0}^{2} |A_{\mathrm{ns},n}^l|^2 \left[\mathrm{e}^{m_{\mathrm{ns},n}^l(\omega_n) x_1} \mathrm{e}^{-m_{\mathrm{ns},n}^l(\omega_n)\frac{L}{2}} + \mathrm{e}^{-m_{\mathrm{ns},n}^l(\omega_n) x_1} \mathrm{e}^{m_{\mathrm{ns},n}^l(\omega_n)\frac{L}{2}} \right] - (\mathrm{ns}\leftrightarrow\mathrm{st}) \\ &= \sum_{l=0}^{2} \frac{|A_{\mathrm{ns},n}^l|^2}{2} \mathrm{e}^{m_{\mathrm{ns},n}^l(\omega_n)\frac{L}{2}} \left[\mathrm{e}^{-(m_{\mathrm{ns},n}^l(\omega_n) - \Omega_n) x_1} + \mathrm{e}^{-(m_{\mathrm{ns},n}^l(\omega_n) + \Omega_n) x_1} \right] - (\mathrm{ns}\leftrightarrow\mathrm{st}))\,, \end{aligned} \tag{7.3.2}$$

where, in the third line, the exponentially suppressed term, which vanishes as $L \to \infty$, has been omitted. This expression is amenable to analytical integration [6]. To construct the standard-subtracted quantity H_E, as defined in Eq. (7.2.20), we partition the integral over $x_1 \in [0, L/2]$ into two distinct regions. For the short-distance (sd) region, where $x_1 \in [0, x_w]$, we numerically evaluate the subtracted integrand using the trapezoidal rule, as specified in Eq. (7.2.31). For the long-distance region, where $x_1 \in [x_w, \infty)$, we perform an analytical integration of Eq. (7.3.2). This approach effectively suppresses statistical noise at large x_1 and inherently eliminates the leading finite-volume effects.

7.4 The Thermal Photon Rate

The rates of photon and dilepton production per unit volume in a thermal medium such as the QGP, at temperature $T = \frac{1}{\beta}$, computed to LO in the electromagnetic coupling constant $\alpha_{\rm em} = \frac{e^2}{4\pi}$, but to all orders of the strong coupling, are given by [195, 257, 266]

$$\frac{\mathrm{d}\Gamma_\gamma(\mathbf{k})}{\mathrm{d}^3\mathbf{k}} = \frac{\alpha_{\rm em}}{4\pi^2 k}\frac{-\rho^\mu{}_\mu(\omega = k, \mathbf{k})}{\mathrm{e}^{\beta k} - 1}\,, \tag{7.4.1}$$

$$\frac{\mathrm{d}\Gamma_{l^+l^-}(\mathcal{K})}{\mathrm{d}^4\mathcal{K}} = \frac{\alpha_{\rm em}^2}{6\pi^3\mathcal{K}^2}\frac{-\rho^\mu{}_\mu(\mathcal{K})}{\mathrm{e}^{\beta\omega} - 1}\,, \tag{7.4.2}$$

where $\rho^\mu{}_\mu$ is the trace of the spectral function of the isospin current defined in Eq. (7.2.4) and ω and $\mathbf{k}$ denote the photon energy and momentum in the medium rest frame. Equations (7.4.1) and (7.4.2) apply locally, i.e. cell by cell, in simulations of HICs. As the thermal medium expands, the local temperature evolves, and the four-momentum $\mathcal{K} = (\omega, \mathbf{k})$ must be boosted to the laboratory frame according to the local fluid velocity [44].

For completeness, we recall the expression for the electrical conductivity of the QGP [266]:

$$\sigma_{\rm el} = \sum_{\rm f} Q_{\rm f}^2 \lim_{\omega\to 0}\frac{\rho^i{}_i(\omega, \mathbf{0})}{\omega}\,, \tag{7.4.3}$$

where $\rho^i{}_i(\omega, \mathbf{0})$ denotes the spatial components of the spectral function at zero spatial momentum. The kinematic regimes for electrical conductivity, photon, and dilepton production are shown in Fig. 7.2. In the spacelike region ($\mathcal{K}^2 < 0$), the vector spectral functions quantify the medium's efficiency in dissipating the energy of external electromagnetic fields into heat [257, 262].

However, in this thesis, we focus exclusively on the photon production rate. After integrating Eq. (7.4.1) over the solid angle, and using the relation[7] $-\rho^\mu{}_\mu(\omega = k, k) = 2\rho^{\rm T}(\omega = k, k)$, we obtain:

$$\frac{\mathrm{d}\Gamma_\gamma}{\mathrm{d}\omega} = \frac{\alpha_{\rm em}}{\pi}\frac{2\omega}{\mathrm{e}^{\beta\omega} - 1}\,\sigma(\omega) + \mathcal{O}(\alpha_{\rm em}^2)\,, \tag{7.4.4}$$

where ω is the energy of the emitted photon from a fluid cell at rest and in thermal equilibrium. Thus, the thermal photon production rate per unit volume of the QGP, $\frac{d\Gamma_\gamma}{d\omega}$, is related to the transverse channel spectral function evaluated at light-like kinematics (see Eq. (7.2.3)),

$$\sigma(\omega) \equiv \rho^{\rm T}(\omega, k = \omega)\,. \tag{7.4.5}$$

On the l.h.s. of Fig. 7.3 this spectral function is shown for QCD at complete LO (blue line) and for the strongly-coupled $\mathcal{N} = 4$ SYM theory (green line).

The integral of the above spectral function at vanishing virtuality is related to the spatially transverse Euclidean correlator $H_E(\omega_n)$ via a once-subtracted dispersion relation [256]:

$$H_E(\omega_n) - H_E(\omega_r) = \int_0^\infty \frac{\mathrm{d}\omega}{\pi}\omega\sigma(\omega)\left[\frac{1}{\omega^2 + \omega_n^2} - \frac{1}{\omega^2 + \omega_r^2}\right]\,. \tag{7.4.6}$$

[6] This corresponds to a truncation of Eq. (7.2.14) for $n > 2$.

[7] Current conservation implies $\omega^2\rho_{00} - k^i k^j \rho_{ij} = 0$; consequently $\rho^{\rm L}(\omega = k, k)$ vanishes in the light-like regime.

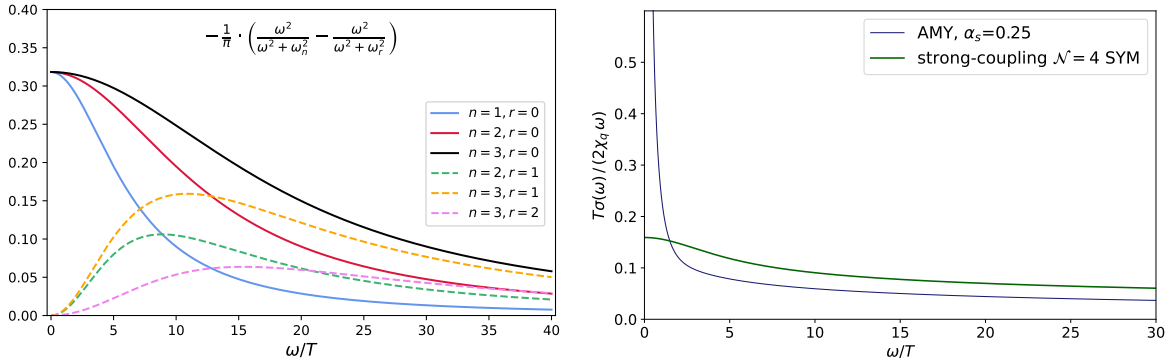

Figure 7.3: **Left panel:** Integration kernels appearing in Eqs. (7.4.6) and (7.4.7), which multiply the transverse channel spectral function at light-like kinematics, $\frac{\sigma_{\rm em}}{\omega}$ [see Eq. (7.2.1)]. **Right panel:** Spectral function at light-like kinematics normalized by $2\chi_q\omega/T$, shown for QCD at complete LO from Refs. [252, 253] and for the strongly-coupled $\mathcal{N}=4$ SYM theory [269].

The l.h.s. of Eq. (7.4.6) is directly accessible in lattice simulations. This enables the computation of *energy moments* of the spectral function, as defined in Eq. (7.4.5). These moments vanish in the case of thermal, non-interacting quarks [256], making them ideal probes for medium effects.

Carlson's theorem implies that knowing $H_E(\omega_n)$ for all $n \geq n_0 \in \mathbb{N}$ uniquely determines the spectral function $\sigma_{\rm em}(\omega)$ [34, 267, 268]. Although this is not numerically feasible, it is still valuable to compute a lattice QCD quantity that is sensitive to QGP interactions and is directly related to the photon emission rate [256].

In the absence of massless screening modes, one has $H_E(0)=0$, which allows for a simplified spectral representation of the quantity $H_E(\omega_n)$,

$$H_E(\omega_n) = -\frac{\omega_n^2}{\pi}\int_0^\infty \frac{\mathrm{d}\omega}{\omega}\frac{\sigma(\omega)}{\omega^2+\omega_n^2}\,. \tag{7.4.7}$$

In this form, the Euclidean screening correlator at imaginary spatial momentum is expressed as an integral of the transverse channel spectral function $\sigma(\omega)$, weighted by a Lorentzian kernel. For a discussion on how to interpret the r.h.s. of Eq. (7.4.7) in the limit $\omega_n \to 0$, see Ref. [6]. The integration kernels presented in Eqs. (7.4.6) and (7.4.7), which multiply the transverse channel spectral function at light-like kinematics, $\frac{\sigma}{\omega}$ [cf. Eq. (7.2.1)], are shown on the l.h.s. of Fig. 7.3. Notable differences in the behavior of these integration kernels can be observed. Specifically, the integrand in Eq. (7.4.7) demonstrates significant contributions from soft photons [solid lines on the l.h.s. of Fig. 7.3], as it remains finite in the limit $\omega/T \to 0$. Conversely, the kernel associated with the difference $H_E(\omega_n) - H_E(\omega_r)$ $(n > r)$ [dashed lines on the l.h.s. of Fig. 7.3] approaches zero in this limit, thereby probing the emission of hard photons. This distinction bears important physical implications: the low-frequency behavior of the spectral function, particularly its slope at the origin, offers direct insight into the charge diffusion coefficient D [5, 155, 257]. Specifically, the diffusion coefficient is related to the infrared limit of the spectral function via a Kubo formula

$$\lim_{\omega\to 0}\frac{\sigma(\omega)}{\omega} = 2D\chi_q, \tag{7.4.8}$$

where χ_q denotes the isovector QNS as defined in Eq. (6.7.1). For free massless quarks, as assumed in weak coupling calculations, it is given by [6]

$$\chi_q = \Big(\sum_{\mathrm{f}} Q_{\mathrm{f}}^2\Big)\frac{N_c}{3}T^2\,. \tag{7.4.9}$$

It is crucial to note that charge factors are incorporated into the definition of susceptibility, as well as into the spectral function of the electromagnetic current (7.2.9). As a result, these factors cancel in normalized quantities, as illustrated, for example, in Fig. 9.18.

Chapter 8

Temperature Scan of the Thermal Photon Emissivity around the Chiral Crossover

In this chapter, we present the results for both static and non-static screening masses, the first energy moment $H_E(\omega_1)$, and the virtuality dependence of this observable. These findings were derived from a coarse temperature scan across the chiral crossover, conducted at a fixed fine lattice spacing of $a = 0.064\,\text{fm}$. The numerical setup employed is consistent with that described in Sec. 6.2.5. Some of these findings have been previously presented in the following reference:

Authors:	**Ardit Krasniqi**, Marco Cè, Renwick J. Hudspith, Harvey B. Meyer, Csaba Török
Title	The thermal photon emissivity at the QCD chiral crossover from imaginary momentum correlators
Year:	2024
Journal:	*Proceedings of Science*
Volume/Issue:	453
DOI:	doi.org/10.22323/1.453.0180

8.1 Screening Masses in the First Matsubara Sector

In this section, we present our findings regarding the static and non-static screening masses within the $n = 1$ Matsubara sector, derived from a coarse temperature scan across the chiral

Table 8.1: Static and non-static screening masses in the $n = 1$ Matsubara sector, extracted from two-state fits using the ansatz in Eq. (7.3.1). We also report the mass gap $\Delta m^{0,\text{ratio}}_{\text{ns}-\text{st}}/T \equiv [m^{0,\text{ratio}}_{\text{ns}}(\omega_1) - m^{0,\text{ratio}}_{\text{st}}(\omega_1)]/T$, obtained from a single-exponential fit to the correlator ratio $G^{\text{T}}_{\text{ns}}(\omega_1, x_1)/G^{\text{T}}_{\text{st}}(\omega_1, x_1)$. For comparison, we also list the completely static (i.e., zero momentum) screening masses [see also Table 6.5 and Fig. 6.9]. All results are expressed in temperature units and were obtained on the `E250` ensembles with $N_\tau \in \{24, 20, 16\}$, corresponding to $T \in \{128, 154, 192\}$ MeV.

Ensemble	`E250Nt24`	`E250Nt20`	`E250Nt16`
$m^0_{\text{st},0}(\omega_0)/T$	4.77(26)	4.44(17)	5.56(2)
$m^0_{\text{st},1}(\omega_1)/T$	9.6(2)	8.8(3)	8.70(9)
$m^0_{\text{ns},1}(\omega_1)/T$	9.9(3)	10.0(3)	9.97(12)
$\Delta m^{0,\text{ratio}}_{\text{ns}-\text{st}}(\omega_1)/T$	0.40(11)	1.18(12)	1.28(4)

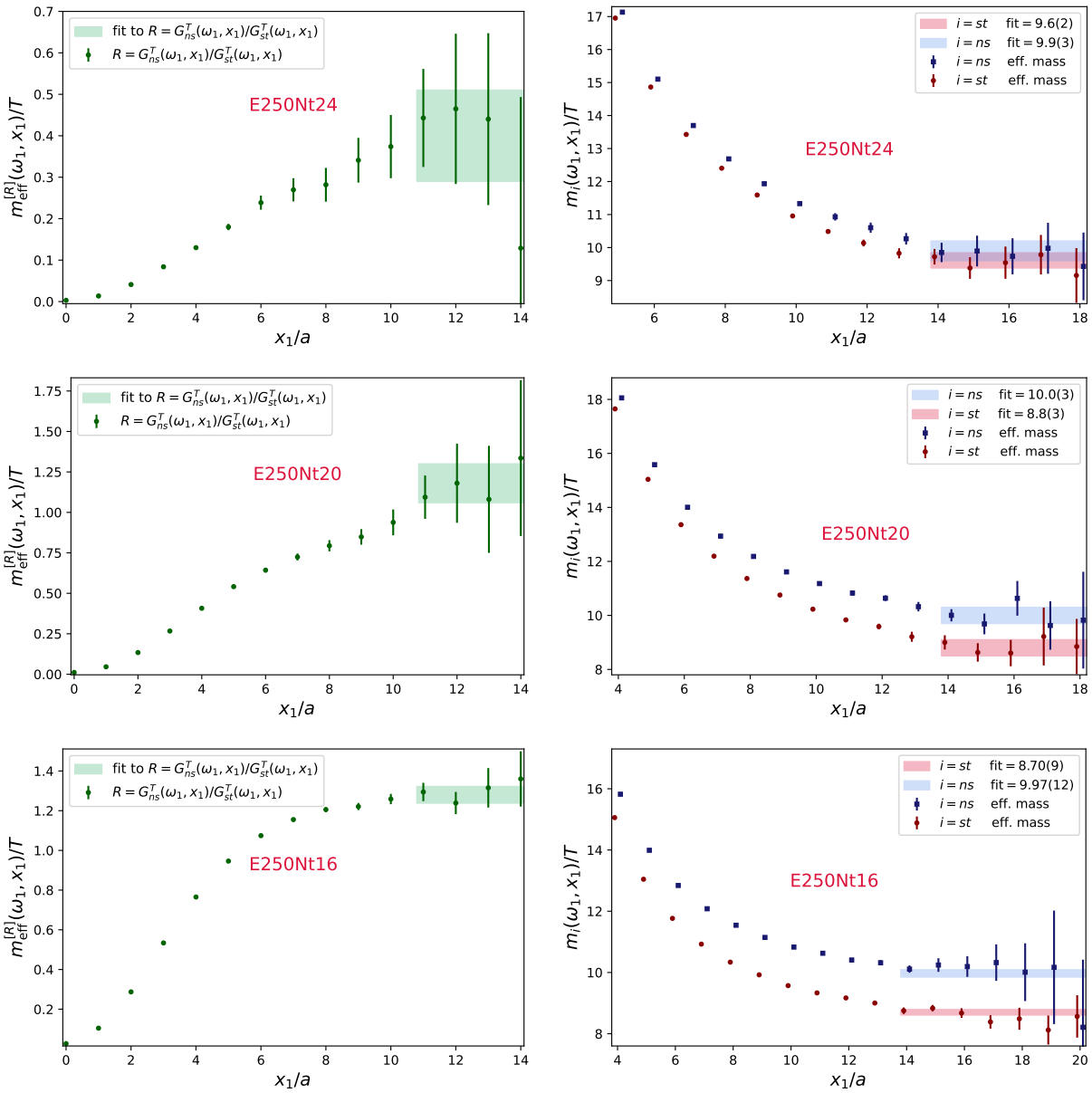

Figure 8.1: **Left column:** Effective masses based on Eq. (I.6) for the ratios of the non-static and static screening correlators in the first Matsubara sector ω_1. **Right column:** Effective masses and fit results from two-state fits with the fit ansatz Eq. (7.3.1) for the non-static (blue) and static (red) screening correlators at spatial momentum $\omega_1 = 2\pi T$ with $T \in \{128, 154, 192\}$ MeV.

crossover region. As discussed in Sec. 7.3.1, these screening masses are pivotal in modeling the long-distance behavior of the quantity H_E, as defined in Eq. (7.2.20).

The right column of Fig. 8.1 illustrates the effective masses of the non-static and static transverse screening correlators, while the left column displays the effective masses extracted from the ratio $G^{\mathrm{T}}_{\mathrm{ns}}(\omega_1, x_1)/G^{\mathrm{T}}_{\mathrm{st}}(\omega_1, x_1)$. The numerical results for the three temperatures $T \in \{128, 154, 192\}$ MeV are summarized in Table 8.1.

Across all three temperatures, the mass gap between the non-static and static sectors can be

determined from the ratio of correlators via,

$$\frac{|A^0_{i,r}(\omega_r)|^2}{|A^0_{j,n}(\omega_n)|^2}\frac{\cosh\left[m^0_{i,r}(\omega_r)\cdot(x_1-L/2)\right]}{\cosh\left[m^0_{j,n}(\omega_n)\cdot(x_1-L/2)\right]} \approx C\,\mathrm{e}^{-\left[m^0_{i,r}(\omega_r)-m^0_{j,n}(\omega_n)\right]x_1}, \quad i,j\in\{\mathrm{ns},\mathrm{st}\}, \quad (x_1\ll L/2), \tag{8.1.1}$$

with $i=\mathrm{ns}$, $j=\mathrm{st}$ and $r=n=1$. The values derived from a single-exponential fit align with the mass differences obtained from the multi-state fits based on Eq. (7.3.1) [refer to Table 8.1].

In the hadronic phase ($T=128\,\mathrm{MeV}$), the static and non-static screening masses are as follows:

$$m^0_{\mathrm{st},1}(\omega_1)/T|_{T=128\,\mathrm{MeV}} = 9.6(2)\,, \tag{8.1.2}$$
$$m^0_{\mathrm{ns},1}(\omega_1)/T|_{T=128\,\mathrm{MeV}} = 9.9(3)\,. \tag{8.1.3}$$

These values are degenerate within the uncertainties, suggesting minimal photon emissivity at this temperature.

At a temperature of $T=154\,\mathrm{MeV}$, the non-static screening mass is given by:

$$m^0_{\mathrm{ns},1}(\omega_1)/T|_{T=154\,\mathrm{MeV}} = 10.0(3)\,. \tag{8.1.4}$$

This value, expressed in temperature units, remains approximately constant compared to $T=128\,\mathrm{MeV}$. In contrast, the static screening mass is:

$$m^0_{\mathrm{st},1}(\omega_1)/T|_{T=154\,\mathrm{MeV}} = 8.8(3)\,. \tag{8.1.5}$$

This represents a decrease of approximately 8%. A similar pattern was observed in the completely static ($n=0$) channel. Consequently, a significant mass gap is observed, $\Delta m^0_{\mathrm{ns-st}}(\omega_1, T=154\,\mathrm{MeV})/T \approx 1.2(1)$, implying enhanced photon emissivity near the chiral crossover.

In the high-temperature phase ($T=192\,\mathrm{MeV}$), both the static and non-static screening masses,

$$m^0_{\mathrm{st},1}(\omega_1)/T|_{T=192\,\mathrm{MeV}} = 8.70(9)\,, \tag{8.1.6}$$
$$m^0_{\mathrm{ns},1}(\omega_1)/T|_{T=192\,\mathrm{MeV}} = 9.97(12)\,, \tag{8.1.7}$$

are statistically consistent with their counterparts at $T=154\,\mathrm{MeV}$. However, the results at $T=192\,\mathrm{MeV}\approx 1.2\,T_{\mathrm{pc}}$ [36] exhibit approximately threefold greater precision and suggest a marginally increased mass gap. When compared to the continuum extrapolated $N_{\mathrm{f}}=2$ results at $T=254\,\mathrm{MeV}\approx 1.2\,T_{\mathrm{pc}}$ [270], the ground-state static screening mass of 8.70(9) aligns closely with the $N_{\mathrm{f}}=2$ value of 8.65(10) as presented in Eq. (9.3.1). Conversely, the non-continuum extrapolated non-static screening mass of 9.97(12) lies above the $N_{\mathrm{f}}=2$ result of 9.17(16) [cf. Eq. (9.3.1)] by about $4\,\sigma$. This discrepancy may indicate more significant discretization effects in the non-static sector.

8.2 Temperature Scan of $H_E(\omega_1)$

From Eq. (7.4.7), it is evident that $H_E(\omega_n)$ contains information regarding the integrated photon emissivity. Figure 8.2 illustrates the temperature dependence of the integrand $h_E(\omega_1, x_1, T)$,

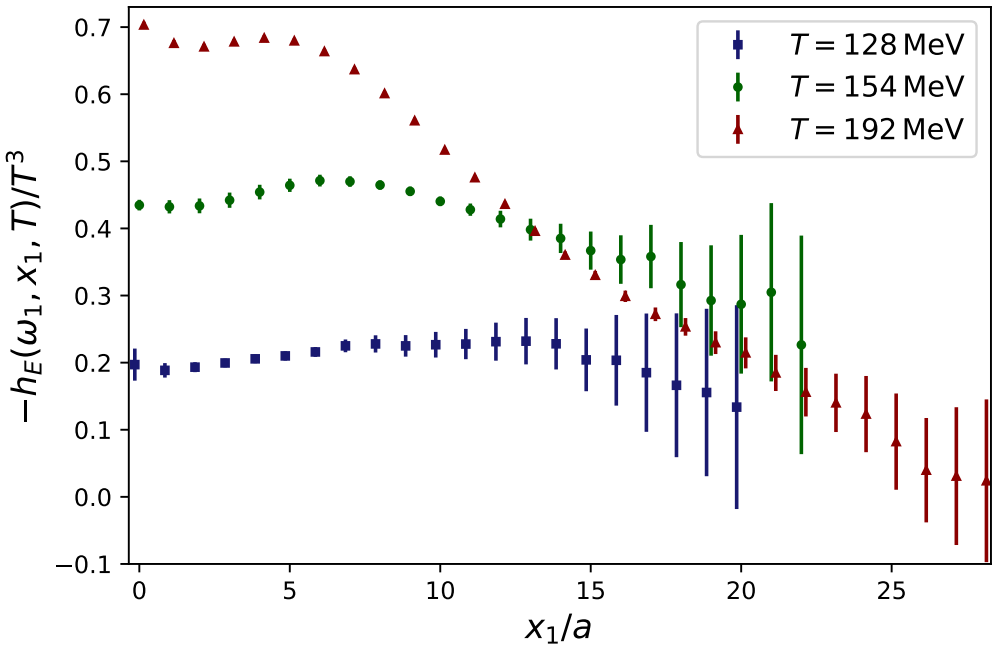

Figure 8.2: The temperature dependence of the integrand, as defined in Eq. (7.2.21) with $\Omega_n = \omega_n$, corresponding to the quantity $H_E(\omega_1, T)$, is presented. All values are expressed in temperature units and were derived using the E250 ensembles. For enhanced visibility, data points at varying temperatures are slightly offset along the x_1-axis.

which contributes to $H_E(\omega_1, T)$.

The signal significantly deteriorates at the lowest temperature, $T = 128\,\mathrm{MeV}$, representative of the hadronic phase; the signal is lost well before $x_1 T = 1$. The situation improves with increasing temperature, and at $T = 192\,\mathrm{MeV}$, the relative uncertainty at $x_1 T = 1$ is approximately 3%. The structure of the integrand exhibits substantial variation with temperature. First, the intercept of the integrand increases with temperature. At $T = 128\,\mathrm{MeV}$, the integrand remains nearly flat over an extensive range of x_1, reflecting long-range correlations in the hadronic phase. Conversely, at $T = 192\,\mathrm{MeV}$, it begins to decay more rapidly.

Additionally, it is observed that at $T = 128\,\mathrm{MeV}$, the integrand remains smaller than at higher temperatures throughout. However, the curves for $T = 154\,\mathrm{MeV}$ and $T = 192\,\mathrm{MeV}$ intersect around $\frac{x_1}{a} = 13$. Beyond this point, the $T = 154\,\mathrm{MeV}$ integrand becomes slightly larger than the $T = 192\,\mathrm{MeV}$ one within statistical uncertainties, suggesting enhanced photon emissivity around

Table 8.2: Results of the temperature scan conducted around the chiral crossover of the standard-subtracted quantity $H_E(\omega_1)$ [cf. Eq. (7.2.20)] in the $n = 1$ Matsubara sector. Additionally, we report the associated virtuality dependence, defined as $-H_{Q^2}(\omega_1, Q^2) \equiv -\frac{\mathrm{d}}{\mathrm{d}Q^2}[H_E(\omega_1, Q^2) - H_E(0, Q^2)]_{Q^2=0}$ [cf. Eq. (7.2.27)]. All quantities are expressed in temperature units. The results are derived from the E250 ensembles with $N_\tau \in \{24, 20, 16\}$, corresponding to $T \in \{128, 154, 192\}$ MeV.

Ensemble	E250Nt24	E250Nt20	E250Nt16
$-H_E(\omega_1)/T^2$	0.26(4)	0.56(5)	0.693(11)
$-H_{Q^2}(\omega_1, Q^2)$	0.031(4)	0.0423(11)	0.0297(3)

the chiral crossover.

To obtain the quantity $H_E(\omega_1)$, it is necessary to integrate the integrand defined in Eq. (7.2.21) over the decay direction x_1. The short-distance contribution to $H_E(\omega_1)$ is determined using the trapezoidal formula Eq. (7.2.31). However, as discussed in Sec. 7.3, the integrand $h_E(\omega_1, x_1, T)$ is affected by an exponential signal-to-noise problem. Therefore, to obtain the long-distance contribution of the integrand, the tail of $h_E(\omega_1, x_1, T)$ is modeled using Eq. (7.3.2) [see left column of Fig. 8.3]. The transition to the modeled tail has been seamlessly incorporated by employing a smooth step function as proposed in [6]. The selection of different switching points introduces a minor systematic error that is negligible compared to the substantial statistical error.

At the chiral crossover, the following result is obtained:

$$-\left.\frac{H_E(\omega_1)}{T^2}\right|_{\text{model}}^{T=154\,\text{MeV}} = 0.56(5)\,. \tag{8.2.1}$$

This value is approximately 2.15 times greater than the corresponding value at $T = 128\,\text{MeV}$:

$$-\left.\frac{H_E(\omega_1)}{T^2}\right|_{\text{model}}^{T=128\,\text{MeV}} = 0.26(4)\,. \tag{8.2.2}$$

Moreover, it is about 0.81 times the value observed in the high-temperature ensemble:

$$-\left.\frac{H_E(\omega_1)}{T^2}\right|_{\text{model}}^{T=192\,\text{MeV}} = 0.693(11)\,. \tag{8.2.3}$$

The measurement at $T = 192\,\text{MeV}$ aligns well with the continuum-extrapolated $N_\text{f} = 2$ result as presented in Eq. (9.3.8). The temperature trends and associated virtuality derivatives are detailed in Table 8.2. In the subsequent section, an independent cross-check of the chiral crossover result is conducted employing the bounding method. This approach does not rely on a specific model for the long-distance behavior of the correlator but instead exploits rigorous upper and lower bounds derived from known pseudoscalar ground-state energies. Applying it at $T = 154\,\text{MeV}$ provides a valuable test of the robustness of the sizeable increase in $H_E(\omega_1)$ observed in the model analysis.

8.2.1 Bounding Method

The transverse screening correlators, as defined in Eqs. (7.2.12) and (7.2.13), are amenable to the spectral representation outlined in Eq. (7.2.14). By employing the methodology developed in the study of the muon anomalous magnetic moment $(g-2)$ [271–273] and exploiting the positivity of both amplitudes and energies, it is possible to establish rigorous upper and lower bounds on each correlator for any separation $x_1 \geq x_\text{cut}$, given a fixed reference point x_cut. For any channel i, these bounds are expressed as:

$$\begin{aligned} 0 &\leq G_i^\text{T}(\omega_1, x_\text{cut}) \mathrm{e}^{-m_\text{eff}(x_\text{cut})\cdot(x_1 - x_\text{cut})} \\ &\leq G_i^\text{T}(\omega_1, x_1) \leq G_i^\text{T}(\omega_1, x_\text{cut}) \mathrm{e}^{-E_{i,1}^0 \cdot (x_1 - x_\text{cut})}\,, \quad x_1 \geq x_\text{cut}\,. \end{aligned} \tag{8.2.4}$$

Here, $m_\text{eff}(x_\text{cut})$ represents the effective mass evaluated at the reference separation, and $E_{i,1}^0$ denotes the ground-state energy in the corresponding channel, as defined below in Eqs. (8.2.7)

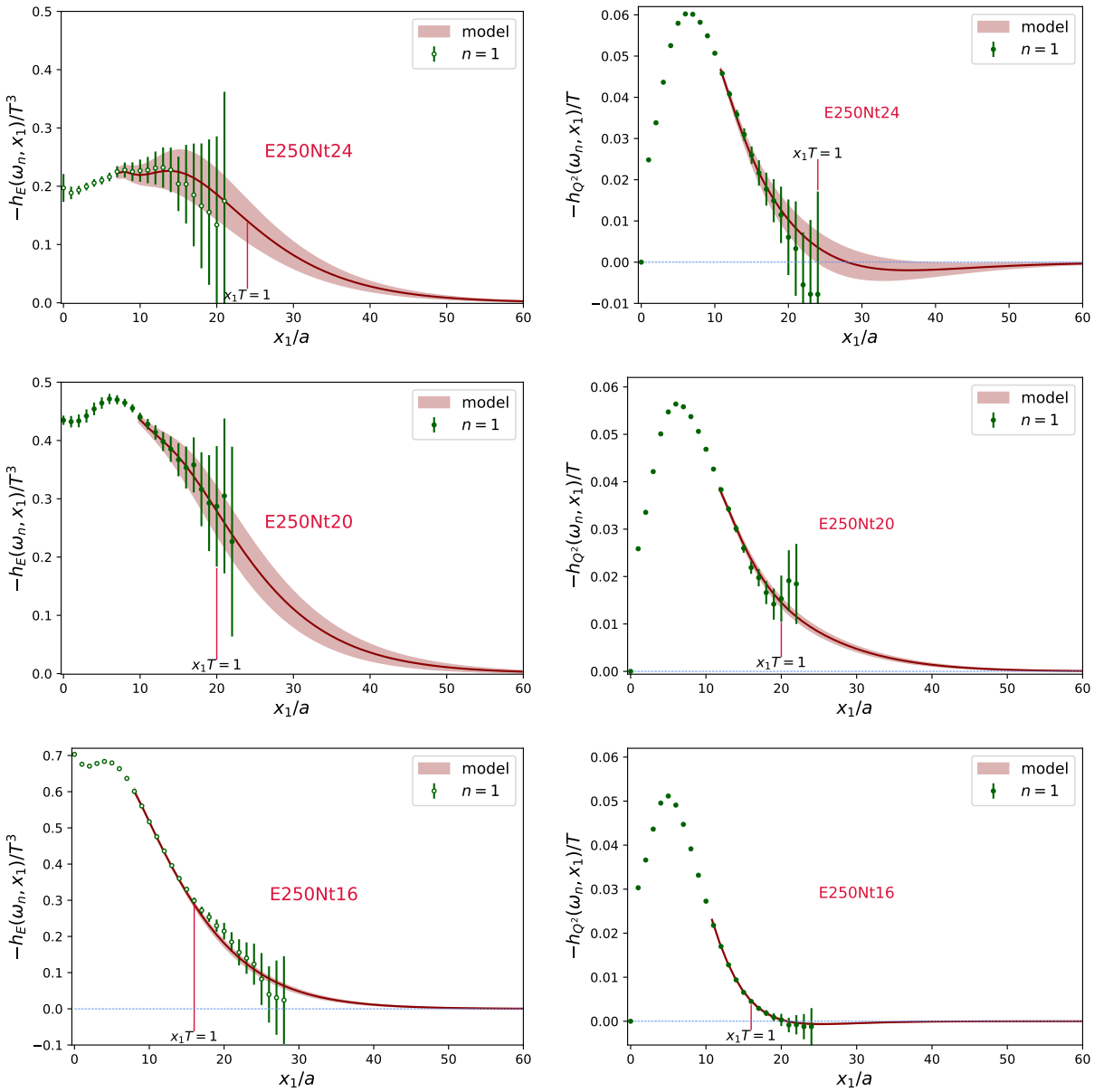

Figure 8.3: Symmetrized integrands and their modeled tail contributions for three temperatures $T \in \{128, 154, 192\}$ MeV. **Left column:** x_1-symmetrized integrand $h_E(\omega_1, x_1)$ from Eq. (7.2.21) with its modeled tail from Eq. (7.3.2). **Right column:** x_1-symmetrized integrand $h_{Q^2}(\omega_1, x_1)$ from Eq. (7.2.32) with an analogous modeled tail.

and (8.2.8). These bounds offer a systematic approach to constrain the long-distance behavior of the correlator beyond x_{cut}. Given that the estimator H_E in Eq. (7.2.20) is defined as the difference of two correlators, rigorous bounds on H_E can be derived by combining the individual bounds on the non-static and static correlators. Denoting the upper (lower) bound of a correlator G by $G|_{\text{ub}}$ ($G|_{\text{lb}}$), we obtain

$$H_E(\omega_1)|_{\text{ub}} \propto G^{\text{T}}_{\text{ns}}(\omega_1, x_1)\Big|_{\text{ub}} - G^{\text{T}}_{\text{st}}(\omega_1, x_1)\Big|_{\text{lb}} , \tag{8.2.5}$$

$$H_E(\omega_1)|_{\text{lb}} \propto G^{\text{T}}_{\text{ns}}(\omega_1, x_1)\Big|_{\text{lb}} - G^{\text{T}}_{\text{st}}(\omega_1, x_1)\Big|_{\text{ub}} . \tag{8.2.6}$$

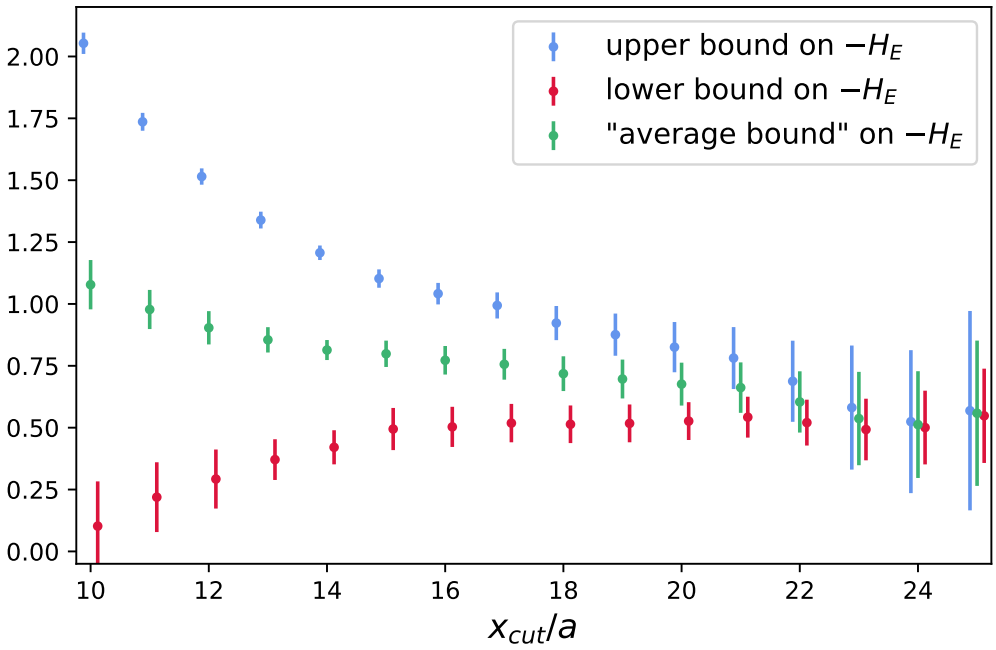

Figure 8.4: Lower and upper bounds on $H_E(\omega_1)$ at a temperature $T = 154$ MeV, based on Eqs. (8.2.5) and (8.2.6). These bounds converge toward that quantity for $x_{\text{cut}} \to \infty$.

Assuming that the long-distance spectrum is predominantly influenced by two-pion states, the rationale for the ground-state energies employed herein is as follows. For the static correlator, which involves two pions with back-to-back momenta transverse to both the decay direction and the vector index, we consider

$$E^0_{\text{st},1}(p) = 2\sqrt{\left(\frac{p}{2}\right)^2 + m_\pi^2 + \left(\frac{2\pi}{L}\right)^2}, \tag{8.2.7}$$

where each pion possesses transverse momentum $\frac{p}{2} = \pi T$, and m_π denotes the zero-momentum pion mass; the term $2\pi/L$ represents the minimal momentum in the spatial direction of the vector index. In the non-static sector, where one pion is at rest and the other carries the first Matsubara frequency in the temporal direction, we utilize

$$E^0_{\text{ns},1}(\omega_1) = \sqrt{m_\pi^2 + \left(\frac{2\pi}{L}\right)^2} + \sqrt{E_\pi(\omega_1)^2 + \left(\frac{2\pi}{L}\right)^2}, \tag{8.2.8}$$

where $E_\pi(\omega_1)$ represents the pion energy at temporal momentum ω_1. Figure 8.4 illustrates the resultant upper and lower bounds on $H_E(\omega_1)$ at $T = 154\,\text{MeV}$. The correlators were constrained from below using the measured effective masses and from above using the two-pion ground-state energies as defined above. As $x_{\text{cut}} \to \infty$, it is anticipated that the two bounds will converge to the true value of $H_E(\omega_1)$. We report the average value of the upper and lower bounds as our estimate,

$$-\left.\frac{H_E(\omega_1)}{T^2}\right|^{T=154\,\text{MeV}}_{\text{bound}} = 0.62(13)\,, \tag{8.2.9}$$

at $\frac{x_{\text{cut}}}{a} = 22$. At this source–sink separation, both the upper and lower bounds (each depicted in Fig. 8.4 with their respective statistical error bars) are consistent with the quoted central value within one standard deviation. Within the uncertainties, this bound-based determination agrees with the model result in Eq. (8.2.1), thereby providing an independent validation of the significant enhancement of $H_E(\omega_1)$ at the chiral crossover.

8.3 Temperature Scan of the Q^2 Derivative of $H_E(\omega_1, Q^2)$ at $Q^2 = 0$

To examine the Q^2-dependence of the quantity H_E, we focus on the Q^2-derivative of the difference $H_E(\omega_1, Q^2) - H_E(0, Q^2)$, as introduced in Sec. 7.2.2. The corresponding continuum expression is provided in Eq. (7.2.27), with the associated lattice integrand defined in Eq. (7.2.32).

It is instructive to analyze this integrand—displayed in the right column of Fig. 8.3—which demonstrates a stronger emphasis on short distances compared to the integrand $h_E(\omega_1, x_1)$ shown in the left column of Fig. 8.3. Starting quadratically at small source-sink separations x_1, the integrand reaches a pronounced peak around $x_1 T \approx \frac{1}{3}$. For $T \in \{128, 192\}$ MeV, it subsequently crosses zero slightly beyond $x_1 T \approx 1$, turns mildly negative, and approaches the x_1-axis asymptotically from below. In contrast, at $T = 154$ MeV, the integrand remains strictly positive and does not cross zero. Compared to the case of $H_E(\omega_1)$, long-distance contributions are significantly more suppressed for all three temperatures.

At the chiral crossover, the derivative of $H_E(\omega_1, Q^2)$ w.r.t. Q^2 at $Q^2 = 0$, evaluates to

$$-\frac{\mathrm{d}}{\mathrm{d}Q^2}\left[H_E(\omega_1, Q^2) - H_E(0, Q^2)\right]_{Q^2=0}^{T=154\,\text{MeV}} = 0.0423(11)\,, \tag{8.3.1}$$

which is about 40% larger than in both the low- and high-temperature phases, the latter two being mutually compatible within uncertainties [see Table 8.2]. For reference, in the high-temperature phase we obtain

$$-\frac{\mathrm{d}}{\mathrm{d}Q^2}\left[H_E(\omega_1, Q^2) - H_E(0, Q^2)\right]_{Q^2=0}^{T=192\,\text{MeV}} = 0.0297(3)\,. \tag{8.3.2}$$

Chapter 9

$N_f = 2$ Continuum Extrapolated Results on the First Three Matsubara Sectors

In this chapter, we present continuum-extrapolated $N_f = 2$ results concerning the static and non-static screening masses in both the completely static (ω_0) and the first three Matsubara sectors. We utilize lattice QCD with two flavors of $\mathcal{O}(a)$-improved Wilson fermions. These findings are compared to predictions derived from the continuum dispersion relation (static) and EQCD (non-static). We further analyze the first three energy moments $H_E(\omega_n)$ without encountering an inverse problem. In addition, we examine the virtuality dependence of $H_E(\omega_1)$. Furthermore, we compare our results in the first two Matsubara sectors with weak-coupling predictions. Parts of this chapter are based on the following references:

Authors:	Marco Cè, Tim Harris, **Ardit Krasniqi**, Harvey B. Meyer, Csaba Török
Title	Probing the photon emissivity of the quark-gluon plasma without an inverse problem in lattice QCD
Year:	2024
Journal:	*Physical Review D*
Volume/Issue:	109, 1
DOI:	10.1103/PhysRevD.109.014507

Authors:	**Ardit Krasniqi**, Marco Cè, Tim Harris, Renwick J. Hudspith, Harvey B. Meyer
Title:	Probing how bright the quark-gluon plasma glows in lattice QCD
Year:	2025
Journal:	*Physical Review D*
Volume/Issue:	112, 7
DOI:	10.1103/PhysRevD.112.074503

9.1 Simulation Details and Algorithmic Aspects

Our lattice simulations are conducted on three ensembles, labeled as X7, W7, and O7, with lattice spacings $a \in \{0.033, 0.039, 0.049\}$ fm, calibrated to a uniform temperature of $T \approx 254$ MeV. We utilize $N_f = 2$ flavors of dynamical $\mathcal{O}(a)$-improved Wilson fermions together with the Wilson gauge action. The simulations are performed at an unphysical *in vacuo* pion mass of $m_\pi \approx 270$ MeV [270]. Despite this, quark-mass effects on the correlators are anticipated to be suppressed by a factor of $(m_q/T)^2$ in the high-temperature phase.

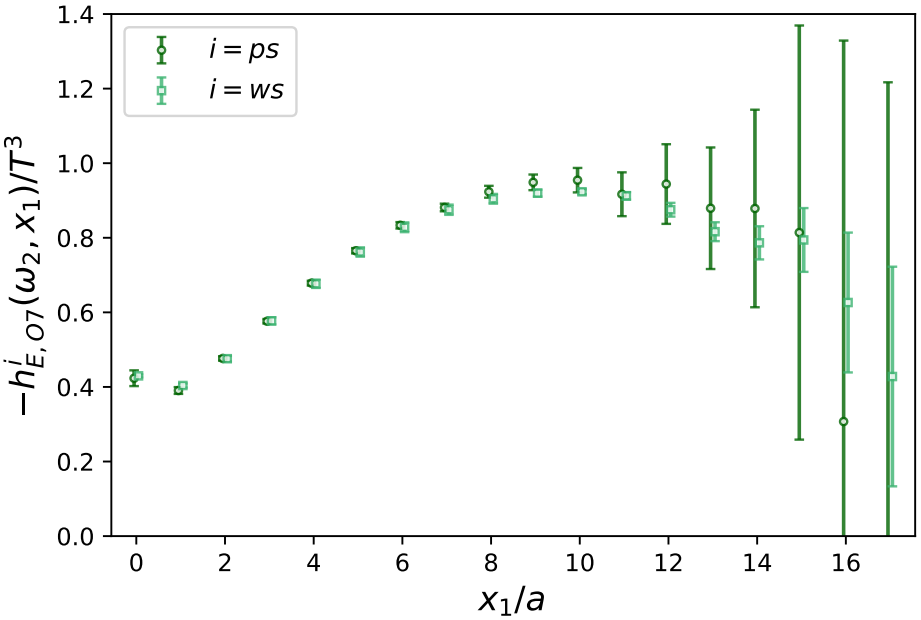

Figure 9.1: Comparison of the integrand $-h_E^{\mathrm{ps}}(\omega_2, x_1)$ $(k = \infty)$ used in [6] with $-h_E^{\mathrm{ws}}(\omega_2, x_1)$ utilized in this thesis, for the coarsest ensemble O7. At $x_1 = 15a$, the statistical error is reduced by a factor of ≈ 6.5.

High statistical accuracy is achieved for the relevant correlators: the propagators involved in Eq. (7.2.21) are computed using "`Z2SEMWall`" [170, 173, 174] stochastic momentum [176] wall sources, in combination with the truncated solver method [178]. In practice, this entails performing a significantly greater number of low-precision solves for spatial translations across the lattice than high-precision solves. The Dirac equation is solved using the DFL+SAP+GCR algorithm as described in [274], where the cost of generating the deflation subspace is amortized by the large number of low-precision translations and stochastic "hits" we perform. The combination of stochastic momentum wall sources with the truncated solver method results in substantially higher statistical precision than the exact point sources used in the previous study. [6], typically at a reduced overall cost. The only limitation of this approach is that the momenta must be fixed *a priori*.

Simulations were performed at a constant temperature and an aspect ratio of $L/\beta = 4$, where L and β represent the spatial and temporal lattice extents, respectively. The parameters of the en-

Table 9.1: Overview of the $N_f = 2$ ensembles used in this study. The parameters given are the bare gauge coupling g_0, the Wilson hopping parameter κ, the lattice spacing a, the temporal size β in units of the lattice spacing a, the number of configurations N_{con}, and the total number of Dirac operator inversions N_{inv} for the first and second Mastubara sectors.

label	$6/g_0^2$	κ	a [fm]	β/a	N_{con}	$\frac{N_{\mathrm{inv}}^{\omega_1}}{10^7}$	$\frac{N_{\mathrm{inv}}^{\omega_2}}{10^7}$
O7	5.5	0.13671	0.049	16	1400	2.15	8.60
W7	5.685727	0.136684	0.039	20	1600	1.54	4.61
X7	5.827160	0.136544	0.033	24	1500	1.73	5.18

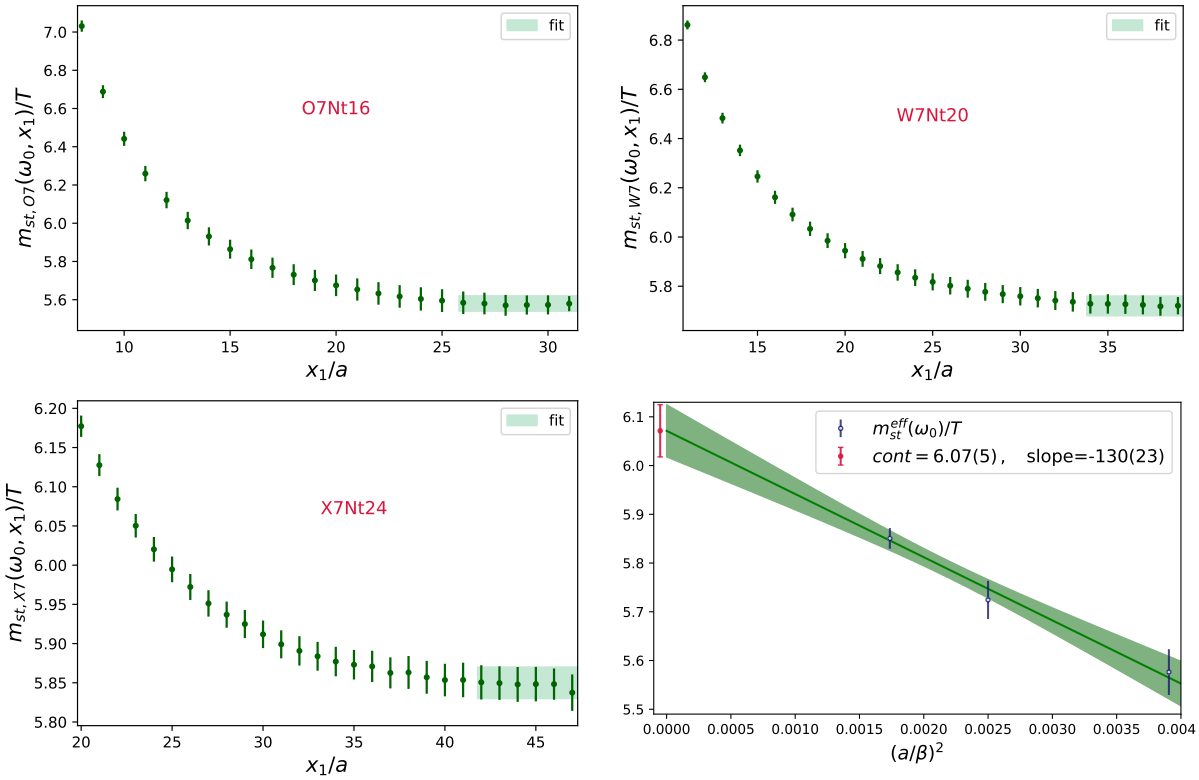

Figure 9.2: **First three panels:** Effective masses for the completely static (zero momentum) local-local isovector vector correlator on the three ensembles O7, W7, and X7. The light green horizontal band indicates the fit result derived from the ansatz in Eq. (7.3.1). **Last panel:** Corresponding continuum extrapolation.

semble are detailed in Table 9.1. The number of Dirac operator inversions is calculated as follows:

$$N_{\text{inv}} = N_{\text{trans}} \times N_{\text{hits}} \times N_{\text{con}} \times N_p \times 4 \times 3\,,$$

where N_{trans} indicates the number of spatial translations, set to L/a, N_{hits} represents the number of stochastic draws of the source, N_p denotes the number of momentum sources, the factor of 4 corresponds to the number of spin indices, and 3 is the number of spatial decay directions employed. It is important to note that no color dilution is applied. The enhanced statistical precision achieved with wall sources, as opposed to point sources, is demonstrated in Fig. 9.1 for the integrand $h_E(\omega_2, x_1)$ on the coarsest ensemble O7.

9.2 The Completely Static ω_0-sector

The completely static (i.e. zero momentum) ground state screening mass $m^0_{\text{st},0}(\omega_0)$ can be determined with sub-percent precision. This is possible because of the long-distance behavior of the correlator,

$$G^{\text{T}}_{\text{st},0}(\omega_0, x_1) = \frac{1}{2}\sum_{i=2,3}\int_0^\beta \mathrm{d}x_0 \int \mathrm{d}^2x_\perp \langle j_i(x) j_i^\dagger(0)\rangle\,, \tag{9.2.1}$$

and hence its effective mass remains well controlled up to the correlator midpoint [see the first three panels of Fig. 9.2]. The continuum extrapolation [last panel of Fig. 9.2] result, yields

$$m_{\mathrm{st},0}^{0,\mathrm{fit}}(\omega_0)/T = 6.071(54)\,, \tag{9.2.2}$$

which is in excellent agreement with our previous determination $m_{\mathrm{st},0}^{0,\mathrm{ps}}(\omega_0)/T = 6.04(2)$ obtained using point sources [6]. In the continuum and infinite-volume limit, the static screening masses are derived from the relativistic dispersion relation

$$m_{\mathrm{st},n}^{0,\mathrm{disp}}(\omega_n)/T = \sqrt{(m_{\mathrm{st},0}^{0,\mathrm{fit}}(\omega_0)/T)^2 + (2\pi n)^2}\,. \tag{9.2.3}$$

Consequently, we obtain the static screening masses in the higher Matsubara sectors:

$$m_{\mathrm{st},1}^{0,\mathrm{disp}}(\omega_1)/T = 8.737(37)\,, \tag{9.2.4}$$
$$m_{\mathrm{st},2}^{0,\mathrm{disp}}(\omega_2)/T = 13.956(23)\,, \tag{9.2.5}$$
$$m_{\mathrm{st},3}^{0,\mathrm{disp}}(\omega_3)/T = 19.803(16)\,. \tag{9.2.6}$$

These will be compared with the corresponding direct lattice determinations in the following sections.

9.3 Continuum Extrapolated Observables in the ω_1-Sector

In this section, we present the continuum-extrapolated results for both the static and non-static screening masses within the first Matsubara sector. Additionally, we provide results for the standard-subtracted quantity $H_E(\omega_1)$, as defined in Eq. (7.2.20), along with its derivative w.r.t. Q^2 at $Q^2 = 0$ [cf. Eq. (7.2.27)].

9.3.1 Screening Masses in the First Matsubara Sector

For the continuum results of the static and non-static screening masses in the first Matsubara sector [see Figs. 9.3 - 9.4], we obtain

$$m_{\mathrm{st},1}^{0,\mathrm{fit}}(\omega_1)/T = 8.65(10)\,, \tag{9.3.1}$$
$$m_{\mathrm{ns},1}^{0,\mathrm{fit}}(\omega_1)/T = 9.17(16)\,, \tag{9.3.2}$$
$$[m_{\mathrm{ns},1}^{0,\mathrm{fit}}(\omega_1) - m_{\mathrm{st},1}^{0,\mathrm{fit}}(\omega_1)]/T = 0.53(19)\,. \tag{9.3.3}$$

The continuum-extrapolated mass gap between the non-static screening mass and the static screening mass in the first Matsubara sector (9.3.3) is in good agreement with the continuum estimate,

$$m_{\mathrm{ns},1}^{0,\mathrm{ratio}}(\omega_1)/T - m_{\mathrm{st},1}^{0,\mathrm{ratio}}(\omega_1)/T = 0.549(58)\,, \tag{9.3.4}$$

obtained from a single-exponential fit [cf. Eq. (8.1.1)] to the ratio of the non-static and the static screening correlator, both evaluated in the first Matsubara sector.

The continuum extrapolated static screening mass (9.3.1) agrees well with the dispersive pre-

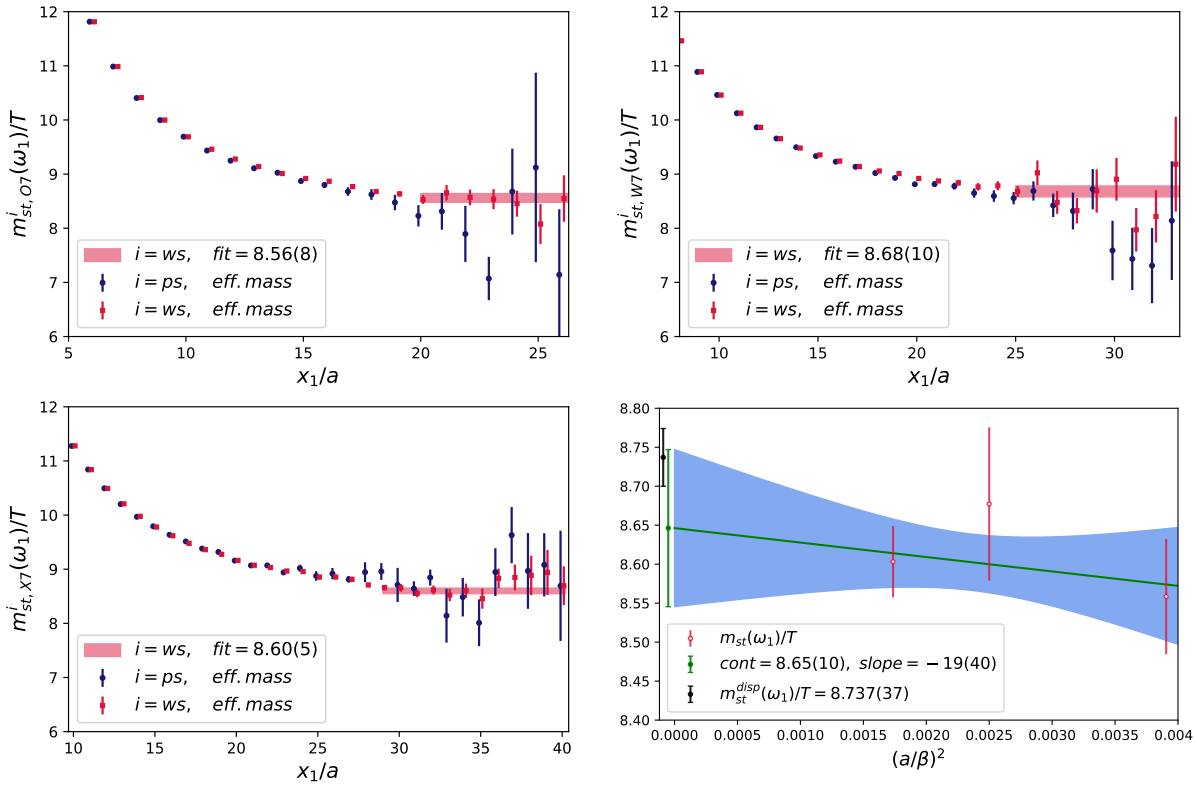

Figure 9.3: **First three panels:** Effective masses (represented by red bars) for the static local-local isovector vector correlator in the first Matsubara sector are depicted for the O7, W7, and X7 ensembles. The red horizontal band indicates the fit result derived using the ansatz specified in Eq. (7.3.1). For comparative purposes, effective masses from the earlier point-source data presented in Ref. [6] are illustrated as blue bars. For this comparison, the outlier elimination procedure detailed in Appendix A of Ref. [6] has not been applied. **Last panel:** The corresponding continuum extrapolation is shown, alongside the prediction derived from the dispersion relation [cf. Eq. (9.2.4)].

diction derived from the $n = 0$ estimate in Eq. (9.2.4). Given that the slope of the continuum extrapolation is statistically indistinguishable from zero, we also conducted an extrapolation with the slope constrained to zero, resulting in $m^{0,\mathrm{fit}}_{\mathrm{st},1}(\omega_1)/T = 8.60(4)$, which aligns with the aforementioned free-slope result. We note that our estimate in Eq. (9.3.1) is also consistent, within the margin of error, with our previous point-source result $m^{0,\mathrm{ps}}_{\mathrm{st},1}(\omega_1)/T = 8.81(10)$ [6]. A direct comparison of the effective masses obtained from point-source and wall-source data, as depicted in the first three panels of Fig. 9.3 reveals two significant distinctions. First, on the coarsest ensemble (O7), the wall-source data exhibit a more pronounced and earlier onset of a plateau compared to the point-source data. Second, even on the finest ensemble (X7), the point-source data display a non-monotonic increase in statistical errors with x_1, a phenomenon absent in the wall-source results. These observations underscore the enhanced statistical quality and plateau stability achieved utilizing the wall-source set-up

Similarly, the continuum-extrapolated non-static screening mass (9.3.2) demonstrates a strong

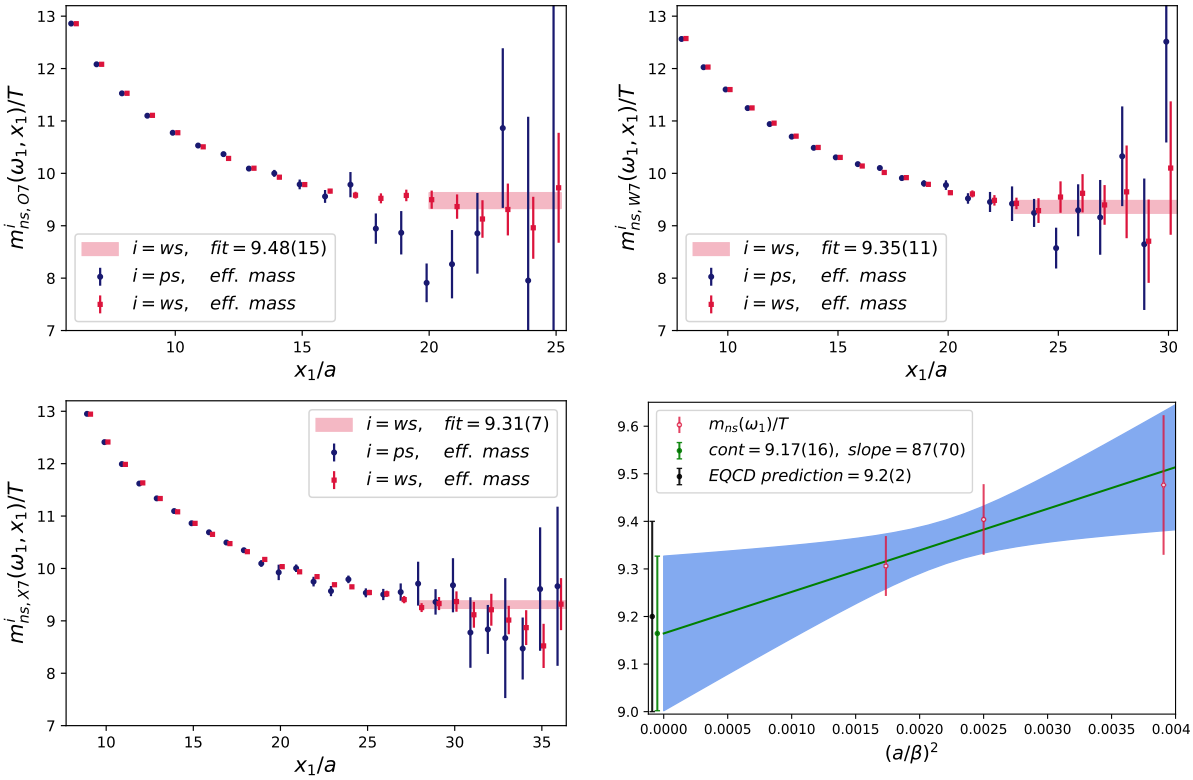

Figure 9.4: **First three panels:** Effective masses (red bars) for the non–static local–local isovector vector correlator in the first Matsubara sector on the O7, W7, and X7 ensembles. The red horizontal line indicates the fit result from ansatz Eq. (7.3.1). For comparison, effective masses from the earlier point–source data of Ref. [6] are shown as blue bars. **Last panel:** Corresponding continuum extrapolation, shown together with the EQCD prediction of Ref. [261].

concordance with the EQCD prediction from Ref. [261], given by:

$$m^{0,\mathrm{EQCD}}_{\mathrm{ns},1}(\omega_1)/T = 9.2(2)\,. \tag{9.3.5}$$

In contrast to our previous point-source result, $m^{0,\mathrm{ps}}_{\mathrm{ns},1}(\omega_1)/T = 9.57(22)$ [6], the slope of the continuum extrapolation has undergone a sign change [cf. the right panel of Fig. 8 in Ref. [6] with the last panel of Fig. 9.4]. This inversion in sign is primarily attributable to the coarsest ensemble (O7), where the point-source data underestimate the non-static mass in comparison to the wall-source results (see first panel of Fig. 9.4). The upward adjustment of the O7 value in the wall-source analysis aligns the coarse-lattice point more closely with the finer ensembles, thereby resulting in the observed positive slope.

As a cross-check of the non-static screening mass in the first Matsubara sector (9.3.2), we determine it iteratively, starting from the completely static screening mass (9.2.2). Initially, we incorporate the mass gap between the completely static screening mass and the static screening mass in the first Matsubara sector,

$$m^{0,\mathrm{ratio}}_{\mathrm{st},1}(\omega_1)/T - m^{0,\mathrm{ratio}}_{\mathrm{st},0}(\omega_0)/T = 2.749(88)\,, \tag{9.3.6}$$

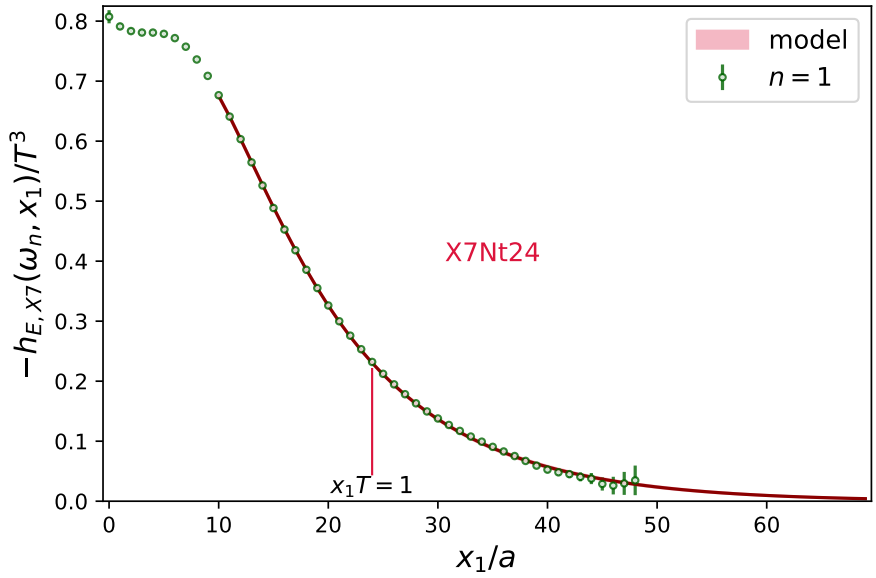

Figure 9.5: Integrand $-h_E(\omega_1, x_1)/T^3$ from Eq. (7.2.21) computed on the finest ensemble X7 using the standard cosh-kernel [$k = \infty$ in Eq. (7.2.19)]. The result includes the tail modification from Eq. (7.3.2). The red vertical line marks the source–sink separation $x_1T = 1$; here the relative error on the integrand is 0.7%. For the largest values of x_1, the influence of the variable's periodicity is evident.

and subsequently, we add the corresponding static-to-non-static mass gap (9.3.6)). Following this procedure, we obtain

$$m_{\mathrm{ns},1}^{0,\mathrm{gaps}}(\omega_1)/T = 9.285(84)\,, \tag{9.3.7}$$

which agrees within errors with the direct determination in Eq. (9.3.2).

9.3.2 Continuum Extrapolation of $H_E(\omega_1)$

In accordance with Eq. (7.2.20), the evaluation of H_E uses the transverse non-static and static screening correlators at finite spatial momentum together with the corresponding screening masses, which are then used to model the long-distance tail contribution via the fit ansatz (7.3.2). As shown in Fig. 9.5, $H_E(\omega_1)$ is predominantly influenced by contributions from the region where $x_1T \lesssim 1$–1.5, a range in which our current statistical data provides a well-controlled signal. Notably, on the finest ensemble X7, the relative error of the integrand at $x_1T = 1$ is merely 0.7%.

We assess the quantity H_E as delineated in Sec. 7.3.1. The findings demonstrate robustness against variations in the switching point x_w employed for tail modification. Our final estimate is

$$-\frac{H_E(\omega_1, k = \infty)}{T^2} = 0.676(7)\,, \tag{9.3.8}$$

as illustrated in the left panel of Fig. 9.6. Here, $k = \infty$ refers to potential kernel modifications as specified in Eq. (7.2.19). These modifications become significant in the $n = 2$ sector, as discussed in Sec. 9.4.2. For $H_E(\omega_1)$, even the selection $k = 1$ results in $-H_E(\Omega_1(k = 1))/T^2 = 0.668(7)$, which is in good agreement with Eq. (9.3.8). The slope of the quoted continuum extrapolated result is zero within the margin of error. Our findings also align with the previous point-source

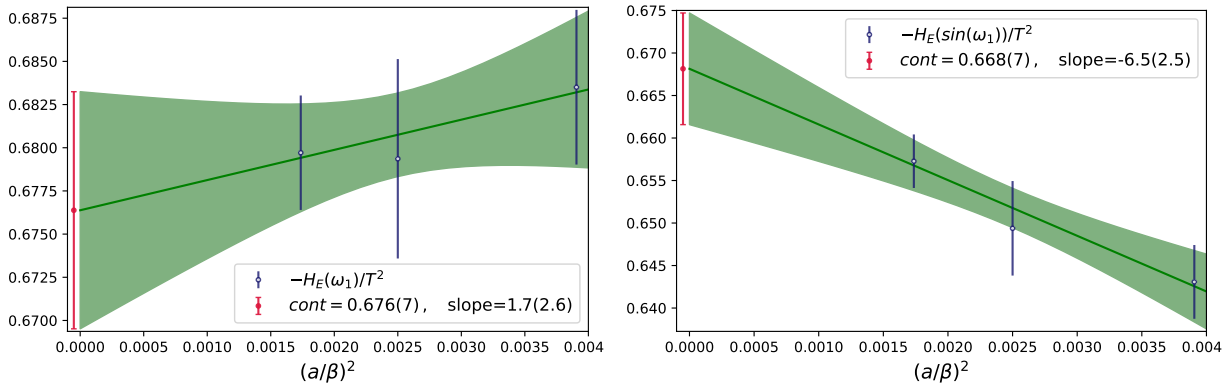

Figure 9.6: **Left panel:** Continuum extrapolation of $-H_E(\omega_1)/T^2$ using the standard cosh kernel ($k = \infty$ in Eq. (7.2.19)). **Right panel:** Continuum extrapolation of $-H_E(\sin(\omega_1))/T^2$ using the modified cosh(sin)-kernel ($k = 1$ in Eq. (7.2.19)).

determination [6]

$$-\frac{H_E(\omega_1)}{T^2} = 0.670(6)\,, \tag{9.3.9}$$

suggesting that systematic effects are negligible in this context and require further consideration solely in the $n = 2$ sector presented in Sec. 9.4.2.

9.3.3 Continuum Extrapolation of the Q^2 Derivative of $H_E(\omega_1, Q^2)$ at $Q^2 = 0$

To evaluate the Q^2-dependence of $H_E(\omega_1, Q^2)$, we follow the methodology outlined in Sec. 8.3. The integrand, depicted in the top panel of Fig. 9.7, exhibits a quadratic increase at small source–sink separations x_1 and features a notable peak near $x_1 T \approx \frac{1}{4}$. In comparison to the high-temperature scenario of the temperature scan, $H_E(\omega_1, Q^2, T = 192\,\text{MeV})$ (bottom right of Fig. 8.3), the integrand again intersects zero around $x_1 T \approx 1$, remains negative even for $x_1 T \gtrsim 2$, and asymptotically approaches the x_1-axis from below. Our final continuum-extrapolated estimate of the derivative of $H_E(\omega_1, Q^2)$ w.r.t. Q^2 at $Q^2 = 0$ is

$$-\frac{\mathrm{d}}{\mathrm{d}Q^2}\left[H_E(\omega_1, Q^2) - H_E(0, Q^2)\right]^{\text{continuum}}_{Q^2=0} = 0.02750(32)\,, \tag{9.3.10}$$

which is approximately 7% smaller than the non-continuum-extrapolated $N_f = 2+1$ high-temperature result in Eq. (8.3.2).

9.4 Continuum Extrapolated Observables in the ω_2-Sector

In this section, we present the continuum-extrapolated results for both the static and non-static screening masses within the second Matsubara sector. Additionally, we provide results for the standard-subtracted quantity $H_E(\omega_2)$, as defined in Eq. (7.2.20).

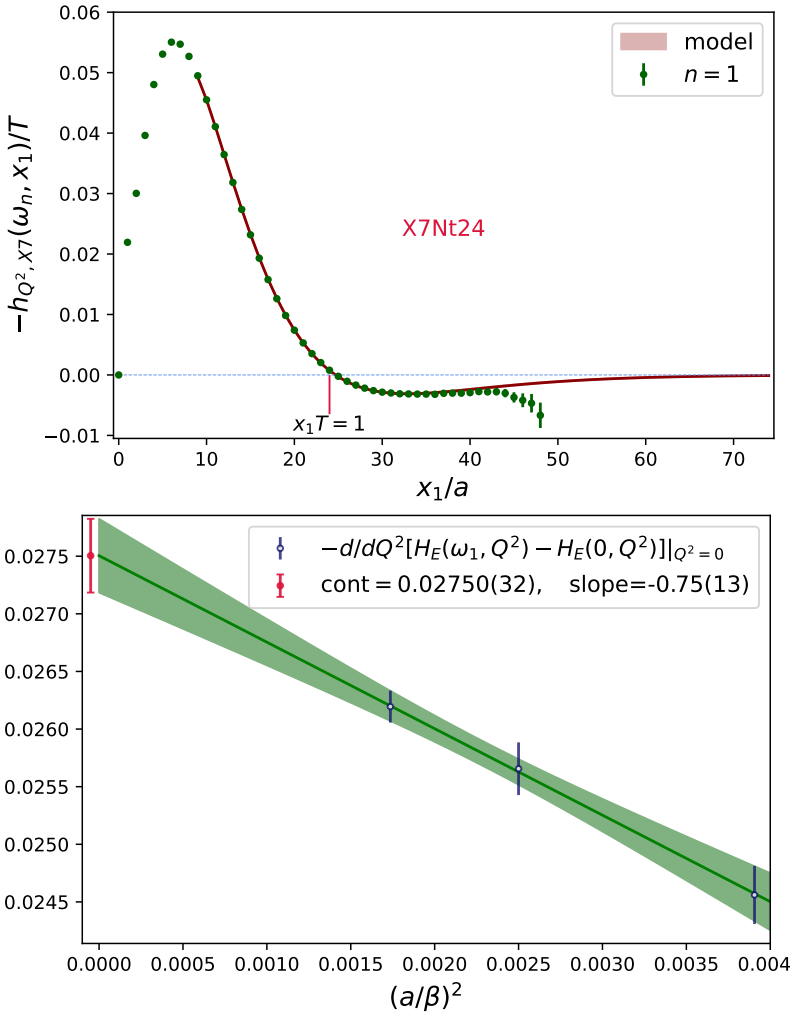

Figure 9.7: **Top panel:** The integrand $-h_{Q^2}(\omega_1, x_1)$ from Eq. (7.2.32), which contributes to the derivative of $-H_E(\omega_1, Q^2)$ w.r.t. Q^2 at $Q^2 = 0$, is depicted for the X7 ensemble. The result incorporates the tail modification analogous to Eq. (7.3.2). The red vertical line indicates the source–sink separation $x_1 T = 1$. **Bottom panel:** Corresponding continuum extrapolation of $-\frac{\mathrm{d}}{\mathrm{d}Q^2}[H_E(\omega_1, Q^2) - H_E(0, Q^2)]|_{Q^2=0}$.

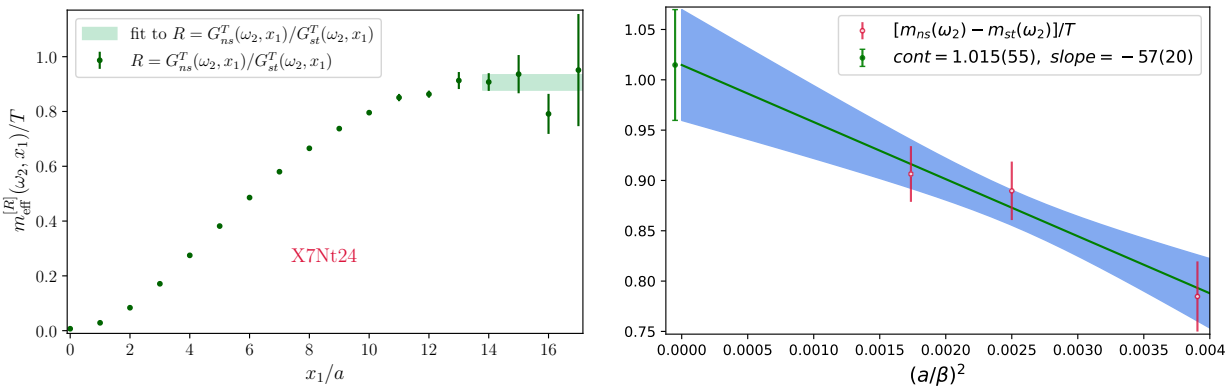

Figure 9.8: **Left panel:** The effective mass gap between the non-static and static screening masses in the second Matsubara channel, as derived from the correlator ratio on the X7 ensemble. **Right panel:** The corresponding continuum extrapolation.

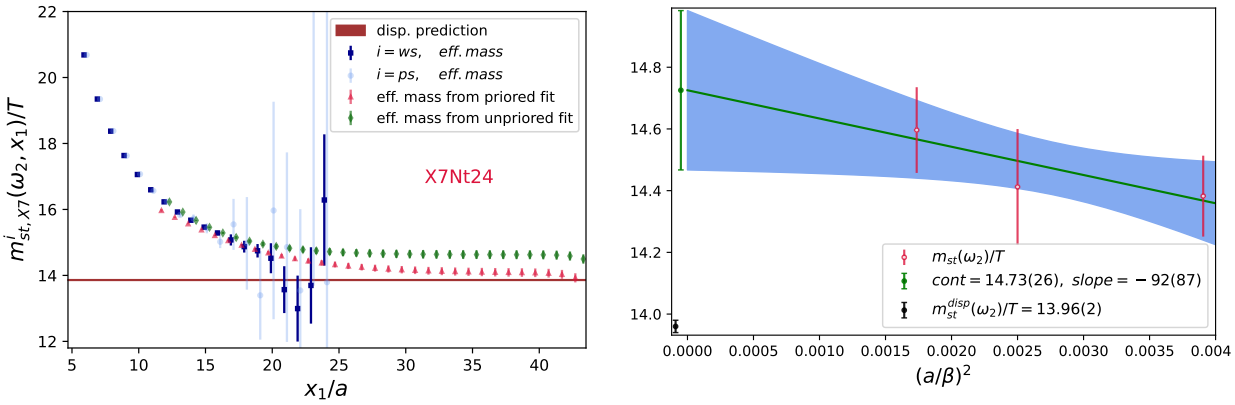

Figure 9.9: **Left panel:** The effective mass of the static local-local isovector vector correlator in the second Matsubara sector on the X7 ensemble. Additionally, effective masses derived from fits using the ansatz (7.3.1) are presented both *with* a prior (red bars) and *without* a prior (green bars). The dark red horizontal line represents the dispersive prediction (9.2.5). For comparative purposes, effective masses from the earlier point-source data of Ref. [6] are illustrated as light blue bars. **Right panel:** Corresponding continuum extrapolation together with the dispersive prediction.

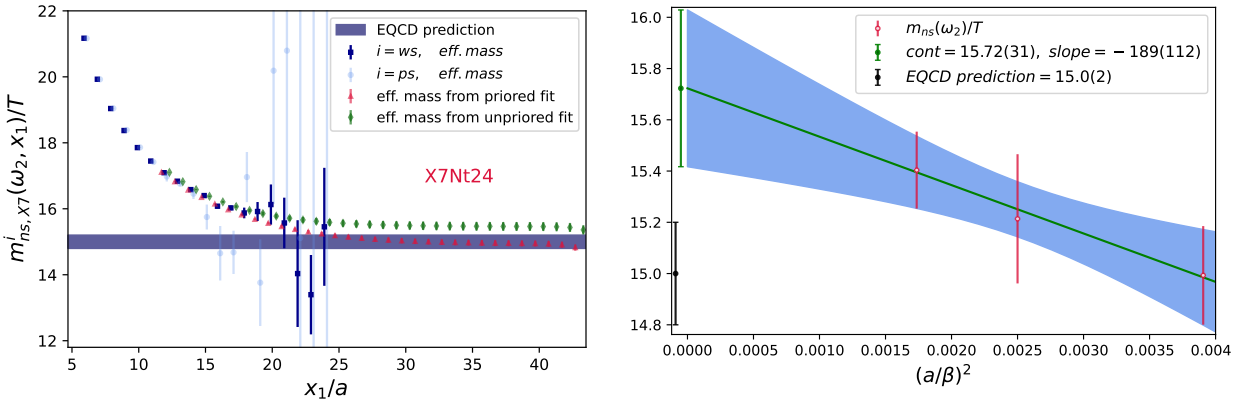

Figure 9.10: **Left panel:** The effective mass of the non-static local-local isovector vector correlator in the second Matsubara sector on the X7 ensemble is. Additionally, effective masses derived from fits using the ansatz (7.3.1) are presented both *with* a prior (red bars) and *without* a prior (green bars), alongside the EQCD prediction from Ref. [261] (dark blue band). For comparative purposes, results from the earlier point–source data of Ref. [6] are illustrated as light–blue bars. **Right panel:** Corresponding continuum extrapolation, including the EQCD prediction from Ref. [261].

9.4.1 Screening Masses in the Second Matsubara Sector

By employing the multi-state fit ansatz (7.3.1) for the static screening correlator $G^{\mathrm{T}}_{\mathrm{st}}(p = \omega_2, x_1)$ and taking the continuum limit, we obtain for the ground state:

$$m^{0,\mathrm{fit}}_{\mathrm{st},2}(\omega_2)/T = 14.73(26)\,, \tag{9.4.1}$$

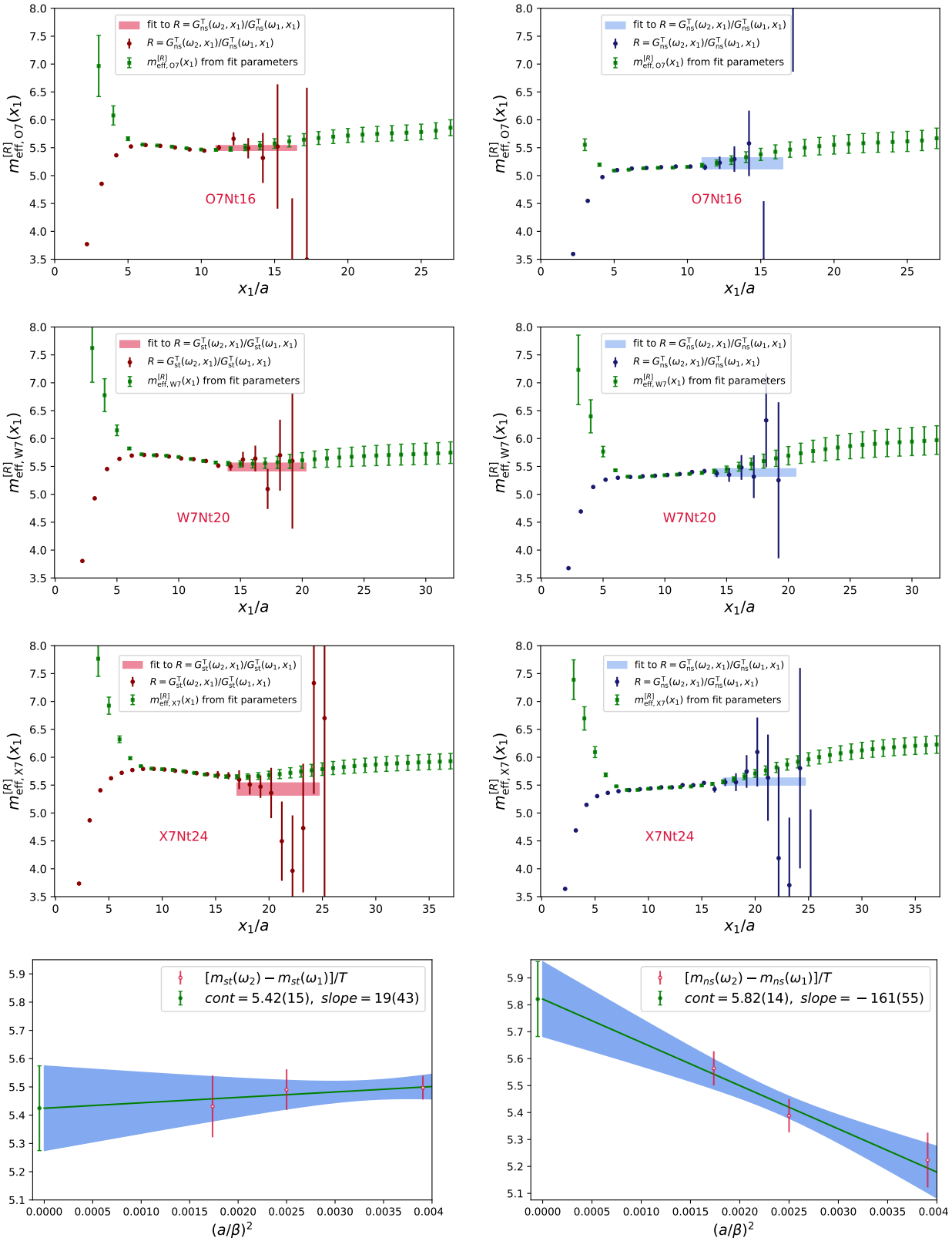

Figure 9.11: The effective masses, as defined in Eq. (I.6), for the ratios of the $n = 2$ to the $n = 1$ Matsubara sector screening correlators are presented for both the static (**left column**) and non-static (**right panel**) scenarios, on ensembles O7, W7, and X7. The green bars represent the effective masses derived from a single exponential fit, of the correlator ratios $G^{\mathrm{T}}_i(\omega_2, x_1)/G^{\mathrm{T}}_i(\omega_1, x_1)$. **Bottom row:** Corresponding continuum extrapolations.

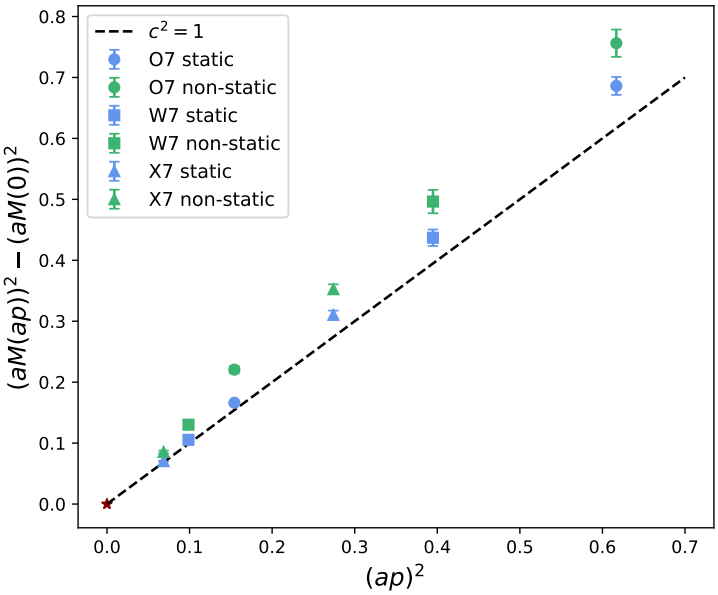

Figure 9.12: The deviation of the $n = 1$ and $n = 2$ static screening masses (represented by blue bars) from the continuum relativistic dispersion relation (9.2.3) is depicted at finite lattice spacing across the three ensembles O7, W7, and X7 (expressed in lattice units). For comparative purposes, the non-static screening masses are also displayed (indicated by green bars), although no corresponding continuum dispersion relation exists for them.

which exhibits a discrepancy of approximately 3σ from the dispersive prediction presented (9.2.5) [refer also to Fig. 9.12]. In the non-static channel, fitting $G^{\mathrm{T}}_{\mathrm{ns}}(\omega_2, x_1)$ results in

$$m^{0,\mathrm{fit}}_{\mathrm{ns},2}(\omega_2)/T = 15.72(31)\,, \tag{9.4.2}$$

which deviates from the EQCD estimate [261] ,

$$m^{0,\mathrm{EQCD}}_{\mathrm{ns},2}(\omega_2)/T = 15.0(2)\,, \tag{9.4.3}$$

by about 2σ. The impact of including additional states in the fit ansatz (7.3.1) is illustrated in Fig. 32 (Appendix L), where one-, two-, and three-state results are compared. The mass gap between the non-static and static screening masses in the second Matsubara sector is

$$m^{0,\mathrm{fit}}_{\mathrm{ns},2}(\omega_2)/T - m^{0,\mathrm{fit}}_{\mathrm{st},2}(\omega_2)/T = 0.99(41)\,, \tag{9.4.4}$$

in good agreement with the continuum estimate obtained from the correlator ratio,

$$m^{0,\mathrm{ratio}}_{\mathrm{ns},2}(\omega_2)/T - m^{0,\mathrm{ratio}}_{\mathrm{st},2}(\omega_2)/T = 1.015(66)\,, \tag{9.4.5}$$

using Eq. (8.1.1) with $i = \mathrm{ns}$, $j = \mathrm{st}$, and $r = n = 2$; see Fig. 9.8.

Given the systematic error associated with the selection of the fit range and the number of states included, we adopt an alternative methodology involving constrained fits with priors on the $n = 2$ screening masses. The rationale for this alternative approach is that the local effective

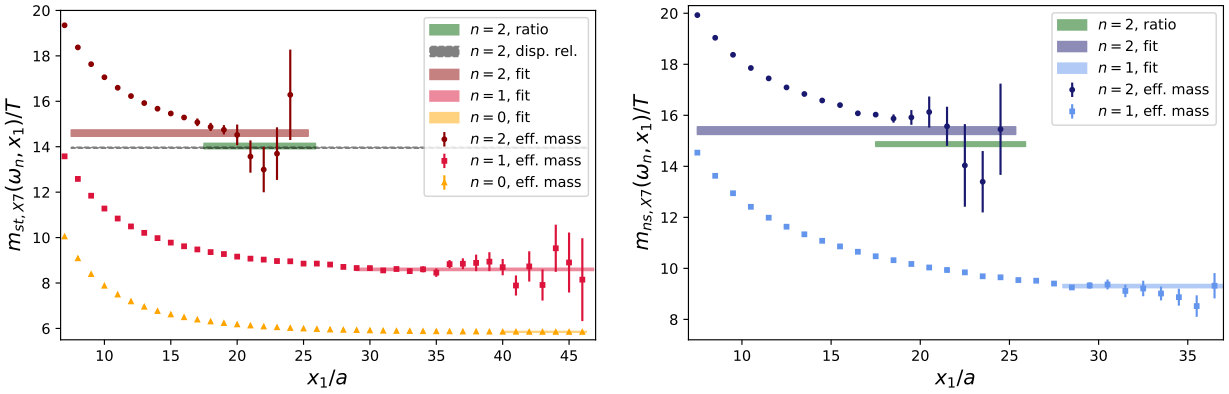

Figure 9.13: **Left panel:** The effective mass [cf. Eq. (I.6)] and the fit results for the static correlators at spatial momenta ω_0, ω_1, and ω_2 on the X7 ensemble. **Right panel:** The effective mass and the fit results for the non-static screening correlator in the $n = 1$ and $n = 2$ Matsubara sector.

masses, as defined in Eq. (I.6), exhibit similarities in the $n = 2$ and $n = 1$ sectors [cf. Fig. 9.13]. The priors are derived from single-exponential fits to the ratios $G_i^{\mathrm{T}}(\omega_2, x_1)/G_i^{\mathrm{T}}(\omega_1, x_1)$ [cf. Eq. (8.1.1)].

The rate at which the ratio approaches its asymptotic value is determined by the mass gap between the $n = 2$ and $n = 1$ sectors. A practical challenge of this "ratio method" is that this approach can be slow—typically dictated by the slowest-plateauing correlator—which often results in the loss of signal before a plateau is reached, particularly when the mass difference between the two channels is small. This limitation is indeed observed: the ratio becomes noisy once the ω_2 correlator loses signal (around $x_1 T \simeq \frac{3}{4}$), even though the ω_1 channel has not yet reached its asymptotic regime. In the $n = 1$ sector, this regime is typically attained only around $x_1 T \simeq \frac{5}{4}$ (see Figs. 9.3 and 9.4). Consequently, in Fig. 9.11, we also present the multi-cosh fit [cf. Eq. (7.3.1)] effective masses of the correlator ratios $G_i^{\mathrm{T}}(\omega_2, x_1)/G_i^{\mathrm{T}}(\omega_1, x_1)$, depicted as green bars. In both sectors and across all three ensembles, these multi-cosh fit effective masses continue to exhibit slight growth until the ω_1 channel also plateaus.

The mass gaps and continuum extrapolations in both the static and non-static sectors are depicted in Fig. 9.11. The results are as follows:

$$m_{\mathrm{st},2}^{0,\mathrm{ratio}}(\omega_2)/T - m_{\mathrm{st},1}^{0,\mathrm{ratio}}(\omega_1)/T = 5.42(15)\,, \tag{9.4.6}$$
$$m_{\mathrm{ns},2}^{0,\mathrm{ratio}}(\omega_2)/T - m_{\mathrm{ns},1}^{0,\mathrm{ratio}}(\omega_1)/T = 5.82(14)\,. \tag{9.4.7}$$

When these values are combined with the continuum $n = 1$ screening masses [cf. Eqs. (9.3.1) and (9.3.2)], they provide the continuum-extrapolated priors for the $n = 2$ sector:

$$m_{\mathrm{st},2}^{0,\mathrm{ratio}}(\omega_2)/T = 14.07(18)\,, \tag{9.4.8}$$
$$m_{\mathrm{ns},2}^{0,\mathrm{ratio}}(\omega_2)/T = 14.99(21)\,. \tag{9.4.9}$$

At the finest lattice spacing, the results of this procedure are depicted in Fig. 9.13 with the green

band. Utilizing Eqs. (9.4.8)- (9.4.9) as priors in the multi-state fits, we obtain the continuum results:

$$m_{\text{st},2}^{0,\text{w/ prior}}(\omega_2)/T = 14.22(23)\,, \tag{9.4.10}$$

$$m_{\text{ns},2}^{0,\text{w/ prior}}(\omega_2)/T = 15.09(20)\,. \tag{9.4.11}$$

Note that the constrained result in the static sector, as presented in Eq. (9.4.10), now deviates from the dispersive prediction (9.2.5), by only about one standard deviation. In the non-static sector, the constrained result (9.4.11) is entirely consistent with the EQCD prediction (9.4.3).

However, the difference between the unconstrained fits [Eqs. (9.4.1)–(9.4.2)] and the constrained fits [Eqs. (9.4.10)–(9.4.11)] primarily reflects the systematic uncertainty associated with modeling the long-distance tail of the screening correlators. Insights from analogous ratio-based analyses in the literature (e.g., Refs. [275–277]) indicate that employing ratios of correlators, whose plateaus are reached at different times, can result in misleading"fake plateau" and inaccurate estimates of the relevant mass gaps. A pertinent example is the dibaryon system, where the dibaryon correlator plateaus early but experiences significant signal-to-noise degradation, while the nucleon correlator plateaus more slowly due to the presence of $N + \pi$ states. Utilizing the ratio of correlators in this context would have suggested binding, whereas independent treatment of the correlators indicates repulsion; a change in sign and qualitative physics purely from statistical limitations. [1]

In our analysis, we consider the two approaches as complementary, providing estimates that collectively bracket the true screening mass. The ratio of ω_2 to ω_1 correlators can only offer a lower bound: the ω_1 effective mass has not yet plateaued when the signal of ω_2 is lost, thus the ratio alone would systematically underestimate the screening mass. Conversely, the multi-state fit provides an upper bound.

9.4.2 Continuum Extrapolation of $H_E(\omega_2)$

In comparison to the $n = 1$ integrand, the $n = 2$ contribution depicted in Fig. 9.14 is reduced by approximately a factor of two at the shortest source-sink separations x_1. However, as x_1 increases, the $n = 2$ integrand exhibits a more rapid growth, surpassing the $n = 1$ integrand around $x_1 T = \frac{1}{3}$. Near $x_1 T = \frac{1}{2}$, it develops a pronounced peak before falling off at larger separations. In contrast to the smooth behavior observed for the $n = 1$ case, the extraction of $H_E(\omega_2)$ is hindered by a significant, exponentially increasing signal-to-noise issue: at $x_1 T = 1$, the relative error of the integrand already approaches nearly 20%, and the $\cosh(4\pi T)$ factor further amplifies the noise [see Fig. 9.14]. Furthermore, unlike the $n = 1$ case, the $n = 2$ integrand derives a substantial portion of its weight from the long-distance region, with the tail effectively contributing significantly to compensate for the initial short-distance suppression. The top panel of Fig. 9.15 demonstrates that the integrand continues to provide a non-negligible contribution even at $x_1 T \simeq 3$, underscoring the persistent influence of the long-distance tail.

The evaluation of $H_E(\omega_2)$ using the standard subtraction method (7.2.20) with $\Omega_2 = \omega_2$ proved infeasible with the available statistical data when utilizing point-sources. In Ref. [6], the following

[1] I would like to thank Jamie Hudspith for emphasizing this point.

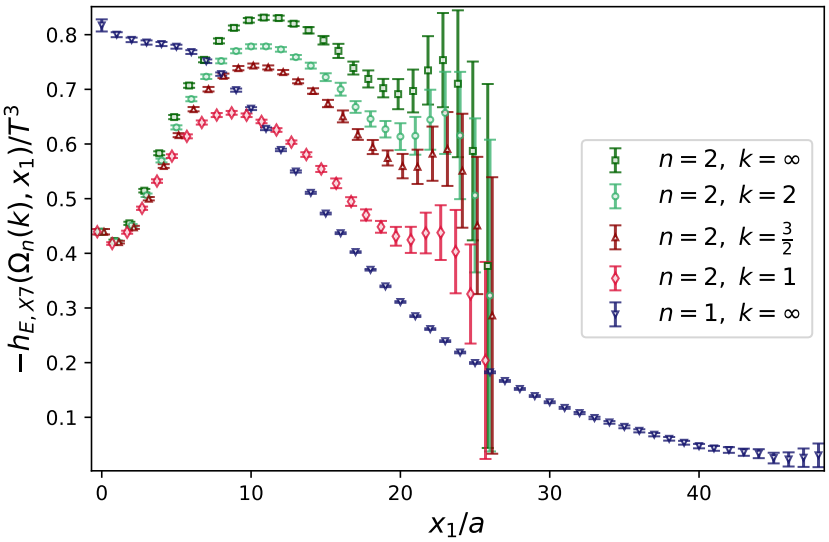

Figure 9.14: Standard-subtracted integrands $-h_E(\omega_2, x_1)$ [cf. Eq. (7.2.21)] with different kernel modifications based on the parameter k [cf. Eq. (7.2.19)] as well as $-h_E(\omega_1, x_1)$ on the finest ensemble X7.

result was reported:

$$-H^{\mathrm{ps}}_{E,p=\omega_2}(\omega_2)/T^2 = 0.54(13)_{\mathrm{stat}}(13)_{\mathrm{sys}}\,, \tag{9.4.12}$$

indicating that $|H_E(\omega_2)| < |H_E(\omega_1)|$ [cf. Eq. (9.3.8)], thereby contravening the positivity of the transverse-channel spectral function $\sigma(\omega)$. To address this discrepancy, Ref. [6] investigated alternative subtraction schemes [cf. Eq. (7.2.22)] and presented the following as the final result:

$$-H^{\mathrm{ps}}_{E,p=\omega_1,\alpha=3.5}(\omega_2)/T^2 = 0.90(10)_{\mathrm{stat}}(4)_{\mathrm{sys}}\,. \tag{9.4.13}$$

In contrast, the present study focuses on the standard subtraction method for the reasons elaborated in Sec. 7.2.1. Unlike Ref. [6], our analysis benefits from significantly enhanced statistical precision—improved by up to a factor of 6.5 in the integrand at separations around $x_1 \approx \beta$ [see Fig. 9.1]—which facilitates a thorough examination of systematic uncertainties related to the large-x_1 contributions. Moreover, as discussed in Sec. 7.2.1, one may opt for $\Omega_n = \omega_n(1 + \mathcal{O}(a^2))$ [cf. Eq. (7.2.19)] to mitigate artifacts arising from the finite lattice spacing a [262].

In our final analysis, we incorporate continuum extrapolations for two specific choices: $k = 2$, which is motivated by the dispersion relation of a free lattice scalar field, and $k = 3/2$, which empirically results in the flattest continuum extrapolation (see Fig. 9.15, bottom panel). As a third variant for Ω_n, we employ a smooth interpolation centered at $x_1 = \beta$, transitioning between ω_n at short distances and $\frac{1}{a}\sin(a\omega_n)$ at long distances. This choice is motivated by an examination of cut-off effects in leading-order lattice perturbation theory; see Appendix M. Utilizing the fitted parameters $m^l_{i,2}$ and $A^l_{i,2}$, we extend the correlators $G^{\mathrm{T}}_i(\omega_2, x_1)$ beyond the reference distance $x_1 = \beta$ as a sum of exponentials [cf. Eq. 7.3.2]. This controlled extension, illustrated in the top panel of Fig. 9.15, provides the necessary input for computing $H_E(\omega_2)$ according to Eq. (7.2.20).

We perform simultaneous, correlated continuum extrapolations for two out of the three data sets associated with a particular choice of Ω_n, enforcing a common continuum limit between them.

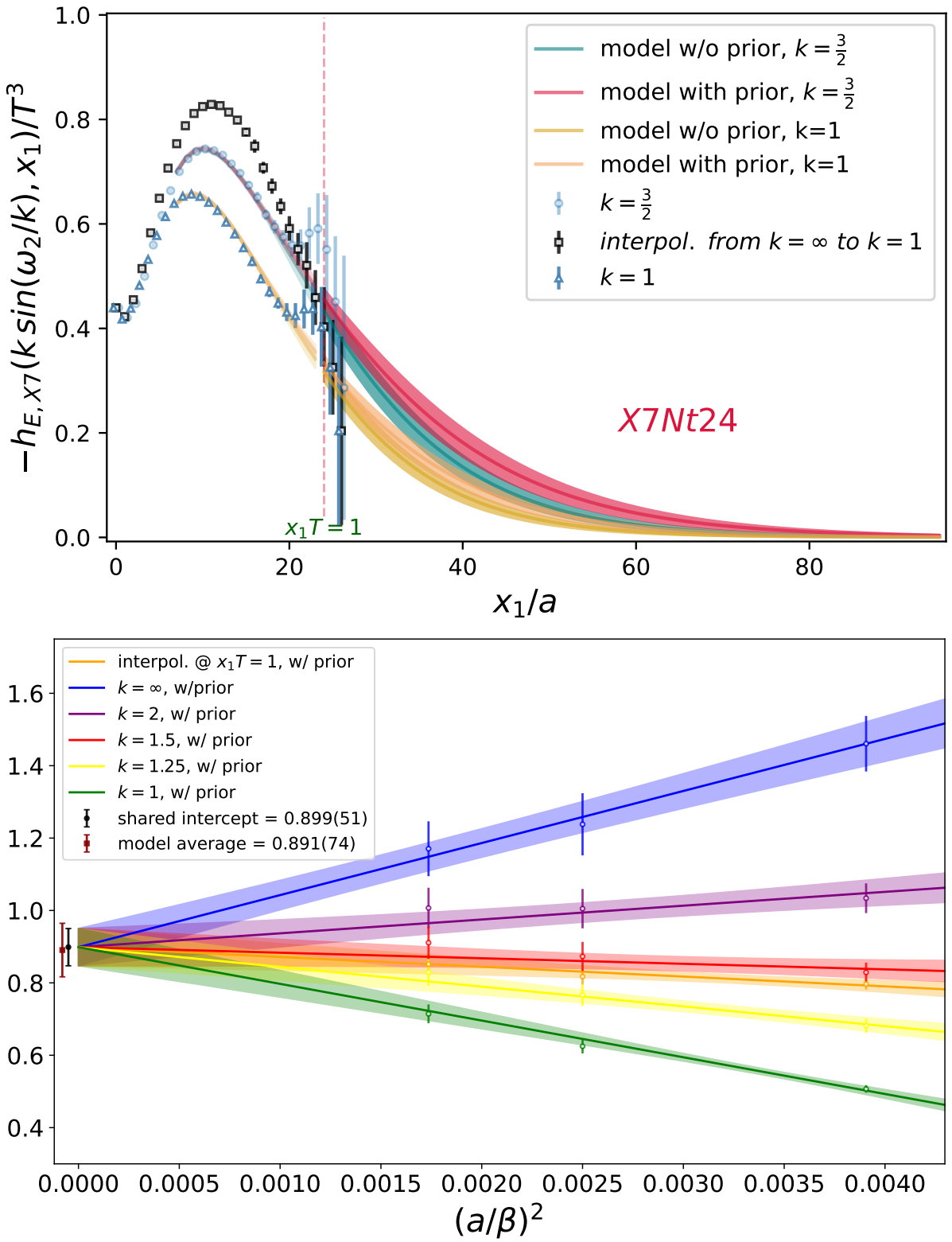

Figure 9.15: **Top panel:** Integrands $-h_E(\Omega_n(k), x_1)/T^3$ for $k \in \{1, \frac{3}{2}, \infty\}$, alongside the interpolation between the prescriptions $k = \infty$ and $k = 1$ at $x_1T = 1$, with $d \approx 0.15\,\text{fm}$ as specified in Eq. (M.1). These integrands are depicted on the X7 ensemble, incorporating the tail modification. **Bottom panel:** A simultaneous (uncorrelated) continuum extrapolation is conducted with a shared intercept for $-H_E(\omega_2)/T^2$, utilizing priors from the "ratio method". The resulting value $[-H_E(\omega_2)/T^2]^{\text{uncorr.}}_{\text{w/ prior}} = 0.899(51)_{\text{stat}}$ demonstrates strong agreement with our previously reported MAV result (9.4.16).

For each of the three pairs, we consider four combinations based on whether the coarsest lattice spacing ensemble (O7) is included or excluded independently in each extrapolation (i.e., both extrapolations include O7, only one includes O7, or both exclude it). This results in $3 \times 4 = 12$ fit models.

The final result is derived by model averaging across these extrapolations, utilizing the Akaike Information Criterion (AIC) [278] and the model-averaging framework of Refs. [279, 280], with weights w_i assigned according to Eq. (I.7). The central value and statistical uncertainty of an observable $\mathcal{O}$ are obtained from a weighted average over all fit models,

$$\bar{\mathcal{O}} = \sum_i w_i \mathcal{O}_i \,. \tag{9.4.14}$$

The systematic uncertainty associated with the continuum extrapolation is quantified by the variance of the model distribution, as expressed in the following equation:

$$(\delta\mathcal{O})^2_{\text{sys}} = \sum_i w_i (\mathcal{O}_i - \bar{\mathcal{O}})^2 \,. \tag{9.4.15}$$

We perform separate model averages (MAV) for analyses conducted both with and without the application of a prior, yielding the following results:

$$[-H_E(\omega_2)/T^2]^{\text{MAV}}_{\text{w/ prior}} = 0.891(24)_{\text{stat}}(54)^{\text{cont}}_{\text{sys}}[59] \,, \tag{9.4.16}$$

$$[-H_E(\omega_2)/T^2]^{\text{MAV}}_{\text{w/o prior}} = 0.846(27)_{\text{stat}}(40)^{\text{cont}}_{\text{sys}}[48] \,. \tag{9.4.17}$$

These results are in agreement with those derived from a simultaneous, uncorrelated continuum extrapolation employing a common intercept across a spectrum of k-values (see Fig. 9.15, bottom panel). The systematic uncertainty, as estimated by Eq. (9.4.15), reflects the spread among continuum extrapolations corresponding to different selections of Ω_n; cf. Eq. (7.2.19). As our final estimate, we present the average of Eqs. (9.4.16)-(9.4.17):

$$-H_E(\omega_2)/T^2 = 0.869(24)_{\text{stat}}(54)^{\text{cont}}_{\text{sys}}(44)^{\text{tail}}_{\text{sys}}[74]_{\text{tot}} \,, \tag{9.4.18}$$

where the systematic uncertainty associated with the tail extension is considered as the complete, statistically significant difference of $0.044(17)$ between the MAV results with and without the prior. The total uncertainty is calculated by combining the individual contributions in quadrature. In comparison to the previous determination in Ref. [6] [cf. Eq. (9.4.13)], our result remains entirely consistent while achieving a 1.5-fold reduction in overall uncertainty. When directly compared to the previous result obtained using the standard subtraction method [cf. Eq. (9.4.12)], the improvement is even more substantial, with the total error reduced by a factor of 2.5.

9.4.3 Evaluation of the Difference $H_E(\omega_2) - H_E(\omega_1)$

As highlighted in the discussion of Fig. 7.3, the difference between the $n = 2$ and $n = 1$ moments exclusively probes photons at non-zero frequencies, thereby suppressing the contribution from very soft photons. Consequently, it is sensitive to the kinematically relevant region $\omega \gtrsim \pi T \approx 1\,\text{GeV}$. This region is directly associated with the direct-photon puzzle and represents

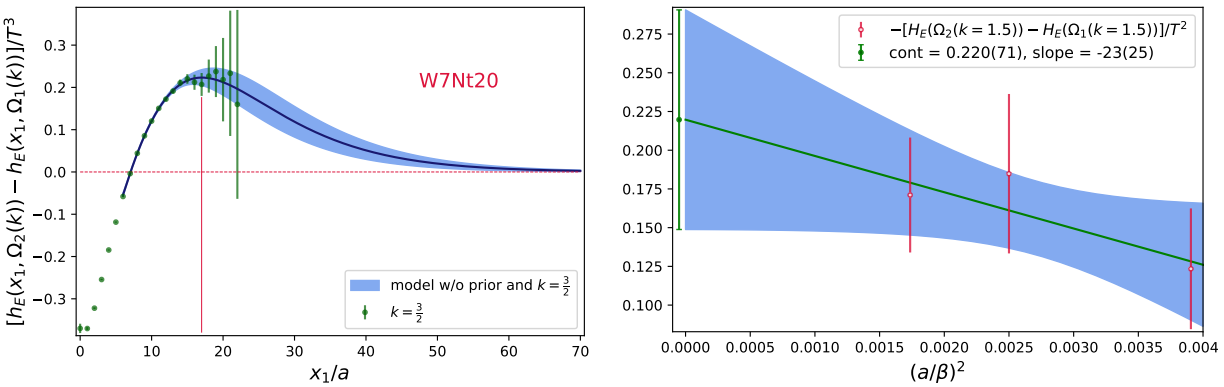

Figure 9.16: **Left panel:** Integrand entering the difference of the H_E quantities in Eq. (9.4.20) on the ensemble W7, together with its tail extension analogous to Eq. (7.3.2). The vertical red line marks the separation x_1 at which the cumulative integral of Eq. (9.4.20) changes sign and becomes positive. **Right panel:** Corresponding continuum extrapolation.

a phenomenologically significant observable in its own right, as it facilitates more reliable comparisons to weak-coupling predictions. By subtracting the precisely determined first moment, as given in Eq. (9.3.8), from the result for $H_E(\omega_2)$, we obtain

$$-\left[H_E(\omega_2) - H_E(\omega_1)\right]/T^2 = 0.193(74)\,. \tag{9.4.19}$$

This value is derived from separate evaluations of $H_E(\omega_2)$ and $H_E(\omega_1)$. As a rigorous cross-check, we also compute the difference directly from the combination,

$$\begin{aligned} H_E(\omega_2) - H_E(\omega_1) = \int_{\mathbb{R}} \mathrm{d}x_1 \Big[& G^{\mathrm{T}}_{\mathrm{ns}}(\omega_2, x_1)\mathrm{e}^{-\Omega_2(k)x_1} - G^{\mathrm{T}}_{\mathrm{ns}}(\omega_1, x_1)\mathrm{e}^{-\Omega_1(k)x_1} \\ & - G^{\mathrm{T}}_{\mathrm{st}}(\omega_2, x_1)\mathrm{e}^{-\Omega_2(k)x_1} + G^{\mathrm{T}}_{\mathrm{st}}(\omega_1, x_1)\mathrm{e}^{-\Omega_1(k)x_1} \Big]\,, \end{aligned} \tag{9.4.20}$$

where $k = \frac{3}{2}$, as this selection results in the mildest continuum slope (cf. bottom panel of Fig. 9.15). From this approach, we obtain in the continuum limit:

$$-\left[H_E(\omega_2) - H_E(\omega_1)\right]/T^2 = 0.220(71)\,, \tag{9.4.21}$$

which is consistent with Eq. (9.4.19). The slope of the continuum extrapolation is consistent with zero (cf. right panel of Fig. 9.16). Furthermore, the continuum difference in Eq. (9.4.21) aligns well with the value 0.23(13) reported in Ref. [6], although this was obtained using an alternative subtraction scheme.

Upon examining the left panel of Fig. 9.16, it becomes evident that for short source-sink separations up to $x_1 T \approx \frac{1}{3}$, the $n = 1$ contribution predominates, and it takes up to to nearly $x_1 \approx \beta$ before the cumulative integral undergoes a sign change. This underscores the necessity of managing the tail contribution, particularly concerning the relevant screening masses. Consequently, the significantly enhanced statistical precision—improved by a factor of up to 6.5 in the integrand at separations around $x_1 \approx \beta$ (cf. Fig. 9.1)—was essential for conducting a thorough investigation of the systematic uncertainties associated with the large-x_1 contribution.

9.5 Comparisons

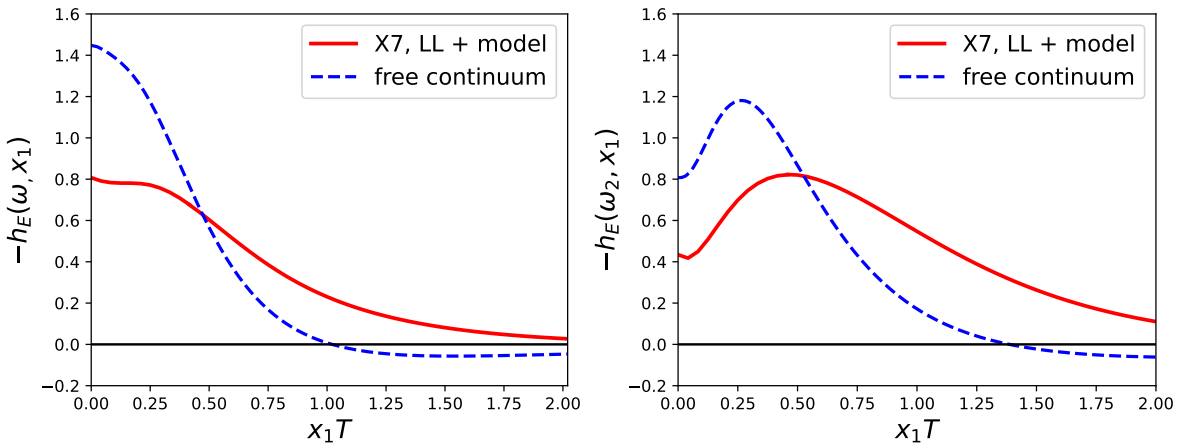

Figure 9.17: Integrand for extracting $H_E(\omega_n)$ from the free continuum theory (blue dashed line) and from lattice QCD combined with the tail modification of Eq. (7.3.2) on the finest ensemble X7 (red solid line). **Left panel:** $n = 1$ sector with the local-local discretization of the vector current **Right panel:** $n = 2$ sector with the local-local discretization of the vector current. In both panels, only central values are displayed.

In this section, we compare our findings with results derived from analytical approaches. Both $H_E(\omega_1)$ [cf. Eq. (9.3.8)] and the difference $H_E(\omega_2) - H_E(\omega_1)$ [cf. Eq. (9.4.19)] demonstrate strong concordance with our previous results as reported in Ref. [6]. Consequently, the physical interpretation of the outcomes remains the same, and the present comparisons closely parallel those made therein.

In Fig. 9.17, we confront the integrands used to compute $H_E(\omega_1)$ (left panel) and $H_E(\omega_2)$ (right panel) obtained in the free continuum theory with those extracted using lattice QCD on our finest ensemble X7. In both Matsubara sectors, the integrands from free theory and lattice QCD exhibit markedly different behaviors. At $x_1 = 0$, all curves remain finite, with the free-theory values approximately twice as large as the corresponding lattice results in both sectors. Additionally, the $n = 1$ integrands start out about twice as large as their $n = 2$ counterparts. In both sectors, the free-theory result decays significantly more rapidly and intersects the lattice curve around $x_1T = \frac{1}{2}$. At larger separations—$x_1T = 1$ for $n = 1$ and $x_1T \approx 1.4$ for $n = 2$—the free-theory prediction even becomes slightly negative. A key qualitative difference between the two Matsubara sectors is that, in the $n = 1$ case, both curves decay immediately with increasing x_1, whereas in the $n = 2$ case, both curves initially rise and reach a maximum around $x_1T \approx \frac{1}{4}$ (free theory) and $x_1T \approx \frac{1}{2}$ (lattice).

In the context of the free massless theory, one finds $\frac{H_E(\omega_n)}{T^2} = -\frac{N_c}{6}$ (for all n [256]), corresponding to the free spectral function given by

$$\frac{\sigma^{\text{free}}(\omega)}{\omega} = \frac{N_c}{3}\pi T^2\,\delta(\omega)\,, \qquad \chi_q^{\text{free}} = \frac{N_c}{3}T^2, \tag{9.5.1}$$

resulting in $\frac{H_E(\omega_1)}{\chi_q^{\text{free}}} = -0.500$. In the framework of strongly coupled $\mathcal{N} = 4$ super-Yang-Mills (SYM) theory, utilizing the AdS/CFT correspondence, the value $\frac{H_E(\omega_1)}{\chi_q^{\text{free}}} = -0.336$ [256] is obtained,

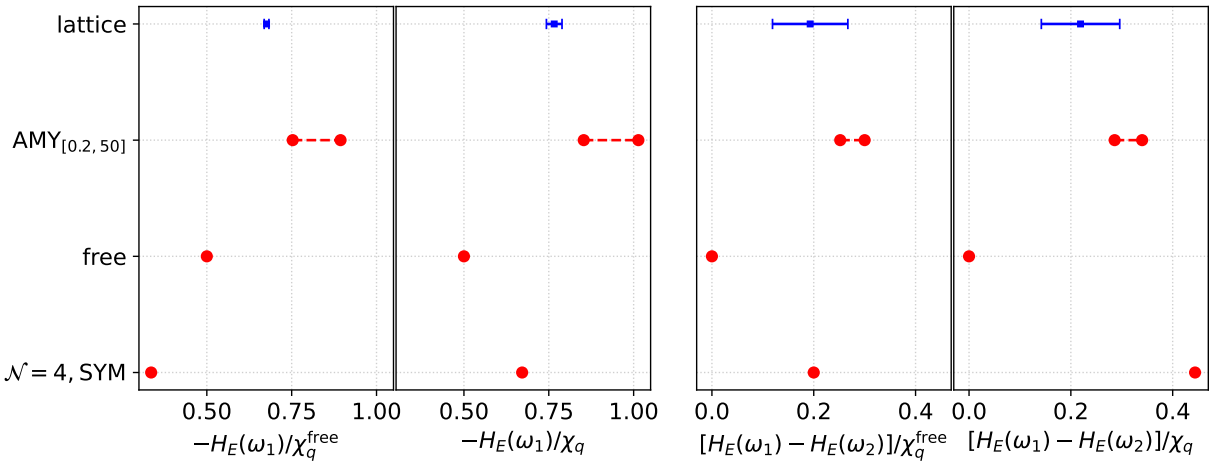

Figure 9.18: **Left panel:** The results for $H_E(\omega_1)$ are compared across several frameworks: lattice QCD, leading-order weak coupling with $\alpha_s = 0.25$ (left point) and $\alpha_s = 0.31$ (right point), the free theory, and strongly coupled $\mathcal{N} = 4$ SYM. The values are presented normalized either to the non-interacting susceptibility (*left column*) or to the interacting susceptibility (*right column*). For the free-theory points, both normalizations coincide, whereas for the weak-coupling prediction, we utilize either unity or the lattice value $\chi_q/T^2 = 0.882$ [5]. **Right panel:** A comparison is made for the difference $H_E(\omega_2) - H_E(\omega_1)$, employing the same normalization choices.

employing $\chi_q^{\text{free}} = \frac{N_c^2 T^2}{4}$ [281], which is lower than the result from the free theory.

By normalizing with the interacting susceptibility, χ_q, one obtains $\left[\frac{H_E}{\chi_q}\right]^{\text{SYM}} = -0.6715$, where $\chi_q = \frac{N_c^2 T^2}{8}$. It should be noted that temporal correlators have not been measured for this project. Consequently, we rely on the determination from Ref. [5] for the susceptibility,[2]

$$\frac{\chi_q^{\text{lat}}}{T^2} = 0.882(22)\,, \tag{9.5.2}$$

and the lattice result becomes $\left[\frac{H_E}{\chi_q}\right]^{\text{lat}} \simeq -0.766(23)$. In both normalizations, our lattice result in Eq. (9.3.8) is largest in magnitude [see left panel of Fig. 9.18]. In the second Matsubara sector, the strongly coupled $\mathcal{N} = 4$ SYM theory yields $H_E(\omega_2)/T^2 = -1.115$ [256]. Consequently, the difference $\frac{H_E(\omega_2) - H_E(\omega_1)}{\chi_q} = -0.444$ surpasses our lattice result in Eq. (9.4.19) by 3.4 standard deviations.

Utilizing the complete LO result of Arnold, Moore and Yaffe (AMY) for the spectral function $\sigma(\omega)$ [252, 253], it is possible to directly evaluate the difference $[H_E(\omega_2) - H_E(\omega_1)]$, whereas individual moments $H_E(\omega_n)$ are complicated by the singular behavior of $\sigma_{\text{AMY}}(\omega)$, which is associated with very soft photons. To demonstrate this sensitivity, Ref. [6] integrated the AMY spectral function with $\alpha_s = 0.25$ against the kernel $\omega_n^2/[\pi\omega(\omega^2 + \omega_n^2)]$ over the range $0.2 < \omega/T < 50$, where the parametrization is reliable. For the case where $n = 1$, this yields [6]

$$-\left[H_E(\omega_1)/T^2\right]_{\text{LO}, 0.2<\omega/T<50} \approx 0.75\,, \tag{9.5.3}$$

[2]This result is $\approx 1.2\,\sigma$ above our $N_f = 2+1$ estimate at $T = 192\,\text{MeV} \approx 1.2\,T_{\text{pc}}$ [cf. Eq. (6.7.4)]. However, it is important to note that Eq. (6.7.4) is not continuum-extrapolated, whereas the continuum extrapolation leading to Eq. (9.5.2) exhibits a negative slope. Therefore, we anticipate improved agreement in the continuum limit.

indicating a magnitude that surpasses the corresponding lattice determination presented in Eq. (9.3.8).

In contrast, the difference $[H_E(\omega_2) - H_E(\omega_1)]/T^2$ is significantly less influenced by uncertainties in the small-ω region. By employing the AMY spectral function [253], the following result is obtained [7]:

$$-\left[H_E(\omega_2)/T^2 - H_E(\omega_1)/T^2\right]_{\mathrm{LO},0.2<\omega/T<50} = [0.25,\, 0.30]\,, \quad \text{for } \alpha_s \in [0.25,\, 0.31]\,. \tag{9.5.4}$$

Consequently, our lattice result, as shown in Eq. (9.4.19), is positioned on the lower end of, yet remains consistent with the weak-coupling prediction in Eq. (9.5.4) [cf. right panel of Fig. 9.18]. This concordance underscores the robustness of this observable against infrared uncertainties, rendering it more suitable for direct comparison with lattice results. It is important to note, however, that the next-to-leading-order (NLO) correction to the AMY prediction is positive [282], and extending the integral to $\omega = \infty$ under the assumption $\sigma(\omega) \propto \sqrt{\omega}$ [253] results in a slightly larger value. Previous lattice investigations [5, 155, 257, 258] have reported photon emissivities in the QGP that align with the AMY prediction. Nonetheless, we emphasize that our findings are free of systematic uncertainties associated with an inverse problem and provide evidence at the $2.6\,\sigma$ level for a non-zero photon emissivity.

To utilize our precise lattice result for $H_E(\omega_1)$, it is necessary to examine the region of validity of the weak-coupling spectral function. The leading-order (LO) calculation [252, 253] assumes that photon wavelengths are short relative to the mean free path for large-angle scattering of a quark or gluon, resulting in $\sigma(\omega) \propto 1/\sqrt{\omega}$ at low frequencies. Given that $\sigma(\omega)/(2\chi_q\omega) \to D$ as $\omega \to 0$ [cf. Eq. (7.4.8)], this functional form must eventually become invalid below a certain frequency ω. Next-to-leading-order (NLO) corrections [282] are modest (approximately 10%) for $\omega \gtrsim 2\pi T$, but increase to approximately 30% near $\omega \lesssim \pi T$[6].

Consequently, we model $\sigma(\omega)$ by aligning the LO expression [252] at $\omega < \omega_{\mathrm{m}}$ with a Lorentzian [6],

$$\frac{\sigma(\omega)}{2\chi_q\omega} = \frac{A}{\omega^2+\eta^2}, \tag{9.5.5}$$

ensuring continuity and differentiability at $\omega = \omega_m$. This approach yields values of $H_E(\omega_1)$ and the diffusion coefficient $D = A/\eta^2$ that are contingent on ω_{m}. For $\omega > 50T$, we extend $\sigma(\omega) \propto \sqrt{\omega}$, which influences $-H_E(\omega_1)/T^2$ by only approximately 0.01 [6].

The LO weak-coupling result for the diffusion coefficient, derived from Ref. [283] with $\alpha_s = 0.25$ and $m_D/T = 2.05$, yields $T\cdot D \simeq 2.3$. Matching this weak-coupling spectral function $\sigma(\omega)$ [253] at $\omega_{\mathrm{m}} = 0.5T$ using $\alpha_s = 0.25$ reproduces this value but results in a dispersive estimate of $-H_E(\omega_1)/T^2 = 0.99$ [6], which is inconsistent with our lattice result in Eq. (9.3.8).

Instead, we follow the methodology outlined in Ref. [6]. We extend the weak-coupling form by employing a Lorentzian ansatz to constrain the low-frequency behavior of $\sigma(\omega)$. This ansatz is calibrated to replicate $H_E(\omega_1)$. For $\alpha_s = 0.25$, this method results in $T\cdot D \simeq 0.56(2)$, whereas for $\alpha_s = 0.31$, the estimate decreases to $T\cdot D \simeq 0.36(2)$ [6]. The error is determined by reproducing $H_E(\omega_1)$, adjusted by one standard deviation (0.007). Both values are significantly lower than the weak coupling result [283], yet they remain considerably larger than the AdS/CFT prediction $D = (2\pi T)^{-1}$ [284]. The corresponding spectral functions are illustrated in Fig. 9.19.

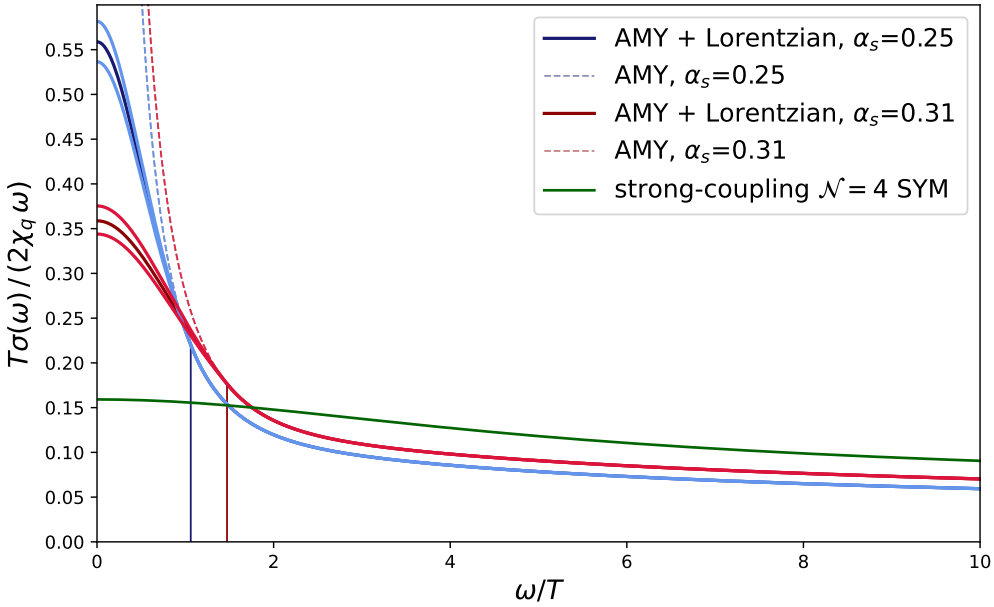

Figure 9.19: Spectral functions derived from the weak-coupling result [253] at two values of α_s are supplemented for $\omega < \omega_m$ with a Lorentzian, selected to replicate our lattice result for $H_E(\omega_1)$ as presented in Eq. (9.3.8). The vertical lines indicate the matching points $\omega = \omega_m$, while the dashed curves represent the unmodified weak-coupling form [also depicted in the right panel of Fig. 7.3]. For comparison, we additionally show the spectral function in strongly-coupled $\mathcal{N} = 4$ SYM theory [269]. The intercept at $\omega = 0$ provides the corresponding isospin diffusion coefficient $T \cdot D$.

Additional details regarding the construction of the spectral functions, parameter selections, and their alignment with weak-coupling expectations are available in Ref. [6].

9.6 Continuum Extrapolated Observables in the ω_3-Sector

In this section, we present the continuum-extrapolated results for both static and non-static screening masses within the third Matsubara sector. Additionally, we offer an initial conservative estimate of the standard-subtracted quantity $H_E(\omega_3)$, as defined in Eq. (7.2.20). It is important to note, however, that the injected momentum $p = \omega_3 = 6\pi T \approx 5\,\text{GeV}$ is already approaching the lattice momentum cut-off. For instance, on the coarsest ensemble O7, we have

$$\frac{\pi}{a} \approx \frac{0.197\pi\,\text{GeV fm}}{0.049\,\text{fm}} \approx 12.6\,\text{GeV}\,, \tag{9.6.1}$$

indicating that significant cut-off effects are anticipated. This study is based on approximately one-tenth of the Dirac operator inversions used for computing the screening correlators in the $n = 2$ sector (cf. Table 9.1). Consequently, the $n = 3$ results should be regarded as exploratory, intended primarily to provide a qualitative assessment of how the situation deteriorates in the next Matsubara sector.

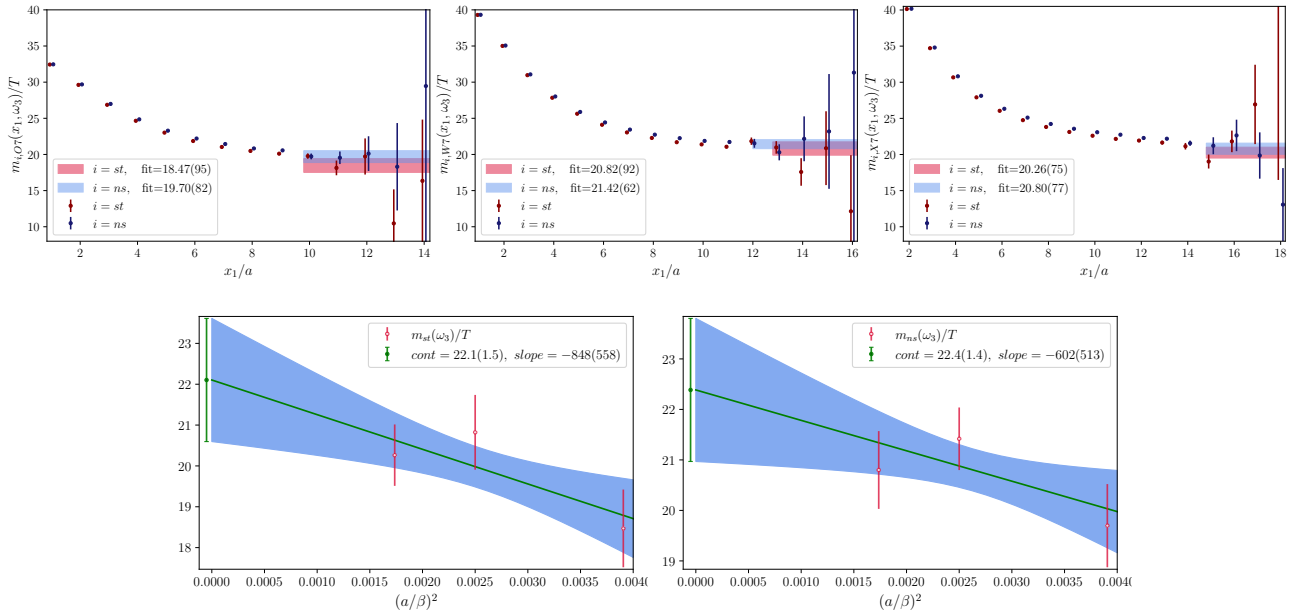

Figure 9.20: **First row:** Effective masses of the static (red bars) and non-static (blue bars) local-local isovector vector correlator in the third Matsuara sector for the O7, W7, and X7 ensembles. The horizontal bands represent the fit result derived from the ansatz (7.3.1). **Second row:** Continuum extrapolations of the same quantities .

9.6.1 Screening Masses in the Third Matsubara Sector

Utilizing the multi-state fit ansatz (7.3.1) applied to the static screening correlator $G^{\mathrm{T}}_{\mathrm{st}}(p = \omega_3, x_1)$, we obtain for the ground state in the continuum,

$$m^{0,\mathrm{fit}}_{\mathrm{st},3}(\omega_3)/T = 22.1(1.5)\,. \tag{9.6.2}$$

This value exceeds the continuum dispersive prediction of 19.80(2) as indicated in Eq. (9.2.6).

For the non-static channel, fitting $G^{\mathrm{T}}_{\mathrm{ns}}(\omega_3, x_1)$ results in,

$$m^{0,\mathrm{fit}}_{\mathrm{ns},3}(\omega_3)/T = 22.4(1.4)\,. \tag{9.6.3}$$

An examination of the effective masses in the first row of Fig. 9.20 reveals significant cut-off effects: within the plateau region, the static and non-static channels overlap leading to fitted results that are consistent within the margin of error. The continuum extrapolations, depicted in the second row of Fig. 9.20, exhibit slopes that are statistically indistinguishable from zero due to substantial uncertainties. To further illustrate the systematic uncertainties, constant fits were performed instead of linear extrapolations in a^2, yielding:

$$\left[m^{0,\mathrm{fit}}_{\mathrm{st},3}(\omega_3)/T\right]_{\text{zero slope}} = 19.94(50)\,, \tag{9.6.4}$$

$$\left[m^{0,\mathrm{fit}}_{\mathrm{ns},3}(\omega_3)/T\right]_{\text{zero slope}} = 20.80(42)\,. \tag{9.6.5}$$

The static value (9.6.4)aligns with the dispersive prediction (9.2.6).

To further cross-check the results, we employ the"ratio metho" as introduced in Sec. 9.4.1, by

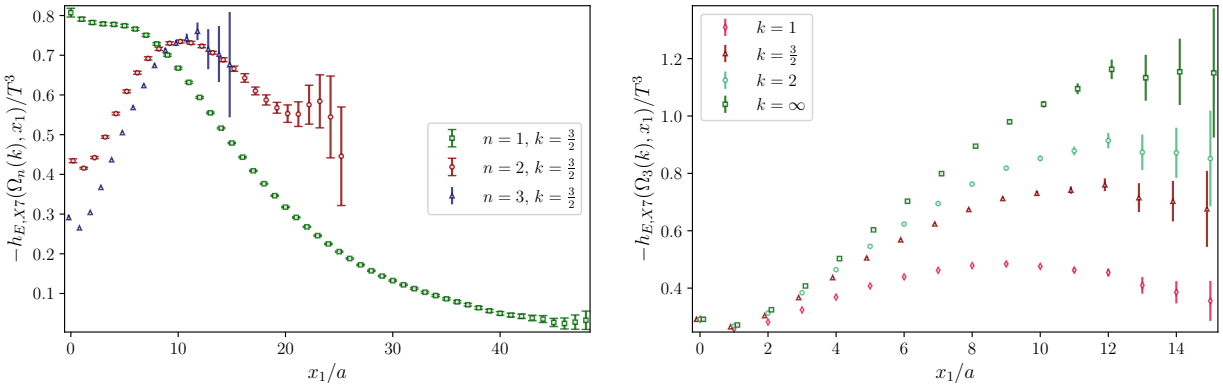

Figure 9.21: **Left panel:** Standard-subtracted integrands $-h_E(\Omega_n(k), x_1)/T^3$ [cf. Eq. (7.2.21) with $n \in \{1,2,3\}$ and $k = \frac{3}{2}$] on the finest ensemble X7. **Right panel:** The same quantity for $n = 3$ and $k \in \{1, \frac{3}{2}, 2, \infty\}$.

fitting the correlator ratios $G_i^{\mathrm{T}}(\omega_3, x_1)/G_i^{\mathrm{T}}(\omega_1, x_1)$. This approach yields the continuum extrapolated mass gaps,

$$m_{\mathrm{st},3}^{0,\mathrm{ratio}}(\omega_3)/T - m_{\mathrm{st},1}^{0,\mathrm{ratio}}(\omega_1)/T = 12.46(45)\,, \tag{9.6.6}$$
$$m_{\mathrm{ns},3}^{0,\mathrm{ratio}}(\omega_3)/T - m_{\mathrm{ns},1}^{0,\mathrm{ratio}}(\omega_1)/T = 11.91(29)\,, \tag{9.6.7}$$

which, when combined with the continuum $n = 1$ screening masses, result in:

$$m_{\mathrm{st},3}^{0,\mathrm{ratio}}(\omega_3)/T = 21.11(46)\,, \tag{9.6.8}$$
$$m_{\mathrm{ns},3}^{0,\mathrm{ratio}}(\omega_3)/T = 21.08(33)\,. \tag{9.6.9}$$

Once again, the static and non-static screening masses are indistinguishable and align with the direct fit results presented in Eqs. (9.6.2) and (9.6.3).

Subsequently, we directly determine the mass gap between the non-static and static screening masses in the third Matsubara sector by utilizing the correlator ratio $G_{\mathrm{ns}}^{\mathrm{T}}(\omega_3, x_1)/G_{\mathrm{st}}^{\mathrm{T}}(\omega_3, x_1)$. This analysis yields:

$$\left[m_{\mathrm{ns},3}^{0,\mathrm{ratio}}(\omega_3) - m_{\mathrm{st},3}^{0,\mathrm{ratio}}(\omega_3)\right]/T = 0.82(11)\,, \tag{9.6.10}$$

which is consistent with the mass gap derived from the continuum extrapolations with zero slope [cf. Eqs. (9.6.4) and (9.6.5)].

9.6.2 Continuum Extrapolation of $H_E(\omega_3)$

In comparison to the integrands for $n = 1$ and $n = 2$, the contribution for $n = 3$ is further suppressed at short distances, remaining significantly lower than the others up to $x_1 T \simeq \frac{1}{3}$ [see left panel of Fig. 9.21]. Around $x_1 T \approx \frac{1}{2}$, it develops a broad peak, qualitatively similar to the $n = 2$ case but shifted to slightly larger separations. Beyond this point, the statistical uncertainties increase rapidly, and the $n = 3$ integrand barely exceeds the $n = 2$ signal before it is lost entirely. Given that the positivity of the transverse spectral function $\sigma(\omega)$ necessitates

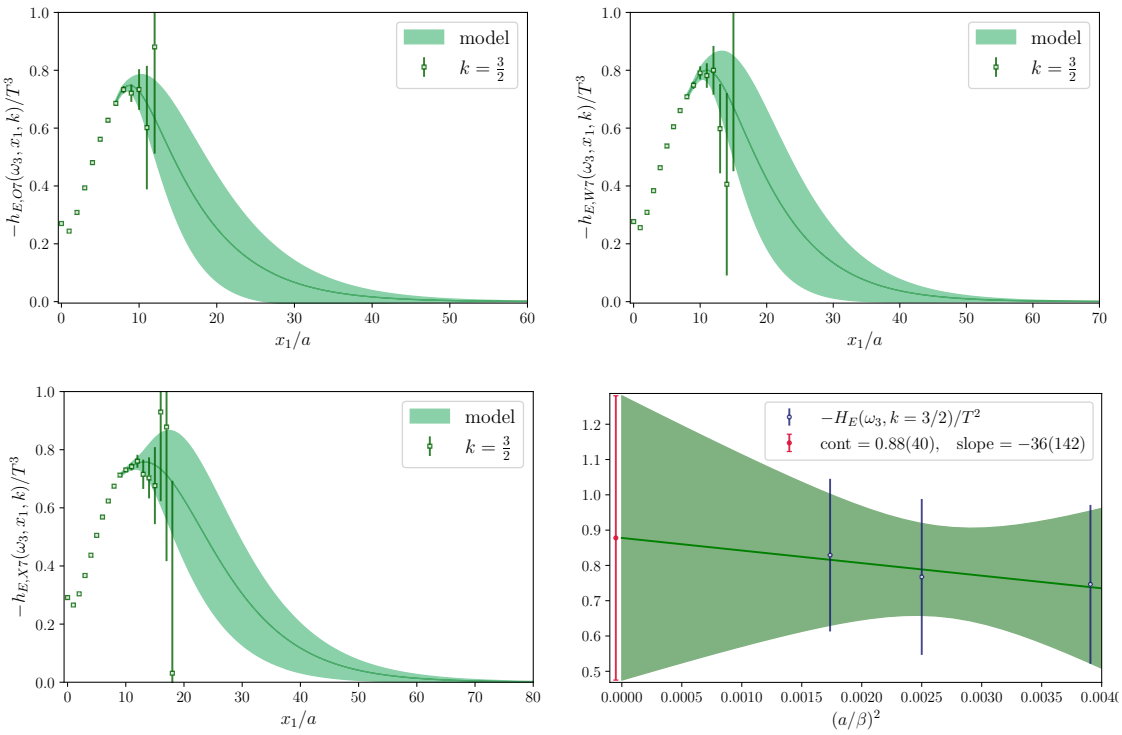

Figure 9.22: **First three panels:** Integrands $-h_E(\Omega_3(k = 3/2), x_1)/T^3$ from Eq. (7.2.21), computed for three ensembles: O7, W7, and X7. The results incorporate the tail modification as described in Eq. (7.3.2). **Last panel:** Corresponding continuum extrapolation.

$|H_E(\omega_3)| > |H_E(\omega_2)|$, a great fraction of the $n = 3$ contribution must therefore originate from the long-distance regime governed by the screening masses (9.6.2) and (9.6.3).

In the right panel of Fig. 9.21, we present the standard-subtracted integrand $-h_E(\Omega_3(k), x_1)$ for various values of k on X7. As k increases, the broad peak shifts to larger x_1, and its height increases substantially: for $k = \infty$, the peak value is approximately 2.4 times greater than for $k = 1$, indicating significant discretization effects. For comparison, in the second Matsubara sector, the corresponding enhancement is only about a factor of 1.4 [cf. Fig. 9.14]. It is important to emphasize that in the continuum, the corresponding values for $H_E(\Omega_n(k))$ must converge to the same value for all k.[3]

Similar to the scenario when $n = 2$, selecting $k = \frac{3}{2}$ results in the flattest continuum extrapolation. Our estimation reads,

$$-H_E(\Omega_3(k = 3/2))/T^2 = 0.88(40)\,. \tag{9.6.11}$$

The modification of the tail across the three ensembles, along with the corresponding continuum extrapolation, is depicted in Fig. 9.22. Due to the positivity of the transverse spectral function, this outcome should be regarded as a relatively coarse upper bound and lacks quantitative reliability, given the substantial cut-off effects.

[3]For the $n = 2$ case, this convergence is illustrated in the bottom panel of Fig. 9.15.

9.7 Conclusion

Estimating the full energy-differential photon emissivity of a medium in thermal equilibrium from lattice QCD is challenging because it involves solving a numerically ill-posed inverse problem. In the "traditional" approach, correlation functions are computed at fixed spatial momenta and contain contributions from all photon virtualities when related to the photon production rate. In this thesis, we instead employed spatially-transverse Euclidean correlators $H_E(\omega_n)$ evaluated at imaginary spatial momentum, which enforces the on-shell condition for the photon [256]. These observables admit an integral representation in terms of the transverse spectral function of the electromagnetic current–current correlator, $\sigma(\omega)$, and a Lorentzian kernel [see Eq. (7.4.7)], providing a non-perturbative handle on the thermal photon emissivity without confronting an inverse problem. Nevertheless, any attempt to reconstruct $\sigma(\omega)$ from a finite set of moments inevitably re-encounters the fundamentally ill-posed character of the inverse problem [6].

A key technical challenge of this approach lies in the presence of a large discretization effect due to the breaking of Lorentz invariance on the lattice. We mitigated this by subtracting a correlator with the same short-distance behavior that vanishes in the continuum limit. Additional $\mathcal{O}(a^2)$ kernel modifications further suppress discretization effects [cf. Eq. (7.2.19)]. This strategy enabled controlled continuum extrapolations and precise determinations of the first two energy moments $H_E(\omega_n), n = 1, 2$, in $N_f = 2$ QCD.

At a temperature of about 250 MeV, corresponding to the quark–gluon plasma phase, we obtained a continuum result for $|H_E(\omega_1)|$ with a precision of around 1% [cf. Eq. (9.3.8)]. We compared this benchmark to predictions from free theory, $\mathcal{N} = 4$ SYM and the full leading-order weak-coupling calculation of AMY [253]. Our result is significantly smaller than the weak-coupling prediction, suggesting that the AMY spectral function overestimates the soft-photon contribution. Using a simple Lorentzian model for the low-frequency region, we estimated the isospin diffusion coefficient to be $T \cdot D \simeq 0.34 - 0.58$, consistent with previous lattice studies employing dispersion relations at fixed spatial momentum [111, 112, 155, 224, 285–287], though studies with dynamical quarks often report values below 0.3 at similar temperatures [98].

Furthermore, employing stochastic momentum wall sources we computed the challenging second moment, $H_E(\omega_2)$. The long-distance behavior of the screening correlators is controlled by the screening masses. By building correlator ratios [cf. Eq. (8.1.1)] with the corresponding $n = 1$ correlator counterparts, we were able to bound the true $n = 2$ screening masses from below. Conversely, the multi-state fits provided an upper bound on the true screening mass, enabling an extensive examination of systematic uncertainties related to the tail contribution.

The integration kernel in the spectral representation of $H_E(\omega_n)$ [cf. Eq. (7.4.7)] remains finite in the limit $\omega \to 0$, whereas the kernel of the difference of two H_Es suppresses soft-photon contributions [see Fig. 7.3]. As a result $|H_E(\omega_2) - H_E(\omega_1)|/T^2$ probes the emissivity of hard photons. We obtain $|H_E(\omega_2) - H_E(\omega_1)|/T^2 = 0.193(74)$, which is lower than, but compatible with the result obtained by integrating the leading-order weak-coupling photon spectrum [see Fig. 9.18], with next-to-leading-order corrections being positive [282]. Together, these results suggest that the AMY prediction for the photon spectral function holds within uncertainties for $\omega \gtrsim \pi T$, while the precise lattice determination of $H_E(\omega_1)$ imposes strong constraints in the soft regime, where deviations from weak-coupling expectations are observed. Overall, the lattice results provide

non-perturbative constraints on the photon spectral function directly relevant for heavy-ion phenomenology.

In addition, we performed a temperature scan at fixed lattice spacing using $N_f = 2+1$ ensembles with physical up, down and strange quark masses. From the long-distance behavior of the screening correlators we determined the static and non-static screening masses in the first Matsubara sector. In the hadronic phase at $T = 128\,\text{MeV}$ the two channels were found to be degenerate within uncertainties. At the chiral crossover ($T = 154\,\text{MeV}$) the non-static mass remained nearly unchanged, while the static mass decreased by about 8%, generating a sizeable mass gap. In the high-temperature phase at $T = 192\,\text{MeV}$ both screening masses were consistent with their crossover values, with the gap persisting at improved precision. For the static channel, our results agree with continuum-extrapolated $N_f = 2$ findings at comparable relative temperature, while in the non-static channel we find a few-sigma tension, potentially indicating stronger discretization effects.

We also examined the temperature dependence of the first energy moment $H_E(\omega_1)$. At the chiral crossover, the QNS $\chi_q/T^2 = 0.74(1)$ agrees well with the HRG estimate $\chi_q/T^2|_{\text{HRG}} = 0.70$, indicating that bulk thermodynamics can still be described in terms of hadronic degrees of freedom. In contrast, $H_E(\omega_1)$ shows a pronounced enhancement, more than doubling its value compared to the hadronic phase [cf. Table 8.2]. Expressed in temperature units, its value at $T = 154\,\text{MeV}$ is already comparable to that at $T = 192\,\text{MeV}$, despite the reduced number of effective charge carriers at the crossover. At $T = 192\,\text{MeV}$, we further find good agreement with the continuum-extrapolated $N_f = 2$ determination [cf. Eq. (9.3.8)]. For the crossover ensemble, an independent bounding-method analysis corroborates the model determination, lending confidence to the robustness of the observed enhancement. A study of the virtuality dependence revealed a similar pattern: the Q^2-derivative of H_E at $T = 154\,\text{MeV}$ is about 40% larger than in both the hadronic and high-temperature phases. These findings carry potential implications for the phenomenology of heavy-ion collisions. As $|H_E(\omega_1)|/T^2$ near the crossover is already comparable to our result in the high-temperature phase, this implies substantial photon emission at late stages of heavy ion collisions. This may help alleviate the so-called direct photon puzzle, since the azimuthal anisotropy of photons naturally increases if a significant fraction is emitted closer to freeze-out [250]. A systematic study of the impact of our lattice results on the hydrodynamics-based predictions for photon yields and anisotropies at RHIC and the LHC constitutes a promising future direction.

In the second Matsubara sector we have conducted a comprehensive analysis of systematic uncertainties related to the tail contribution and have effectively managed cut-off effects. One possible subsequent step involves conducting simulations at identical bare parameters while varying the spatial volume L^3 of the box to systematically investigate finite-volume effects. It may be argued that the signal on the correlators in the second Matsubara sector Ω_2 deteriorates well before reaching the spatial midpoint of the box $\frac{L}{2}$. However, the kernel $\cosh(\Omega_n x_1)$ acts infrared-enhancing, thereby attributing greater weight to the long-distance tail, where finite-volume artifacts may become significant. As an exploratory endeavor, this thesis presents the initial examination of $H_E(\omega_3)$. In addition to the large statistical errors on the position space integrand [see left panel of Fig. 9.21], we also observe very large discretization effects when considering various kernel modifications [see right panel of Fig. 9.21]. Furthermore, the effective non-static and static

screening masses in the $n = 3$ sector start to overlap in the plateau region, making a systematic analysis of the tail contribution infeasible. Consequently, we conclude that extremely fine lattice spacings, potentially utilizing anisotropic lattices, are necessary for accurate resolution of this sector.

9.8 Outlook

As an alternative, we intend to generate LQCD ensembles with an aspect-ratio of 6 at a significantly higher temperature, $T \approx 1.4\,\mathrm{GeV}$ [cf. Appendix N], where weak-coupling predictions are anticipated to be reliable, making it advantageous to compare continuum-extrapolated lattice results with the AMY prediction [252, 253] and the free continuum prediction. At the current temperature of $T = 254\,\mathrm{MeV}$, the pion screening mass m_π remains approximately 30% below the asymptotic free $2\pi T$ regime. Therefore, by simulating at this elevated temperature, a reduction in the variance of the non-static isovector vector screening correlator is anticipated, as the pion screening mass will approach $2\pi T$, thereby contributing less to the noise.

Our focus thus far has been on the isovector contribution of the electromagnetic current. It is assumed that in the high-temperature phase of QCD, the disconnected contribution, which is of $\mathcal{O}(\alpha_s^3)$, can be neglected [98]. Additionally, we have assumed a minimal dependence on the (valence) quark mass when comparing the light-light and strange-strange components of the vector current. It is interesting to examine, whether this assumption still holds at temperatures near the crossover, as investigations related to the $g-2$ have revealed that the strange-connected and light-connected contributions are highly sensitive to quark mass effects. Additionally, it would also be valuable to extrapolate the $N_f = 2+1$ results for the screening masses and the first energy moment around the chiral crossover to the continuum. This would allow for an assessment of discretization effects and the derivation of fully physical predictions across the transition region.

In preparation for the LHC Run4 (2030-2033), there are plans to measure electromagnetic radiation, specifically direct photons and dileptons below the J/ψ mass, using a forward calorimeter (FoCal) system [288]. A possible extension of the existing framework for investigating photon emissivity [256] is the incorporation of non-zero fixed virtualities. This enables the examination of dilepton pairs with small invariant masses M^2. A significant challenge will be to derive a convergent quantity $H_E(\kappa_n)$, where $\kappa_n \equiv \sqrt{M^2 + \omega_n^2}$, as the kernel will grow like $\exp(\kappa_n x_1)$.

Part IV

Appendices

Appendices

A Derivation of the Spectral Representation of the Euclidean Correlator

This derivation is based on arguments presented in Ref. [96]. Starting from Eq. (4.4.9) and inserting Eq. (4.4.12) we arrive at

$$G_E(\tau) = \int_{\mathbb{R}} \mathrm{d}\omega \left[\frac{1}{\beta}\sum_{n\in\mathbb{Z}} \frac{\mathrm{e}^{-\mathrm{i}\omega_n\tau}}{\omega - i\omega_n}\right]\rho(\omega) \equiv \int_{\mathbb{R}} \mathrm{d}\omega\, \tilde{K}(\tau,\omega)\rho(\omega)\,, \tag{A.1}$$

where the kernel $\tilde{K}(\tau,\omega)$ has simple poles $z = i\omega_n$ on the imaginary axis. The Bose-Einstein distribution function $n_B(z) = \frac{1}{\mathrm{e}^{\beta z}-1}$ also has simple poles $z = i\omega_n$, and is analytical elsewhere. Furthermore, by expanding in a Laurent series around the poles, we obtain

$$n_B(z + i\omega_n) = \frac{1}{\mathrm{e}^{\beta(z+\mathrm{i}\omega_n)} - 1} = \frac{1}{\beta}\frac{1}{z} + \mathcal{O}(1)\,, \tag{A.2}$$

implying that the residue of each pole is $\frac{1}{\beta}$. Consequently, we can replace the Matsubara sum appearing in Eq. (A.1) by a complex contour integral

$$\begin{aligned}
\frac{1}{\beta}\sum_{n\in\mathbb{Z}} \frac{\mathrm{e}^{-\mathrm{i}\omega_n\tau}}{\omega - i\omega_n} &= \frac{1}{2\pi i}\oint_\Gamma \mathrm{d}z\, \frac{\mathrm{e}^{-z\tau}}{\omega - z}\, n_B(z)\,, \\
&= \sum \mathrm{Res}_{z\to\omega}\left(\frac{\mathrm{e}^{-z\tau}}{\omega - z}\right) n_B(z) \\
&= -(-\mathrm{e}^{-\omega\tau})\, n_B(\omega) \\
&= \mathrm{e}^{-\omega\tau}\frac{1}{\mathrm{e}^{\beta\omega} - 1}\,.
\end{aligned} \tag{A.3}$$

The complex contour Γ is initially composed of small loops that enclose the Matsubara poles at $z = i\omega_n$ counterclockwise. Subsequently, it can be continuously deformed, without intersecting any singularities of the integrand, into a contour that encloses solely the simple pole at $z = \omega$ clockwise, producing a minus sign [see Fig. 23]. The integral along the large semicircle at infinity vanishes due to the exponential factor $e^{-z\tau}$, in accordance with Jordan's Lemma. As the spectral function $\rho(\omega)$ is antisymmetric w.r.t. ω, only the antisymmetric part of the kernel $\tilde{K}(\tau,\omega)$ con-

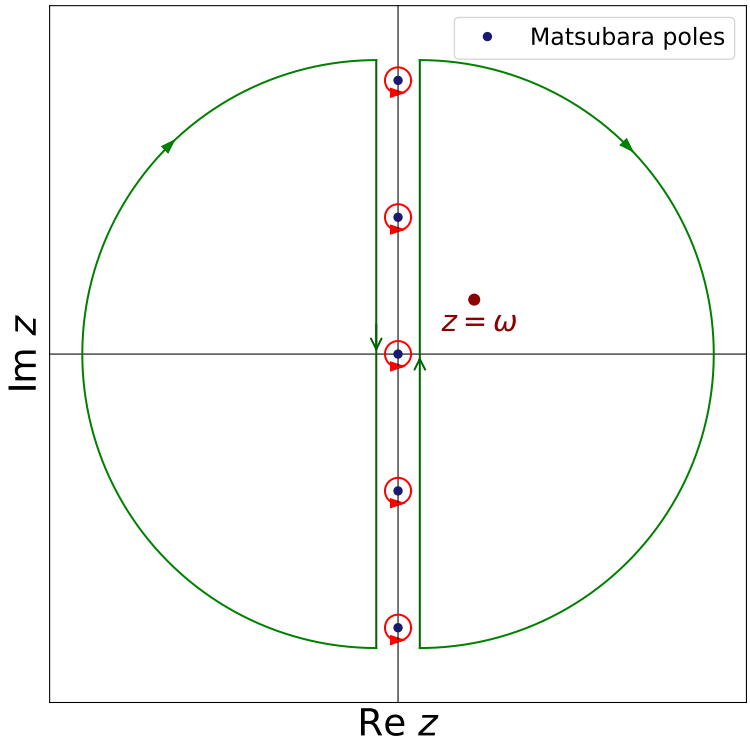

Figure 23: The Bose distribution function $n_B(z)$ generates poles at $z = i\omega_n$ (indicated by blue dots), which are traversed in a counterclockwise direction. Upon deforming the contour, the pole at $z = \omega$ is traversed in a clockwise direction, resulting in a negative residue.

tributes to the integral, i.e.,

$$\begin{aligned} 2K(\tau,\omega) &= \tilde{K}(\tau,\omega) - \tilde{K}(\tau,-\omega) \\ &= \mathrm{e}^{-\omega\tau} n_B(\omega) - \mathrm{e}^{\omega\tau} n_B(-\omega) \\ &= \mathrm{e}^{-\omega\tau} n_B(\omega) + \mathrm{e}^{\omega\tau}(1 + n_B(\omega)) \\ &= \frac{\mathrm{e}^{-\omega\tau} + \mathrm{e}^{\omega\tau}\mathrm{e}^{\beta\omega}}{\mathrm{e}^{\beta\omega} - 1} \\ &= \frac{\mathrm{e}^{\beta\omega/2}\left(\mathrm{e}^{\omega(\tau-\beta/2)} + \mathrm{e}^{-\omega(\tau-\beta/2)}\right)}{\mathrm{e}^{\beta\omega/2}(\mathrm{e}^{\beta\omega/2} - \mathrm{e}^{-\beta\omega/2})} \\ &= \frac{\cosh[\omega(\frac{\beta}{2} - \tau)]}{\sinh(\frac{\omega\beta}{2})} \end{aligned} \tag{A.4}$$

By substituting Eq. (A.4) into Eq. (A.1), the factor $\frac{1}{2}$ in the kernel is canceled by the factor of 2 that arises from restricting the integration over ω from $\mathbb{R}$ to $\mathbb{R}^+$. Consequently, we derive Eq. (6.2.15), which establishes the relationship between the time-dependent Euclidean correlator and the spectral function, a crucial aspect for spectral reconstruction methoda.

B Improvement Process

Lattice derivatives introduce cut-off effects. Consequently, in this section, we specify the lattice discretized (improved) derivatives employed in this study, along with the $\mathcal{O}(a)-$improvement process of the axial-vector and vector current. We define a forward and backward derivative as

$$\partial_\mu f(x) = \frac{1}{a}\left(f(x+a\hat{\mu}) - f(x)\right) + \mathcal{O}(a)\,, \tag{B.1}$$

$$\partial^*_\mu f(x) = \frac{1}{a}\left(f(x) - f(x-a\hat{\mu})\right) + \mathcal{O}(a)\,. \tag{B.2}$$

A symmetrized version with reduced discretization errors can be obtained by combining forward and backward derivative as follows

$$\widetilde{\partial}_\mu f(x) = \frac{1}{2}\left(\partial_\mu f(x) + \partial^*_\mu f(x)\right) = \frac{1}{2a}\left(f(x+a\hat{\mu}) - f(x-a\hat{\mu})\right) + \mathcal{O}(a^2)\,. \tag{B.3}$$

Note the absence of $\mathcal{O}(a)$ discretization errors. The aforementioned symmetrized derivative can be further refined by implementing the substitution [289].

$$\begin{aligned}\widetilde{\partial}_\mu f(x) \to \bar{\partial}_\mu f(x) &:= \widetilde{\partial}_\mu f(x)\left(1 - \frac{1}{6}a^2\partial^*_\mu\partial_\mu f(x)\right)\,,\\ &= \frac{1}{12a^2}\left[f(x-2a\hat{\mu}) - 8f(x-a\hat{\mu}) + 8f(x+a\hat{\mu}) - f(x+2a\hat{\mu})\right]\,.\end{aligned} \tag{B.4}$$

When acting on smooth functions this improved lattice derivative has $\mathcal{O}(a^4)$ discretization errors.

Subsequently, we define the $\mathcal{O}(a)-$improved axial-vector and vector current as

$$A^{\mathrm{imp},b}_\mu(x) = A^b_\mu(x) + ac_A(g^2)\widetilde{\partial}_\mu P^b(x)\,, \tag{B.5}$$

$$V^{\mathrm{imp},b}_\mu(x) = V^b_\mu(x) + ac_V(g^2)\bar{\partial}_\nu\, T_{\mu\nu}(x)\,, \tag{B.6}$$

where

$$T^a_{\mu\nu}(x) \equiv -\frac{1}{2}\bar{\psi}[\gamma_\mu,\gamma_\nu]\frac{\tau^a}{2}\psi \tag{B.7}$$

is the tensor current.

The non-perturbatively calculated coefficient c_A was taken from Ref. [290], and the coefficient c_V from Ref. [291]. For the analysis of the '$V-A$' correlators in Sec. 6.8.3, we use an improved version of the symmetric derivative defined in Eq. (B.4).

Table 2: Summary of the non-singlet renormalization and improvement parameters.

$Z_V(g^2)$	[291]	0.735 71(10)
$Z_A(g^2)$	[264]	0.769 00(42)
$Z_P(g^2)$	[206]	0.347 68
$b_V(g^2)$	[293]	1.388(17)
$b_A(g^2)$	[293]	1.232(15)
$\widetilde{b}_V(g^2)$	[293]	0.069(42)
$\widetilde{b}_A(g^2)$	[293]	−0.03(13)
$\kappa_{\text{cr.}}$	[294]	0.137 172 6(13)
κ_{l}	[295]	0.137 232 867
κ_{s}	[295]	0.136 536 633

C Renormalization Process

As we have already mentioned in Sec. 5.4.4, due to the explicit breaking of the chiral symmetry by the Wilson term the quark mass m_q needs an additional additive renormalization parameter,

$$am_q = am_0 - am_{\text{cr.}}\,, \tag{C.1}$$

where $m_{\text{cr.}}$ is called the critical mass (i.e. the value of the bare mass m_0, where the pion mass vanishes.). In practical lattice simulations with Wilson fermions this is done by measuring the PCAC mass m_{PCAC} (cf. Sec. 6.3.1) and tuning the hopping parameter $\kappa_q = \frac{1}{2am_0+8}$ [see Eq. (5.4.33)] to its critical value $\kappa_{\text{cr.}}$. Inserting $am_0 = \frac{1}{2\kappa_q} - 4$ into Eq. (C.1) we get

$$am_q = \frac{1}{2\kappa_q} - 4 - \left(\frac{1}{2\kappa_{\text{cr.}}} - 4\right) = \frac{1}{2}\left(\frac{1}{\kappa_q} - \frac{1}{\kappa_{\text{cr.}}}\right)\,, \quad q \in \{l, s\}\,, \tag{C.2}$$

$$m_{\text{av}} = \frac{1}{3}\left(2m_l + m_s\right)\,, \tag{C.3}$$

where am_q denotes the bare subtracted quark mass and m_{av} the "average quark mass". The values for the renormalization constants Z_J and the finite quark mass parameters b_J are listed in Table 2.

Following Ref. [292], we renormalize the correlators as follows:

$$G_V^{\text{ren.}} = Z_V^2(g^2)\left[1 + 2am_l b_V(g^2) + 6am_{\text{av}}\widetilde{b}_V(g^2) + \mathcal{O}(a^2)\right] G_V\,, \tag{C.4}$$

$$G_A^{\text{ren.}} = Z_A^2(g^2)\left[1 + 2am_l b_A(g^2) + 6am_{\text{av}}\widetilde{b}_A(g^2) + \mathcal{O}(a^2)\right] G_A\,, \tag{C.5}$$

$$G_{A_0}^{\text{ren.}} = Z_A^2(g^2)\left[1 + 2am_l b_A(g^2) + 6am_{\text{av}}\widetilde{b}_A(g^2) + \mathcal{O}(a^2)\right] G_{A_0}\,, \tag{C.6}$$

$$G_{PA_0}^{\text{ren.}} = Z_P(g^2)Z_A(g^2)\left[1 + am_l b_A(g^2) + 3am_{\text{av}}\widetilde{b}_A(g^2) + \mathcal{O}(a^2)\right] G_{PA_0}\,, \tag{C.7}$$

$$G_P^{\text{ren.}} = Z_P^2(g^2) G_P\,, \tag{C.8}$$

with $g^2 = 6/\beta$ being the bare gauge coupling.

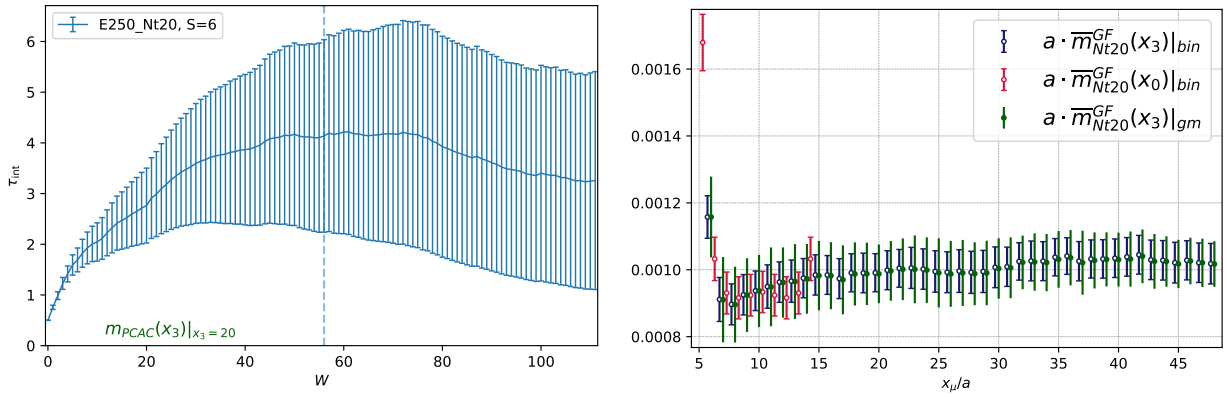

Figure 24: **Left panel**: Integrated autocorrelation time $(S = 6)$ of the PCAC mass at fixed source-sink separation $x_3/a = 20$ on the `E250Nt20` ensemble at the chiral crossover. **Right panel**: Comparison of the PCAC mass obtained from binning and jackknife procedure with the corresponding PCAC mass obtained using the gamma method in the implementation of the `pyerrors` package on the `E250Nt20` ensemble at the chiral crossover.

D Error Analysis

Data from Markov Chain Monte Carlo (MCMC) simulations exhibit autocorrelation, indicating that successive measurements are not independent. This phenomenon arises because the underlying distributions evolve through sequential updates, thereby diminishing the effective number of independent measurements. To accurately estimate the statistical uncertainty of an observable, it is essential to appropriately account for autocorrelation.

Within the lattice community, it is a well-established practice to estimate uncertainties in Monte Carlo observables using resampling methods, such as the Jackknife or Bootstrap techniques. When addressing autocorrelation, the data obtained from MCMC simulations are binned into blocks. The bin size, measured in Monte Carlo time, must be selected to be significantly larger than the autocorrelation time of the observable in question. However, regardless of the chosen bin size, the data within adjacent bins remain in close proximity in Monte Carlo time. Moreover, this approach may be questionable if long-range autocorrelation is present only in highly derived observables and not evident in the underlying correlators used to determine an appropriate bin size.

In practical lattice computations, measurements of primary observables, denoted by a Greek index with an (unknown) exact mean value A_α, are performed. In this thesis, these primary observables are Euclidean two-point correlation functions. These measurements must be conducted on a set of $N^{(i)}$ gauge configurations[4]. In practice, we can only perform measurements

$$a_\alpha(t)\,, \qquad t \in \{1, \cdots, N\}\,, \tag{D.1}$$

[4]The index (i) denotes different ensembles that may vary in physical and/or algorithmic parameters. Occasionally, as in our `E250Nt16` ensemble, multiple chains (replicas) are generated that differ only in the seed of the random number generator while maintaining identical parameters. This can be advantageous when generating multiple chains simultaneously or simply enhancing statistical precision. To avoid cumbersome notation, this index will be suppressed in the following.

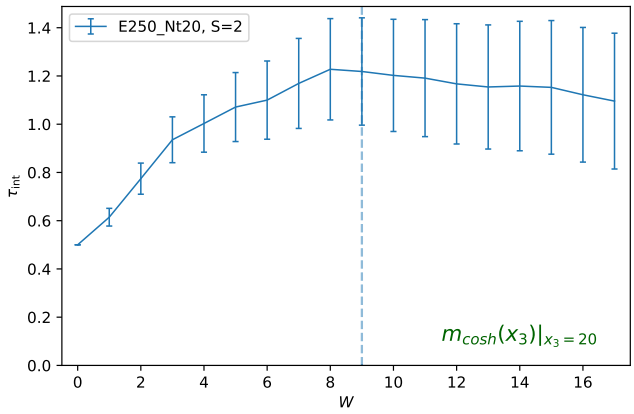

Figure 25: Integrated autocorrelation time for the cosh mass, defined in Eq. (I.6) at source-sink separation $x_3 = 20$, well in the region where a plateau is observed (see middle plot of Fig. 29)

on a finite number of configurations N, thus obtaining

$$\bar{a}_\alpha = \frac{1}{N}\sum_{t=1}^{N} a_\alpha(t)\,, \tag{D.2}$$

as a lattice estimate for A_α. We then need to perform a sufficiently large number of measurements, such that our lattice estimator approaches the primary observable in the limit

$$\lim_{N\to\infty} \bar{a}_\alpha = A_\alpha\,. \tag{D.3}$$

A lattice measurement of a given observable on a specific configuration $a_\alpha(t)$ varies over the mean defined in Eq. (D.2). Consequently, we define the fluctuations

$$\delta_\alpha(t) = \bar{a}_\alpha - a_\alpha(t)\,. \tag{D.4}$$

Usually, we are interested in objects that are functions of our primary observables $f(A_1, A_2, \cdots)$. These objects

$$F \equiv f(A_1, A_2, \cdots) = f(A_\alpha)\,, \tag{D.5}$$

are called *derived observables*. Under the assumption that our primary observables have been determined accurately enough, we use Taylor expansion in the fluctuations Eq. (D.4),

$$f(A_\alpha + \delta_\alpha) = f(A_\alpha) + \delta_\alpha \left.\frac{\partial f}{\partial A_\alpha}\right|_{A_\alpha=\bar{a}_\alpha} + \mathcal{O}(\delta_\alpha^2) \;\equiv\; F + \delta_\alpha \bar{f}_\alpha + \mathcal{O}(\delta_\alpha^2)\,, \tag{D.6}$$

and truncate after the first order (linear error propagation). A useful quantity for error estimation is the *autocorrelation function*,

$$\Gamma_{\alpha\beta}(t) = \frac{1}{N-t}\sum_{t'=1}^{N-t} \delta_\alpha(t+t')\delta_\beta(t')\,, \tag{D.7}$$

defined in terms of the fluctuations δ_α. From the autocorrelation function for primary observables,

Eq. (D.7), we can get the autocorrelation function for any derived observable F,

$$\Gamma_F(t) = \sum_{\alpha,\beta} \bar{f}_\alpha \bar{f}_\beta \Gamma_{\alpha\beta}(t)\,. \tag{D.8}$$

Choosing $t = 0$ this reduces to the symmetric covariance matrix with ordinary variances as diagonal elements. If τ_{exp} (*exponential autocorrelation time*) denotes the largest autocorrelation time in the system, the autocorrelation function typically exhibits an asymptotic exponential behavior,

$$\frac{\Gamma_F(t)}{\Gamma_F(0)} \sim \exp\left(-\frac{t}{\tau_{\text{exp}}}\right). \tag{D.9}$$

For any (derived) observable F, one defines [213]

$$\tau_{\text{int},F}(W) = \frac{1}{2} + \sum_{t=1}^{W} \frac{\Gamma_F(t)}{\Gamma_F(0)}\,, \tag{D.10}$$

as the *integrated autocorrelation time*. In practice one needs to choose an appropriate window W. In doing so, one is confronted with a trade-off between capturing all the relevant information in the chosen window and simultaneously not being dominated by noise contributions to τ_{int} for large values of t. In Ref. [213] an automatic windowing procedure was introduced to determine W in actual data analysis. Based on the hypothesis $\tau_{\text{exp}} = S\,\tau_{\text{int},F}(W)$ one chooses[5] the factor S such that the sum of systematic and statistical error is minimized on the integrated autocorrelation time $\tau_{\text{int},F}$ [213]. The default value is $S = 2$. However, for the correct error estimation of the PCAC mass on the `E250Nt20` ensemble, we choose $S = 6$ [see left panel of Fig. 24]. The final error based on the integrated autocorrelation time reads [215]

$$\sigma_F = \sqrt{2\tau_{\text{int},F}\frac{\Gamma_F(0)}{N}}\,. \tag{D.11}$$

Upon comparison of the error of the PCAC mass on the `E250Nt20` ensemble obtained with the above prescription to that using binning with a bin size of 20, we find that near the midpoint the error estimates are in good agreement. However, for shorter source-sink separations, the gamma method shows a larger error [see right panel of Fig. 24].

We utilize the robust median and median absolute deviation (MAD) described in Refs. [4, 296] to identify two outliers (out of 1000 configurations) on the `E250Nt20` ensemble. If autocorrelation is absent $\tau_{\text{int}} = 0.5$ and Eq. (D.11) reduces to the standard error. In the presence of autocorrelation, however, the "effective number of configurations" is reduced by a factor of $1/(2\tau_{\text{int},F})$.

For the estimation of the statistical errors of our (derived) observables we use the Γ method [212–214] in the implementation of the `pyerrors` package introduced in Ref. [215].

[5] Values between 2 and 5 are usually chosen for S [214].

E Chiral Effective Theory Lagrangian of Son and Stephanov

In the chiral effective theory approach of Son and Stephanov [191, 192] the dynamics of the pions at finite temperature is described by the Lagrangian,

$$\mathcal{L}_{\text{eff}} = \frac{f_t^2}{4}\langle \nabla_0 \Sigma \nabla_0 \Sigma^\dagger \rangle - \frac{f_\pi^2}{4}\langle \partial_i \Sigma \partial_i \Sigma^\dagger \rangle + \frac{m_\pi^2 f_\pi^2}{2}\text{Re}\langle \Sigma \rangle \,, \tag{E.1}$$

where Σ denotes an $\text{SU}(2)$ matrix whose phase describes the pions, $\nabla_0 \Sigma = \partial_0 \Sigma - \frac{i}{2}\mu_{I5}(\tau_3 \Sigma + \Sigma \tau_3)$ is the covariant derivative, μ_{I5} denotes the axial-isospin chemical potential and the trace is taken in flavor space. Note that in the presence of a thermal medium Lorentz invariance is broken resulting in two independent decay constants which are related through the pion velocity as follows [191],

$$u = \frac{f_\pi}{f_t} \,. \tag{E.2}$$

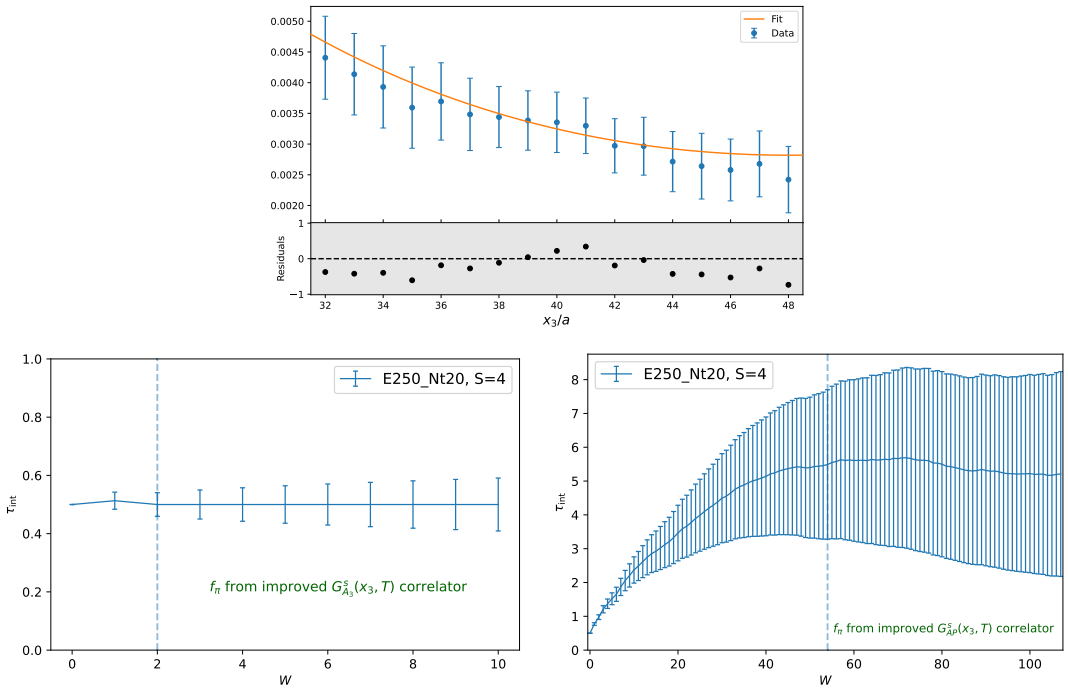

Figure 26: **Upper panel**: Screening correlator $G^s_A(x_3, T = 154\,\text{MeV})$ [defined in Eq. (6.2.5)] together with the corresponding fit. **Left panel**: Integrated autocorrelation time τ_{int} for f_π determined as described in Sec. 6.3.2. **Right panel**: Integrated autocorrelation time τ_{int} for f_π determined from $G^s_A(x_3, T)$.

F Alternative Determination of the Screening Pion Decay Constant

In Section 6.3.2, we have determined the screening pion decay constant f_π across all three ensembles. The methodology employed therein involves a simultaneous fitting approach to the screening pseudoscalar and axial-pseudoscalar correlators. Given that the latter correlator serves as an order parameter for chiral symmetry restoration, we encounter significant integrated autocorrelation times τ_{int} within the `E250Nt20` ensemble, which is generated at a temperature proximate to the pseudocritical temperature T_{pc} [cf. Fig. 6.5]. Alternatively, as demonstrated in Ref. [1], the pion decay constant can be simultaneously extracted from the pseudoscalar and axial correlators. However, this fitting approach necessitates the extraction of the PCAC mass from the axial-pseudoscalar correlator. Therefore, as a verification measure, we determine the screening decay constant on the `E250Nt20` ensemble exclusively from the noisy axial correlator G^s_A [see the top panel of Fig. 26]. The asymptotic behavior of this correlator delineates the screening pion decay constant f_π [cf. Eq. (6.2.5)]. Consequently, employing a cosh fit ansatz

$$G^s_A(x_3, T) \overset{\circ}{=} A_1^2 \cosh[m_1(x_3 - L/2)]\,, \tag{F.1}$$

the screening pion decay constant f_π is obtained as

$$f_\pi = A_1 \sqrt{e^{m_1 L/2}\, m_1}\,. \tag{F.2}$$

We extract $f_\pi/T = 0.179(24)$, compatible with our result $f_\pi/T = 0.172(12)$ [cf. Table 6.3].

Table 3: Comparison of the E250 unimproved and improved PCAC masses for $N_\tau \in \{24, 20, 16\}$.

Ensemble	E250Nt24	E250Nt20	E250Nt16
$a \cdot m_{\mathrm{PCAC}}^{\mathrm{unimpr.}}$	0.001575(44)	0.001193(90)	0.001335(86)
$a \cdot m_{\mathrm{PCAC}}^{\mathrm{impr.}}$	0.001466(41)	0.001003(90)	0.000060(88)

G The Influence of the $\mathcal{O}(a)$-Improvement Process on the PCAC Mass

The improvement of the AP-correlator in the chirally symmetric phase is a general challenge one has to face when dealing specifically with Wilson fermions. The AP-correlator is of order of the quark mass m_{q} and therefore serves as an order parameter for chiral symmetry restoration. However, at high temperatures, the standard power-counting breaks down. In fact, at these temperatures, the $\mathcal{O}(a)$-improvement starts to interfere with chiral symmetry restoration, meaning that the correction terms of order $a \cdot T^2$ are no longer sub-leading.

One potential approach to address this issue is to increase the (valence) quark mass until the hierarchy is restored. We do not directly solve this problem here; instead, we sidestep it by using the unimproved version of the AP-correlator on our E250Nt16 box. Table 3 summarizes the effect of the improvement process on the PCAC masses for our three thermal boxes. As can be seen, the improved PCAC mass in the high-temperature phase is compatible with zero within errors. However, we once more stress that we use the improved PCAC mass on the E250Nt24 ensemble at all three temperatures.

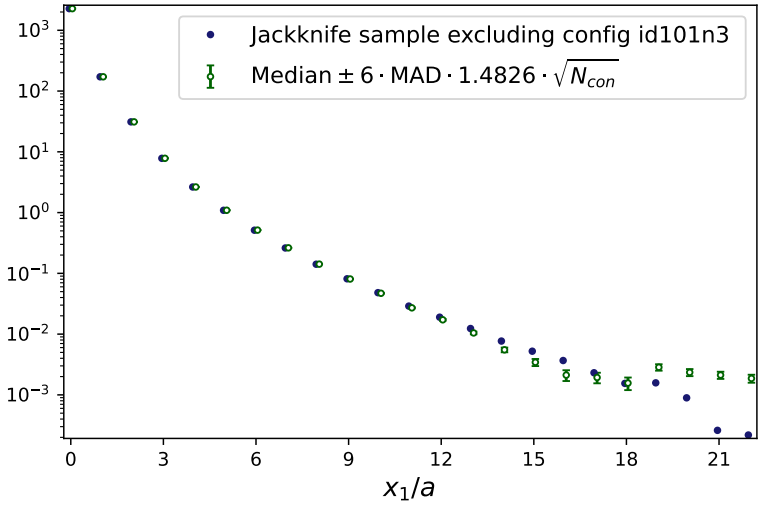

Figure 27: The blue points denote the jackknife sample of the static correlator $G^{\mathrm{T}}_{\mathrm{st}}(\omega_1, x_1)$ on the $N_\tau = 20$ ensemble at $T = 154\,\mathrm{MeV}$, obtained by removing one of the outlier configurations. The green points represent the median and median absolute deviation scaled by appropriate factors described in the text.

H Dealing with Outliers

One of the ensembles in this thesis, the `E250Nt20` ensemble [cf. Tab. 6.2] was generated in a parameter range that is difficult to access with Wilson fermions, namely physical up, down and strange quark masses right in the vicinity of the pseudo-critical temperature. Therefore, in addition to the signal-to-noise problem mentioned in Sec. 7.2, we encounter outliers that significantly exceed the ensemble average, and accurately estimating errors becomes a challenging endeavor.

Given the sensitivity of the mean value of correlators to extreme values, we aim for a more robust statistical approach. Instead of relying on the mean and standard deviation of the sampling distribution, we utilize the robust median and median absolute deviation (MAD) to identify exceptional configurations [296]. The latter can be related to the standard deviation via

$$\sigma = 1.4826 \cdot \mathrm{MAD}\,. \tag{H.1}$$

We primarily seek significant deviations from the central position of the sampling distribution on each time slice and for every source-sink separation. Whenever we encounter a value that deviates by approximately more than $6 - \sigma$, we declare the configuration in question to be exceptional. Following this method, we have removed 5 out of 1000 configurations from our analysis in Chap. 8. In Fig. 27 this procedure is shown for one outlier of the static screening correlator $G^{\mathrm{T}}_{\mathrm{st}}(\omega_1, x_1)$.

I Determination of Static Screening Properties in the Pseudoscalar Channel

In this appendix, we describe how the screening pion mass m_π and the screening decay constant f_π can be calculated. To accomplish this, we perform a simultaneous fit of the static screening pseudoscalar and axial-pseudoscalar correlator [see Eqs. (6.2.6) and (6.2.7)]. The spectral decomposition of the aforementioned correlators reads

$$G_P^s(x_3,T) = \frac{\langle 0|\,\bar{u}\gamma_5 d\,|\pi\rangle\,\langle\pi|\,\bar{d}\gamma_5 u\,|0\rangle}{2\,m_\pi}\left(\mathrm{e}^{-m_\pi x_3}+\mathrm{e}^{-m_\pi\cdot(L-x_3)}\right), \tag{I.1}$$

$$G_{AP}^s(x_3,T) = \frac{\langle 0|\,\bar{u}\gamma_3\gamma_5 d\,|\pi\rangle\,\langle\pi|\,\bar{d}\gamma_5 u\,|0\rangle}{2\,m_\pi}\left(\mathrm{e}^{-m_\pi x_3}-\mathrm{e}^{-m_\pi\cdot(L-x_3)}\right), \tag{I.2}$$

which suggests the following one-state fit ansatz:

$$G_P^{\mathrm{fit}}(x_3,T) = |A|^2\left(\mathrm{e}^{-Cx_3}+\mathrm{e}^{-C\cdot(L-x_3)}\right), \tag{I.3}$$

$$G_{AP}^{\mathrm{fit}}(x_3,T) = |A|\cdot|B|\left(\mathrm{e}^{-Cx_3}-\mathrm{e}^{-C\cdot(L-x_3)}\right), \tag{I.4}$$

A, B and C being free fit parameters. The pion screening mass m_π and the screening pion decay constant f_π are obtained from the fit parameters via

$$m_\pi \mathrel{\overset{\circ}{=}} C, \qquad f_\pi \mathrel{\overset{\circ}{=}} \sqrt{\frac{2\,|B|^2}{C}}\,. \tag{I.5}$$

The "cosh mass" is defined as the solution of the algebraic equation

$$\frac{\cosh[(x_{\mathrm{dec}}+a/2-L/2)m_{\cosh}^{[G]}(x_{\mathrm{dec}})]}{\cosh[(x_{\mathrm{dec}}-a/2-L/2)m_{\cosh}^{[G]}(x_{\mathrm{dec}})]} = \frac{G(x_{\mathrm{dec}}+a/2)}{G(x_{\mathrm{dec}}-a/2)}\,. \tag{I.6}$$

This is shown in Fig. 29. It is important to note that there exists a distinct equation and solution for $m_{\cosh}$ corresponding to each value of the decay direction $x_{\mathrm{dec}} = x_3$. The fitting procedures were conducted using the Levenberg-Marquardt method [297]; the outcomes are illustrated in Fig. 28. As demonstrated in Fig. 25, the cosh mass at the chiral crossover does not display the pronounced autocorrelation effects observed in the AP-correlator [cf. right panel of Fig. 6.5]. It is essential to emphasize that while the pion mass functions as an order parameter for the restoration of chiral symmetry, the PP-correlator does not fulfill this role. Similarly, although the AP-correlator serves as an order parameter for chiral symmetry restoration, the first derivative employed to define the PCAC mass does not serve this function.

To assign fit qualities in view of different fit windows, we applied the Akaike information criterion [278] and the model-averaging method from Ref. [279]. We assign a weight

$$w_i = N\cdot\exp\left[-\frac{1}{2}\left(\chi_i^2+2p_i-2n_i\right)\right], \tag{I.7}$$

where p_i is the number of fit parameters and n_i the number of data points in the fit[6] with mini-

[6] Since we are performing simultaneous one-state fits according to Eqs. (I.3)-(I.4) the number of fit parameters is three and we vary only the starting points and lengths of the fit intervals.

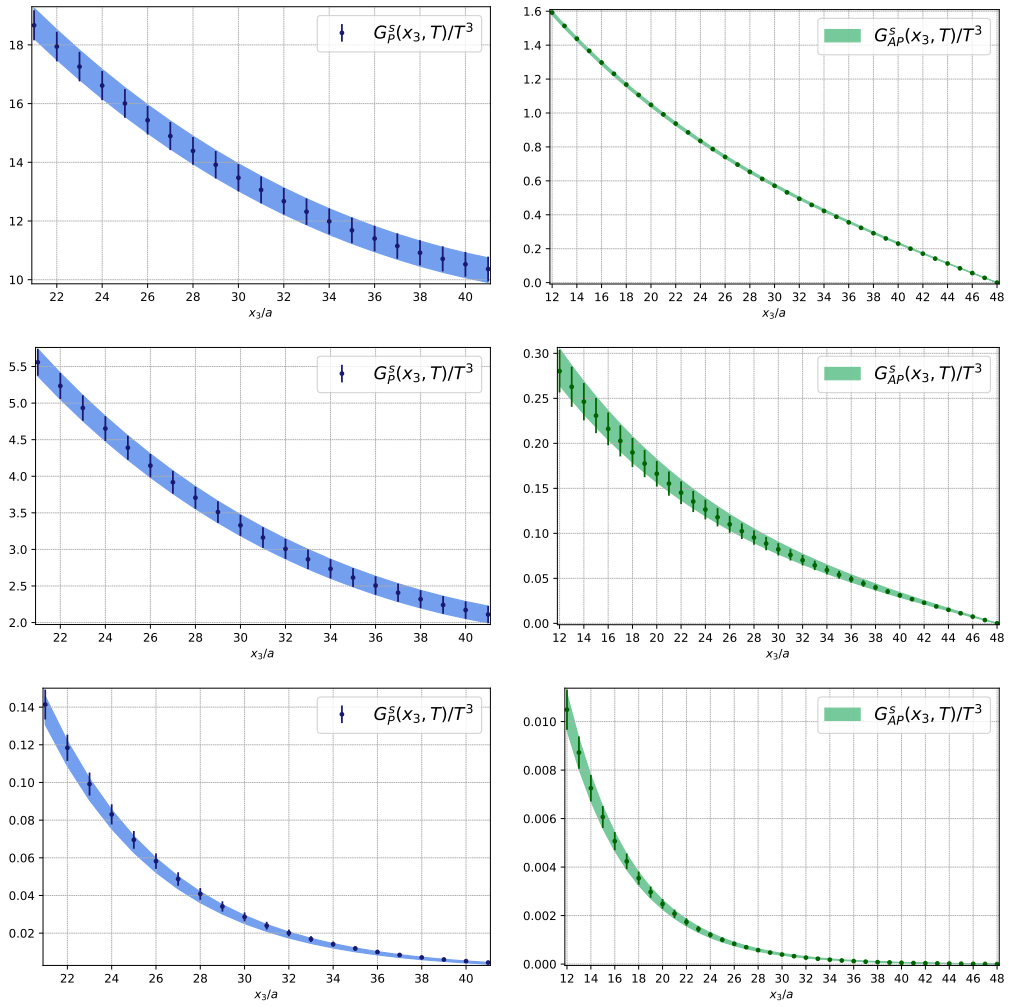

Figure 28: Renormalized screening correlation functions in temperature units $G_P^s(x_3,T)/T^3$ (l.h.s) and $G_{AP}^s(x_3,T)/T^3$ (r.h.s.) and the result of the simultaneous fit. **Top panels**: Correlators measured on the hadronic `E250Nt24` ensemble. **Middle panels**: Correlators measured on the chiral crossover `E250Nt20` ensemble. **Bottom panels**: Correlators measured on the high-temperature `E250Nt16` ensemble.

mized χ_i^2. N is chosen such that the weights w_i are normalized according to $\sum_i w_i = 1$. The results of the fits are shown in Fig. 28.

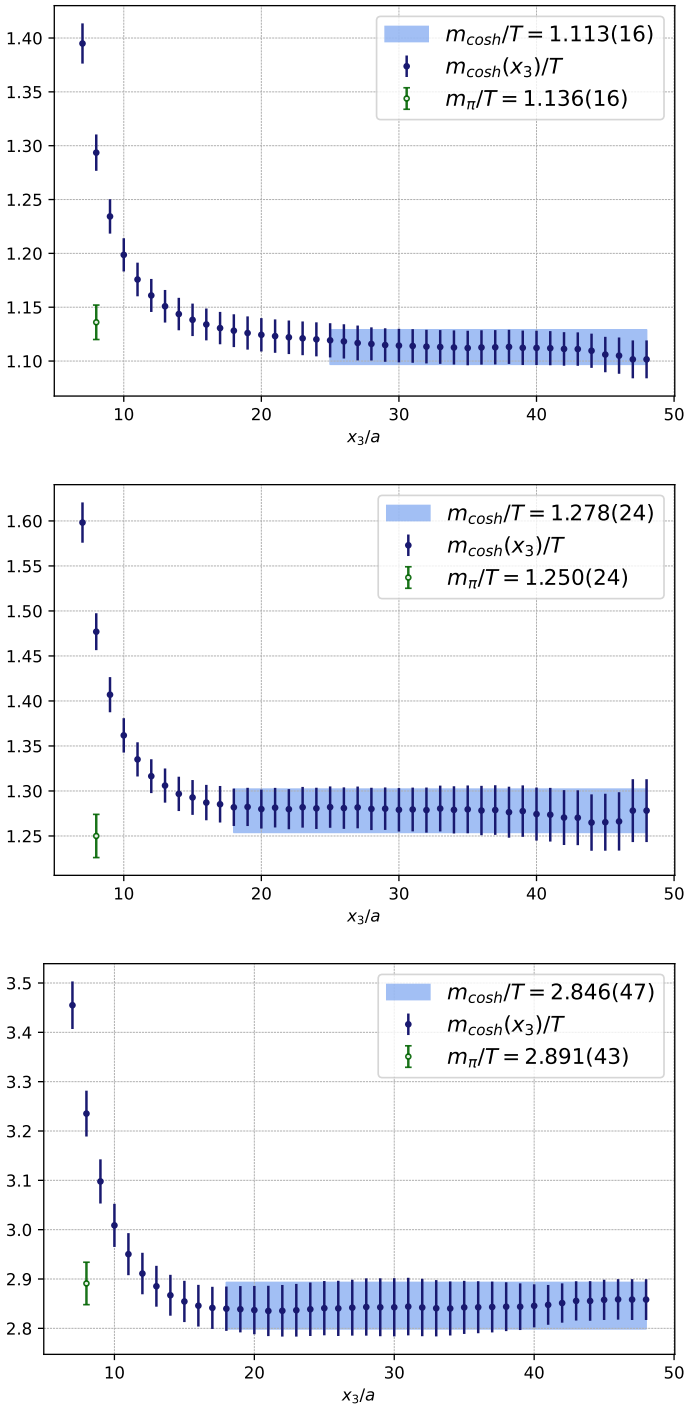

Figure 29: Effective mass plots for the cosh mass $m_{\cosh}(x_3)/T$ as a function of the x_3-coordinate in temperature units, obtained from the pseudoscalar screening correlation function at zero spatial momentum $G_P^s(x_3, T)$. For comparison the value for the screening pion mass m_π/T, obtained from a simultaneous fit of the pseudoscalar and axial-pseudoscalar correlator is also included (green bars). **Top panel**: Hadronic `E250Nt24` ensemble. The effective mass plateau is assumed to start at $x_3/a = 25$. **Middle panel**: `E250Nt20` ensemble at the chiral crossover. The effective mass plateau is assumed to start at $x_3/a = 18$. **Bottom panel**: `E250Nt16` ensemble in the high-temperature phase. It is assumed that the effective mass plateau starts at $x_3/a = 18$. For all three ensembles he result of the fit to the effective mass values is represented by a $1-\sigma$ band.

J Free Theory Expression for the Spectral Function of the Axial Charge

The spectral representation for the axial-charge correlator reads

$$\int \mathrm{d}^3x \, \langle A_0^a(x) A_0^b(0)\rangle = \delta^{ab} \int_0^\infty \mathrm{d}\omega \, \frac{\cosh(\omega(\beta/2-\tau))}{\sinh(\omega\beta/2)} \rho_A(\omega,\mathbf{0}). \tag{J.1}$$

For non-interacting quarks of mass m, the spectral function reads

$$\rho_A(\omega,\mathbf{0}) = \chi_A \, \omega \, \delta(\omega) + \frac{m^2 N_c}{4\pi^2} \, \theta(\omega^2-4m^2) \sqrt{1-\frac{4m^2}{\omega^2}} \, \tanh\left(\frac{\beta\omega}{4}\right), \tag{J.2}$$

with the axial-charge susceptibility reading

$$\chi_A = 2\beta N_c \int \frac{d^3p}{(2\pi)^3} \, \frac{\boldsymbol{p}^2}{E_{\boldsymbol{p}}^2} \, f_{\boldsymbol{p}}^F (1-f_{\boldsymbol{p}}^F). \tag{J.3}$$

It is worth noting that the analogue of Eq. (J.2) for the isospin charge,

$$\int \mathrm{d}^3x \, \langle V_0^a(x) V_0^b(0)\rangle = \delta^{ab} \int_0^\infty \mathrm{d}\omega \, \frac{\cosh(\omega(\beta/2-\tau))}{\sinh(\omega\beta/2)} \rho_{00}(\omega,\mathbf{0}), \tag{J.4}$$

reads

$$\rho_{00}(\omega,\mathbf{0}) = \chi_s \, \omega \, \delta(\omega) \tag{J.5}$$

with

$$\chi_s - \chi_A = 2\beta N_c m^2 \int \frac{\mathrm{d}^3p}{(2\pi)^3} \, \frac{1}{E_{\boldsymbol{p}}^2} \, f_{\boldsymbol{p}}^F (1-f_{\boldsymbol{p}}^F). \tag{J.6}$$

Table 4: Temporal symmetrized '$V - A$' correlators projected to zero momentum. All errors quoted are purely statistical. The correlators are renormalized and quoted in units of temperature (i.e. scaled by a factor N_τ^3).

	$T = 128\,\mathrm{MeV}$		$T = 154\,\mathrm{MeV}$		$T = 192\,\mathrm{MeV}$	
τ/a	$\frac{G_{(V-A)}(\tau)}{T^3}$	$\frac{G^{\mathrm{rec}}_{(V-A)}(\tau)}{T^3}$	$\frac{G_{(V-A)}(\tau)}{T^3}$	$\frac{G^{\mathrm{rec}}_{(V-A)}(\tau)}{T^3}$	$\frac{G_{(V-A)}(\tau)}{T^3}$	$\frac{G^{\mathrm{rec}}_{(V-A)}(\tau)}{T^3}$
3	2.7840(56)	2.971(67)	1.4447(32)	1.761(40)	0.73012(30)	0.917(21)
4	0.5508(54)	0.725(17)	0.1571(30)	0.461(11)	0.06793(26)	0.2554(58)
5	0.3230(50)	0.482(11)	0.0360(29)	0.3220(68)	0.00468(25)	0.1889(42)
6	0.2760(44)	0.4170(95)	0.0215(28)	0.2868(62)	-0.00288(24)	0.1768(39)
7	0.2504(36)	0.3755(85)	0.0197(25)	0.2673(60)	-0.00373(21)	0.1725(39)
8	0.2295(31)	0.3415(81)	0.0191(25)	0.2532(59)	-0.00373(24)	0.1713(40)
9	0.2127(28)	0.3133(79)	0.0188(23)	0.2441(59)		
10	0.2001(26)	0.2918(72)	0.0186(23)	0.2415(59)		
11	0.1914(26)	0.2780(72)				
12	0.1888(26)	0.2741(74)				

K Numerical Values for Temporal Correlators

In this appendix we list the means and errors of the (anti)symmetrized temporal correlators used in this thesis. For convenience, the PA_0 and '$V - A$' correlators are displayed in Figs. 30 and 31, respectively.

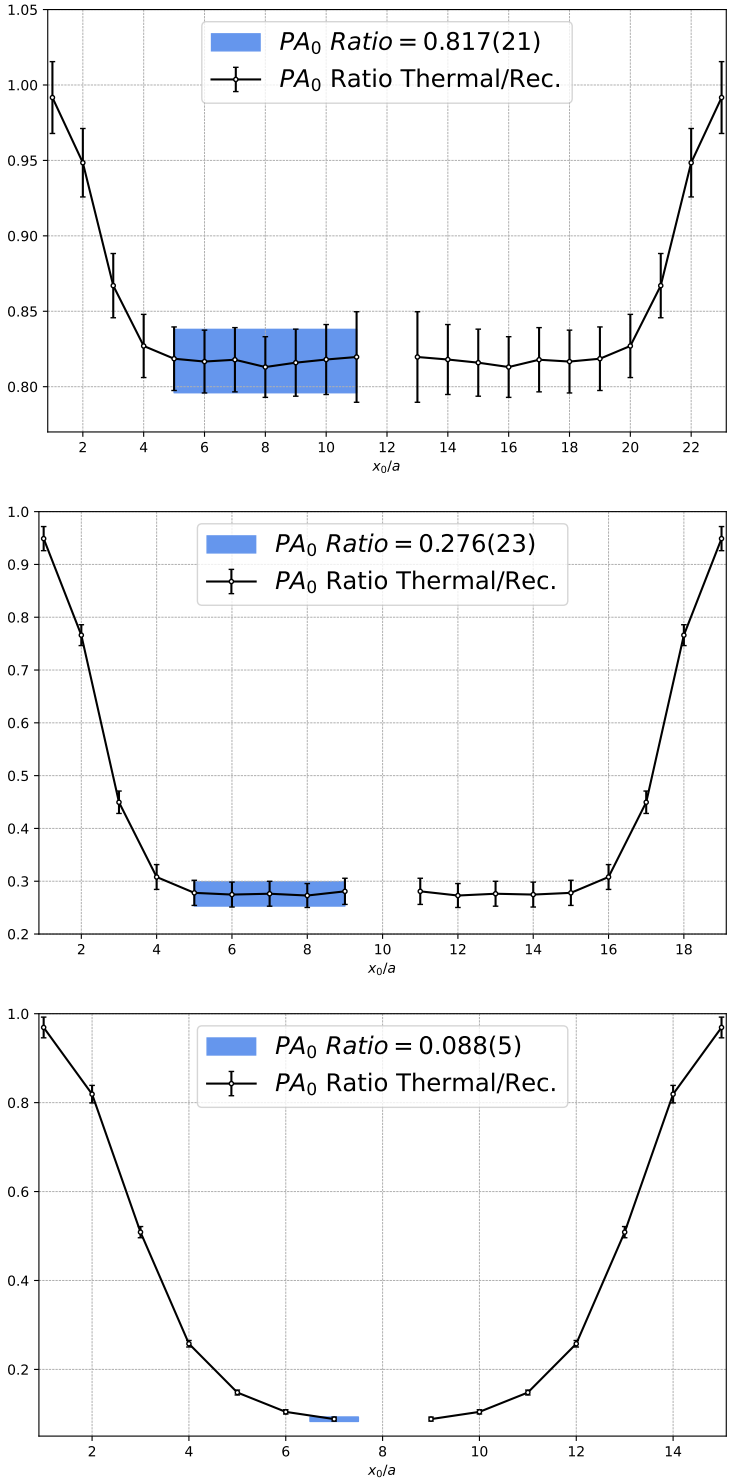

Figure 30: Ratios of the temporal thermal (PA_0)-correlators and the reconstructed correlator (PA_0)-correlator. **Top and middle panel**: Results for the `E250Nt24` and `E250Nt20` ensembles, respectively. The blue band shows the result of a correlated fit to the plateau. In both cases the $(PA_0)-$correlators have been $\mathcal{O}(a)$-improved. **Bottom panel**: Result for the `E250Nt16` ensemble. Because there is no clear plateau visible we quote the result for $\tau/a = 7$. In the high-temperature phase the $(PA_0)-$correlators have not been $\mathcal{O}(a)$-improved.

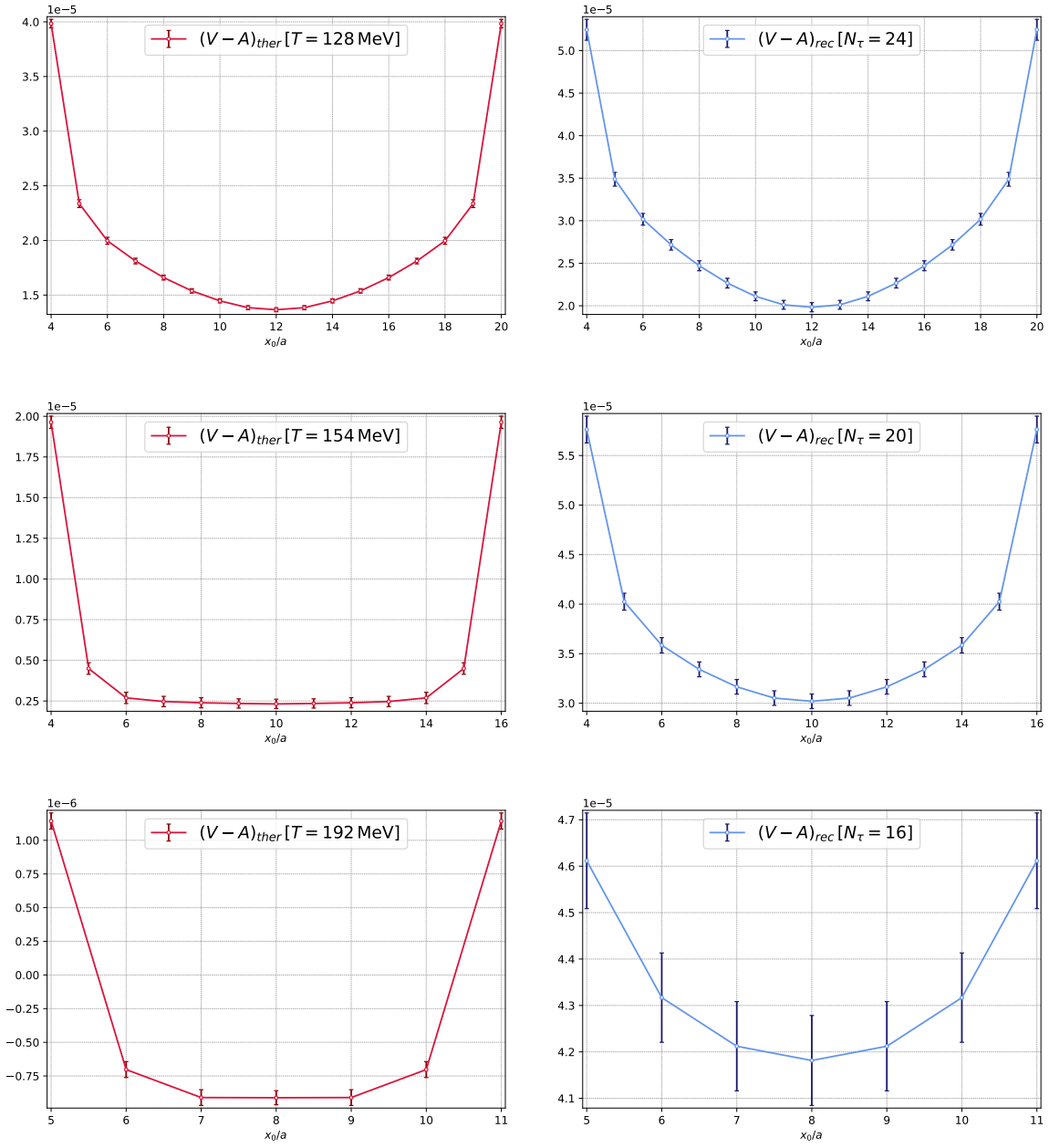

Figure 31: **L.h.s.**: The improved thermal correlator for the difference '$(V-A)$'. The top, middle, and bottom panels show the results in the hadronic phase, finite-temperature crossover, and high-temperature phase, respectively. **R.h.s.**: The corresponding reconstructed correlators [following Eq. (6.8.9)] for the $\mathcal{O}(a)-$improved difference '$(V-A)$'. All correlators have been renormalized and the corresponding ratios are shown in Fig. 6.12.

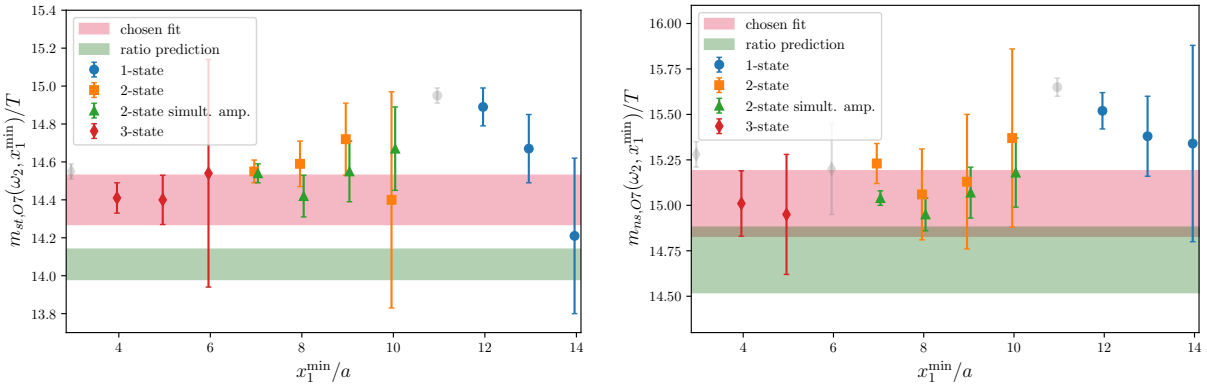

Figure 32: Fit results along with the ratio prediction [finite lattice spacing pendant of Eqs. (9.4.8)-(9.4.9)] for the ground-state static (top) and non-static (bottom) screening masses in the second Matsubara channel on O7. The fit range is set by choosing $x_1^{\max}/a$ as the first point where the correlator is consistent with zero, while $x_1^{\min}/a$ is varied systematically. One-, two-, and three-state fits are shown; for the two-state case, simultaneous fits to static and non-static amplitudes are also included. Grayed-out points correspond to fits with p-value > 0.95 or < 0.05.

L Correlator Fits: Varying the Number of States

As a consistency check, we have fitted the static and non-static correlators in sector ω_2 with various numbers of states included in the ansatz Eq. (7.3.1). The impact of these variations on the lowest screening mass is illustrated in Fig. 32 for ensemble O7. Compatible results are found, provided the lower end $x_1^{\min}$ of the fit range is chosen sufficiently large.

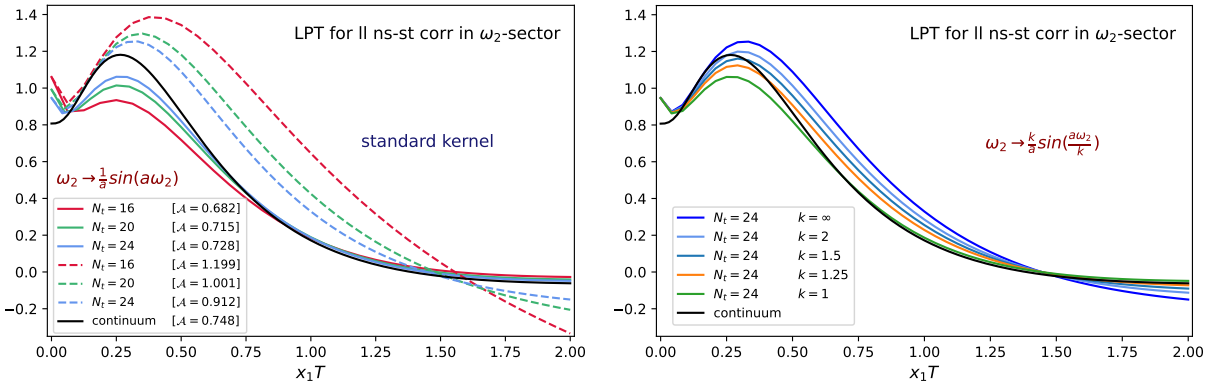

Figure 33: **Top panel:** Leading-order lattice perturbation theory prediction for the standard subtracted correlator (using the local discretization of the vector current) with the cosh-kernel (dashed lines) and with the modified ($k = 1$) sine-kernel (solid line) in the free theory for the second Matsubara sector ω_2. **Bottom panel:** Comparison of modifications with different k-values for the $\beta/a = 24$ case.

M Lattice Perturbation Theory and Choice of Kernel

To guide the choice of the kernel, we analyze the behavior of the integrand $h_E(\omega_2, x_1)$ in leading-order lattice perturbation theory with the local discretization of the current. Figure 33 (top panel) shows this quantity multiplied by the standard kernel (dashed lines) and the $k = 1$ kernel (solid lines). The standard kernel leads to large cut-off effects in the intermediate region $x_1 T \in [\frac{1}{3}, \frac{3}{2}]$, while the modified kernel ($k = 1$) reduces these substantially at $x_1 T > 3/4$.

Notably, with the standard kernel, the continuum limit is approached from above, whereas with the modified kernel ($k = 1$), it is approached from below, which implies a potential benefit of interpolating between them. We employ the smooth Heaviside function,

$$\Theta(x, x_w, d) = \frac{1}{2}\left[1 + \tanh\left(\frac{x - x_w}{d}\right)\right], \tag{M.1}$$

to achieve a controlled transition between the two kernels: unmodified at short distances $x_1 < x_w$ and modified at long distances $x_1 > x_w$. For $d \approx 0.15\,\text{fm}$ this results in a flat continuum extrapolation, as shown in Fig. 9.15 (bottom panel). Additionally, the bottom panel of Fig. 33 compares different kernel modifications for the $\beta/a = 24$ case, corresponding to our finest ensemble, X7. It is evident that the modifications with $k = \frac{3}{2}$ and $k = 2$ also reduce cut-off effects, although neither performs as well as the $k = 1$ prescription.

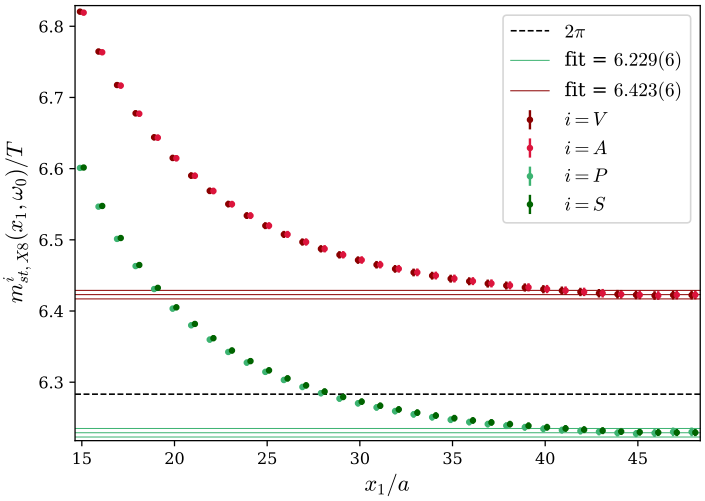

Figure 34: Effective screening masses for the completely static (zero-momentum) local–local transverse isovector vector (dark red) and axial-vector (light red) correlator, as well as the scalar (dark green) and pseudoscalar (light green) correlator, on the X8 ensemble at $T \approx 1.4\,\mathrm{GeV}$. The horizontal bands indicate the fit results obtained from the ansatz in Eq. (7.3.1). For orientation, the black dashed line denotes the 2π limit. We observe clear mass degeneracy within the V/A and S/P chiral partner channels.

N Non-Continuum Extrapolated Results at $T \approx 1.4\,\mathrm{GeV}$

This section offers a concise overview of some initial findings, concentrating on $H_E(\omega_1)$ and $H_E(\omega_2)$, which were derived from a single 16×96^3 box at $T \approx 1.4\,\mathrm{GeV}$.

N.1 The ω_0 Sector

To facilitate a comparison of static screening masses at higher Matsubara frequencies with the continuum dispersive prediction (9.2.3), we have determined the completely static (zero momentum) vector screening mass

$$m^{0,\mathrm{fit}}_{\mathrm{st},0}(\omega_0)/T = 6.423(6)\,. \tag{N.1}$$

In contrast to the $T \approx 250\,\mathrm{MeV}$ counterpart (9.2.2) it lies above the 2π limit and exhibits a strong mass degeneracy with the corresponding axial-vector chiral partner [cf. Fig. 34].

N.2 The ω_1 Sector

The static vector screening mass in the first Matsubara sector

$$m^{0,\mathrm{fit}}_{\mathrm{st},1}(\omega_1)/T = 8.99(2)\,, \tag{N.2}$$

aligns closely with the dispersive prediction of 8.985(4), even though the results are derived at a fixed lattice spacing [cf. left panel of Fig. 36]. It is also in very good agreement with the value obtained when adding the mass gap derived from the correlator ratio $G^{\mathrm{T}}_{\mathrm{st}}(\omega_1,x_1)/G^{\mathrm{T}}_{\mathrm{st}}(\omega_0,x_1)$ to the completely static screening mass (N.1) [cf. left panel of Fig. 35].

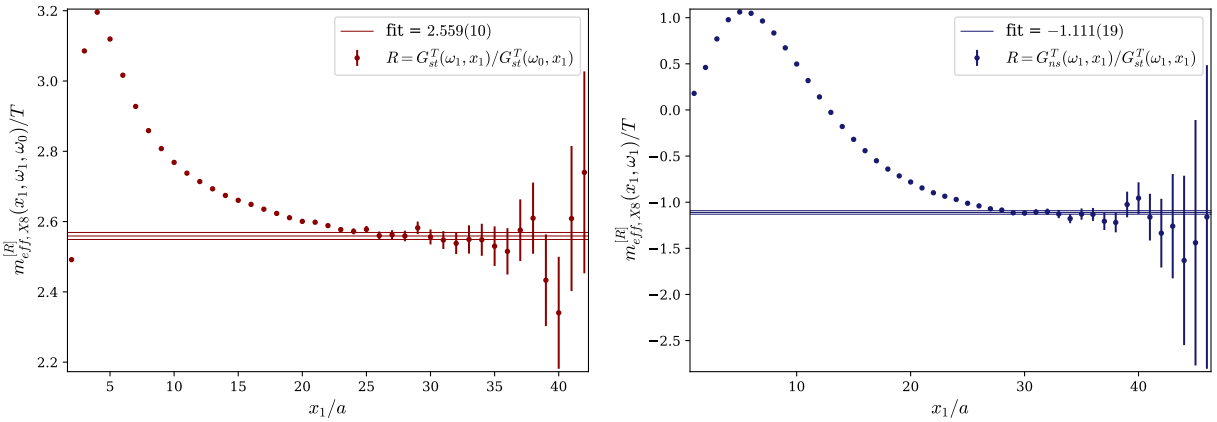

Figure 35: The effective masses, as defined in Eq. (I.6), for the ratios of the static $n = 1$ to $n = 0$ Matsubara-sector screening correlators (**left panel**) and the ratio of the $n = 1$ non-static to static (**right panel**) screening correlators on the X8 ensemble. The bars represent the effective masses derived from a single exponential fit.

It is noteworthy that the effective non-static vector screening mass intersects with its static equivalent at approximately $x_1 T \approx 1$ [cf. left panel of Fig. 36]. We find

$$m^{0,\mathrm{fit}}_{\mathrm{ns},1}(\omega_1)/T = 7.850(12)\,, \tag{N.3}$$

which is considerably lower than N.2, indicating that the integrand $-h_E(\omega_1, x_1)$ could become negative at large source-sink separations x_1. This is consistent with the value 7.88(2) obtained by adding the mass gap obtained from the correlator ratio $G^{\mathrm{T}}_{\mathrm{ns}}(\omega_1, x_1)/G^{\mathrm{T}}_{\mathrm{st}}(\omega_1, x_1)$ [cf. right panel of Fig. 35] to (N.2).

The r.h.s. of Fig. 36 displays the standard-subtracted integrand $-h_E(\omega_1, x_1)$ for various kernel modifications, along with the tail modeling based on Eq. (7.3.2). We also compare this with the prediction from the free theory and note that the integrands intersect at approximately $x_1 T = 0.5$. While the integrand from the free theory becomes negative at $x_1 T = 1$, the lattice integrand does so around $x_1 T = 1.5$. Comparing to the situation at $T \approx 250\,\mathrm{MeV}$ depicted on the l.h.s. of Fig. 9.17, the free theory prediction reproduces the overall shape of the lattice integrand more closely, which is anticipated at this elevated temperature.

At fixed lattice spacing our preliminary estimate of $H_E(\omega_1)$ reads

$$-\frac{H_E(\omega_1, k = \infty, T \approx 1.4\,\mathrm{GeV})}{T^2} = 0.6741(7)\,. \tag{N.4}$$

Remarkably, this is in very good agreement with the continuum extrapolated result 0.676(7) at $T \approx 250\,\mathrm{MeV}$ [cf. Eq. (9.3.8)], especially since the continuum extrapolation of this quantity was very mild [cf. left panel of Fig. 9.6].

N.3 The ω_2 Sector

The static vector screening mass in the second Matsubara sector

$$m^{0,\mathrm{fit}}_{\mathrm{st},2}(\omega_2)/T = 14.11(9)\,, \tag{N.5}$$

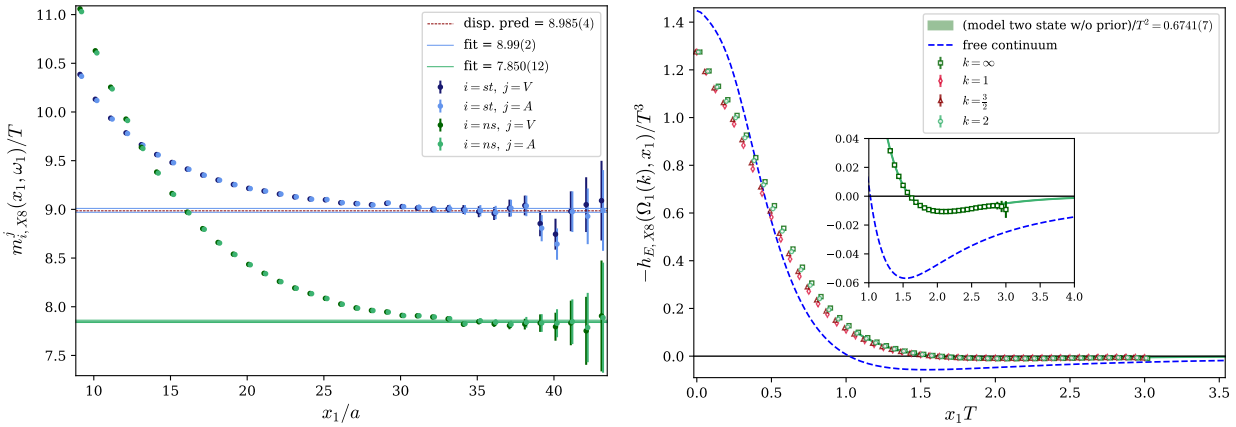

Figure 36: **Left panel:** Effective screening masses in the first Matsubara sector for static and non-static transverse isovector vector (dark colors) and axial-vector (light colors) correlators on the X8 ensemble at $T \approx 1.4\,\mathrm{GeV}$. The horizontal bands indicate the fit results from Eq. (7.3.1). Again, we observe clear mass degeneracy within the V/A chiral partner channel. **Right panel:** Standard-subtracted integrands $-h_E(\omega_1, x_1)$ [cf. Eq. (7.2.21)] with different kernel modifications based on the parameter k [cf. Eq. (7.2.19)] together with the tail modification from Eq. (7.3.2). For comparison also the free continuum prediction is shown as a dashed blue line.

again aligns closely with the dispersive prediction of 14.112(3) [cf. l.h.s. of Fig. 37]. By conducting an unpriored fit of the non-static screening correlator, we derive a degenerated non-static screening mass

$$m^{0,\mathrm{fit}}_{\mathrm{ns},2}(\omega_2)/T = 14.06(14)\,, \tag{N.6}$$

As in Chap. 9, we use the "ratio method" to obtain lower bounds on the screening masses. Adding the mass gaps [cf. left panel of Fig. 38] obtained from the correlator ratios $G^{\mathrm{T}}_{\mathrm{st}}(\omega_2, x_1)/G^{\mathrm{T}}_{\mathrm{st}}(\omega_1, x_1)$ respectively $G^{\mathrm{T}}_{\mathrm{ns}}(\omega_2, x_1)/G^{\mathrm{T}}_{\mathrm{ns}}(\omega_1, x_1)$ to (N.2) and (N.3) respectively, we obtain priors that enter the fits of the corresponding correlators.

As in Chap. 9, we use the "ratio method" [cf. left panel of Fig. 38] to obtain lower bounds on the screening masses. We obtain:

$$m^{0,\mathrm{pr.\,fit}}_{\mathrm{ns},2}(\omega_2)/T = 13.90(6)\,, \tag{N.7}$$
$$m^{0,\mathrm{pr.\,fit}}_{\mathrm{ns},2}(\omega_2)/T = 13.64(13)\,. \tag{N.8}$$

We have constructed a model for the tail [cf. r.h.s. of Fig. 39] utilizing the screening masses from both the unpiored and priored fits. For the kernel modification, we selected $k = \frac{3}{2}$, as this choice resulted in the smoothest continuum extrapolation at $T \approx 250\,\mathrm{MeV}$. The left panel of Fig. 39 displays a comparison of integrands with various k values alongside the free continuum prediction. At a constant lattice spacing, our preliminary calculation of $H_E(\omega_2)$, determined as the average of both the priored and unpriored results, is as follows:

$$-\frac{H_E(\omega_2, k = \frac{3}{2}, T \approx 1.4\,\mathrm{GeV})}{T^2} = 0.968(22)\,. \tag{N.9}$$

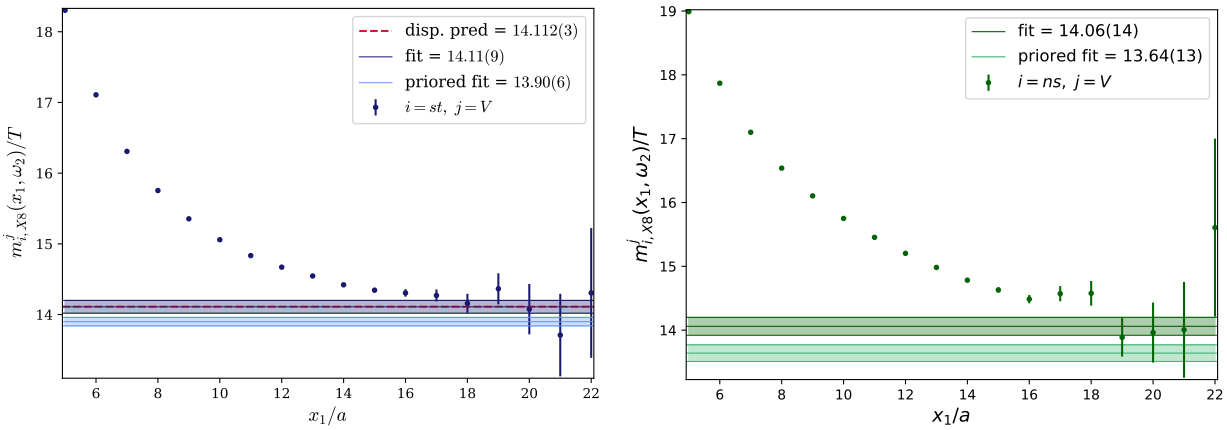

Figure 37: The effective screening masses in the ω_2-sector are shown for both the static (**left panel**) and non-static (**right panel**) transverse isovector vector correlators on the X8 ensemble at $T \approx 1.4\,\text{GeV}$. The horizontal bands represent the fit results derived from Eq. (7.3.1), both without (dark color) and with priors from the "ratio method". In the static scenario, the dispersive prediction (illustrated as a dashed red line) is in very good agreement with the unpriored fit result.

For comparison at $T \approx 250$ MeV, we have obtained a continuum extrapolated lower value of 0.869(74) [cf. Eq. (9.4.18)]. It will be intriguing to observe whether the proposed increased value for the expression $-[H_E(\omega_2) - H_E(\omega_1)]/T^2$ remains valid in the continuum.

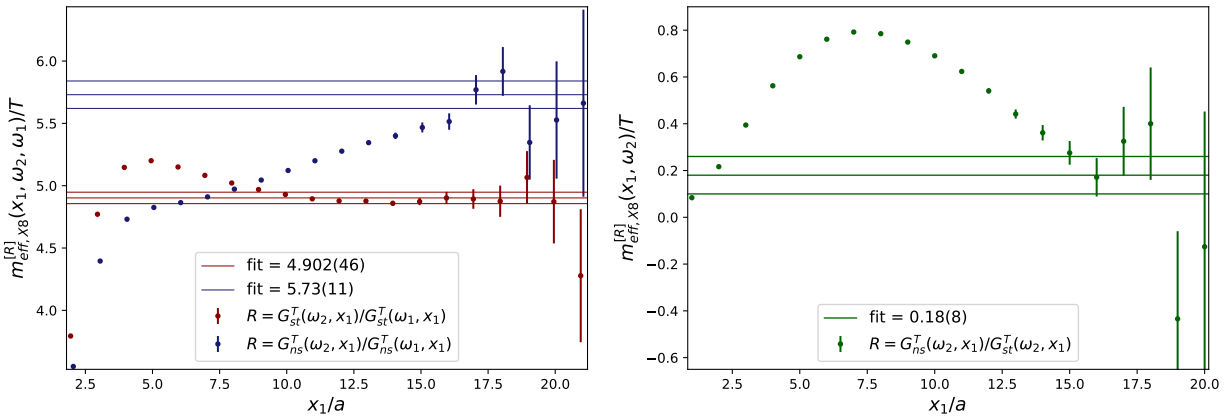

Figure 38: The effective masses, as defined in Eq. (I.6), for the ratios of the static (red) and non-static (blue) $n = 2$ to $n = 1$ Matsubara-sector screening correlators (**left panel**) and the ratio of the $n = 2$ non-static to static (**right panel**) screening correlators on the X8 ensemble. The bars denote the effective masses obtained from a single exponential fit.

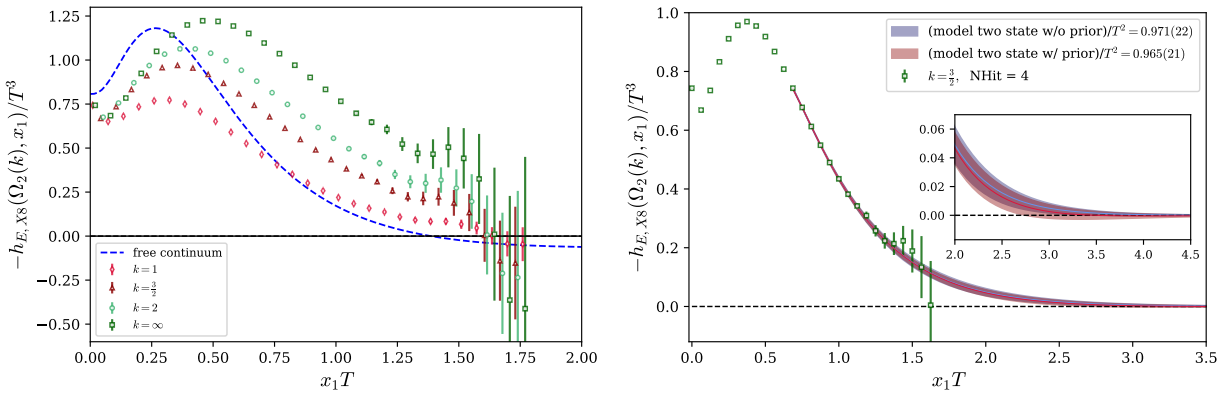

Figure 39: **Left panel:** Standard-subtracted integrands $-h_E(\omega_2, x_1)$ [cf. Eq. (7.2.21)] with different kernel modifications based on the parameter k [cf. Eq. (7.2.19)] as well as the free continuum prediction on the X8 ensemble. **Right panel:** The integrand $-h_E(\Omega_n(k = \frac{3}{2}), x_1)/T^3$, along with the tail modification from Eq. (7.3.2), is shown on the X8 ensemble. The value $k = \frac{3}{2}$ is selected since it has led to the smoothest continuum extrapolation at $T \approx 250\,\mathrm{MeV}$. The blue band represents the unpriored tail modification, whereas the red band illustrates the tail modification incorporating a prior derived from the "ratio method".

Eigenständigkeitserklärung

Hiermit erkläre ich, dass ich die vorliegende Arbeit selbstständig verfasst und keine anderen als die angegebenen Quellen und Hilfsmittel (dazu zählen auch KI-basierte Anwendungen oder Werkzeuge *) benutzt habe. Sämtliche wörtlichen oder sinngemäßen Übernahmen und Zitate sind kenntlich gemacht und nachgewiesen. In der Tabelle „Nutzung KI-Tools“ habe ich die verwendeten KI-Tools dokumentiert. Mit Abgabe der vorliegenden Leistung übernehme ich die Verantwortung für das eingereichte Gesamtprodukt. Ich verantworte damit auch jegliche KI-generierten Inhalte, die ich in meine Arbeit übernommen habe. Die Richtigkeit übernommener (KI-generierter) Aussagen und Inhalte habe ich nach bestem Wissen und Gewissen geprüft. Mir ist bekannt, dass ein Verstoß gegen die genannten Punkte prüfungsrechtliche Konsequenzen hat.

Ardit Krasniqi
Mainz, 16.12.2025

Table 5: „Nutzung KI-Tools

KI-Tool	Genutzt für	Warum	Wann bzw. Wo
DeepL Translate	Übersetzung deutscher Vorformulierungen ins Englische	bessere Lesbarkeit	vereinzelt über die gesamte Arbeit hinweg
ChatGPT	Neuformulierung meiner Textentwürfe	bessere Lesbarkeit	vereinzelt über die gesamte Arbeit hinweg
Paperpal	Glätten von Textformulierungen	bessere Lesbarkeit	vereinzelt über die gesamte Arbeit hinweg

References

[1] Marco Cè, Tim Harris, Ardit Krasniqi, Harvey B. Meyer, and Csaba Török. "Aspects of chiral symmetry in QCD at T=128 MeV". *Phys. Rev. D* 107 2023, pp. 054509. DOI: 10.1103/PhysRevD.107.054509.

[2] Ardit Krasniqi, Marco Cè, Tim Harris, Harvey B. Meyer, Csaba Török, et al. "A $(2+1)$-flavor lattice study of the pion quasiparticle in the thermal hadronic phase at physical quark masses". *PoS* Lattice2022 2022, pp. 0181. DOI: 10.22323/1.430.0181.

[3] Ardit Krasniqi, Marco Cè, Renwick J. Hudspith, and Harvey B. Meyer. "Hot QCD matter around the chiral crossover: A lattice study with O(a)-improved Wilson fermions". *Phys. Rev. D* 110 2024, pp. 114506. DOI: 10.1103/PhysRevD.110.114506.

[4] Ardit Krasniqi, Marco Cè, Tim Harris, Renwick J. Hudspith, Harvey B. Meyer, et al. "The thermal photon emissivity at the QCD chiral crossover from imaginary momentum correlators". *PoS* LATTICE2023 2024, pp. 180. DOI: 10.22323/1.453.0180.

[5] Marco Cè, Tim Harris, Ardit Krasniqi, Harvey B. Meyer, and Csaba Török. "Photon emissivity of the quark-gluon plasma: A lattice QCD analysis of the transverse channel". *Phys. Rev. D* 106 2022, pp. 054501. DOI: 10.1103/PhysRevD.106.054501.

[6] Marco Cè, Tim Harris, Ardit Krasniqi, Harvey B. Meyer, and Csaba Török. "Probing the photon emissivity of the quark-gluon plasma without an inverse problem in lattice QCD". *Phys. Rev. D* 109 2024, pp. 014507. DOI: 10.1103/PhysRevD.109.014507.

[7] Ardit Krasniqi, Marco Cè, Tim Harris, Renwick J. Hudspith, and Harvey B. Meyer. "Probing how bright the quark-gluon plasma glows in lattice QCD". *Phys. Rev. D* 112 2025, pp. 074503. DOI: 10.1103/8dq9-q62p.

[8] H. C. Lange, A. Krasniqi, and S. Scherer. "Quark-mass and 1/Nc corrections to the vector-meson pseudoscalar-meson photon (VPγ) interaction". *Phys. Rev. D* 105 2022, pp. 054001. DOI: 10.1103/PhysRevD.105.054001.

[9] Csaba Török, Marco Cè, Tim Harris, Ardit Krasniqi, Arianna Toniato, et al. "Estimating the thermal photon production rate using lattice QCD". *PoS* LATTICE2021 2021, pp. 172. DOI: 10.22323/1.396.0172.

[10] Csaba Török, Marco Cè, Tim Harris, Ardit Krasniqi, Harvey B. Meyer, et al. "Estimation of the photon production rate using imaginary momentum correlators". *PoS* LATTICE2022 2023, pp. 193. DOI: 10.22323/1.430.0193.

[11] Harvey B. Meyer, Marco Cè, Tim Harris, Ardit Krasniqi, and Csaba Török. "Photon and dilepton production rate in the quark-gluon plasma from lattice QCD". *PoS* LATTICE2022 2023, pp. 186. DOI: 10.22323/1.430.0186.

[12] Elliott D. Bloom et al. "High-Energy Inelastic e p Scattering at 6-Degrees and 10-Degrees". *Phys. Rev. Lett.* 23 1969, pp. 930–934. DOI: 10.1103/PhysRevLett.23.930.

[13] Martin Breidenbach, Jerome I. Friedman, Henry W. Kendall, Elliott D. Bloom, D. H. Coward, et al. "Observed behavior of highly inelastic electron-proton scattering". *Phys. Rev. Lett.* 23 1969, pp. 935–939. DOI: 10.1103/PhysRevLett.23.935.

[14] R. Brandelik et al. "Evidence for a Spin One Gluon in Three Jet Events". *Phys. Lett. B* 97 1980, pp. 453–458. DOI: 10.1016/0370-2693(80)90639-5.

[15] David J. Gross and Frank Wilczek. "Ultraviolet Behavior of Nonabelian Gauge Theories". *Phys. Rev. Lett.* 30 1973, pp. 1343–1346. DOI: 10.1103/PhysRevLett.30.1343.

[16] Steven Weinberg. "The U(1) Problem". *Phys. Rev. D* 11 1975, pp. 3583–3593. DOI: 10.1103/PhysRevD.11.3583.

[17] H. Fritzsch, Murray Gell-Mann, and H. Leutwyler. "Advantages of the Color Octet Gluon Picture". *Phys. Lett. B* 47 1973, pp. 365–368. DOI: 10.1016/0370-2693(73)90625-4.

[18] D. J. Gross and Frank Wilczek. "Asymptotically Free Gauge Theories - I". *Phys. Rev. D* 8 1973, pp. 3633–3652. DOI: 10.1103/PhysRevD.8.3633.

[19] H. David Politzer. "Reliable Perturbative Results for Strong Interactions?" *Phys. Rev. Lett.* 30 1973, pp. 1346–1349. DOI: 10.1103/PhysRevLett.30.1346.

[20] Edward Shuryak. *Quark-Gluon Plasma, Heavy Ion Collisions and Hadrons*. World Scientific, Apr. 2024. ISBN: 978-981-12-8234-8, 978-981-12-8236-2. DOI: 10.1142/13570.

[21] R. Rapp, J. Wambach, and H. van Hees. "The Chiral Restoration Transition of QCD and Low Mass Dileptons". *Landolt-Bornstein* 23 2010, pp. 134. DOI: 10.1007/978-3-642-01539-7_6.

[22] T. D. Lee. "Abnormal Nuclear States and Vacuum Excitations". *Rev. Mod. Phys.* 47 1975, pp. 267–275. DOI: 10.1103/RevModPhys.47.267.

[23] K. H. Ackermann et al. "Elliptic flow in Au + Au collisions at (S(NN))**(1/2) = 130 GeV". *Phys. Rev. Lett.* 86 2001, pp. 402–407. DOI: 10.1103/PhysRevLett.86.402.

[24] K. Adcox et al. "Suppression of hadrons with large transverse momentum in central Au+Au collisions at $\sqrt{s_{NN}}$ = 130-GeV". *Phys. Rev. Lett.* 88 2002, pp. 022301. DOI: 10.1103/PhysRevLett.88.022301.

[25] Adam Bzdak, Shinichi Esumi, Volker Koch, Jinfeng Liao, Mikhail Stephanov, et al. "Mapping the Phases of Quantum Chromodynamics with Beam Energy Scan". *Phys. Rept.* 853 2020, pp. 1–87. DOI: 10.1016/j.physrep.2020.01.005.

[26] G. Policastro, Dan T. Son, and Andrei O. Starinets. "The Shear viscosity of strongly coupled N=4 supersymmetric Yang-Mills plasma". *Phys. Rev. Lett.* 87 2001, pp. 081601. DOI: 10.1103/PhysRevLett.87.081601.

[27] Thomas Schäfer and Derek Teaney. "Nearly Perfect Fluidity: From Cold Atomic Gases to Hot Quark Gluon Plasmas". *Rept. Prog. Phys.* 72 2009, pp. 126001. DOI: 10.1088/0034-4885/72/12/126001.

[28] Ulrich Heinz and Björn Schenke. "Hydrodynamic Description of the Quark-Gluon Plasma". In: Dec. 2024. arXiv: 2412.19393 [nucl-th].

[29] Vishnu M. Bannur. "Strongly coupled quark gluon plasma (SCQGP)". *J. Phys. G* 32 2006, pp. 993–1002. DOI: 10.1088/0954-3899/32/7/008.

[30] Jorge Casalderrey-Solana, Hong Liu, David Mateos, Krishna Rajagopal, and Urs Achim Wiedemann. *Gauge/String Duality, Hot QCD and Heavy Ion Collisions*. Cambridge Univer-

sity Press, 2014. ISBN: 978-1-009-40350-4, 978-1-009-40349-8, 978-1-009-40352-8, 978-1-139-13674-7. DOI: 10.1017/9781009403504. arXiv: 1101.0618 [hep-th].

[31] Peter F. Kolb and Ulrich W. Heinz. "Hydrodynamic description of ultrarelativistic heavy ion collisions". 2003, pp. 634–714.

[32] Tapan K. Nayak. "Probing the QCD phase structure using event-by-event fluctuations". *J. Phys. Conf. Ser.* 1602 2020, pp. 012003. DOI: 10.1088/1742-6596/1602/1/012003.

[33] R. Rapp and J. Wambach. "Chiral symmetry restoration and dileptons in relativistic heavy ion collisions". *Adv. Nucl. Phys.* 25 2000, pp. 1. DOI: 10.1007/0-306-47101-9_1.

[34] Harvey B. Meyer. "Transport Properties of the Quark-Gluon Plasma: A Lattice QCD Perspective". *Eur. Phys. J. A* 47 2011, pp. 86. DOI: 10.1140/epja/i2011-11086-3.

[35] Y. Aoki, G. Endrodi, Z. Fodor, S. D. Katz, and K. K. Szabo. "The Order of the quantum chromodynamics transition predicted by the standard model of particle physics". *Nature* 443 2006, pp. 675–678. DOI: 10.1038/nature05120.

[36] A. Bazavov et al. "Chiral crossover in QCD at zero and non-zero chemical potentials". *Phys. Lett. B* 795 2019, pp. 15–21. DOI: 10.1016/j.physletb.2019.05.013.

[37] Szabolcs Borsányi, Zoltán Fodor, Jana N. Guenther, Ruben Kara, Paolo Parotto, et al. "Chiral versus deconfinement properties of the QCD crossover: Differences in the volume and chemical potential dependence from the lattice". *Phys. Rev. D* 111 2025, pp. 014506. DOI: 10.1103/PhysRevD.111.014506.

[38] Peter Kovács, Zsolt Szép, and György Wolf. "Existence of the critical endpoint in the vector meson extended linear sigma model". *Phys. Rev. D* 93 2016, pp. 114014. DOI: 10.1103/PhysRevD.93.114014.

[39] Fei Gao and Jan M. Pawlowski. "QCD phase structure from functional methods". *Phys. Rev. D* 102 2020, pp. 034027. DOI: 10.1103/PhysRevD.102.034027.

[40] Wei-jie Fu, Xiaofeng Luo, Jan M. Pawlowski, Fabian Rennecke, Rui Wen, et al. "Hyper-order baryon number fluctuations at finite temperature and density". *Phys. Rev. D* 104 2021, pp. 094047. DOI: 10.1103/PhysRevD.104.094047.

[41] Philipp Isserstedt, Michael Buballa, Christian S. Fischer, and Pascal J. Gunkel. "Baryon number fluctuations in the QCD phase diagram from Dyson-Schwinger equations". *Phys. Rev. D* 100 2019, pp. 074011. DOI: 10.1103/PhysRevD.100.074011.

[42] J. Adam et al. "Nonmonotonic Energy Dependence of Net-Proton Number Fluctuations". *Phys. Rev. Lett.* 126 2021, pp. 092301. DOI: 10.1103/PhysRevLett.134.139902.

[43] Szabolcs Borsanyi, Zoltan Fodor, Jana N. Guenther, Paolo Parotto, Attila Pasztor, et al. "Lattice QCD constraints on the critical point from an improved precision equation of state". 2025,

[44] Greg Jackson. "Theory overview: electroweak emission from heavy-ion collisions". In: *31st International Conference on Ultra-relativistic Nucleus-Nucleus Collisions*. Aug. 2025. arXiv: 2509.00262 [hep-ph].

[45] O. W. Greenberg. "Spin and Unitary Spin Independence in a Paraquark Model of Baryons and Mesons". *Phys. Rev. Lett.* 13 1964, pp. 598–602. DOI: 10.1103/PhysRevLett.13.598.

[46] M. Y. Han and Yoichiro Nambu. "Three Triplet Model with Double SU(3) Symmetry". *Phys. Rev.* 139 1965, pp. B1006–B1010. DOI: 10.1103/PhysRev.139.B1006.

[47] N. Cabibbo, G. Parisi, and M. Testa. "Hadron Production in e+ e- Collisions". *Lett. Nuovo Cim.* 4S1 1970, pp. 35–39. DOI: 10.1007/BF02755392.

[48] T. Aoyama et al. "The anomalous magnetic moment of the muon in the Standard Model". *Phys. Rept.* 887 2020, pp. 1–166. DOI: 10.1016/j.physrep.2020.07.006.

[49] R. L. Workman et al. "Review of Particle Physics". *PTEP* 2022 2022, pp. 083C01. DOI: 10.1093/ptep/ptac097.

[50] Yuval Ne'eman. "Derivation of strong interactions from a gauge invariance". *Nucl. Phys.* 26 1961, pp. 222–229. DOI: 10.1016/0029-5582(61)90134-1.

[51] Murray Gell-Mann. "A Schematic Model of Baryons and Mesons". *Phys. Lett.* 8 1964, pp. 214–215. DOI: 10.1016/S0031-9163(64)92001-3.

[52] C. Patrignani et al. "Review of Particle Physics". *Chin. Phys. C* 40 2016, pp. 100001. DOI: 10.1088/1674-1137/40/10/100001.

[53] Francesco Knechtli, Michael Günther, and Michael Peardon. *Lattice Quantum Chromodynamics: Practical Essentials*. SpringerBriefs in Physics. Springer, 2017. DOI: 10.1007/978-94-024-0999-4.

[54] Mattia Bruno, Mattia Dalla Brida, Patrick Fritzsch, Tomasz Korzec, Alberto Ramos, et al. "QCD Coupling from a Nonperturbative Determination of the Three-Flavor Λ Parameter". *Phys. Rev. Lett.* 119 2017, pp. 102001. DOI: 10.1103/PhysRevLett.119.102001.

[55] Kenneth G. Wilson. "Confinement of Quarks". *Phys. Rev. D* 10 1974, pp. 2445–2459. DOI: 10.1103/PhysRevD.10.2445.

[56] Steven Weinberg. "Phenomenological Lagrangians". *Physica A* 96 1979, pp. 327–340. DOI: 10.1016/0378-4371(79)90223-1.

[57] J. Gasser and H. Leutwyler. "Chiral Perturbation Theory to One Loop". *Annals Phys.* 158 1984, pp. 142. DOI: 10.1016/0003-4916(84)90242-2.

[58] J. Gasser and H. Leutwyler. "Chiral Perturbation Theory: Expansions in the Mass of the Strange Quark". *Nucl. Phys. B* 250 1985, pp. 465–516. DOI: 10.1016/0550-3213(85)90492-4.

[59] Stefan Scherer. "Introduction to chiral perturbation theory". *Adv. Nucl. Phys.* 27 2003, pp. 277.

[60] Stefan Scherer and Matthias R. Schindler. "A Chiral perturbation theory primer". 2005,

[61] Aneesh Manohar and Howard Georgi. "Chiral Quarks and the Nonrelativistic Quark Model". *Nucl. Phys. B* 234 1984, pp. 189–212. DOI: 10.1016/0550-3213(84)90231-1.

[62] Emmy Noether. "Invariant Variation Problems". *Gott. Nachr.* 1918 1918, pp. 235–257. DOI: 10.1080/00411457108231446.

[63] Stephen L. Adler and William A. Bardeen. "Absence of higher order corrections in the anomalous axial vector divergence equation". *Phys. Rev.* 182 1969, pp. 1517–1536. DOI: 10.1103/PhysRev.182.1517.

[64] Stephen L. Adler. "Axial vector vertex in spinor electrodynamics". *Phys. Rev.* 177 1969, pp. 2426–2438. DOI: 10.1103/PhysRev.177.2426.

[65] J. S. Bell and R. Jackiw. "A PCAC puzzle: $\pi^0 \to \gamma\gamma$ in the σ model". *Nuovo Cim. A* 60 1969, pp. 47–61. DOI: 10.1007/BF02823296.

[66] C. Vafa and Edward Witten. "Restrictions on Symmetry Breaking in Vector-Like Gauge Theories". *Nucl. Phys. B* 234 1984, pp. 173–188. DOI: 10.1016/0550-3213(84)90230-X.

[67] Jeffrey Goldstone, Abdus Salam, and Steven Weinberg. "Broken Symmetries". *Phys. Rev.* 127 1962, pp. 965–970. DOI: 10.1103/PhysRev.127.965.

[68] Sidney Coleman. "The Invariance of the Vacuum is the Invariance of the World". *Journal of Mathematical Physics* 7 1966, pp. 787–787. DOI: 10.1063/1.1931207.

[69] Helmut Satz. *Extreme States of Matter in Strong Interaction Physics: An Introduction*. Vol. 945. Cham: Springer, 2018. DOI: 10.1007/978-3-319-71894-1.

[70] Ernst Ising. "Contribution to the Theory of Ferromagnetism". *Z. Phys.* 31 1925, pp. 253–258. DOI: 10.1007/BF02980577.

[71] Lars Onsager. "Crystal statistics. 1. A Two-dimensional model with an order disorder transition". *Phys. Rev.* 65 1944, pp. 117–149. DOI: 10.1103/PhysRev.65.117.

[72] R. J. Glauber. "Lectures in Theoretical Physics". *Interscience* Vol. 1 1959, pp. 315.

[73] C. Y. Wong. *Introduction to high-energy heavy ion collisions*. 1995. ISBN: 978-981-02-0263-7.

[74] V. N. Gribov. "Glauber corrections and the interaction between high-energy hadrons and nuclei". *Soviet Physics - JETP* 29 1969, pp. 483.

[75] K. Yagi, T. Hatsuda, and Y. Miake. *Quark-gluon plasma: From big bang to little bang*. Vol. 23. 2005.

[76] J. D. Bjorken. "Highly Relativistic Nucleus-Nucleus Collisions: The Central Rapidity Region". *Phys. Rev. D* 27 1983, pp. 140–151. DOI: 10.1103/PhysRevD.27.140.

[77] R. Baier, Alfred H. Mueller, D. Schiff, and D. T. Son. "'Bottom up' thermalization in heavy ion collisions". *Phys. Lett. B* 502 2001, pp. 51–58. DOI: 10.1016/S0370-2693(01)00191-5.

[78] Francois Gelis. "Some Aspects of the Theory of Heavy Ion Collisions". *Rept. Prog. Phys.* 84 2021, pp. 056301. DOI: 10.1088/1361-6633/abec2e.

[79] A. Bazavov, D. Bollweg, O. Kaczmarek, F. Karsch, Swagato Mukherjee, et al. "Charm degrees of freedom in hot matter from lattice QCD". *Phys. Lett. B* 850 2024, pp. 138520. DOI: 10.1016/j.physletb.2024.138520.

[80] Sipaz Sharma. "Charm Fluctuations and Deconfinement". *PoS* LATTICE2023 2024, pp. 200. DOI: 10.22323/1.453.0200.

[81] "The ALICE experiment – A journey through QCD". 2022,

[82] W. Heisenberg. "Zur Theorie der explosionsartigen Schauer in der kosmischen Strahlung. II". *Zeitschrift für Physik* 113 1939, pp. 61–86. DOI: 10.1007/BF01371656.

[83] E. Fermi. "High Energy Nuclear Events". *Progress of Theoretical Physics* 5 1950, pp. 570–583.

[84] L. D. Landau. "On the multiparticle production in high-energy collisions". *Izv. Akad. Nauk Ser. Fiz.* 17 1953, pp. 51–64.

[85] R. Hagedorn. "Statistical thermodynamics of strong interactions at high-energies". *Nuovo Cim. Suppl.* 3 1965, pp. 147–186.

[86] Johann Rafelski, ed. *Melting Hadrons, Boiling Quarks - From Hagedorn Temperature to Ultra-Relativistic Heavy-Ion Collisions at CERN: With a Tribute to Rolf Hagedorn*. Springer, 2016. DOI: 10.1007/978-3-319-17545-4.

[87] R. Hagedorn. "How We Got to QCD Matter from the Hadron Side: 1984". *Lect. Notes Phys.* 221 1985, pp. 53–76. DOI: 10.1007/978-3-319-17545-4_25.

[88] W. Nahm. "Analytical solution of the statistical bootstrap model". *Nucl. Phys. B* 45 1972, pp. 525–553. DOI: 10.1016/0550-3213(72)90257-X.

[89] R. Hagedorn. "Hadronic matter near the boiling point". *Nuovo Cim. A* 56 1968, pp. 1027–1057. DOI: 10.1007/BF02751614.

[90] Helmut Satz. "The Limits of Hadron Thermodynamics". *Fortsch. Phys.* 33 1985, pp. 259.

[91] Anton Andronic, Peter Braun-Munzinger, Krzysztof Redlich, and Johanna Stachel. "Decoding the phase structure of QCD via particle production at high energy". *Nature* 561 2018, pp. 321–330. DOI: 10.1038/s41586-018-0491-6.

[92] R. Hagedorn and Johann Rafelski. "Hot Hadronic Matter and Nuclear Collisions". *Phys. Lett. B* 97 1980, pp. 136. DOI: 10.1016/0370-2693(80)90566-3.

[93] Anton Andronic, Peter Braun-Munzinger, Markus K. Köhler, Aleksas Mazeliauskas, Krzysztof Redlich, et al. "The multiple-charm hierarchy in the statistical hadronization model". *JHEP* 07 2021, pp. 035. DOI: 10.1007/JHEP07(2021)035.

[94] Wojciech Florkowski. *Phenomenology of Ultra-Relativistic Heavy-Ion Collisions*. World Scientific, 2010. ISBN: 978-981-4280-66-2. DOI: https://doi.org/10.1142/7396.

[95] Joseph I. Kapusta and Charles Gale. *Finite-Temperature Field Theory : Principles and Applications, 2nd edition*. Cambridge University Press, 2007. ISBN: 978-1-009-40196-8, 978-1-009-40195-1, 978-1-009-40198-2. DOI: 10.1017/9781009401968.

[96] Mikko Laine and Aleksi Vuorinen. *Basics of Thermal Field Theory*. Vol. 925. Springer, 2016. DOI: 10.1007/978-3-319-31933-9. arXiv: 1701.01554 [hep-ph].

[97] Michael E. Peskin and Daniel V. Schroeder. *An Introduction to quantum field theory*. Reading, USA: Addison-Wesley, 1995. ISBN: 978-0-201-50397-5.

[98] Gert Aarts and Aleksandr Nikolaev. "Electrical conductivity of the quark-gluon plasma: perspective from lattice QCD". *Eur. Phys. J. A* 57 2021, pp. 118. DOI: 10.1140/epja/s10050-021-00436-5.

[99] M. Lüscher. "A journey with Roberto in lattice QCD". *Nuovo Cim. C* 40 2017, pp. 152. DOI: 10.1393/ncc/i2017-17152-0.

[100] Christof Gattringer and Christian B. Lang. *Quantum chromodynamics on the lattice*. Vol. 788. Berlin: Springer, 2010. ISBN: 978-3-642-01849-7, 978-3-642-01850-3. DOI: 10.1007/978-3-642-01850-3.

[101] H. J. Rothe. "AN INTRODUCTION TO LATTICE GAUGE THEORIES". 1987,

[102] I. Montvay and G. Munster. *Quantum fields on a lattice*. Cambridge Monographs on Mathematical Physics. Cambridge University Press, Mar. 1997. ISBN: 978-0-521-59917-7, 978-0-511-87919-7. DOI: 10.1017/CBO9780511470783.

[103] Jan Smit. *Introduction to Quantum Fields on a Lattice*. Vol. 15. Cambridge University Press, 2003. ISBN: 978-1-009-40270-5, 978-1-009-40274-3, 978-1-009-40275-0, 978-0-511-89373-5, 978-0-521-89051-9. DOI: 10.1017/9781009402705.

[104] Thomas DeGrand and Carleton E. Detar. *Lattice methods for quantum chromodynamics*. 2006.

[105] Daniel Robaina Fernandez. "Static and dynamic properties of QCD at finite temperature". PhD thesis. Mainz: Johannes Gutenberg-Universität Mainz, 2016.

[106] Andreas Risch. "Isospin breaking effects in hadronic matrix elements on the lattice". PhD thesis. Mainz U., 2021. DOI: 10.25358/openscience-6314.

[107] Kai Zapp. "A Study of Spectral Functions in Lattice QCD". PhD thesis. Mainz: Johannes Gutenberg-Universität Mainz, 2021.

[108] Miguel Salg. "Electromagnetic form factors and radii of the nucleon from Lattice QCD and the proton radius puzzles". PhD thesis. Mainz U., 2024. DOI: 10.25358/openscience-10797.

[109] Jonas Wilhelm. "The strangeness form factors of the nucleon from lattice QCD". PhD thesis. Mainz: Johannes Gutenberg-Universität Mainz, 2019.

[110] Benjamin Jäger. "Hadronic Matrix Elements in Lattice QCD". PhD thesis. Mainz U., 2014.

[111] Alessandro Amato, Gert Aarts, Chris Allton, Pietro Giudice, Simon Hands, et al. "Electrical conductivity of the quark-gluon plasma across the deconfinement transition". *Phys. Rev. Lett.* 111 2013, pp. 172001. DOI: 10.1103/PhysRevLett.111.172001.

[112] Gert Aarts, Chris Allton, Alessandro Amato, Pietro Giudice, Simon Hands, et al. "Electrical conductivity and charge diffusion in thermal QCD from the lattice". *JHEP* 02 2015, pp. 186. DOI: 10.1007/JHEP02(2015)186.

[113] Gert Aarts, Chris Allton, Mehmet Bugrahan Oktay, Mike Peardon, and Jon-Ivar Skullerud. "Charmonium at high temperature in two-flavor QCD". *Phys. Rev. D* 76 2007, pp. 094513. DOI: 10.1103/PhysRevD.76.094513.

[114] G. Aarts, C. Allton, S. Kim, M. P. Lombardo, M. B. Oktay, et al. "What happens to the Y and η_b in the quark-gluon plasma? Bottomonium spectral functions from lattice QCD". *JHEP* 11 2011, pp. 103. DOI: 10.1007/JHEP11(2011)103.

[115] Gert Aarts, Chris Allton, Tim Harris, Seyong Kim, Maria Paola Lombardo, et al. "The bottomonium spectrum at finite temperature from $N_f = 2 + 1$ lattice QCD". *JHEP* 07 2014, pp. 097. DOI: 10.1007/JHEP07(2014)097.

[116] Aoife Kelly, Alexander Rothkopf, and Jon-Ivar Skullerud. "Bayesian study of relativistic open and hidden charm in anisotropic lattice QCD". *Phys. Rev. D* 97 2018, pp. 114509. DOI: 10.1103/PhysRevD.97.114509.

[117] Gert Aarts, Chris Allton, M. Naeem Anwar, Ryan Bignell, Timothy J. Burns, et al. "Non-zero temperature study of spin 1/2 charmed baryons using lattice gauge theory". *Eur. Phys. J. A* 60 2024, pp. 59. DOI: 10.1140/epja/s10050-024-01261-2.

[118] Gert Aarts, Chris Allton, Simon Hands, Benjamin Jäger, Chrisanthi Praki, et al. "Nucleons and parity doubling across the deconfinement transition". *Phys. Rev. D* 92 2015, pp. 014503. DOI: 10.1103/PhysRevD.92.014503.

[119] Gert Aarts, Chris Allton, Davide De Boni, Simon Hands, Benjamin Jäger, et al. "Light baryons below and above the deconfinement transition: medium effects and parity doubling". *JHEP* 06 2017, pp. 034. DOI: 10.1007/JHEP06(2017)034.

[120] Gert Aarts, Chris Allton, Davide De Boni, and Benjamin Jäger. "Hyperons in thermal QCD: A lattice view". *Phys. Rev. D* 99 2019, pp. 074503. DOI: 10.1103/PhysRevD.99.074503.

[121] Jon-Ivar Skullerud et al. "Approaching the continuum with anisotropic lattice thermodynamics". In: *21th International Conference on QCD in Extreme Conditions*. Oct. 2025. arXiv: 2510.02954 [hep-lat].

[122] J. M. Flynn, A. Juttner, C. T. Sachrajda, P. A. Boyle, and J. M. Zanotti. "Hadronic form factors in Lattice QCD at small and vanishing momentum transfer". *JHEP* 05 2007, pp. 016. DOI: 10.1088/1126-6708/2007/05/016.

[123] A. Holl, A. Krassnigg, and C. D. Roberts. "Pseudoscalar meson radial excitations". *Phys. Rev. C* 70 2004, pp. 042203. DOI: 10.1103/PhysRevC.70.042203.

[124] R. Sommer. "A New way to set the energy scale in lattice gauge theories and its applications to the static force and α_s in SU(2) Yang-Mills theory". *Nucl. Phys. B* 411 1994, pp. 839–854. DOI: 10.1016/0550-3213(94)90473-1.

[125] Rainer Sommer. "Scale setting in lattice QCD". *PoS* LATTICE2013 2014, pp. 015. DOI: 10.22323/1.187.0015.

[126] Patrick Fritzsch, Francesco Knechtli, Bjorn Leder, Marina Marinkovic, Stefan Schaefer, et al. "The strange quark mass and Lambda parameter of two flavor QCD". *Nucl. Phys. B* 865 2012, pp. 397–429. DOI: 10.1016/j.nuclphysb.2012.07.026.

[127] Mattia Bruno et al. "Simulation of QCD with $N_f = 2 + 1$ flavors of non-perturbatively improved Wilson fermions". *JHEP* 02 2015, pp. 043. DOI: 10.1007/JHEP02(2015)043.

[128] Martin Lüscher. "Properties and uses of the Wilson flow in lattice QCD". *JHEP* 08 2010, pp. 071. DOI: 10.1007/JHEP08(2010)071.

[129] Mattia Bruno, Tomasz Korzec, and Stefan Schaefer. "Setting the scale for the CLS $2 + 1$ flavor ensembles". *Phys. Rev.* D95 2017, pp. 074504. DOI: 10.1103/PhysRevD.95.074504.

[130] Stefano Capitani, Michele Della Morte, Georg von Hippel, Bastian Knippschild, and Hartmut Wittig. "Scale setting via the Ω baryon mass". *PoS* LATTICE2011 2011, pp. 145. DOI: 10.22323/1.139.0145.

[131] Renwick J. Hudspith, Matthias F. M. Lutz, and Daniel Mohler. "Precise Omega baryons from lattice QCD". 2024,

[132] K. Symanzik. "Continuum Limit and Improved Action in Lattice Theories. 1. Principles and φ^4 Theory". *Nucl. Phys. B* 226 1983, pp. 187–204. DOI: 10.1016/0550-3213(83)90468-6.

[133] K. Symanzik. "Continuum Limit and Improved Action in Lattice Theories. 2. O(N) Nonlinear Sigma Model in Perturbation Theory". *Nucl. Phys. B* 226 1983, pp. 205–227. DOI: 10.1016/0550-3213(83)90469-8.

[134] P. Weisz. "Continuum Limit Improved Lattice Action for Pure Yang-Mills Theory. 1." *Nucl. Phys. B* 212 1983, pp. 1–17. DOI: 10.1016/0550-3213(83)90595-3.

[135] M. Luscher and P. Weisz. "On-shell improved lattice gauge theories". *Commun. Math. Phys.* 98 1985, pp. 433. DOI: 10.1007/BF01205792.

[136] John Bulava and Stefan Schaefer. "Improvement of $N_f = 3$ lattice QCD with Wilson fermions and tree-level improved gauge action". *Nucl. Phys. B* 874 2013, pp. 188–197. DOI: 10.1016/j.nuclphysb.2013.05.019.

[137] Kenneth G. Wilson. "Quarks and Strings on a Lattice". In: *13th International School of Subnuclear Physics: New Phenomena in Subnuclear Physics*. Nov. 1975.

[138] Holger Bech Nielsen and M. Ninomiya. "Absence of Neutrinos on a Lattice. 1. Proof by Homotopy Theory". *Nucl. Phys. B* 185 1981, pp. 20. DOI: 10.1016/0550-3213(82)90011-6.

[139] Holger Bech Nielsen and M. Ninomiya. "Absence of Neutrinos on a Lattice. 2. Intuitive Topological Proof". *Nucl. Phys. B* 193 1981, pp. 173–194. DOI: 10.1016/0550-3213(81)90524-1.

[140] Holger Bech Nielsen and M. Ninomiya. "No Go Theorem for Regularizing Chiral Fermions". *Phys. Lett. B* 105 1981, pp. 219–223. DOI: 10.1016/0370-2693(81)91026-1.

[141] John B. Kogut and Leonard Susskind. "Hamiltonian Formulation of Wilson's Lattice Gauge Theories". *Phys. Rev. D* 11 1975, pp. 395–408. DOI: 10.1103/PhysRevD.11.395.

[142] Roberto Frezzotti, Pietro Antonio Grassi, Stefan Sint, and Peter Weisz. "A Local formulation of lattice QCD without unphysical fermion zero modes". *Nucl. Phys. B Proc. Suppl.* 83 2000, pp. 941–946. DOI: 10.1016/S0920-5632(00)91852-8.

[143] Roberto Frezzotti, Pietro Antonio Grassi, Stefan Sint, and Peter Weisz. "Lattice QCD with a chirally twisted mass term". *JHEP* 08 2001, pp. 058. DOI: 10.1088/1126-6708/2001/08/058.

[144] Roberto Frezzotti, Stefan Sint, and Peter Weisz. "O(a) improved twisted mass lattice QCD". *JHEP* 07 2001, pp. 048. DOI: 10.1088/1126-6708/2001/07/048.

[145] Paul H. Ginsparg and Kenneth G. Wilson. "A Remnant of Chiral Symmetry on the Lattice". *Phys. Rev. D* 25 1982, pp. 2649. DOI: 10.1103/PhysRevD.25.2649.

[146] P. Hasenfratz. "Prospects for perfect actions". *Nucl. Phys. B Proc. Suppl.* 63 1998, pp. 53–58. DOI: 10.1016/S0920-5632(97)00696-8.

[147] Herbert Neuberger. "More about exactly massless quarks on the lattice". *Phys. Lett. B* 427 1998, pp. 353–355. DOI: 10.1016/S0370-2693(98)00355-4.

[148] David B. Kaplan. "A Method for simulating chiral fermions on the lattice". *Phys. Lett. B* 288 1992, pp. 342–347. DOI: 10.1016/0370-2693(92)91112-M.

[149] Karl Jansen. "Overlap and domain wall fermions: What is the price of chirality?" *Nucl. Phys. B Proc. Suppl.* 106 2002, pp. 191–192. DOI: 10.1016/S0920-5632(01)01660-7.

[150] B. Sheikholeslami and R. Wohlert. "Improved Continuum Limit Lattice Action for QCD with Wilson Fermions". *Nucl. Phys. B* 259 1985, pp. 572. DOI: 10.1016/0550-3213(85)90002-1.

[151] Martin Luscher, Stefan Sint, Rainer Sommer, and Peter Weisz. "Chiral symmetry and O(a) improvement in lattice QCD". *Nucl. Phys. B* 478 1996, pp. 365–400. DOI: 10.1016/0550-3213(96)00378-1.

[152] Martin Lüscher, Stefan Sint, Rainer Sommer, Peter Weisz, and Ulli Wolff. "Nonperturbative O(a) improvement of lattice QCD". *Nucl. Phys. B* 491 1997, pp. 323–343. DOI: 10.1016/S0550-3213(97)00080-1.

[153] Karl Jansen, Chuan Liu, Martin Luscher, Hubert Simma, Stefan Sint, et al. "Nonperturbative renormalization of lattice QCD at all scales". *Phys. Lett. B* 372 1996, pp. 275–282. DOI: 10.1016/0370-2693(96)00075-5.

[154] Tanmoy Bhattacharya, Rajan Gupta, Weonjong Lee, Stephen R. Sharpe, and Jackson M. S. Wu. "Improved bilinears in lattice QCD with non-degenerate quarks". *Phys. Rev. D* 73 2006, pp. 034504. DOI: 10.1103/PhysRevD.73.034504.

[155] J. Ghiglieri, O. Kaczmarek, M. Laine, and F. Meyer. "Lattice constraints on the thermal photon rate". *Phys. Rev. D* 94 2016, pp. 016005. DOI: 10.1103/PhysRevD.94.016005.

[156] D. H. Weingarten and D. N. Petcher. "Monte Carlo Integration for Lattice Gauge Theories with Fermions". *Phys. Lett. B* 99 1981, pp. 333–338. DOI: 10.1016/0370-2693(81)90112-X.

[157] Herbert W. Hamber. "Monte Carlo Simulations of Systems With Fermions". *Phys. Rev. D* 24 1981, pp. 951. DOI: 10.1103/PhysRevD.24.951.

[158] D. J. Scalapino and R. L. Sugar. "A Method for Performing Monte Carlo Calculations for Systems with Fermions". *Phys. Rev. Lett.* 46 1981, pp. 519. DOI: 10.1103/PhysRevLett.46.519.

[159] J. Frison, R. Kitano, H. Matsufuru, S. Mori, and N. Yamada. "Topological susceptibility at high temperature on the lattice". *JHEP* 09 2016, pp. 021. DOI: 10.1007/JHEP09(2016)021.

[160] N. Metropolis, A. Rosenbluth, M. Rosenbluth, A. Teller, and E. Teller. "Equation of State Calculations by Fast Computing Machines". *The Journal of Chemical Physics* 21 1953, pp. 1087–1092. DOI: 10.1063/1.1699114.

[161] Simon Duane and John B. Kogut. "Hybrid Stochastic Differential Equations Applied to Quantum Chromodynamics". *Phys. Rev. Lett.* 55 1985, pp. 2774. DOI: 10.1103/PhysRevLett.55.2774.

[162] S. Duane and J. B. Kogut. "The Theory of Hybrid Stochastic Algorithms". *Nucl. Phys. B* 275 1986, pp. 398–420. DOI: 10.1016/0550-3213(86)90606-1.

[163] S. Duane, A. D. Kennedy, B. J. Pendleton, and D. Roweth. "Hybrid Monte Carlo". *Phys. Lett. B* 195 1987, pp. 216–222. DOI: 10.1016/0370-2693(87)91197-X.

[164] Stefan Schaefer. "Simulations with the hybrid Monte Carlo algorithm: Implementation and data analysis". In: *Les Houches Summer School: Session 93: Modern perspectives in lattice QCD: Quantum field theory and high performance computing*. Aug. 2009, pp. 401–422.

[165] Steven A. Gottlieb, W. Liu, D. Toussaint, R. L. Renken, and R. L. Sugar. "Hybrid Molecular Dynamics Algorithms for the Numerical Simulation of Quantum Chromodynamics". *Phys. Rev. D* 35 1987, pp. 2531–2542. DOI: 10.1103/PhysRevD.35.2531.

[166] A. D. Kennedy, Ivan Horvath, and Stefan Sint. "A New exact method for dynamical fermion computations with nonlocal actions". *Nucl. Phys. B Proc. Suppl.* 73 1999, pp. 834–836. DOI: 10.1016/S0920-5632(99)85217-7.

[167] M. A. Clark and A. D. Kennedy. "Accelerating dynamical fermion computations using the rational hybrid Monte Carlo (RHMC) algorithm with multiple pseudofermion fields". *Phys. Rev. Lett.* 98 2007, pp. 051601. DOI: 10.1103/PhysRevLett.98.051601.

[168] A. M. Ferrenberg and R. H. Swendsen. "New Monte Carlo Technique for Studying Phase Transitions". *Phys. Rev. Lett.* 61 1988, pp. 2635–2638. DOI: 10.1103/PhysRevLett.61.2635.

[169] Alan M. Ferrenberg and Robert H. Swendsen. "Optimized Monte Carlo analysis". *Phys. Rev. Lett.* 63 1989, pp. 1195–1198. DOI: 10.1103/PhysRevLett.63.1195.

[170] P. A. Boyle, A. Juttner, C. Kelly, and R. D. Kenway. "Use of stochastic sources for the lattice determination of light quark physics". *JHEP* 08 2008, pp. 086. DOI: 10.1088/1126-6708/2008/08/086.

[171] Philippe Boucaud et al. "Dynamical Twisted Mass Fermions with Light Quarks: Simulation and Analysis Details". *Comput. Phys. Commun.* 179 2008, pp. 695–715. DOI: 10.1016/j.cpc.2008.06.013.

[172] M. Foster and Christopher Michael. "Quark mass dependence of hadron masses from lattice QCD". *Phys. Rev. D* 59 1999, pp. 074503. DOI: 10.1103/PhysRevD.59.074503.

[173] C. McNeile and Christopher Michael. "Decay width of light quark hybrid meson from the lattice". *Phys. Rev. D* 73 2006, pp. 074506. DOI: 10.1103/PhysRevD.73.074506.

[174] Ph. Boucaud et al. "Dynamical twisted mass fermions with light quarks". *Phys. Lett. B* 650 2007, pp. 304–311. DOI: 10.1016/j.physletb.2007.04.054.

[175] J. Viehoff, N. Eicker, S. Gusken, H. Hoeber, P. Lacock, et al. "Improving stochastic estimator techniques for disconnected diagrams". *Nucl. Phys. B Proc. Suppl.* 63 1998, pp. 269–271. DOI: 10.1016/S0920-5632(97)00742-1.

[176] M. Gockeler, R. Horsley, H. Oelrich, H. Perlt, D. Petters, et al. "Nonperturbative renormalization of composite operators in lattice QCD". *Nucl. Phys. B* 544 1999, pp. 699–733. DOI: 10.1016/S0550-3213(99)00036-X.

[177] R. Frezzotti, V. Lubicz, and S. Simula. "Electromagnetic form factor of the pion from twisted-mass lattice QCD at N(f) = 2". *Phys. Rev. D* 79 2009, pp. 074506. DOI: 10.1103/PhysRevD.79.074506.

[178] Gunnar S. Bali, Sara Collins, and Andreas Schafer. "Effective noise reduction techniques for disconnected loops in Lattice QCD". *Comput. Phys. Commun.* 181 2010, pp. 1570–1583. DOI: 10.1016/j.cpc.2010.05.008.

[179] Thomas Blum, Taku Izubuchi, and Eigo Shintani. "New class of variance-reduction techniques using lattice symmetries". *Phys. Rev. D* 88 2013, pp. 094503. DOI: 10.1103/PhysRevD.88.094503.

[180] Eigo Shintani, Rudy Arthur, Thomas Blum, Taku Izubuchi, Chulwoo Jung, et al. "Covariant approximation averaging". *Phys. Rev. D* 91 2015, pp. 114511. DOI: 10.1103/PhysRevD.91.114511.

[181] Szabolcs Borsanyi et al. "Is there still any Tc mystery in lattice QCD? Results with physical masses in the continuum limit III". *JHEP* 09 2010, pp. 073. DOI: 10.1007/JHEP09(2010)073.

[182] H. T. Ding et al. "Chiral Phase Transition Temperature in (2+1)-Flavor QCD". *Phys. Rev. Lett.* 123 2019, pp. 062002. DOI: 10.1103/PhysRevLett.123.062002.

[183] Andrey Yu. Kotov, Maria Paola Lombardo, and Anton Trunin. "QCD transition at the physical point, and its scaling window from twisted mass Wilson fermions". *Phys. Lett. B* 823 2021, pp. 136749. DOI: 10.1016/j.physletb.2021.136749.

[184] Edward V. Shuryak. "Physics of the pion liquid". *Phys. Rev. D* 42 1990, pp. 1764–1776. DOI: 10.1103/PhysRevD.42.1764.

[185] J.L. Goity and H. Leutwyler. "On the Mean Free Path of Pions in Hot Matter". *Phys.Lett.* B228 1989, pp. 517. DOI: 10.1016/0370-2693(89)90985-4.

[186] J. Gasser and H. Leutwyler. "Thermodynamics of Chiral Symmetry". *Phys. Lett. B* 188 1987, pp. 477–481. DOI: 10.1016/0370-2693(87)91652-2.

[187] P. Gerber and H. Leutwyler. "Hadrons Below the Chiral Phase Transition". *Nucl. Phys. B* 321 1989, pp. 387–429. DOI: 10.1016/0550-3213(89)90349-0.

[188] A. Schenk. "Pion propagation at finite temperature". *Phys.Rev.* D47 1993, pp. 5138–5155. DOI: 10.1103/PhysRevD.47.5138.

[189] D. Toublan. "Pion dynamics at finite temperature". *Phys.Rev.* D56 1997, pp. 5629–5645. DOI: 10.1103/PhysRevD.56.5629.

[190] Robert D. Pisarski and Michel Tytgat. "Propagation of cool pions". *Phys.Rev.* D54 1996, pp. 2989–2993. DOI: 10.1103/PhysRevD.54.R2989.

[191] D. T. Son and Misha A. Stephanov. "Pion propagation near the QCD chiral phase transition". *Phys. Rev. Lett.* 88 2002, pp. 202302. DOI: 10.1103/PhysRevLett.88.202302.

[192] D. T. Son and Misha A. Stephanov. "Real time pion propagation in finite temperature QCD". *Phys. Rev. D* 66 2002, pp. 076011. DOI: 10.1103/PhysRevD.66.076011.

[193] Bastian B. Brandt, Anthony Francis, Harvey B. Meyer, and Daniel Robaina. "Chiral dynamics in the low-temperature phase of QCD". *Phys. Rev. D* 90 2014, pp. 054509. DOI: 10.1103/PhysRevD.90.054509.

[194] Bastian B. Brandt, Anthony Francis, Harvey B. Meyer, and Daniel Robaina. "Pion quasiparticle in the low-temperature phase of QCD". *Phys. Rev. D* 92 2015, pp. 094510. DOI: 10.1103/PhysRevD.92.094510.

[195] Larry D. McLerran and T. Toimela. "Photon and Dilepton Emission from the Quark - Gluon Plasma: Some General Considerations". *Phys.Rev.* D31 1985, pp. 545. DOI: 10.1103/PhysRevD.31.545.

[196] Peter Braun-Munzinger, Volker Koch, Thomas Schäfer, and Johanna Stachel. "Properties of hot and dense matter from relativistic heavy ion collisions". *Phys. Rept.* 621 2016, pp. 76–126. DOI: 10.1016/j.physrep.2015.12.003.

[197] M. Laine. "NLO thermal dilepton rate at non-zero momentum". *JHEP* 11 2013, pp. 120. DOI: 10.1007/JHEP11(2013)120.

[198] Martin Lüscher. "Advanced lattice QCD". In: *Les Houches Summer School in Theoretical Physics, Session 68: Probing the Standard Model of Particle Interactions*. Feb. 1998, pp. 229–280. arXiv: hep-lat/9802029.

[199] Bastian B. Brandt, Anthony Francis, Harvey B. Meyer, and Daniel Robaina. "The pion quasiparticle in the low-temperature phase of QCD". *PoS* CD15 2016, pp. 061. DOI: 10.22323/1.253.0061.

[200] Stephen. R. Sharpe. "Applications of Chiral Perturbation theory to lattice QCD". In: *Workshop on Perspectives in Lattice QCD*. July 2006. arXiv: hep-lat/0607016.

[201] Adrien Florio, Eduardo Grossi, Alexander Soloviev, and Derek Teaney. "Dynamics of the $O(4)$ critical point in QCD". *Phys. Rev. D* 105 2022, pp. 054512. DOI: 10.1103/PhysRevD.105.054512.

[202] P. C. Hohenberg and B. I. Halperin. "Theory of Dynamic Critical Phenomena". *Rev. Mod. Phys.* 49 1977, pp. 435–479. DOI: 10.1103/RevModPhys.49.435.

[203] Adrien Florio, Eduardo Grossi, Aleksas Mazeliauskas, Alexander Soloviev, and Derek Teaney. "Quenching through the QCD chiral phase transition". 2025,

[204] Adrien Florio, Eduardo Grossi, Aleksas Mazeliauskas, Alexander Soloviev, and Derek Teaney. "Supercooled Goldstones at the QCD chiral phase transition". 2025,

[205] Olaf Kaczmarek, Frithjof Karsch, Anirban Lahiri, Lukas Mazur, and Christian Schmidt. "QCD phase transition in the chiral limit". In: Mar. 2020. arXiv: 2003.07920 [hep-lat].

[206] Isabel Campos, Patrick Fritzsch, Carlos Pena, David Preti, Alberto Ramos, et al. "Non-perturbative quark mass renormalisation and running in $N_f = 3$ QCD". *Eur. Phys. J. C* 78 2018, pp. 387. DOI: 10.1140/epjc/s10052-018-5870-5.

[207] Daniel Mohler, Stefan Schaefer, and Jakob Simeth. "CLS 2+1 flavor simulations at physical light- and strange-quark masses". *EPJ Web Conf.* 175 2018, pp. 02010. DOI: 10.1051/epjconf/201817502010.

[208] Marco Cè et al. "Window observable for the hadronic vacuum polarization contribution to the muon $g-2$ from lattice QCD". 2022,

[209] Martin Lüscher and Stefan Schaefer. "Lattice QCD with open boundary conditions and twisted-mass reweighting". *Comput. Phys. Commun.* 184 2013, pp. 519–528. DOI: 10.1016/j.cpc.2012.10.003.

[210] Daniel Mohler and Stefan Schaefer. "Remarks on strange-quark simulations with Wilson fermions". *Phys. Rev. D* 102 2020, pp. 074506. DOI: 10.1103/PhysRevD.102.074506.

[211] Simon Kuberski. "Low-mode deflation for twisted-mass and RHMC reweighting in lattice QCD". *Comput. Phys. Commun.* 300 2024, pp. 109173. DOI: 10.1016/j.cpc.2024.109173.

[212] Neal Madras and Alan D. Sokal. "The Pivot algorithm: a highly efficient Monte Carlo method for selfavoiding walk". *J. Statist. Phys.* 50 1988, pp. 109–186. DOI: 10.1007/BF01022990.

[213] Ulli Wolff. "Monte Carlo errors with less errors". *Comput. Phys. Commun.* 156 2004, pp. 143–153. DOI: 10.1016/S0010-4655(03)00467-3.

[214] Alberto Ramos. "Automatic differentiation for error analysis of Monte Carlo data". *Comput. Phys. Commun.* 238 2019, pp. 19–35. DOI: 10.1016/j.cpc.2018.12.020.

[215] Fabian Joswig, Simon Kuberski, Justus T. Kuhlmann, and Jan Neuendorf. "pyerrors: A python framework for error analysis of Monte Carlo data". *Comput. Phys. Commun.* 288 2023, pp. 108750. DOI: 10.1016/j.cpc.2023.108750.

[216] George Backus and Freeman Gilbert. "The Resolving Power of Gross Earth Data". *Geophysical Journal International* 16 1968, pp. 169–205. DOI: 10.1111/j.1365-246X.1968.tb00216.x.

[217] Nanxiang Wen, Xuanmin Cao, Jingyi Chao, and Hui Liu. "Neutral pion masses within a hot and magnetized medium in a lattice-improved soft-wall AdS/QCD model". 2024,

[218] D. Goderidze, A. Friesen, and Yu. Kalinovsky. "Pion damping width and pion spectral function in hot pion gas". *Int. J. Mod. Phys. A* 37 2022, pp. 2250135. DOI: 10.1142/S0217751X22501354.

[219] Sourendu Gupta and Rishi Sharma. "Real time warm pions from the lattice using an effective theory". *Int. J. Mod. Phys. A* 35 2020, pp. 2030021. DOI: 10.1142/S0217751X20300215.

[220] Sourendu Gupta and Rishi Sharma. "Effective field theory for warm QCD". *Phys. Rev. D* 97 2018, pp. 036025. DOI: 10.1103/PhysRevD.97.036025.

[221] Alexei Bazavov et al. "Meson screening masses in (2+1)-flavor QCD". *Phys. Rev. D* 100 2019, pp. 094510. DOI: 10.1103/PhysRevD.100.094510.

[222] Szabolcs Borsanyi, Zoltan Fodor, Sandor D. Katz, Stefan Krieg, Claudia Ratti, et al. "Fluctuations of conserved charges at finite temperature from lattice QCD". *JHEP* 01 2012, pp. 138. DOI: 10.1007/JHEP01(2012)138.

[223] F. Karsch, K. Redlich, and A. Tawfik. "Hadron resonance mass spectrum and lattice QCD thermodynamics". *Eur. Phys. J. C* 29 2003, pp. 549–556. DOI: 10.1140/epjc/s2003-01228-y.

[224] Bastian B. Brandt, Anthony Francis, Benjamin Jäger, and Harvey B. Meyer. "Charge transport and vector meson dissociation across the thermal phase transition in lattice QCD with two light quark flavors". *Phys. Rev. D* 93 2016, pp. 054510. DOI: 10.1103/PhysRevD.93.054510.

[225] Michel Davier, Andreas Hocker, and Zhiqing Zhang. "The Physics of hadronic tau decays". *Rev.Mod.Phys.* 78 2006, pp. 1043–1109. DOI: 10.1103/RevModPhys.78.1043.

[226] Joseph I. Kapusta and Edward V. Shuryak. "Weinberg type sum rules at zero and finite temperature". *Phys. Rev.* D49 1994, pp. 4694–4704. DOI: 10.1103/PhysRevD.49.4694.

[227] Paul M. Hohler and Ralf Rapp. "Is ρ-Meson Melting Compatible with Chiral Restoration?" *Phys.Lett.* B731 2014, pp. 103–109. DOI: 10.1016/j.physletb.2014.02.021.

[228] M. Dey, V. L. Eletsky, and B. L. Ioffe. "Mixing of vector and axial mesons at finite temperature: an Indication towards chiral symmetry restoration". *Phys. Lett. B* 252 1990, pp. 620–624. DOI: 10.1016/0370-2693(90)90495-R.

[229] V. L. Eletsky and B. L. Ioffe. "On the current correlators in QCD at finite temperature". *Phys. Rev. D* 47 1993, pp. 3083–3085. DOI: 10.1103/PhysRevD.47.3083.

[230] V. L. Eletsky and B. L. Ioffe. "Next-to-leading order temperature corrections to correlators in QCD". *Phys. Rev. D* 51 1995, pp. 2371–2376. DOI: 10.1103/PhysRevD.51.2371.

[231] Thomas D. Cohen and Xiang-Dong Ji. "Chiral multiplets of hadron currents". *Phys. Rev. D* 55 1997, pp. 6870–6876. DOI: 10.1103/PhysRevD.55.6870.

[232] H. B. Meyer. "The bulk channel in thermal gauge theories". *JHEP 04 (2010) 099* 2010,

[233] J. Gasser and H. Leutwyler. "Light Quarks at Low Temperatures". *Phys. Lett. B* 184 1987, pp. 83–88. DOI: 10.1016/0370-2693(87)90492-8.

[234] David Bernecker and Harvey B. Meyer. "Vector Correlators in Lattice QCD: Methods and applications". *Eur.Phys.J.* A47 2011, pp. 148. DOI: 10.1140/epja/i2011-11148-6.

[235] S. Caron-Huot. "Asymptotics of thermal spectral functions". *Phys. Rev. D* 79 2009, pp. 125009. DOI: 10.1103/PhysRevD.79.125009.

[236] Steven Weinberg. "Precise relations between the spectra of vector and axial vector mesons". *Phys. Rev. Lett.* 18 1967, pp. 507–509. DOI: 10.1103/PhysRevLett.18.507.

[237] Bruce T. Draine. *Physics of the interstellar and intergalactic medium*. English (US). United States: Princeton University Press, Dec. 2010. ISBN: 9780691122137.

[238] Gabor David. "Direct real photons in relativistic heavy ion collisions". *Rept. Prog. Phys.* 83 2020, pp. 046301. DOI: 10.1088/1361-6633/ab6f57.

[239] A. Adare et al. "Enhanced production of direct photons in Au+Au collisions at $\sqrt{s_{NN}} = 200$ GeV and implications for the initial temperature". *Phys. Rev. Lett.* 104 2010, pp. 132301. DOI: 10.1103/PhysRevLett.104.132301.

[240] A. Adare et al. "Observation of direct-photon collective flow in $\sqrt{s_{NN}} = 200$ GeV Au+Au collisions". *Phys. Rev. Lett.* 109 2012, pp. 122302. DOI: 10.1103/PhysRevLett.109.122302.

[241] S. Afanasiev et al. "Measurement of Direct Photons in Au+Au Collisions at $\sqrt{s_{NN}} = 200$ GeV". *Phys. Rev. Lett.* 109 2012, pp. 152302. DOI: 10.1103/PhysRevLett.109.152302.

[242] A. Adare et al. "Centrality dependence of low-momentum direct-photon production in Au+Au collisions at $\sqrt{s_{NN}} = 200$ GeV". *Phys. Rev. C* 91 2015, pp. 064904. DOI: 10.1103/PhysRevC.91.064904.

[243] A. Adare et al. "Azimuthally anisotropic emission of low-momentum direct photons in Au+Au collisions at $\sqrt{s_{NN}} = 200$ GeV". *Phys. Rev. C* 94 2016, pp. 064901. DOI: 10.1103/PhysRevC.94.064901.

[244] U. A. Acharya et al. "Nonprompt direct-photon production in Au+Au collisions at $\sqrt{s_{NN}} = 200$ GeV". 2022,

[245] N. J. Abdulameer et al. "Azimuthal anisotropy of direct photons in Au+Au collisions at $\sqrt{s_{NN}} = 200$ GeV". 2025,

[246] L. Adamczyk et al. "Direct virtual photon production in Au+Au collisions at $\sqrt{s_{NN}}$ = 200 GeV". *Phys. Lett. B* 770 2017, pp. 451–458. DOI: 10.1016/j.physletb.2017.04.050.

[247] Jaroslav Adam et al. "Direct photon production in Pb-Pb collisions at $\sqrt{s_{NN}} = 2.76$ TeV". *Phys. Lett. B* 754 2016, pp. 235–248. DOI: 10.1016/j.physletb.2016.01.020.

[248] Shreyasi Acharya et al. "Direct photon elliptic flow in Pb-Pb collisions at $\sqrt{s_{\mathrm{NN}}}$ = 2.76 TeV". *Phys. Lett. B* 789 2019, pp. 308–322. DOI: 10.1016/j.physletb.2018.11.039.

[249] Charles Gale, Jean-François Paquet, Björn Schenke, and Chun Shen. "Multimessenger heavy-ion collision physics". *Phys. Rev. C* 105 2022, pp. 014909. DOI: 10.1103/PhysRevC.105.014909.

[250] Hendrik van Hees, Charles Gale, and Ralf Rapp. "Thermal Photons and Collective Flow at the Relativistic Heavy-Ion Collider". *Phys. Rev. C* 84 2011, pp. 054906. DOI: 10.1103/PhysRevC.84.054906.

[251] Frank Geurts and Ralf-Arno Tripolt. "Electromagnetic probes: Theory and experiment". *Prog. Part. Nucl. Phys.* 128 2023, pp. 104004. DOI: 10.1016/j.ppnp.2022.104004.

[252] Peter Brockway Arnold, Guy D. Moore, and Laurence G. Yaffe. "Photon emission from ultrarelativistic plasmas". *JHEP* 11 2001, pp. 057. DOI: 10.1088/1126-6708/2001/11/057.

[253] Peter Brockway Arnold, Guy D. Moore, and Laurence G. Yaffe. "Photon emission from quark gluon plasma: Complete leading order results". *JHEP* 12 2001, pp. 009. DOI: 10.1088/1126-6708/2001/12/009.

[254] Jean-François Paquet, Chun Shen, Gabriel S. Denicol, Matthew Luzum, Björn Schenke, et al. "Production of photons in relativistic heavy-ion collisions". *Phys. Rev. C* 93 2016, pp. 044906. DOI: 10.1103/PhysRevC.93.044906.

[255] Simon Turbide, Ralf Rapp, and Charles Gale. "Hadronic production of thermal photons". *Phys. Rev. C* 69 2004, pp. 014903. DOI: 10.1103/PhysRevC.69.014903.

[256] Harvey B. Meyer. "Euclidean correlators at imaginary spatial momentum and their relation to the thermal photon emission rate". *Eur. Phys. J. A* 54 2018, pp. 192. DOI: 10.1140/epja/i2018-12633-0.

[257] Marco Cè, Tim Harris, Harvey B. Meyer, Aman Steinberg, and Arianna Toniato. "Rate of photon production in the quark-gluon plasma from lattice QCD". *Phys. Rev. D* 102 2020, pp. 091501. DOI: 10.1103/PhysRevD.102.091501.

[258] Sajid Ali, Dibyendu Bala, Anthony Francis, Greg Jackson, Olaf Kaczmarek, et al. "Lattice QCD estimates of thermal photon production from the QGP". *Phys. Rev. D* 110 2024, pp. 054518. DOI: 10.1103/PhysRevD.110.054518.

[259] Anthony Francis, Benjamin Jaeger, Harvey B. Meyer, and Hartmut Wittig. "A new representation of the Adler function for lattice QCD". *Phys. Rev. D* 88 2013, pp. 054502. DOI: 10.1103/PhysRevD.88.054502.

[260] Samuel Bruno Nikolaus Ruhl. "Quark mass dependence of current-current correlators in the quark-gluon plasma". MA thesis. Johannes Gutenberg-Universität Mainz, 2023.

[261] B. B. Brandt, A. Francis, M. Laine, and H. B. Meyer. "A relation between screening masses and real-time rates". *JHEP* 05 2014, pp. 117. DOI: 10.1007/JHEP05(2014)117.

[262] Harvey B. Meyer, Marco Cè, Tim Harris, Arianna Toniato, and Csaba Török. "Deep inelastic scattering off quark-gluon plasma and its photon emissivity". *PoS* LATTICE2021 2022, pp. 269. DOI: 10.22323/1.396.0269.

[263] Marco Cè, Tim Harris, Harvey B. Meyer, and Arianna Toniato. "Deep inelastic scattering on the quark-gluon plasma". *JHEP* 03 2021, pp. 035. DOI: 10.1007/JHEP03(2021)035.

[264] Mattia Dalla Brida, Tomasz Korzec, Stefan Sint, and Pol Vilaseca. "High precision renormalization of the flavour non-singlet Noether currents in lattice QCD with Wilson quarks". *Eur. Phys. J. C* 79 2019, pp. 23. DOI: 10.1140/epjc/s10052-018-6514-5.

[265] Harvey B. Meyer. *Lattice QCD and the photon emission rate of the quark-gluon plasma*. Talk at EMMI Physics Day, GSI. 19 November 2019. 2019. URL: https://indico.gsi.de/event/9482/contributions/41038/attachments/29473/36657/meyerhEMMIdayNov2019.pdf.

[266] H. -T. Ding, A. Francis, O. Kaczmarek, F. Karsch, E. Laermann, et al. "Thermal dilepton rate and electrical conductivity: An analysis of vector current correlation functions in quenched lattice QCD". *Phys. Rev. D* 83 2011, pp. 034504. DOI: 10.1103/PhysRevD.83.034504.

[267] Gianaurelio Cuniberti, Enrico De Micheli, and Giovanni Alberto Viano. "Reconstructing the thermal Green functions at real times from those at imaginary times". *Commun. Math. Phys.* 216 2001, pp. 59–83. DOI: 10.1007/s002200000324.

[268] Frank Ferrari. "The Analytic Renormalization Group". *Nucl. Phys. B* 909 2016, pp. 880–920. DOI: 10.1016/j.nuclphysb.2016.06.003.

[269] Simon Caron-Huot, Pavel Kovtun, Guy D. Moore, Andrei Starinets, and Laurence G. Yaffe. "Photon and dilepton production in supersymmetric Yang-Mills plasma". *JHEP* 12 2006, pp. 015. DOI: 10.1088/1126-6708/2006/12/015.

[270] Bastian B. Brandt, Anthony Francis, Harvey B. Meyer, Owe Philipsen, Daniel Robaina, et al. "On the strength of the $U_A(1)$ anomaly at the chiral phase transition in $N_f = 2$ QCD". *JHEP* 12 2016, pp. 158. DOI: 10.1007/JHEP12(2016)158.

[271] Sz. Borsanyi et al. "Hadronic vacuum polarization contribution to the anomalous magnetic moments of leptons from first principles". *Phys. Rev. Lett.* 121 2018, pp. 022002. DOI: 10.1103/PhysRevLett.121.022002.

[272] T. Blum, P. A. Boyle, V. Gülpers, T. Izubuchi, L. Jin, et al. "Calculation of the hadronic vacuum polarization contribution to the muon anomalous magnetic moment". *Phys. Rev. Lett.* 121 2018, pp. 022003. DOI: 10.1103/PhysRevLett.121.022003.

[273] Antoine Gérardin, Marco Cè, Georg von Hippel, Ben Hörz, Harvey B. Meyer, et al. "The leading hadronic contribution to $(g-2)_\mu$ from lattice QCD with $N_f = 2+1$ flavours of O(a) improved Wilson quarks". *Phys. Rev. D* 100 2019, pp. 014510. DOI: 10.1103/PhysRevD.100.014510.

[274] Martin Luscher. "Local coherence and deflation of the low quark modes in lattice QCD". *JHEP* 07 2007, pp. 081. DOI: 10.1088/1126-6708/2007/07/081.

[275] Anthony Francis, Renwick J. Hudspith, Randy Lewis, and Kim Maltman. "Lattice Prediction for Deeply Bound Doubly Heavy Tetraquarks". *Phys. Rev. Lett.* 118 2017, pp. 142001. DOI: 10.1103/PhysRevLett.118.142001.

[276] Anthony Francis, Renwick J. Hudspith, Randy Lewis, and Kim Maltman. "Evidence for charm-bottom tetraquarks and the mass dependence of heavy-light tetraquark states from lattice QCD". *Phys. Rev. D* 99 2019, pp. 054505. DOI: 10.1103/PhysRevD.99.054505.

[277] R. J. Hudspith, B. Colquhoun, A. Francis, R. Lewis, and K. Maltman. "A lattice investigation of exotic tetraquark channels". *Phys. Rev. D* 102 2020, pp. 114506. DOI: 10.1103/PhysRevD.102.114506.

[278] Hirotogu Akaike. "Information Theory and an Extension of the Maximum Likelihood Principle". In: New York: Springer Science+Business Media, 1998. DOI: 10.1007/978-1-4612-1694-0_15.

[279] William I. Jay and Ethan T. Neil. "Bayesian model averaging for analysis of lattice field theory results". *Phys. Rev. D* 103 2021, pp. 114502. DOI: 10.1103/PhysRevD.103.114502.

[280] Simon Kuberski, Marco Cè, Georg von Hippel, Harvey B. Meyer, Konstantin Ottnad, et al. "Hadronic vacuum polarization in the muon g − 2: the short-distance contribution from lattice QCD". *JHEP* 03 2024, pp. 172. DOI: 10.1007/JHEP03(2024)172.

[281] Derek Teaney. "Finite temperature spectral densities of momentum and R-charge correlators in N=4 Yang Mills theory". *Phys. Rev. D* 74 2006, pp. 045025. DOI: 10.1103/PhysRevD.74.045025.

[282] Jacopo Ghiglieri, Juhee Hong, Aleksi Kurkela, Egang Lu, Guy D. Moore, et al. "Next-to-leading order thermal photon production in a weakly coupled quark-gluon plasma". *JHEP* 05 2013, pp. 010. DOI: 10.1007/JHEP05(2013)010.

[283] Peter Brockway Arnold, Guy D Moore, and Laurence G. Yaffe. "Transport coefficients in high temperature gauge theories. 2. Beyond leading log". *JHEP* 05 2003, pp. 051. DOI: 10.1088/1126-6708/2003/05/051.

[284] Giuseppe Policastro, Dam T. Son, and Andrei O. Starinets. "From AdS / CFT correspondence to hydrodynamics". *JHEP* 09 2002, pp. 043. DOI: 10.1088/1126-6708/2002/09/043.

[285] Bastian B. Brandt, Anthony Francis, Harvey B. Meyer, and Hartmut Wittig. "Thermal Correlators in the \rho\ channel of two-flavor QCD". *JHEP* 03 2013, pp. 100. DOI: 10.1007/JHEP03(2013)100.

[286] Heng-Tong Ding, Olaf Kaczmarek, and Florian Meyer. "Thermal dilepton rates and electrical conductivity of the QGP from the lattice". *Phys. Rev. D* 94 2016, pp. 034504. DOI: 10.1103/PhysRevD.94.034504.

[287] Nikita Astrakhantsev, V. V. Braguta, Massimo D'Elia, A. Yu. Kotov, A. A. Nikolaev, et al. "Lattice study of the electromagnetic conductivity of the quark-gluon plasma in an external magnetic field". *Phys. Rev. D* 102 2020, pp. 054516. DOI: 10.1103/PhysRevD.102.054516.

[288] Felix Reidt. "ALICE upgrades". *PoS* LHCP2024 2025, pp. 191. DOI: 10.22323/1.478.0191.

[289] Marco Guagnelli, Roberto Petronzio, Juri Rolf, Stefan Sint, Rainer Sommer, et al. "Nonperturbative results for the coefficients b(m) and b(a) - b(P) in O(a) improved lattice QCD". *Nucl. Phys. B* 595 2001, pp. 44–62. DOI: 10.1016/S0550-3213(00)00675-1.

[290] John Bulava, Michele Della Morte, Jochen Heitger, and Christian Wittemeier. "Non-perturbative improvement of the axial current in N_f=3 lattice QCD with Wilson fermions and tree-level improved gauge action". *Nucl. Phys. B* 896 2015, pp. 555–568. DOI: 10.1016/j.nuclphysb.2015.05.003.

[291] Jochen Heitger, Fabian Joswig, and Anastassios Vladikas. "Ward identity determination of Z_S/Z_P for $N_f = 3$ lattice QCD in a Schrödinger functional setup". *Eur. Phys. J. C* 80 2020, pp. 765. DOI: 10.1140/epjc/s10052-020-8266-2.

[292] Piotr Korcyl and Gunnar S. Bali. "Non-perturbative determination of improvement coefficients using coordinate space correlators in $N_f = 2+1$ lattice QCD". *Phys. Rev. D* 95 2017, pp. 014505. DOI: 10.1103/PhysRevD.95.014505.

[293] Gunnar S. Bali, Sara Collins, Simon Heybrock, Marius Löffler, Rudolf Rödl, et al. "Octet baryon isovector charges from Nf=2+1 lattice QCD". *Phys. Rev. D* 108 2023, pp. 034512. DOI: 10.1103/PhysRevD.108.034512.

[294] Antoine Gerardin, Tim Harris, and Harvey B. Meyer. "Nonperturbative renormalization and $O(a)$-improvement of the nonsinglet vector current with $N_f = 2+1$ Wilson fermions and tree-level Symanzik improved gauge action". *Phys. Rev. D* 99 2019, pp. 014519. DOI: 10.1103/PhysRevD.99.014519.

[295] Marco Cè, Antoine Gérardin, Georg von Hippel, Harvey B. Meyer, Kohtaroh Miura, et al. "The hadronic running of the electromagnetic coupling and the electroweak mixing angle from lattice QCD". *JHEP* 08 2022, pp. 220. DOI: 10.1007/JHEP08(2022)220.

[296] Andria Agadjanov, Dalibor Djukanovic, Georg von Hippel, Harvey B. Meyer, Konstantin Ottnad, et al. "Nucleon Sigma Terms with Nf=2+1 Flavors of O(a)-Improved Wilson Fermions". *Phys. Rev. Lett.* 131 2023, pp. 261902. DOI: 10.1103/PhysRevLett.131.261902.

[297] W.H. Press, S.A. Teukolsky, W.T. Vetterling, and B.P. Flannery. *Numerical Recipes: The Art of Scientific Computing*. 3rd ed. Cambridge University Press, 2007. ISBN: 9780521880688. URL: http://nr.com/.

List of Figures

1.1 A schematic representation of the phase diagram of QCD as a function of temperature T and baryonic chemical potential μ_B. This figure is adapted from Ref. [32]. . . 2

2.1 World data on the ratio $R(\sqrt{s})$ of the total cross-section of the e^+e^- annihilation into hadrons with that into muons. The plot is taken from Ref. [49]. 6
2.2 Running couplings from $N_f = 3$ QCD. The plot is taken from Ref. [54]. 8

3.1 A sketch of the space-time evolution of the matter produced in a heavy-ion collision. The upper plot is taken from Ref. [78], the lower from Ref. [81]. 15
3.2 **Left panel**: Mass dependence of light flavor hadron yields normalized by the spin degeneracy factor $(2J+1)$ obtained from central Pb-Pb collisions at $\sqrt{s_{NN}} = 2.76\,\text{TeV}$ of the ALICE-collaboration. The data is compared to the statistical hadronization model with a chemical freezeout temperature $T_{\text{cf}} = 156.5(1.5)\,\text{MeV}$, baryon chemical potential $\mu_B = 0.7(3.8)\,\text{MeV}$ and a volume $V = 5280(410)\,(\text{fm})^3$. **Right panel**: Chemical freezeout temperature T_{cf} (top) and baryon chemical potential μ_B (bottom) as a function of center-of-mass energies per nucleon pair $\sqrt{s_{NN}}$. The plots are taken from Ref. [91]. 17
3.3 Dilepton production via quark-antiquark annihilation for the reaction $q\bar{q} \to l^- l^+$. . . 18

4.1 The spectral function $\rho(\omega)$ in a typical interacting QFT is characterized as follows: The contribution from one-particle states is represented by a delta function at $\omega = m$, where m denotes the particle's mass, and $Z = |\langle 1|\, A(0)^\dagger\, |0\rangle|^2$ is the field-strength renormalization factor quantifying the overlap strength of the operator with that single-particle state. In contrast, multiparticle states generate a continuous spectrum starting at a threshold of $2m$. Additionally, bound states may be present in the system. At finite temperature, energy can be exchanged with the heat bath; consequently, the discrete peaks broaden into Breit-Wigner type curves. This figure is inspired by Ref. [97]. 25

5.1 Schematic representation of a two-dimensional Euclidean lattice with lattice spacing a. The fermion fields are positioned at the lattice site n, while the link variable $U_\mu(n)$ connects adjacent sites n and $n+\hat{\mu}$. The plaquette variable $U_{\mu\nu}(n)$ is defined as the oriented product of four link variables encircling an elementary square in the $(\hat{\mu}$-$\hat{\nu})$–plane. The circle indicates the direction in which the link variables are traversed. 27
5.2 Visualization of the clover term $Q_{\mu\nu}(x)$ on the lattice, given by the sum of four plaquettes in the $(\hat{\mu}, \hat{\nu})$-plane, [cf. Eq. (5.4.41)]. 38

6.1 A sketch of the trajectory of the pion pole within the pseudoscalar retarded correlator $G_P^R(\omega, \mathbf{p}, T)$ is illustrated on the $(\omega, \mathbf{p})$-plane, whereby the slope corresponds to the squared pion velocity $u^2(T)$. The figure is inspired by Ref. [199]. 56
6.2 Qualitative features of the low-energy poles in the spectral function of the axial charge, in the broken and in the restored phase. 59
6.3 Renormalized PCAC mass in the `E250Nt24` ensemble along the τ and x_3 direction. The final result—obtained from a fit along the x_3 direction—is also shown with a $1-\sigma$ band. We have used the improved axial current together with the symmetrized derivative [see Eqs. (B.3-B.5)]. 62

6.4 Renormalized PCAC masses in the E250Nt20 ensemble (**left**) and E250Nt16 ensemble (**right**) along the τ and x_3 direction. For the E250Nt20 ensemble we used $\mathcal{O}(a)$-improvement of the axial current and the symmetrized derivative [see Eqs. (B.3-B.5)]. In contrast, the PCAC mass on E250Nt16 (**right**) was determined using the unimproved version of the axial current. 63

6.5 Comparison of the integrated autocorrelation times τ_{int} for the AP-correlator at fixed source-sink separation $x_3/a = 10$. The l.h.s. shows the correlator on the hadronic E250Nt24 ensemble and the r.h.s. shows the correlator on the chiral crossover ensemble E250Nt20. 64

6.6 **Left panel**: Examples of resolution functions for different values of λ, centered around $\bar{\omega}/T$. **Right panel**: Estimator of the spectral function $\hat{\rho}_{A_0}(\omega, T = 128\,\text{MeV})/(f\,T^2)$. The blue dashed line corresponds to the location of the expected position of the pole ω_0 according to Eq. (6.2.16). The temporal $G_{A_0}(\tau, T)$-correlator is $\mathcal{O}(a)$-improved. 68

6.7 **Left panel**: Estimator of the spectral function $\hat{\rho}_{A_0}(\omega, T = 154\,\text{MeV})/(f\,T^2)$. The blue dashed line corresponds to the location of the expected position of the pole ω_0 according to Eq. (6.2.16). The temporal $G_{A_0}(\tau, T)$-correlator is $\mathcal{O}(a)$-improved. **Right panel**: Estimator of the spectral function $\hat{\rho}_{A_0}(\omega, T = 192\,\text{MeV})/(f\,T^2)$. The blue dashed line corresponds to the location of the expected position of the pole ω_0 according to Eq. (6.2.16). 68

6.8 Both plots show results from the hadronic E250Nt24 ensemble. **Left panel**: Effective mass plot for the cosh mass $m_{\text{cosh}}(x_0)/T$ as a function of the x_0-coordinate in temperature units, obtained from the temporal axial correlation function at zero spatial momentum $G_{A_0}(x_0, T)$. **Right panel**: The blue bars correspond to the lattice data of the temporal $G_{A_0}(x_0, T)$-correlator in the hadronic phase, while the red bars represent the prediction of the aforementioned correlator in terms of the screening quantities f_π and m_π. The green band represents the result of a direct one-state fit to the temporal correlator. From this fit we obtain $\omega_0/T = 0.91(9)$. 69

6.9 **Top panel**: Screening vector and axial-vector effective masses at $T = 128\,\text{MeV}$. **Middle panel**: Screening vector and axial-vector effective masses at $T = 154\,\text{MeV}$. **Bottom panel**: Screening vector and axial-vector effective masses at $T = 192\,\text{MeV}$. The bands represent correlated fits to the plateau, while the green dashed line represents the $2\pi T$ limit. Furthermore, the values for the screening masses obtained from a direct fit of the axial-vector and vector correlators are also included and represented by a single light bar. The violet dotted line represents the free two-pion states (for $T = 128\,\text{MeV}$ and $T = 154\,\text{MeV}$). 71

6.10 QNS extracted from the local vector current correlator, Eq. (6.7.1). For comparative purposes, $G_{A_0}(\tau, T)$ and its theoretical prediction based on screening quantities are presented. The top panel illustrates the QNS at a temperature of $T = 128\,\text{MeV}$, the middle panel at $T = 154\,\text{MeV}$, and the bottom panel at $T = 192\,\text{MeV}$. The correlators depicted in these figures follow the normalization specified in Eq. (6.7.1), which introduces an additional factor of 2, except for $G_{A_0}(\tau, T = 128\,\text{MeV})$, as noted in the legend, to enhance visibility. 74

6.11 Relative composition of the total QNS predicted by the HRG model in the hadronic phase (**left panel**) and at the chiral crossover (**right panel**). 76

6.12 **Top panel**: Ratio of the difference '$V - A$' [see Eqs. (6.2.13)-(6.2.14)] and the difference of the reconstructed correlator '$(V - A)_{\text{rec}}$' [see Eq. (6.8.9)] at $T = 128\,\text{MeV}$. **Middle panel**: Same quantity at $T = 154\,\text{MeV}$. **Bottom panel**: Same quantity at $T = 192\,\text{MeV}$. The green band shows the result of a correlated fit to the plateau. . . 79

6.13 **Top panel**: The Backus-Gilbert analysis of the difference between the vector and axial-vector channels, as defined in Eqs. (6.2.13)-(6.2.14), is presented. The Backus-Gilbert spectral function $\hat{\rho}^{\text{rec}}_{V-A}(\omega)/(f\,T^2)$, derived from the reconstructed '$V - A$' correlator, is depicted as a blue band at temperatures of $T = 128\,\text{MeV}$ and $154\,\text{MeV}$ for the left and right panels, respectively. The corresponding estimator of the thermal spectral function $\hat{\rho}^{\text{ther}}_{V-A}(\omega)/(f\,T^2)$ is illustrated as a red band. For reference, the blue vertical line indicates the physical mass of the ρ meson, while the red vertical line denotes the vector screening mass at the respective temperature [see Table 6.5]. The underlying temporal vector correlators are $\mathcal{O}(a)$-improved. **Bottom panel**: The ratio of the estimators of the thermal and reconstructed spectral functions is shown, accompanied by the $1-\sigma$ band (dark green) and the $2-\sigma$ band (light green). The red horizontal dashed line represents the $1-\sigma$ band at the correlator level [see top and middle panel of Fig. 6.12]. 81

6.14 **Top panels**: The l.h.s. shows the smeared spectral function of the difference between the finite temperature and reconstructed zero-temperature temporal vector correlators [defined in Eq. (6.2.14))] projected to zero momentum at a temperature $T = 128\,\text{MeV}$. The r.h.s shows the same quantity for the temporal axial-vector correlators [defined in Eq. (6.2.13)] projected to zero momentum. **Middle panels**: The same quantities at a temperature $T = 154\,\text{MeV}$. **Bottom panels**: Again the same quantities at a temperature $T = 192\,\text{MeV}$. 83

7.1 Sources of photons in a relativistic heavy ion collision. Figure is taken from Ref. [4] and was created by Csaba Török. 87

7.2 Sketch of the different kinematic regimes relevant for the electrical conductivity, and for photon and dilepton production rates. The four-momentum of the (virtual) photon is denoted by $\mathcal{K} = (\omega, \mathbf{k})$, which is measured in the rest frame of the thermal medium. The figure is adapted from Ref. [265]. 97

7.3 **Left panel:** Integration kernels appearing in Eqs. (7.4.6) and (7.4.7), which multiply the transverse channel spectral function at light-like kinematics, $\frac{\sigma_{\mathrm{em}}}{\omega}$ [see Eq. (7.2.1)]. **Right panel:** Spectral function at light-like kinematics normalized by $2\chi_q\omega/T$, shown for QCD at complete LO from Refs. [252, 253] and for the strongly-coupled $\mathcal{N}=4$ SYM theory [269]. 99

8.1 **Left column:** Effective masses based on Eq. (I.6) for the ratios of the non-static and static screening correlators in the first Matsubara sector ω_1. **Right column:** Effective masses and fit results from two-state fits with the fit ansatz Eq. (7.3.1) for the non-static (blue) and static (red) screening correlators at spatial momentum $\omega_1 = 2\pi T$ with $T \in \{128, 154, 192\}$ MeV. 102

8.2 The temperature dependence of the integrand, as defined in Eq. (7.2.21) with $\Omega_n = \omega_n$, corresponding to the quantity $H_E(\omega_1, T)$, is presented. All values are expressed in temperature units and were derived using the `E250` ensembles. For enhanced visibility, data points at varying temperatures are slightly offset along the x_1-axis. . . 104

8.3 Symmetrized integrands and their modeled tail contributions for three temperatures $T \in \{128, 154, 192\}$ MeV. **Left column:** x_1-symmetrized integrand $h_E(\omega_1, x_1)$ from Eq. (7.2.21) with its modeled tail from Eq. (7.3.2). **Right column:** x_1-symmetrized integrand $h_{Q^2}(\omega_1, x_1)$ from Eq. (7.2.32) with an analogous modeled tail. 106

8.4 Lower and upper bounds on $H_E(\omega_1)$ at a temperature $T = 154$ MeV, based on Eqs. (8.2.5) and (8.2.6). These bounds converge toward that quantity for $x_{\mathrm{cut}} \to \infty$. . 107

9.1 Comparison of the integrand $-h_E^{\mathrm{ps}}(\omega_2, x_1)$ $(k = \infty)$ used in [6] with $-h_E^{\mathrm{ws}}(\omega_2, x_1)$ utilized in this thesis, for the coarsest ensemble O7. At $x_1 = 15a$, the statistical error is reduced by a factor of ≈ 6.5. 110

9.2 **First three panels:** Effective masses for the completely static (zero momentum) local-local isovector vector correlator on the three ensembles O7, W7, and X7. The light green horizontal band indicates the fit result derived from the ansatz in Eq. (7.3.1). **Last panel:** Corresponding continuum extrapolation. 111

9.3 **First three panels:** Effective masses (represented by red bars) for the static local-local isovector vector correlator in the first Matsubara sector are depicted for the O7, W7, and X7 ensembles. The red horizontal band indicates the fit result derived using the ansatz specified in Eq. (7.3.1). For comparative purposes, effective masses from the earlier point-source data presented in Ref. [6] are illustrated as blue bars. For this comparison, the outlier elimination procedure detailed in Appendix A of Ref. [6] has not been applied. **Last panel:** The corresponding continuum extrapolation is shown, alongside the prediction derived from the dispersion relation [cf. Eq. (9.2.4)]. 113

9.4 **First three panels:** Effective masses (red bars) for the non–static local–local isovector vector correlator in the first Matsubara sector on the O7, W7, and X7 ensembles. The red horizontal line indicates the fit result from ansatz Eq. (7.3.1). For comparison, effective masses from the earlier point–source data of Ref. [6] are shown as blue bars. **Last panel:** Corresponding continuum extrapolation, shown together with the EQCD prediction of Ref. [261]. 114

9.5 Integrand $-h_E(\omega_1, x_1)/T^3$ from Eq. (7.2.21) computed on the finest ensemble X7 using the standard cosh-kernel [$k = \infty$ in Eq. (7.2.19)]. The result includes the tail modification from Eq. (7.3.2). The red vertical line marks the source–sink separation $x_1 T = 1$; here the relative error on the integrand is 0.7%. For the largest values of x_1, the influence of the variable's periodicity is evident. 115

9.6 **Left panel:** Continuum extrapolation of $-H_E(\omega_1)/T^2$ using the standard cosh kernel ($k = \infty$ in Eq. (7.2.19)). **Right panel:** Continuum extrapolation of $-H_E(\sin(\omega_1))/T^2$ using the modified cosh(sin)-kernel ($k = 1$ in Eq. (7.2.19)). 116

9.7 **Top panel:** The integrand $-h_{Q^2}(\omega_1, x_1)$ from Eq. (7.2.32), which contributes to the derivative of $-H_E(\omega_1, Q^2)$ w.r.t. Q^2 at $Q^2 = 0$, is depicted for the X7 ensemble. The result incorporates the tail modification analogous to Eq. (7.3.2). The red vertical line indicates the source–sink separation $x_1 T = 1$. **Bottom panel:** Corresponding continuum extrapolation of $-\frac{\mathrm{d}}{\mathrm{d}Q^2}[H_E(\omega_1, Q^2) - H_E(0, Q^2)]|_{Q^2=0}$. 117

9.8 **Left panel:** The effective mass gap between the non-static and static screening masses in the second Matsubara channel, as derived from the correlator ratio on the X7 ensemble. **Right panel:** The corresponding continuum extrapolation. 117

9.9 **Left panel:** The effective mass of the static local-local isovector vector correlator in the second Matsubara sector on the X7 ensemble. Additionally, effective masses derived from fits using the ansatz (7.3.1) are presented both *with* a prior (red bars) and *without* a prior (green bars). The dark red horizontal line represents the dispersive prediction (9.2.5). For comparative purposes, effective masses from the earlier point-source data of Ref. [6] are illustrated as light blue bars. **Right panel:** Corresponding continuum extrapolation together with the dispersive prediction. 118

9.10 **Left panel:** The effective mass of the non-static local-local isovector vector correlator in the second Matsubara sector on the X7 ensemble is. Additionally, effective masses derived from fits using the ansatz (7.3.1) are presented both *with* a prior (red bars) and *without* a prior (green bars), alongside the EQCD prediction from Ref. [261] (dark blue band). For comparative purposes, results from the earlier point–source data of Ref. [6] are illustrated as light–blue bars. **Right panel:** Corresponding continuum extrapolation, including the EQCD prediction from Ref. [261]. 118

9.11 The effective masses, as defined in Eq. (I.6), for the ratios of the $n = 2$ to the $n = 1$ Matsubara sector screening correlators are presented for both the static (**left column**) and non-static (**right panel**) scenarios, on ensembles O7, W7, and X7. The green bars represent the effective masses derived from a single exponential fit, of the correlator ratios $G_i^{\mathrm{T}}(\omega_2, x_1)/G_i^{\mathrm{T}}(\omega_1, x_1)$. **Bottom row:** Corresponding continuum extrapolations. 119

9.12 The deviation of the $n = 1$ and $n = 2$ static screening masses (represented by blue bars) from the continuum relativistic dispersion relation (9.2.3) is depicted at finite lattice spacing across the three ensembles O7, W7, and X7 (expressed in lattice units). For comparative purposes, the non-static screening masses are also displayed (indicated by green bars), although no corresponding continuum dispersion relation exists for them. 120

9.13 **Left panel:** The effective mass [cf. Eq. (I.6)] and the fit results for the static correlators at spatial momenta ω_0, ω_1, and ω_2 on the X7 ensemble. **Right panel:** The effective mass and the fit results for the non-static screening correlator in the $n = 1$ and $n = 2$ Matsubara sector. 121

9.14 Standard-subtracted integrands $-h_E(\omega_2, x_1)$ [cf. Eq. (7.2.21)] with different kernel modifications based on the parameter k [cf. Eq. (7.2.19)] as well as $-h_E(\omega_1, x_1)$ on the finest ensemble X7. 123

9.15 **Top panel:** Integrands $-h_E(\Omega_n(k), x_1)/T^3$ for $k \in \{1, \frac{3}{2}, \infty\}$, alongside the interpolation between the prescriptions $k = \infty$ and $k = 1$ at $x_1 T = 1$, with $d \approx 0.15\,\mathrm{fm}$ as specified in Eq. (M.1). These integrands are depicted on the X7 ensemble, incorporating the tail modification. **Bottom panel:** A simultaneous (uncorrelated) continuum extrapolation is conducted with a shared intercept for $-H_E(\omega_2)/T^2$, utilizing priors from the "ratio method". The resulting value $[-H_E(\omega_2)/T^2]^{\text{uncorr.}}_{\text{w/ prior}} = 0.899(51)_{\text{stat}}$ demonstrates strong agreement with our previously reported MAV result (9.4.16). 124

9.16 **Left panel:** Integrand entering the difference of the H_E quantities in Eq. (9.4.20) on the ensemble W7, together with its tail extension analogous to Eq. (7.3.2). The vertical red line marks the separation x_1 at which the cumulative integral of Eq. (9.4.20) changes sign and becomes positive. **Right panel:** Corresponding continuum extrapolation. 126

9.17 Integrand for extracting $H_E(\omega_n)$ from the free continuum theory (blue dashed line) and from lattice QCD combined with the tail modification of Eq. (7.3.2) on the finest ensemble X7 (red solid line). **Left panel:** $n = 1$ sector with the local-local discretization of the vector current **Right panel:** $n = 2$ sector with the local-local discretization of the vector current. In both panels, only central values are displayed. 127

9.18 **Left panel:** The results for $H_E(\omega_1)$ are compared across several frameworks: lattice QCD, leading-order weak coupling with $\alpha_s = 0.25$ (left point) and $\alpha_s = 0.31$ (right point), the free theory, and strongly coupled $\mathcal{N} = 4$ SYM. The values are presented normalized either to the non-interacting susceptibility (*left column*) or to the interacting susceptibility (*right column*). For the free-theory points, both normalizations coincide, whereas for the weak-coupling prediction, we utilize either unity or the lattice value $\chi_q/T^2 = 0.882$ [5]. **Right panel:** A comparison is made for the difference $H_E(\omega_2) - H_E(\omega_1)$, employing the same normalization choices. 128

9.19 Spectral functions derived from the weak-coupling result [253] at two values of α_s are supplemented for $\omega < \omega_{\mathrm{m}}$ with a Lorentzian, selected to replicate our lattice result for $H_E(\omega_1)$ as presented in Eq. (9.3.8). The vertical lines indicate the matching points $\omega = \omega_{\mathrm{m}}$, while the dashed curves represent the unmodified weak-coupling form [also depicted in the right panel of Fig. 7.3]. For comparison, we additionally show the spectral function in strongly-coupled $\mathcal{N} = 4$ SYM theory [269]. The intercept at $\omega = 0$ provides the corresponding isospin diffusion coefficient $T \cdot D$. 130

9.20 **First row:** Effective masses of the static (red bars) and non-static (blue bars) local-local isovector vector correlator in the third Matsuara sector for the O7, W7, and X7 ensembles. The horizontal bands represent the fit result derived from the ansatz (7.3.1). **Second row:** Continuum extrapolations of the same quantities 131

9.21 **Left panel:** Standard-subtracted integrands $-h_E(\Omega_n(k), x_1)/T^3$ [cf. Eq. (7.2.21) with $n \in \{1,2,3\}$ and $k = \frac{3}{2}$] on the finest ensemble X7. **Right panel:** The same quantity for $n = 3$ and $k \in \{1, \frac{3}{2}, 2, \infty\}$. 132

9.22 **First three panels:** Integrands $-h_E(\Omega_3(k = 3/2), x_1)/T^3$ from Eq. (7.2.21), computed for three ensembles: O7, W7, and X7. The results incorporate the tail modification as described in Eq. (7.3.2). **Last panel:** Corresponding continuum extrapolation. 133

23 The Bose distribution function $n_B(z)$ generates poles at $z = i\omega_n$ (indicated by blue dots), which are traversed in a counterclockwise direction. Upon deforming the contour, the pole at $z = \omega$ is traversed in a clockwise direction, resulting in a negative residue. X

24 **Left panel**: Integrated autocorrelation time ($S = 6$) of the PCAC mass at fixed source-sink separation $x_3/a = 20$ on the `E250Nt20` ensemble at the chiral crossover. **Right panel**: Comparison of the PCAC mass obtained from binning and jackknife procedure with the corresponding PCAC mass obtained using the gamma method in the implementation of the `pyerrors` package on the `E250Nt20` ensemble at the chiral crossover. XIII

25 Integrated autocorrelation time for the cosh mass, defined in Eq. (I.6) at source-sink separation $x_3 = 20$, well in the region where a plateau is observed (see middle plot of Fig. 29) XIV

26 **Upper panel**: Screening correlator $G_A^s(x_3, T = 154\,\mathrm{MeV})$ [defined in Eq. (6.2.5)] together with the corresponding fit. **Left panel**: Integrated autocorrelation time τ_{int} for f_π determined as described in Sec. 6.3.2. **Right panel**: Integrated autocorrelation time τ_{int} for f_π determined from $G_A^s(x_3, T)$. XVII

27 The blue points denote the jackknife sample of the static correlator $G_{\mathrm{st}}^{\mathrm{T}}(\omega_1, x_1)$ on the $N_\tau = 20$ ensemble at $T = 154\,\mathrm{MeV}$, obtained by removing one of the outlier configurations. The green points represent the median and median absolute deviation scaled by appropriate factors described in the text. XIX

28 Renormalized screening correlation functions in temperature units $G_P^s(x_3,T)/T^3$ (l.h.s) and $G_{AP}^s(x_3,T)/T^3$ (r.h.s.) and the result of the simultaneous fit. **Top panels**: Correlators measured on the hadronic `E250Nt24` ensemble. **Middle panels**: Correlators measured on the chiral crossover `E250Nt20` ensemble. **Bottom panels**: Correlators measured on the high-temperature `E250Nt16` ensemble. XXI

29 Effective mass plots for the cosh mass $m_{\cosh}(x_3)/T$ as a function of the x_3-coordinate in temperature units, obtained from the pseudoscalar screening correlation function at zero spatial momentum $G_P^s(x_3,T)$. For comparison the value for the screening pion mass m_π/T, obtained from a simultaneous fit of the pseudoscalar and axial-pseudoscalar correlator is also included (green bars). **Top panel**: Hadronic `E250Nt24` ensemble. The effective mass plateau is assumed to start at $x_3/a = 25$. **Middle panel**: `E250Nt20` ensemble at the chiral crossover. The effective mass plateau is assumed to start at $x_3/a = 18$. **Bottom panel**: `E250Nt16` ensemble in the high-temperature phase. It is assumed that the effective mass plateau starts at $x_3/a = 18$. For all three ensembles he result of the fit to the effective mass values is represented by a $1-\sigma$ band. XXII

30 Ratios of the temporal thermal (PA_0)-correlators and the reconstructed correlator (PA_0)-correlator. **Top and middle panel**: Results for the `E250Nt24` and `E250Nt20` ensembles, respectively. The blue band shows the result of a correlated fit to the plateau. In both cases the $(PA_0)-$correlators have been $\mathcal{O}(a)$-improved. **Bottom panel**: Result for the `E250Nt16` ensemble. Because there is no clear plateau visible we quote the result for $\tau/a = 7$. In the high-temperature phase the $(PA_0)-$correlators have not been $\mathcal{O}(a)$-improved. XXV

31 **L.h.s.**: The improved thermal correlator for the difference '$(V-A)$'. The top, middle, and bottom panels show the results in the hadronic phase, finite-temperature crossover, and high-temperature phase, respectively. **R.h.s.**: The corresponding reconstructed correlators [following Eq. (6.8.9)] for the $\mathcal{O}(a)-$improved difference '$(V-A)$'. All correlators have been renormalized and the corresponding ratios are shown in Fig. 6.12. XXVI

32 Fit results along with the ratio prediction [finite lattice spacing pendant of Eqs. (9.4.8)-(9.4.9)] for the ground-state static (top) and non-static (bottom) screening masses in the second Matsubara channel on O7. The fit range is set by choosing $x_1^{\max}/a$ as the first point where the correlator is consistent with zero, while $x_1^{\min}/a$ is varied systematically. One-, two-, and three-state fits are shown; for the two-state case, simultaneous fits to static and non-static amplitudes are also included. Grayed-out points correspond to fits with p-value > 0.95 or < 0.05. XXVII

33 **Top panel:** Leading-order lattice perturbation theory prediction for the standard subtracted correlator (using the local discretization of the vector current) with the cosh-kernel (dashed lines) and with the modified ($k = 1$) sine-kernel (solid line) in the free theory for the second Matsubara sector ω_2. **Bottom panel:** Comparison of modifications with different k-values for the $\beta/a = 24$ case. XXVIII

34 Effective screening masses for the completely static (zero-momentum) local–local transverse isovector vector (dark red) and axial-vector (light red) correlator, as well as the scalar (dark green) and pseudoscalar (light green) correlator, on the X8 ensemble at $T \approx 1.4\,\mathrm{GeV}$. The horizontal bands indicate the fit results obtained from the ansatz in Eq. (7.3.1). For orientation, the black dashed line denotes the 2π limit. We observe clear mass degeneracy within the V/A and S/P chiral partner channels. . . . XXIX

35 The effective masses, as defined in Eq. (I.6), for the ratios of the static $n = 1$ to $n = 0$ Matsubara-sector screening correlators (**left panel**) and the ratio of the $n = 1$ non-static to static (**right panel**) screening correlators on the X8 ensemble. The bars represent the effective masses derived from a single exponential fit. XXX

36 **Left panel:** Effective screening masses in the first Matsubara sector for static and non-static transverse isovector vector (dark colors) and axial-vector (light colors) correlators on the X8 ensemble at $T \approx 1.4\,\mathrm{GeV}$. The horizontal bands indicate the fit results from Eq. (7.3.1). Again, we observe clear mass degeneracy within the V/A chiral partner channel. **Right panel:** Standard-subtracted integrands $-h_E(\omega_1, x_1)$ [cf. Eq. (7.2.21)] with different kernel modifications based on the parameter k [cf. Eq. (7.2.19)] together with the tail modification from Eq. (7.3.2). For comparison also the free continuum prediction is shown as a dashed blue line. . . XXXI

37 The effective screening masses in the ω_2-sector are shown for both the static (**left panel**) and non-static (**right panel**) transverse isovector vector correlators on the X8 ensemble at $T \approx 1.4\,\mathrm{GeV}$. The horizontal bands represent the fit results derived from Eq. (7.3.1), both without (dark color) and with priors from the "ratio method". In the static scenario, the dispersive prediction (illustrated as a dashed red line) is in very good agreement with the unpriored fit result. XXXII

38 The effective masses, as defined in Eq. (I.6), for the ratios of the static (red) and non-static (blue) $n = 2$ to $n = 1$ Matsubara-sector screening correlators (**left panel**) and the ratio of the $n = 2$ non-static to static (**right panel**) screening correlators on the X8 ensemble. The bars denote the effective masses obtained from a single exponential fit. XXXIII

39 **Left panel:** Standard-subtracted integrands $-h_E(\omega_2, x_1)$ [cf. Eq. (7.2.21)] with different kernel modifications based on the parameter k [cf. Eq. (7.2.19)] as well as the free continuum prediction on the X8 ensemble. **Right panel:** The integrand $-h_E(\Omega_n(k = \frac{3}{2}), x_1)/T^3$, along with the tail modification from Eq. (7.3.2), is shown on the X8 ensemble. The value $k = \frac{3}{2}$ is selected since it has led to the smoothest continuum extrapolation at $T \approx 250\,\mathrm{MeV}$. The blue band represents the unpriored tail modification, whereas the red band illustrates the tail modification incorporating a prior derived from the "ratio method". XXXIII

List of Tables

2.1 Quark flavors and their charges and masses, taken from Ref. [52] 7

6.1 Parametric size, in terms of the average up-down quark mass m_q, of the low-energy contribution vs. the rest in the axial charge density and in the pseudoscalar density Euclidean-time dependent correlators at zero spatial momentum and $\tau = \beta/2$. The left part of the table concerns the chirally broken phase, and the right-hand part the restored phase. 60

6.2 Parameters and lattice spacing of the ensembles analyzed in this study. The lattice spacing has been determined in Ref. [129]. 61

6.3 Summary of the results of the E250 thermal ensembles with $N_\tau \in \{24, 20, 16\}$. The static screening quantities m_π and f_π are defined by Eq. (6.2.5), and in practice have been computed according to Eq. (I.5). The two estimators u_f and u_m for the pion velocity parameter are defined in Eqs. (6.2.19)- and (6.2.20) and should agree in the broken phase up to higher-order effects in the chiral expansion. The pion quasiparticle mass $\omega_\mathbf{0}$ is calculated using $\omega_\mathbf{0} = u_m m_\pi$ and the corresponding decay constant using $f_\pi^t = f_\pi / u_m$. 65

6.4 Dependence of the pion velocity estimator u_f on a finite pion thermal width $\Gamma(T)$ [see Eq. (6.3.7)] on the E250 thermal ensembles with $N_\tau \in \{24, 20, 16\}$. 66

6.5 Comparison of the screening masses in the $u\bar{d}$ channel extracted at temperatures $T \in \{128, 154, 192\}$ MeV to the continuum-extrapolated results obtained by the HotQCD collaboration [see Ref. [221], Table X]. 72

8.1 Static and non-static screening masses in the $n = 1$ Matsubara sector, extracted from two-state fits using the ansatz in Eq. (7.3.1). We also report the mass gap $\Delta m_{\mathrm{ns-st}}^{0,\mathrm{ratio}}/T \equiv [m_{\mathrm{ns}}^{0,\mathrm{ratio}}(\omega_1) - m_{\mathrm{st}}^{0,\mathrm{ratio}}(\omega_1)]/T$, obtained from a single-exponential fit to the correlator ratio $G_{\mathrm{ns}}^{\mathrm{T}}(\omega_1, x_1)/G_{\mathrm{st}}^{\mathrm{T}}(\omega_1, x_1)$. For comparison, we also list the completely static (i.e., zero momentum) screening masses [see also Table 6.5 and Fig. 6.9]. All results are expressed in temperature units and were obtained on the E250 ensembles with $N_\tau \in \{24, 20, 16\}$, corresponding to $T \in \{128, 154, 192\}$ MeV. . 101

8.2 Results of the temperature scan conducted around the chiral crossover of the standard-subtracted quantity $H_E(\omega_1)$ [cf. Eq. (7.2.20)] in the $n = 1$ Matsubara sector. Additionally, we report the associated virtuality dependence, defined as $-H_{Q^2}(\omega_1, Q^2) \equiv -\frac{\mathrm{d}}{\mathrm{d}Q^2}[H_E(\omega_1, Q^2) - H_E(0, Q^2)]_{Q^2=0}$ [cf. Eq. (7.2.27)]. All quantities are expressed in temperature units. The results are derived from the E250 ensembles with $N_\tau \in \{24, 20, 16\}$, corresponding to $T \in \{128, 154, 192\}$ MeV. 104

9.1 Overview of the $N_f = 2$ ensembles used in this study. The parameters given are the bare gauge coupling g_0, the Wilson hopping parameter κ, the lattice spacing a, the temporal size β in units of the lattice spacing a, the number of configurations N_{con}, and the total number of Dirac operator inversions N_{inv} for the first and second Mastubara sectors. 110
2 Summary of the non-singlet renormalization and improvement parameters. XII
3 Comparison of the E250 unimproved and improved PCAC masses for $N_\tau \in \{24, 20, 16\}$. XVIII
4 Temporal symmetrized '$V - A$' correlators projected to zero momentum. All errors quoted are purely statistical. The correlators are renormalized and quoted in units of temperature (i.e. scaled by a factor N_τ^3). XXIV
5 „Nutzung KI-Tools XXXVI